MPM SCIENTIFIC JOURNAL

ISSN 1605-2730
E-ISSN 1605-8119

MATERIALS PHYSICS AND MECHANICS

Vol. 50, No. 3, 2022

MATERIALS PHYSICS AND MECHANICS

Principal Editors:

Dmitrii Indeitsev
Institute of Problems of Mechanical Engineering of the Russian Academy of Science (RAS), Russia

Andrei Rudskoi
Peter the Great St.Petersburg Polytechnic University, Russia

Founder and Honorary Editor: Ilya Ovid'ko (1961-2017)
Institute of Problems of Mechanical Engineering of the Russian Academy of Sciences (RAS), Russia

Associate Editors:

Anna Kolesnikova
Institute of Problems of Mechanical Engineering of the Russian Academy of Sciences (RAS), Russia

Aleksandra Romashkina
Peter the Great St.Petersburg Polytechnic University, Russia

Editorial Board:

E.C. Aifantis
Aristotle University of Thessaloniki, Greece
K.E. Aifantis
University of Florida, USA
U. Balachandran
Argonne National Laboratory, USA
A. Bellosi
Research Institute for Ceramics Technology, Italy
A.K. Belyaev
Institute of Problems of Mechanical Engineering (RAS), Russia
S.V. Bobylev
Institute of Problems of Mechanical Engineering (RAS), Russia
A.I. Borovkov
Peter the Great St.Petersburg Polytechnic University, Russia
G.-M. Chow
National University of Singapore, Singapore
Yu. Estrin
Monash University, Australia
A.B. Freidin
Institute of Problems of Mechanical Engineering (RAS), Russia
Y. Gogotsi
Drexel University, USA
I.G. Goryacheva
Institute of Problems of Mechanics (RAS), Russia
D. Hui
University of New Orleans, USA
G. Kiriakidis
IESL/FORTH, Greece
D.M. Klimov
Institute of Problems of Mechanics (RAS), Russia
G.E. Kodzhaspirov
Peter the Great St.Petersburg Polytechnic University, Russia
S.A. Kukushkin
Institute of Problems of Mechanical Engineering (RAS), Russia
T.G. Langdon
University of Southampton, U.K.
V.P. Matveenko
Institute of Continuous Media Mechanics (RAS), Russia
A.I. Melker
Peter the Great St.Petersburg Polytechnic University, Russia
Yu.I. Meshcheryakov
Institute of Problems of Mechanical Engineering (RAS), Russia
N.F. Morozov
St.Petersburg State University, Russia
R.R. Mulyukov
Institute for Metals Superplasticity Problems (RAS), Russia
Yu.V. Petrov
St.Petersburg State University, Russia
N.M. Pugno
Politecnico di Torino, Italy
B.B. Rath
Naval Research Laboratory, USA
A.E. Romanov
Ioffe Physico-Technical Institute (RAS), Russia
A.M. Sastry
University of Michigan, Ann Arbor, USA
B.A. Schrefler
University of Padua, Italy
N.V. Skiba
Institute of Problems of Mechanics (RAS), Russia
A.G. Sheinerman
Institute of Problems of Mechanics (RAS), Russia
R.Z. Valiev
Ufa State Aviation Technical University, Russia
K. Zhou
Nanyang Technological University, Singapore

"Materials Physics and Mechanics" Editorial Office:
Phone: +7(812)552 77 78, ext. 224 **E-mail:** mpmjournal@spbstu.ru **Web-site:** http://www.mpm.spbstu.ru

International scientific journal "**Materials Physics and Mechanics**" is published by Peter the Great St.Petersburg Polytechnic University in collaboration with Institute of Problems of Mechanical Engineering of the Russian Academy of Sciences in both hard copy and electronic versions.

The journal provides an international medium for the publication of reviews and original research papers written in English and focused on the following topics:

- Mechanics of composite and nanostructured materials.
- Physics of strength and plasticity of composite and nanostructured materials.
- Mechanics of deformation and fracture processes in conventional materials (solids).
- Physics of strength and plasticity of conventional materials (solids).
- Physics and mechanics of defects in composite, nanostructured, and conventional materials.
- Mechanics and physics of materials in coupled fields.

Owner organizations: Peter the Great St. Petersburg Polytechnic University; Institute of Problems of Mechanical Engineering RAS.

Materials Physics and Mechanics is indexed in Chemical Abstracts, Cambridge Scientific Abstracts, Web of Science Emerging Sources Citation Index (ESCI) and Elsevier Bibliographic Databases (in particular, SCOPUS).

© 2022, Peter the Great St. Petersburg Polytechnic University
© 2022, Institute of Problems of Mechanical Engineering RAS

МЕХАНИКА И ФИЗИКА МАТЕРИАЛОВ

Materials Physics and Mechanics

Том 50, номер 3, 2022 год

Учредители:
ФГАОУ ВО «Санкт-Петербургский политехнический университет Петра Великого»
ФГБУН «Институт проблем машиноведения Российской Академии Наук»

Редакционная коллегия журнала
Главные редакторы:

д.ф.-м.н., чл.-корр. РАН **Д.А. Индейцев**
Институт проблем машиноведения Российской Академии Наук (РАН)

д.т.н., академик РАН **А.И. Рудской**
Санкт-Петербургский политехнический университет Петра Великого

Основатель и почетный редактор: д.ф.-м.н. **И.А. Овидько (1961-2017)**
Институт проблем машиноведения Российской Академии Наук (РАН)

Ответственные редакторы

д.ф.-м.н. **А.Л. Колесникова**
Институт проблем машиноведения Российской Академии Наук (РАН)

к.т.н. **А.Ю. Ромашкина**
Санкт-Петербургский политехнический университет Петра Великого

Международная редакционная коллегия:

д.ф.-м.н., проф. **А.К. Беляев**
Институт проблем машиноведения РАН, Россия
д.ф.-м.н. **С.В. Бобылев**
Институт проблем машиноведения РАН, Россия
к.т.н., проф. **А.И. Боровков**
Санкт-Петербургский политехнический у-т Петра Великого, Россия
д.ф.-м.н., проф. **Р.З. Валиев**
Уфимский государственный технический университет, Россия
д.ф.-м.н., академик РАН **И.Г. Горячева**
Институт проблем механики РАН, Россия
д.ф.-м.н., академик РАН **Д.М. Климов**
Институт проблем механики РАН, Россия
д.т.н., проф. **Г.Е. Коджаспиров**
Санкт-Петербургский политехнический у-т Петра Великого, Россия
д.ф.-м.н., проф. **С.А. Кукушкин**
Институт проблем машиноведения РАН, Россия
д.ф.-м.н., академик РАН **В.П. Матвеенко**
Институт механики сплошных сред РАН, Россия
д.ф.-м.н., проф. **А.И. Мелькер**
Санкт-Петербургский политехнический у-т Петра Великого, Россия
д.ф.-м.н., проф. **Ю.И. Мещеряков**
Институт проблем машиноведения РАН, Россия
д.ф.-м.н., академик РАН **Н.Ф. Морозов**
Санкт-Петербургский государственный университет, Россия
д.ф.-м.н., чл.-корр. РАН **Р.Р. Мулюков**
Институт проблем сверхпластичности металлов РАН, Россия
д.ф.-м.н., чл.-корр. РАН **Ю.В. Петров**
Санкт-Петербургский государственный университет, Россия
д.ф.-м.н., проф. **А.Е. Романов**
Физико-технический институт им. А.Ф. Иоффе РАН, Россия
д.ф-м.н. **Н.В. Скиба**
Институт проблем машиноведения РАН, Россия
д.ф.-м.н., проф. **А.Б. Фрейдин**
Институт проблем машиноведения РАН, Россия
д.ф-м.н. **А.Г. Шейнерман**
Институт проблем машиноведения РАН, Россия

Prof., Dr. **E.C. Aifantis**
Aristotle University of Thessaloniki, Greece
Dr. **K.E. Aifantis**
University of Florida, USA
Dr. **U. Balachandran**
Argonne National Laboratory, USA
Dr. **A. Bellosi**
Research Institute for Ceramics Technology, Italy
Prof., Dr. **G.-M. Chow**
National University of Singapore, Singapore
Prof., Dr. **Yu. Estrin**
Monash University, Australia
Prof., Dr. **Y. Gogotsi**
Drexel University, USA
Prof., Dr. **D. Hui**
University of New Orleans, USA
Prof., Dr. **G. Kiriakidis**
IESL/FORTH, Greece
Prof., Dr. **T.G. Langdon**
University of Southampton, UK
Prof., Dr. **N.M. Pugno**
Politecnico di Torino, Italy
Dr. **B.B. Rath**
Naval Research Laboratory, USA
Prof., Dr. **A.M. Sastry**
University of Michigan, Ann Arbor, USA
Prof., Dr. **B.A. Schrefler**
University of Padua, Italy
Prof. Dr. **K. Zhou**
Nanyang Technological University, Singapore

Тел.: +7(812)552 77 78, доб. 224 **E-mail:** mpmjournal@spbstu.ru **Web-site:** http://www.mpm.spbstu.ru

Тематика журнала

Международный научный журнал "Materials Physics and Mechanics" издается Санкт-Петербургским политехническим университетом Петра Великого в сотрудничестве с Институтом проблем машиноведения Российской Академии Наук в печатном виде и электронной форме. Журнал публикует обзорные и оригинальные научные статьи на английском языке по следующим тематикам:

- Механика композиционных и наноструктурированных материалов.
- Физика прочности и пластичности композиционных и наноструктурированных материалов.
- Механика процессов деформации и разрушения в традиционных материалах (твердых телах).
- Физика прочности и пластичности традиционных материалов (твердых тел).
- Физика и механика дефектов в композиционных, наноструктурированных и традиционных материалах.
- Механика и физика материалов в связанных полях.

Редколлегия принимает статьи, которые нигде ранее не опубликованы и не направлены для опубликования в другие научные издания. Все представляемые в редакцию журнала "Механика и физика материалов" статьи рецензируются. Статьи могут отправляться авторам на доработку. Не принятые к опубликованию статьи авторам не возвращаются.

Журнал "Механика и физика материалов" ("Materials Physics and Mechanics") включен в систему цитирования Web of Science Emerging Sources Citation Index (ESCI), SCOPUS и РИНЦ.

© 2022, Санкт-Петербургский политехнический университет Петра Великого
© 2022, Институт проблем машиноведения Российской Академии Наук

Contents

Heat transfer in infinite one-dimensional crystal considering the third coordination sphere **365-372**
R.V. Rubinova, O.S. Loboda, A.M. Krivtsov

Synthesis and wear behavior of varying particle sized B4C reinforced Al2618 alloy composites **373-387**
G. Veeresha, B. Manjunatha, M. Nagaral, V. Auradi, V. Bharath

Mathematical model of extrusion in FDM 3D printing technology **388-400**
O.B. Kudryashova, N.E. Toropkov, M.I. Lerner, A.B. Vorozhtsov

The void evolution kinetics driven by residual stress in icosahedral particles **401-409**
A.S. Khramov, S.A. Krasnitckii, A.M. Smirnov, M. Yu. Gutkin

Bearing capacity of spherical thick-walled shell taking into account compressibility and nonlinear plasticity **410-419**
I.K. Andrianov, S.I. Feoktistov

Flexible microwave absorbers based on powdered activated coconut charcoal and moisture-containing ceramsite **420-430**
O.V. Boiprav, S.E. Savanovich, E.S. Belousova

Grain-boundary nanoprecipitates-mediated mechanism of strengthening in Al-Cu-Zr alloy structured by high-pressure torsion **431-438**
M.Yu. Gutkin, N.V. Skiba, T.S. Orlova

Effect of reinforcements on mechanical and tribological behavior of magnesium-based composites: a review **439-458**
Dinesh Kumar, Satnam Singh, Surjit Angra

Corrosion cracking of low alloy steels. Testing methods **459-474**
A.A. Alhimenko, A.D. Breki. N.O. Shaposhnikov, A.A. Kharkov, E.L. Alekseeva, A.A. Lapechenkov

Strength analysis of thin-wall structures operating in aggressive environments for prolonged periods **475-484**
I.G. Emelyanov, A.N. Kislov

Applications of waste egg shell and egg shell membrane: a review **485-494**
Naveen Kumar, Ajaya Bharti, Pradeep Kumar

Anisotropic mechanical properties of elastomeric nanocomposites filled by carbon black, few-layer graphene, and carbon nanotubes **495-508**
O.K. Garishin, A.L. Svistkov, A.P. Voznyakovskii, I.M. Tchypkina, A.Yu. Neverovskaya, V.V. Shadrin

Impact of forced cooling of the joint zone and thermal effect on the distribution values of residual stress generated by arc welding **509-517**
A.V. Tkacheva, E.E. Abashkin

Role of in-situ developed intermetallic phases on the mechanical properties and corrosion behaviour of Mg-Sb- Sn and Mg-Sb-Ca ternary alloys **518-535**
S. Vignesh, Rajesh Kumar, A. Srinivasan, U.T.S. Pillai

Materials Physics and Mechanics. 2022;50(3): 365-372
Research article
http://dx.doi.org/10.18149/MPM.5032022_1

Submitted: June 29, 2022
Approved: October 18, 2022
Accepted: November 18, 2022

Heat transfer in infinite one-dimensional crystal considering the third coordination sphere

R.V. Rubinova[1]✉*, O.S. Loboda[2], A.M. Krivtsov[2]

[1]Fraunhofer Institute for Integrated Circuits IIS, Am Wolfsmantel 33, Erlangen, Germany, 91058

[2]Peter the Great St. Petersburg Polytechnic University, 29 Politechnicheskaya St., St. Petersburg, 195251, Russia

✉ rraisa@bk.ru

Abstract. The work focuses on the analytical description of unsteady thermal processes in low-dimensional structures. The object of study is an infinite one-dimensional harmonic crystal with interactions up to the third coordination sphere. The paper explains how a variation in bond stiffness between particles of different coordination spheres affects the behaviour of the system. The fundamental solution to the heat propagation problem has been constructed and investigated. It is shown that the initial thermal perturbation evolves into several consecutive thermal waves propagating with finite velocities. The number, the velocities, and the intensity coefficients of these waves are determined by the bond stiffnesses.

Keywords: harmonic crystal, third coordination sphere, unstationary heat transfer, heat waves, fundamental solution

Acknowledgements. *This work is supported by Russian Science Support Foundation (Grant No. 21-11-00378).*
The authors thank E. Podolskaya and D. Tsvetkov for useful discussions throughout the conducted research.

Citation: Rubinova RV, Loboda OS, Krivtsov AM. Heat transfer in infinite one-dimensional crystal considering the third coordination sphere. *Materials Physics and Mechanics*. 2022;50(3): 365-372. DOI: 10.18149/MPM.5032022_1.

1. Introduction

In most macro-scale objects, heat propagation can be described by the Fourier law, in which the linear relationship between heat flow and temperature gradient is assumed. However, deviations from the law can be observed at the micro/nano-level [1-2] where ballistic and anomalous processes of energy transfer take place. Dynamics of the crystal lattice is widely used in studies of various processes at micro- and macro-levels including thermal [3-9].

The non-diffuse thermal conductivity has been analytically [10-18] and experimentally [19-23] investigated during the last years. Extensive research on unsteady ballistic heat transfer processes was conducted by our scientific group [24-32]. An area of particular interest, where anomalies can be observed the most, is heat transport in harmonic crystals.

* Work was performed while with Peter the Great St. Petersburg Polytechnic University

© R.V. Rubinova, O.S. Loboda, A.M. Krivtsov, 2022. Publisher: Peter the Great St. Petersburg Polytechnic University
This is an open access article under the CC BY-NC 4.0 license (https://creativecommons.org/li-censes/by-nc/4.0/)

The behaviour of such systems can be described by statistical characteristics. For some of them such as kinetic temperature analytical expression can be obtained [25].

An important area of research is heat transport in polyatomic systems or systems with non-neighbouring interactions. Considerable progress has been made in the analysis of the harmonic diatomic crystals as well as the harmonic crystals with the second coordination sphere [33-35]. In this paper, a crystal with interactions up to the third coordination sphere is discussed.

The crystalline model and its equation of motion are analysed to obtain expressions for the dispersion relation and group velocities. Based on a previously developed model of ballistic heat transfer, a fundamental solution is obtained and the influence of non-neighbouring interactions is investigated.

2. Statement of the Problem

A one-dimensional harmonic crystal is a chain of material points linearized along deformation by forces. The system studied consists of equal masses m that interact with their neighbours up to the third coordination sphere (Fig. 1). Equation of motion

$$m\ddot{u}_n = c_1(u_{n+1} - 2u_n + u_{n-1}) + c_2(u_{n+2} - 2u_n + u_{n-2}) + c_3(u_{n+3} - 2u_n + u_{n-3}) \quad (1)$$

describes the system's behaviour where u_n is the displacement of the n-th particle; c_1, c_2, and c_3 are the stiffnesses of couplings between the nearest, second nearest, and third nearest neighbours respectively.

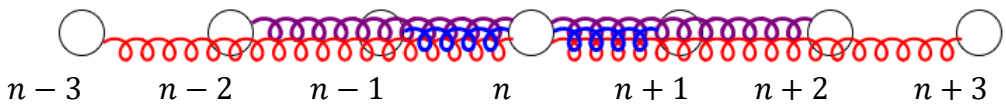

Fig. 1. One-dimensional harmonic crystal considering the third coordination sphere

In [34] the case $c_3 = 0$ was studied. The modified stiffness

$$c_{12} = c_1 + 4c_2 \quad (2)$$

was introduced to emphasize the second-order difference for the particles of the second coordination sphere. To ensure that the model presented in this paper is aligned with previous research, the same procedure was followed. Eq. (1) takes the form:

$$m\ddot{u}_n = c_{12}(u_{n+2} - 2u_n + u_{n-2})/4 - c_1(u_{n+2} - 4u_{n+1} + 6u_n - 4u_{n-1} + u_{n-2})/4 + c_3(u_{n+3} - 2u_n + u_{n-3}). \quad (3)$$

To solve equation (3) initial conditions for displacements and velocities should be specified. In case of instantaneous temperature perturbation, velocities are set to non-zero independent random values:

$$u_n|_{t=0} = 0, \dot{u}_n|_{t=0} = v_n. \quad (4)$$

Expressions (3) and (4) form the stochastic Cauchy problem which can be solved analytically for some crystalline systems.

The concept of kinetic temperature is an essential tool when describing thermal processes at the nanoscale. It depicts the energy transfer taking place through the interactions between the particles and is defined as

$$k_B \mathrm{T_i} \stackrel{\text{def}}{=} m\langle \dot{u}^2{}_i \rangle, \quad (5)$$

where $\mathrm{T_i}$ – kinetic temperature, k_B – Boltzmann constant, $\langle ... \rangle$ – covariance. As shown in [25], the evolution of the temperature field can be described as a superposition of fast and slow processes. The fast processes describe high-frequency oscillations caused by the redistribution of energy among potential and kinetic energy components. The slow processes correspond to the redistribution of energy between particles. This study focuses on the slow processes only.

Given an initial temperature field $T_0(x)$, the temperature at a given time and point is

$$T(x,t) = \frac{1}{8\pi}\int_{-\pi}^{\pi}\left(T_0\big(x + c_{gr}(ak)t\big) + T_0\big(x - c_{gr}(ak)t\big)\right)d(ak), \tag{6}$$

where k is the wavenumber, $c_{gr}(ak)$ is the group velocity, and a is the lattice constant corresponding to the distance between the nearest particles in the equilibrium state.

3. Dispersion Relation

The dispersion relation describes the waves that can propagate in the system. It is obtained via substitution of the wave function

$$u_n = Ae^{i(akn+\Omega t)} \tag{7}$$

into the equation of motion (3):

$$\Omega^2 = 4\left(sin^2\left(\frac{ak}{2}\right)\left(\omega_1^2\, sin^2\left(\frac{ak}{2}\right) + \omega_{12}^2\, cos^2\left(\frac{ak}{2}\right)\right) + \omega_3^2\, sin^2\left(\frac{3ak}{2}\right)\right), \tag{8}$$

where Ω is the wave frequency, ω_1, ω_{12} and ω_3 are constants introduced as follows:

$$\omega_1 \stackrel{\text{def}}{=} \sqrt{c_1/m},\ \ \omega_{12} \stackrel{\text{def}}{=} \sqrt{c_{12}/m} = \sqrt{(c_1 + 4c_2)/m},\ \ \omega_3 \stackrel{\text{def}}{=} \sqrt{c_3/m}. \tag{9}$$

For real values of the wave frequency, constants ω_1^2, ω_{12}^2 and ω_3^2 should be positive, therefore the system will be stable only for stiffnesses:

$$c_1 > 0,\ \ c_1 > -4c_2,\ \ c_3 > 0. \tag{10}$$

Frequencies $\omega_1, \omega_{12}, \omega_3$ can be depicted as Cartesian coordinates in the three-dimensional space of possible configurations and converted to the spherical coordinates:

$$\omega_1 \stackrel{\text{def}}{=} \omega\sqrt{2}\cos\gamma\cos\left(\beta + \frac{\pi}{4}\right),\ \ \omega_{12} \stackrel{\text{def}}{=} \omega\sqrt{2}\cos\gamma\sin\left(\beta + \frac{\pi}{4}\right), \omega_3 \stackrel{\text{def}}{=} \omega\sqrt{2}\, sin\,\gamma, \tag{11}$$

where $\beta \in (-\pi/4; \pi/4)$, $\gamma \in (0; \pi/2)$ and ω is positive. Parameter β describes the transition from interactions between the nearest neighbours to the second coordination sphere, while the third coordination sphere is introduced by parameter γ.

This parametrization allows for a decrease in the dimensionality of the problem. The dispersion relation is rewritten as follows:

$$\Omega = \pm\left(\Omega^0/\sqrt{2}\right)\sqrt{\cos^2\gamma\,(1 - \cos ak)[1 + \cos ak \sin 2\beta] + 2\sin^2\gamma\,(1 - \cos(3ak))}, \tag{12}$$

where $\Omega^0 = 2\omega$ is the maximal frequency in the case of a one-dimensional monoatomic harmonic chain with nearest interactions only.

With an increase of the parameter γ the number of extrema as well as the frequency range increase (Fig 2(a)). For the crystal where the third coordination sphere is dominant, three extrema are observed and the maximal frequency is $\sqrt{2}$ times as high as Ω^0.

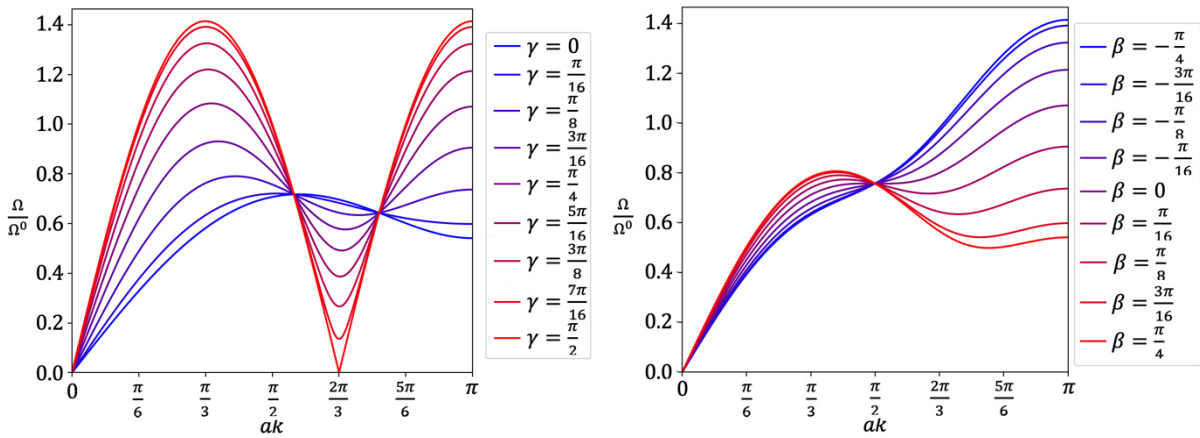

(a) (b)

Fig. 2. Dispersion relation for different values of (a) parameter γ with fixed $\beta = \frac{\pi}{8}$; (b) parameter β with fixed $\gamma = \frac{\pi}{8}$

For large negative values of parameter β, the influence of the third sphere is levelled out by negative stiffness c_2 (Fig. 2(b)). Additionally, the range of possible frequency values is inversely dependent on the parameter β.

4. Group Velocity

The heat waves propagate in the crystal with group velocities, which can be obtained as a derivative of Eq. (12) with respect to the wavenumber k:

$$c_{gr} = (\Omega^0 c_g^0/2\Omega)[\cos^2\gamma \sin(ak)\,[1 + (2\cos(ak) - 1)\sin(2\beta)] + 6\sin^2\gamma \sin(3ak)], \quad (13)$$

where $c_g^0 = a\omega$ is maximal group velocity in a one-dimensional monoatomic harmonic crystal with nearest interactions only.

The shape and the value range of group velocity curves depend on parameters β and γ (Fig. 3). For the case of non-zero parameter γ, group velocity has three extrema, which is also true for cases when interactions with the second coordination sphere can be neglected ($\beta = 0$, Fig. 3(b)). One extremum is always observed for $ak = 0$, while the second and the third extrema are located in the vicinity of $ak = 2\pi/3$.

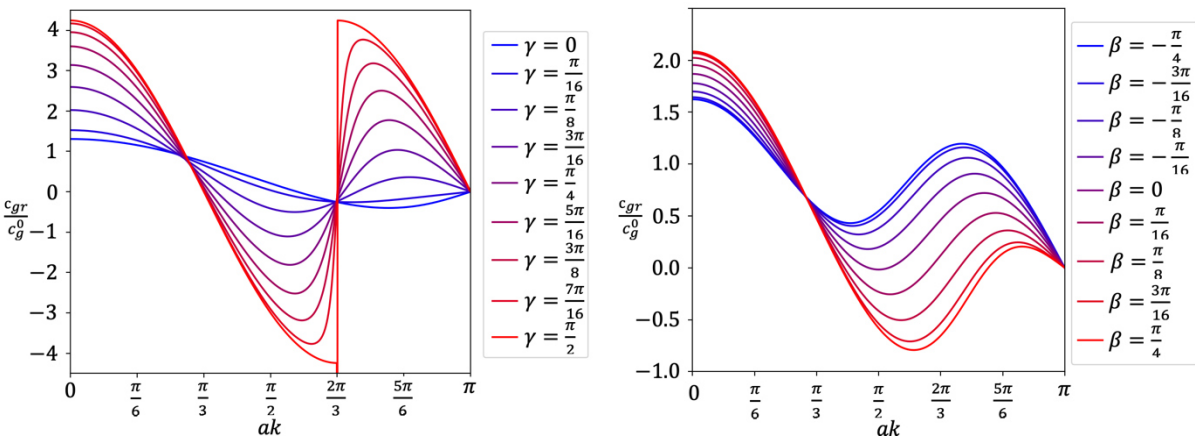

(a) (b)

Fig. 3. Group velocity for different values of (a) parameter γ with fixed $\beta = \frac{\pi}{8}$; (b) parameter β with fixed $\gamma = \frac{\pi}{8}$

5. Fundamental Solution

The initial perturbation corresponding to the single-point heat source takes the form of the delta function $T_0(x) = T_0\delta(x)$, where T_0 is an amplitude. An approximate fundamental solution to the heat transfer problem can hence be written as [35]:

$$T = T_0 \sum_j 1/\left(4\pi t\left|c'_{gr}(ak_j)\right|\right), \quad (14)$$

where k_j are roots of the equation

$$\left|c_{gr}(ak_j)\right| = |x|/t. \quad (15)$$

As time evolves, the initial perturbation is spread across the crystal. The position of the heat front can be derived from the singular point of Eq. (14). For the model under study, the number of fronts is a function of the parameters β and γ and can take integer values from one to three. The velocities of the heat waves have been introduced as $c_{gr}^{extr,1}$, $c_{gr}^{extr,2}$ and $c_{gr}^{extr,3}$ respectively, and are obtained by solving equation:

$$\left|c'_{gr}(ak_j)\right| = 0. \quad (16)$$

To quantify the intensity of the front, an approximation of Eq. (14) near a singular point is constructed as shown in [35]:

$$T(x,t) = T_0 / \left(4\pi t \sqrt{2\left|(\zeta^* - \zeta) c''_{gr}(ak^*)\right|} \right), \tag{17}$$

where ζ^* is group velocity at the singular point, ζ is group velocity in its vicinity. Eq. (17) has a singularity when $\zeta = \zeta^*$. The intensity coefficient for a single wave is then introduced as follows:

$$A = 1 / \left(4\pi t \sqrt{2\left|c''_{gr}(ak^*)\right|} \right). \tag{18}$$

For the case of three waves, normalised intensity coefficients are obtained using the following formula:

$$a_i^2 = A_i^2 / (A_1^2 + A_2^2 + A_3^2),\ i = 1,2,3, \tag{19}$$

where A_i are calculated as shown in Eq. (18). These coefficients allow for comparison of the amount of energy stored by different waves.

Some of the configurations of the system studied are considered in this paper (Table 1). For each set of the parameters β and γ the corresponding stiffnesses, wave velocities, and intensity coefficients have been calculated.

Table 1. Stiffnesses, wave velocities, and wave intensity coefficients

β	γ	c_1	c_2	c_3	c_{gr_1}/c_g^0	c_{gr_2}/c_g^0	c_{gr_3}/c_g^0	a_1	a_2	a_3
$-\pi/8$	$\pi/32$	1.69	−0.35	0.02	0.68	1.15	–	0.65	0.76	–
	$\pi/8$	1.46	−0.30	0.29	1.70	1.06	0.32	0.30	0.69	0.66
	$3\pi/16$	1.18	−0.24	0.62	2.40	1.36	0.42	0.26	0.52	0.82
$3\pi/16$	$\pi/16$	0.07	0.44	0.08	1.60	0.62	–	0.35	0.94	–
	$3\pi/16$	0.05	0.32	0.62	2.60	1.26	1.00	0.24	0.72	0.66
	$\pi/2$	0.00	0.00	2.00	4.24	–	–	1.00	–	–

Wave velocities have been analysed as functions of the parameter γ (Figs. 4 and 5). The values $\beta = -\frac{\pi}{8}$ (Fig. 4) and $\beta = \frac{3\pi}{16}$ (Fig. 5) have been considered. The colour of the curves represents the wave intensity coefficient. The numerical solution of Eq. (6) is depicted in footnotes.

For γ equal or close to zero, two waves (1 and 2) are observed. This corresponds to the crystal considering the second coordination sphere studied in [34,35]. When the parameter γ reaches a certain value in the vicinity of $\pi/16$ a third wave appears. For $\gamma = \pi/2$ three waves propagate with equal velocity and only one heat front is observed.

As γ increases, so do the velocities of the waves. Observations establish the inverse dependency between the intensity coefficient and the velocity: the fastest wave 1 stores the lowest amount of energy.

In the first case considered (Fig. 4) wave 3 propagates in the opposite direction unless the bond with the third coordination sphere begins to prevail. The observed behaviour is a result of the negative stiffness c_2. Therefore, the velocity of the third wave is a non-monotonous function with a global minimum around $\gamma = 5\pi/32$.

In the second case (Fig. 5), all the waves propagate in the same direction for all values of γ. As in the first case, the velocity of the second wave is also a non-monotonous function.

In two cases, the third wave appears differently. In the first case (Fig. 4), wave 1 splits up into waves 1 and 3 propagating close together with finite non-zero velocity. In the second case (Fig. 5), the third wave appears in the vicinity of the initial perturbation. For large γ, both cases exhibit similar behaviour. Hence, the conclusion can be made that for parameter γ equal to or larger than $\pi/4$, the influence of the third coordination sphere starts to prevail.

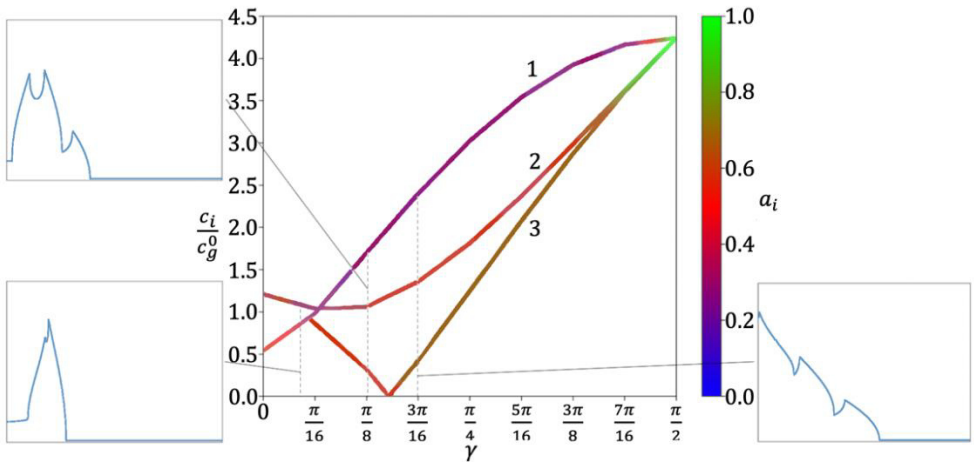

Fig. 4. Velocity and intensity of heat waves as a function of the parameter γ with fixed $\beta = -\frac{\pi}{8}$

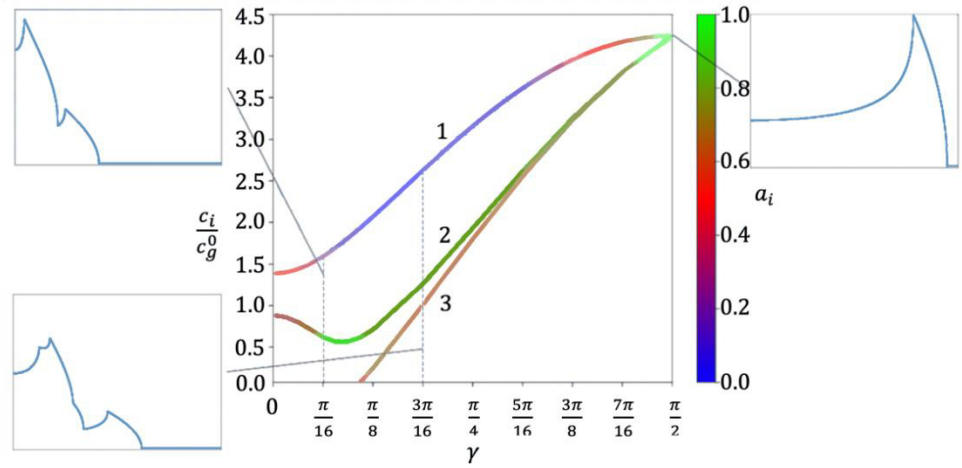

Fig. 5. Velocity and intensity of heat waves as a function of the parameter γ with fixed $\beta = \frac{3\pi}{16}$

6. Conclusion

Heat propagation in a model of a one-dimensional harmonic crystal considering interactions up to the third coordination sphere has been investigated in this study. After the parametrization the system has been described by a function of two dimensionless parameters $\beta \in (-\pi/4; \pi/4)$ and $\gamma \in (0; \pi/2)$. The parameter β characterizes the relative difference in bond stiffnesses of the first and the second coordination spheres. The parameter γ extends the interactions to the third coordination sphere.

The temperature field has been represented as a superposition of several consecutive heat waves propagating with group velocities. There is at least one wave for all stable configurations of the system. When the second coordination sphere is considered, the propagation of two waves with different velocities and intensities is possible. When three coordination spheres are taken into account, up to three heat waves can be observed in the crystal. The second and the third waves occur at certain values of parameters β and γ. In most cases, there is one fast wave accompanied by two slow almost equal velocities waves. The fastest wave as a rule has the lowest intensity coefficient. The deviations can be observed for the border cases when one wave separates into two.

The results can be used for the correct interpretation of experiments on nonstationary ballistic heat transfer in crystals and for further research on crystals with non-neighbouring interactions.

References

1. Peierls RE. *Quantum theory of solids*. Oxford: Clarendon Press; 1996.
2. Ziman JM. *Electrons and phonons: the theory of transport phenomena in solids*. Oxford: Oxford University Press; 2001.
3. Askar A. *Lattice dynamical foundations of continuum theories*. Singapore: Word Scientific; 1985.
4. Maugin GA. *Nonlinear waves in elastic crystals*. Oxford: Oxford University Press; 1999.
5. Askes A, Metrikine AV. Higher-order continua derived from discrete media: continualisation aspects and boundary conditions. *International Journal of Solids and Structures*. 2005;42: 187-202.
6. Askes H, Metrikine AV. An isotropic dynamically consistent gradient elasticity model derived from a 2D lattice. *Philosohical Magazine*. 2006;86: 3259-3286.
7. Potapov AI, Pavlov IS, Gorshkov KA, Maugin GA. Nonlinear interactions of solitary waves in a 2D lattice. *Wave Motion*. 2001;34: 83-96.
8. Potapov AI, Pavlov IS, Maugin GA. A 2D granular medium with rotating particles. *International Journal of Solids and Structures*. 2006;43: 6194-6207.
9. Vasiliev AA, Dmitriev SV, Miroshnichenko AE. Mutlti-field approach in mechanics of structured solids. *International Journal of Solids and Structures*. 2010;47: 510-525.
10. Bonetto F, Lebowitz JL, Rey-Bellet L. Fourier's law: a challenge to theorists. In: Fokas A. (eds.) *Mathematical Physics.* London: Imperial College Press; 2000. p.128-150.
11. Mielke A. Macroscopic behavior of microscopic oscillations in harmonic lattices via Wigner-Husimi transforms. *Archive for Rational Mechanics and Analysis*. 2006;181: 401-448.
12. Dhar A. Heat transport in low-dimensional systems. *Advances in Physics*. 2008;57(5): 457–537.
13. Gendelman O, Savin A. Normal heat conductivity in chains capable of dissociation. *Europhysics Letters*. 2014;106(3): 34004.
14. Lepri S. (ed.) Thermal Transport in Low Dimensions. *Lecture Notes in Physics*. 2016. p.921.
15. Guzev MA. The exact formula for the temperature of a one-dimensional crystal. *Far East Mathematical Journey*. 2018;18: 39-47.
16. Dhar A, Kundu A, Kundu A. Anomalous heat transport in one dimensional systems: a description using non-local fractional-type diffusion equation. *Frontiers in Physics*. 2019;7: 159.
17. Lepri S, Livi R, Politi A. Too Close to Integrable: Crossover from normal to anomalous heat diffusion. *Physical Review Letters*. 2020;125(4): 040604.
18. Gendelman OV, Paul J. Kapitza thermal resistance in linear and nonlinear chain models: Isotopic defect. *Physical Review E*. 2021;103: 052113.
19. Chang CW, Okawa D, Garcia H, Majumdar A, Zettl A. Breakdown of Fourier's law in nanotube thermal conductors. *Physical Review Letters*. 2008;101: 075903.
20. Johnson JA, Maznev AA, Cuffe J, Eliason JK, Minnich AJ, Kehoe T, Torres CM, Chen G, Nelson KA. Direct measurement of room-temperature nondiffusive thermal transport over micron distances in a silicon membrane. *Physical Review Letters*. 2013;110: 025901.
21. Hsiao TK, Huang BW, Chang HK, Liou SC, Chu MW, Lee SC, Chang CW. Micron-scale ballistic thermal conduction and suppressed thermal conductivity in heterogeneously interfaced nanowires. *Physical Review B*. 2015;91: 035406.
22. Huberman S, Duncan RA, Chen K, Song B, Chiloya V, Din Z, Maznev AA, Chen G, Nelson KA. Observation of second sound in graphite at temperatures above 100 K. *Science*. 2019; 364(6438): 375-379.

23. El Sachat A, Konemann F, Menges F, Del Corro E, Garrido JA, Torres C, Alzina F, Gotsmann B. Crossover from ballistic to diffusive thermal transport in suspended graphene membranes. *2D Materials*. 2019;6(2): 025034.
24. Krivtsov AM. Heat transfer in infinite harmonic one dimensional crystals. *Doklady Physics.* 2015;60(9): 407-411.
25. Kuzkin VA, Krivtsov AM. Fast and slow thermal processes in harmonic scalar lattices. *Journal of Physics: Condensed Matter*. 2017;29: 505401.
26. Krivtsov AM, Kuzkin VA. Discrete and continuum thermomechanics. In: Altenbach H, Ochsner A. (eds.) *Encyclopedia of Continuum Mechanics*. Berlin: Springer; 2018.
27. Krivtsov AM. The ballistic heat equation for a one-dimensional harmonic crystal. In: Altenbach H. (ed.) *Dynamical Processes in Generalized Continua and Structures*. *Advanced Structured Materials*. Cham: Springer; 2019. p.345-358.
28. Berinskii IE, Kuzkin VA. Equilibration of energies in a two-dimensional harmonic graphene lattice. In: *Philosophical Transactions of the Royal Society A*. London: The Royal Society; 2019.
29. Kuzkin VA. Unsteady ballistic heat transport in harmonic crystals with polyatomic unit cell. *Continuum Mechanics and Thermodynamics*. 2019;31: 1573-1599.
30. Gavrilov SN, Krivtsov AM. Steady-state kinetic temperature distribution in a two-dimensional square harmonic scalar lattice lying in a viscous environment and subjected to a point heat source. *Continuum Mechanics and Thermodynamics*. 2020;32(1): 41-61.
31. Korznikova EA, Kuzkin VA, Krivtsov AM, Xiong D, Gani V, Kudreyko AA, Dmitriev SV. Equilibration of sinusoidal modulation of temperature in linear and nonlinear chain. *Physical Review E*. 2020;102(6): 062148.
32. Kuzkin VA, Krivtsov AM. Ballistic resonance and thermalization in the Fermi-Pasta-Ulam-Tsingou chain at finite temperature. *Physical Review E*. 2020;101: 042209.
33. Kosevich AM, Savotchenko SE. Peculiarities of dynamics of one-dimensional discrete systems with interaction extending beyond nearest neighbors, and the role of higher dispersion in soliton dynamics. *Low Temperature Physics*. 1999;25(7): 550-557.
34. Loboda OS, Krivtsov AM, Porubov AV, Tsvetkov DV. Thermal processes in a one-dimensional crystal with regard for the second neighbor interaction. *ZAMM*. 2019;99(9): e201900008.
35. Loboda OS, Podolskaya EA, Tsvetkov DV, Krivtsov AM. On the fundamental solution of the heat transfer problem in one-dimensional harmonic crystals. *Continuum Mechanics and Thermodynamics*. 2021;33 (2): 485-496.

THE AUTHORS

Rubinova R.V.
e-mail: rraisa@bk.ru
ORCID: 0000-0002-5852-9367

Loboda O.S.
e-mail: loboda_o@mail.ru

Krivtsov A.M.
e-mail: akrivtsov@bk.ru

Materials Physics and Mechanics. 2022;50(3): 373-387
Research article
http://dx.doi.org/10.18149/MPM.5032022_2

Submitted: June 12, 2022
Approved: October 17, 2022
Accepted: November 11, 2022

Synthesis and wear behavior of varying particle sized B_4C reinforced Al2618 alloy composites

G. Veeresha[1], B. Manjunatha[1], M. Nagaral[2]✉, V. Auradi[3], V. Bharath[4]

[1]New Horizon College of Engineering, Bangalore 560103, India

[2]Aircraft Research and Design Centre, Hindustan Aeronautics Limited, Marathahalli, Bangalore, India

[3]Siddaganga Institute of Technology Tumkur, Tumkur 572103, India

[4]Sri Venkateswara College of Engineering, Bangalore 562157, India

✉ madev.nagaral@gmail.com

Abstract. In this work, the influence of reinforcement particle size and weight percentage on the wear behavior of Al2618 alloy composites was investigated. 63, 44 and 20 microns varying sized B_4C reinforced Al2618 composites were synthesized with 4 and 8 wt. % of B_4C using novel two stages stir cast method. Al2618 alloy with 63, 44, and 20 micron sized B_4C composites were studied for microstructural characterization by SEM and EDS. Further, to know the particle size effect on the behavior of Al2618 alloy, hardness, wear, and worn morphology studies were carried out. Wear tests were conducted at varying loads 10 N to 40 N at a constant sliding velocity of 2.08 m/sec, similarly, one more set of was studies were done by varying speeds of 0.52 m/sec to 2.08 m/sec at a constant 40 N load. Microstructural characterization revealed the uniform distribution of particles in the Al2618 alloy and elements were confirmed by EDS spectrums. The hardness of Al2618 alloy was enhanced with 63, 44, and 20 micron sized B_4C particles. With the addition of varying particle sized B4C all the wear properties were improved. Load and speed affected the wear behavior of all the prepared samples. Worn morphology studies confirmed the various wear mechanisms involved in the tested samples.

Keywords: Al2618 Alloy, B_4C, Microstructure, Hardness, Wear Properties, Worn Morphology

Acknowledgements. *No external funding was received for this study.*

Citation: Veeresha G, Manjunatha B, Nagaral M, Auradi V, Bharath V. Synthesis and wear behavior of varying particle sized B4C reinforced Al2618 alloy composites. *Materials Physics and Mechanics*. 2022;50(2): 373-xxx. DOI: 10.18149/MPM.5032022_2.

1. Introduction

Metal matrix1composites (MMCs) offer1very high temperature1limits, increased toughness, and1strength against1ductility [1,2]. These are used on the skin of a hypersonic aircraft. Some of the metal matrix composites are Al_2O_3 or SiC fibers in Al alloys, glass fibers in lead, SiC coated boron fibers in aluminium matrix, and tungsten carbide particulates in cobalt matrix [3,4]. These have a wide range of application areas like piston rings, connecting rods, battery plates, compressor blades, etc.

© G. Veeresha, B. Manjunatha, M. Nagaral, V. Auradi, V. Bharath, 2022.
Publisher: Peter the Great St. Petersburg Polytechnic University
This is an open access article under the CC BY-NC 4.0 license (https://creativecommons.org/li-censes/by-nc/4.0/)

Aluminium and its alloys are used in industries and structural activities. Many components of aerospace and space vehicles are made out of aluminium alloys. Parts of aluminium used in industry and structural utility are largely produced by both hot and cold extrusion processes. The components of aluminium used in engineering applications are subjected to variable speeds and required to transfer a large intensity of stress. The most demanding and not easy to intervene in is the situation in space where the environment is free from the atmosphere and lacks the facility of direct corrective measures. The above said peculiar situations demand more directed research exploration of tribo-behavior of aluminium in an adverse environment where temperature and lack of atmosphere exist [5].

Processing of MMC composites can be practiced by different strategies of liquid and solid-state processing including stir casting route, spray deposition, fluid penetration, powder metallurgy course, mechanical alloying, centrifugal casting, diffusion bonding, and in-situ process, and so on, most normal being customary melt stir casting and in-situ method as these are savvy when contrasted with other procedure's [6,7]. A few augmentations of the metal composites idea can be imagined. At present, the prime inspiration for creating MMCs lies in the improvement of mechanical properties. In any case, the upgrade of mechanical properties will be critical. Opportunities for further progression around these incorporate the reinforcement of quickly set matrix to give extra reinforcing, and the blend of broken and consistent reinforcements of the matrix to permit both extra reinforcing and to allow the enhancement of mechanical properties. Broad researcher about programs are required to exhibit these ideas on a research facility scale [8,9].

Tribology is the part of designing that manages the investigation of comparative or different materials which are in sliding contact with one another. There is contact produced when the material is scouring with one another subsequent in wear. There are 3 significant divisions in tribology managing corrosion, wear, and lubrication. Wear is the consequence of two materials' surface scouring against one another [10]. Wear brings about the evacuation of material as powder, consequently decreasing the first measurement. The examination of wear gets significant as it prompts a decline in generally speaking effectiveness of the material when exposed to its applications. The ASTM G99 standard portrays the harming of strong material including nonstop wear of materials, because of the scouring of two surfaces [11,12]. In numerous applications where segments slide each other MMCs are supplanting solid alloys. The sliding activity brings about wear of the parts. Testing the wear surface of the MMCs is thusly basic before changing over into an application. The specialists have broadly utilized pin-on-disc wear mechanical assemblies over the globe to test the wear surface of the MMCs [13].

Harun et al [14] examined the wear of B_4C particulates reinforced Al composites with weight percentages of 5 and 10 wt. %. A close look at the microstructure revealed that the boron carbide was widely dispersed throughout the base matrix. As the weight of the particles increased, so did their wear resistance.

Ruth et al. [15] used the gravity casting method to create a composite Al-Cu-Mg material reinforced with hard AlB_2 particles. Wear volume decreases as boron concentrations increase. The improved antifriction behavior of reinforced elements acting as load-bearing components may be to blame for the decreased wear coefficient in Al-Cu-Mg-B composites containing more AlB_2 particles.

Al7075-SiC-Al_2O_3 hybrid composite tensile and hardness were examined by Suresh et al. [16]. When making the composite, they used a constant weight percentage of SiC reinforcement and a variable weight percentage of Al_2O_3. An increase in hardness of up to 120 VHN and tensile strength of 399 MPa can be achieved by adding reinforcement to Al7075. Because of the effective distribution of reinforcements SiC and Al_2O_3 in the Al7075 matrix, the composite exhibits improved properties.

In this, an attempt has been made to develop Al2618 alloy with 4 and 8 wt. % of 63, 44, and 20 micron sized B_4C reinforced composites. Thus developed composites were exposed to microstructural characterization and wear behavior.

2. Experimental details

Materials used and composites preparation. By using the stir method of casting, metal composites with 4 and 8 weight % of 63, 44, and 20 micron sized B_4C composites were created. An Al2618 alloy was employed as the primary material, with B_4C particles having diameters of 63, 44, and 20 microns serving as reinforcements, as illustrated in Fig. 1. Table 1 shows the chemistry of the alloy employed in this experiment.

Table 1. Chemistry of Al2618 alloy by weight %

Zn	Mg	Si	Fe	Cu	Ni	Mn	Cr	Al
0.1	1.8	0.2	1.3	2.7	0.9	0.3	0.1	Balance

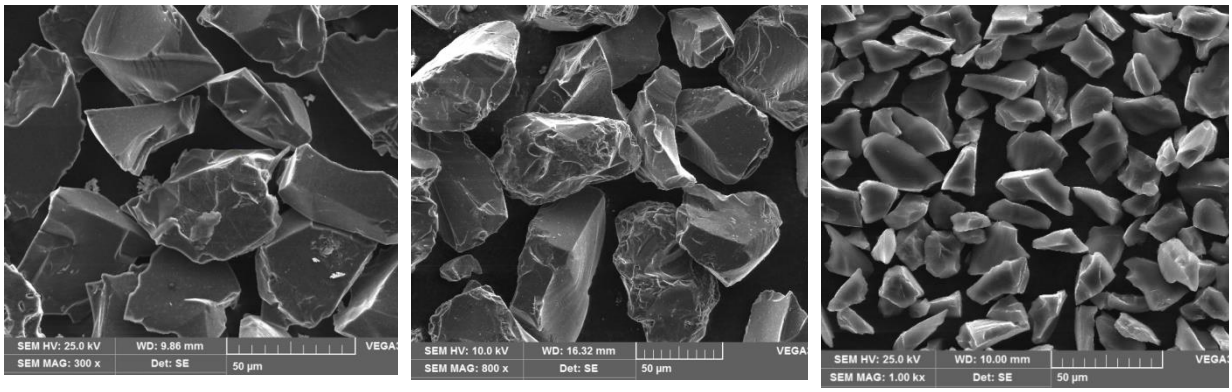

(a) (b) (c)

Fig. 1. SEM micro-photographs of (a) 63 micron (b) 44 micron (c) 20 micron sized B_4C particles

An Al2618 alloy composite with 4 and 8 weight percent of 63, 44, and 20 micron particulates was prepared using a stir casting fabrication method in the current study. When the graphite crucible is inserted into the electrical furnace, it is filled with the pre-weighed Al billet that has been cut into small chunks. The temperature of the electrical resistance furnace is 750°C. They were heated to 500°C in a graphite crucible for the preheating of the micro B_4C reinforcement particles. Temperature readings were taken from a digital controller that was placed in an electrical furnace to monitor the temperature of the aluminium molten melt. An agent known as solid hexachloro-ethane (C_2Cl_6) was used to remove the unwanted gases from the molten melt [17]. Using a zirconia-coated stirrer, molten metal was mechanically stirred at 400 rpm for about 5 minutes before reinforcing particles were added. The preheated B_4C particles were fed into the molten metal at a rate of one gram per second in a two-step addition process once the vortex had formed. After the molten melt is prepared, it is poured into a preheated cast iron die at a temperature of 730°C and indorsed to cool, as shown in Fig. 2 with a diameter of 15 mm, to obtain the necessary samples for further processing.

After casting, the specimen is prepared for SEM microstructural investigation to determine the uniform distribution of reinforcing particles in the Al2618 alloy. Microstructure images of Al2618 alloy and Al2618 reinforced composites with various amounts of B_4C are taken. The microstructure specimen has a diameter of 15 mm and a height of 5 mm. The specimen's surface is ground with 240, 600, and 800 grit paper. On the polishing machine, the surface is next polished with 4 micron polishing paper for a smoother finish. Following that,

the samples are cleaned with distilled water to remove any foreign particles that may have accumulated on the polished surface, such as dirt or other contaminants. The samples are etched using Keller's reagent to create a contrasting surface.

Fig. 2. Al2618 alloy with B_4C composite

Pin-on-disc machine wear tests were used to study the wear behavior (DUCOM, TR-20LE). According to ASTM G99 standards [18], the dry sliding wear tests were conducted on both reinforced and unreinforced materials with an 8-mm diameter and 30-millimeter height. EN32 steel was used in the counter disc of the wear machine. The disc and test pin surface are cleaned with acetone liquid before testing begins. Sliding at 2.08 m/sec at 2000 m distance and 10 N, 20 N, 30 N, and 40 N loads were used for the various experiments. At 40 N constant loads, tests were conducted at 0.52, 1.04, 1.56, and 2.08 m/sec, respectively. During testing, the circular plate was pivoted while the test pin was kept opposite and stationary to the spherical steel disc. A digital electronic machine was used to accurately measure the weight of the test pins samples to the milligramme level of 0.0001 g. The worn surface was cleaned with acetone liquid after each test. Before and after the surface had been worn, a test pin was weighed to determine how much wear had occurred. The weight loss information was transformed and converted into volumetric wear loss using the measured data. In Figure 3 you can see the wear test specimen used in the study.

Fig. 3. Wear test specimen

3. Results and discussion

Microstructural characterization. The microstructure of the cast Al2618 alloy is depicted in Fig. 4 (a), and it is obvious that no B_4C particles are present. SEM microstructures of Al2618-4 wt. % of 63 micron B_4C, Al2618-8 wt. % of 63 micron B_4C composites are shown in Fig. 4 (b-c). Similarly, SEM micrographs of Al2618-4 wt. % of 44 micron B_4C and Al2618-8 wt. % of 44 micron B_4C composites are shown in Fig. 5. SEM micrographs of Al2618-4 wt. % of 20 micron B_4C and Al2618-8 wt. % of 20 micron B_4C composites are shown in Fig. 6.

Figure 4 (a) is demonstrating the SEM of as cast Al2618 alloy. In the Al2618 alloy grain boundaries are visible properly without any particles. The surface of the micrograph is free from pores and cavities which indicate the casting method is suitable for the preparation of composites. Further, Fig. 4(b-c) are representing the micrographs of Al2618 alloy with 4 and 8 wt.% of 63 micron B_4C particles composites. The particles distribution is clear and uniform in these images. Similar observations are made in Fig. 5 and Fig. 6 which are showing SEM micrographs of Al2618 alloy with 4 and 8 wt. % of 44 and 20 micron sized B_4C reinforced composites respectively. All the micrographs exhibit strong bonding between the B_4C particles and Al2618 alloy. This strong bonding helps in the enhancement of the properties of Al2618 alloy composites.

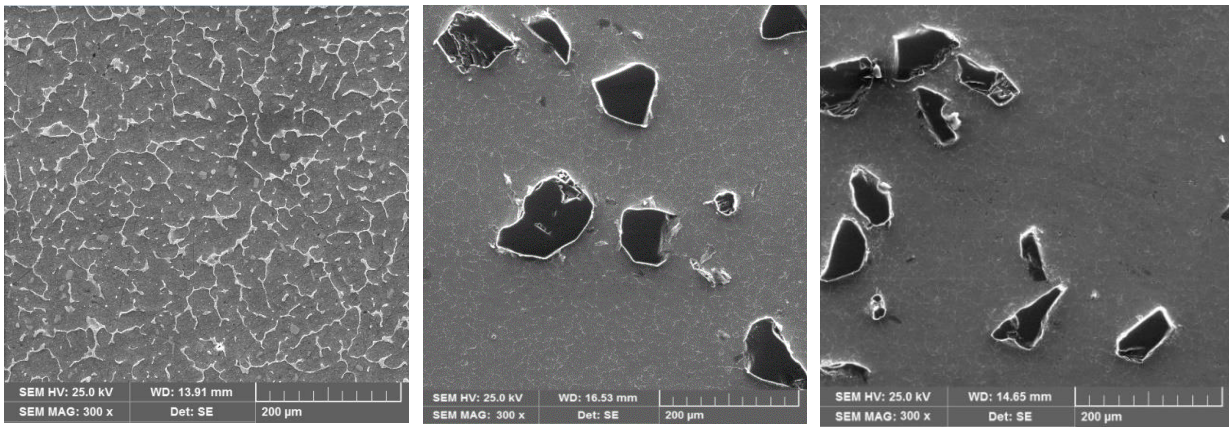

(a) (b) (c)

Fig. 4. SEM micrographs of (a) as cast Al2618 (b) Al2618-4 wt. % of 63 micron B_4C (c) Al2618-8 wt. % of 63 micron B_4C composites

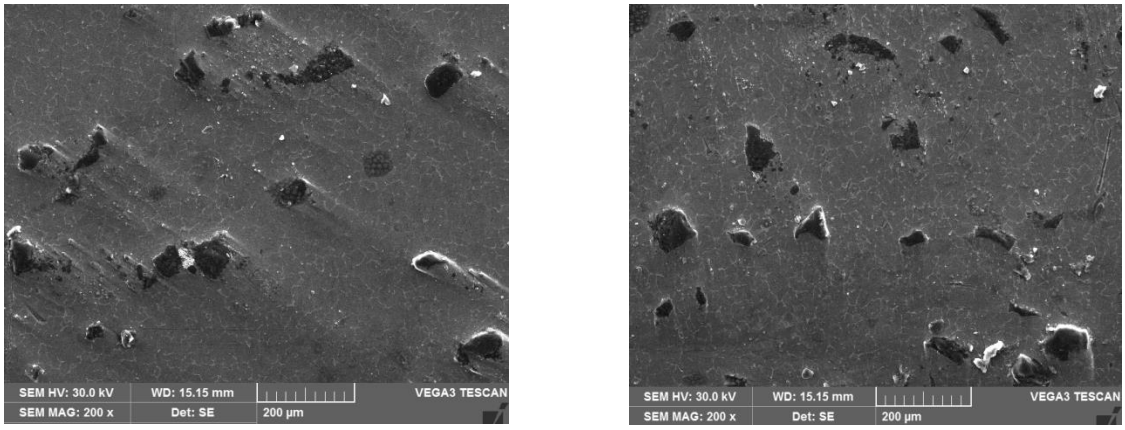

(a) (b)

Fig. 5. SEM micrographs of (a) Al2618-4 wt.% of 44 micron B_4C (b) Al2618-8 wt.% of 44 micron B_4C composites

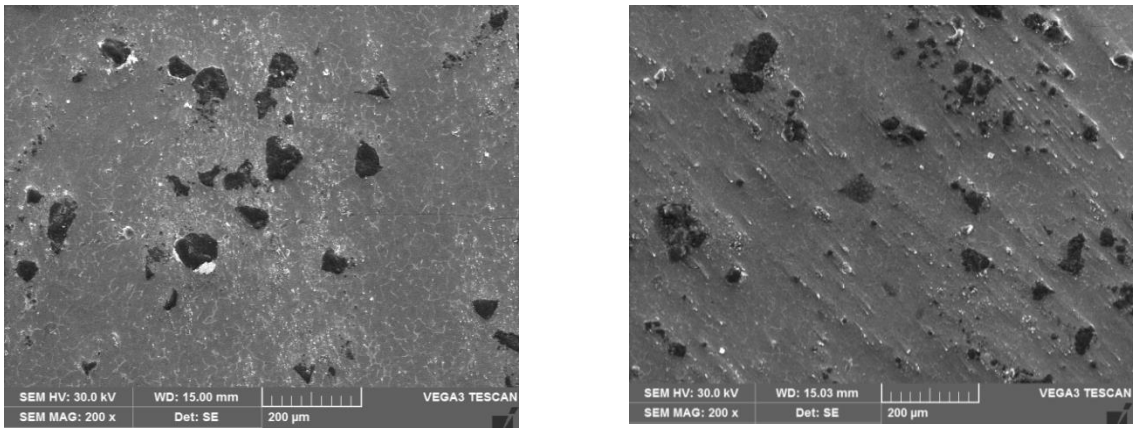

(a) (b)

Fig. 6. SEM micrographs of (a) Al2618-4 wt.% of 20 micron B_4C (b) Al2618-8 wt.% of 20 micron B_4C composites

Figure 7 are demonstrating the EDS of Al2618 alloy, Al2618 with 8 wt. % of 63 micron B_4C, Al2618 with 8 wt. % of 44 micron B_4C, and Al2618 with 8 wt. % of 20 micron B_4C composites respectively. Fig. 7 (a) is showing Al and Cu elements, this Cu element is the major alloying element in the aluminium 2XXX series alloys [19]. Further, Fig. 7 (b-d) is

showing boron (B) and carbon (C) elements along with the Al peaks, which indicates the occurrence of B_4C in the prepared Al2618 alloy with B_4C composites.

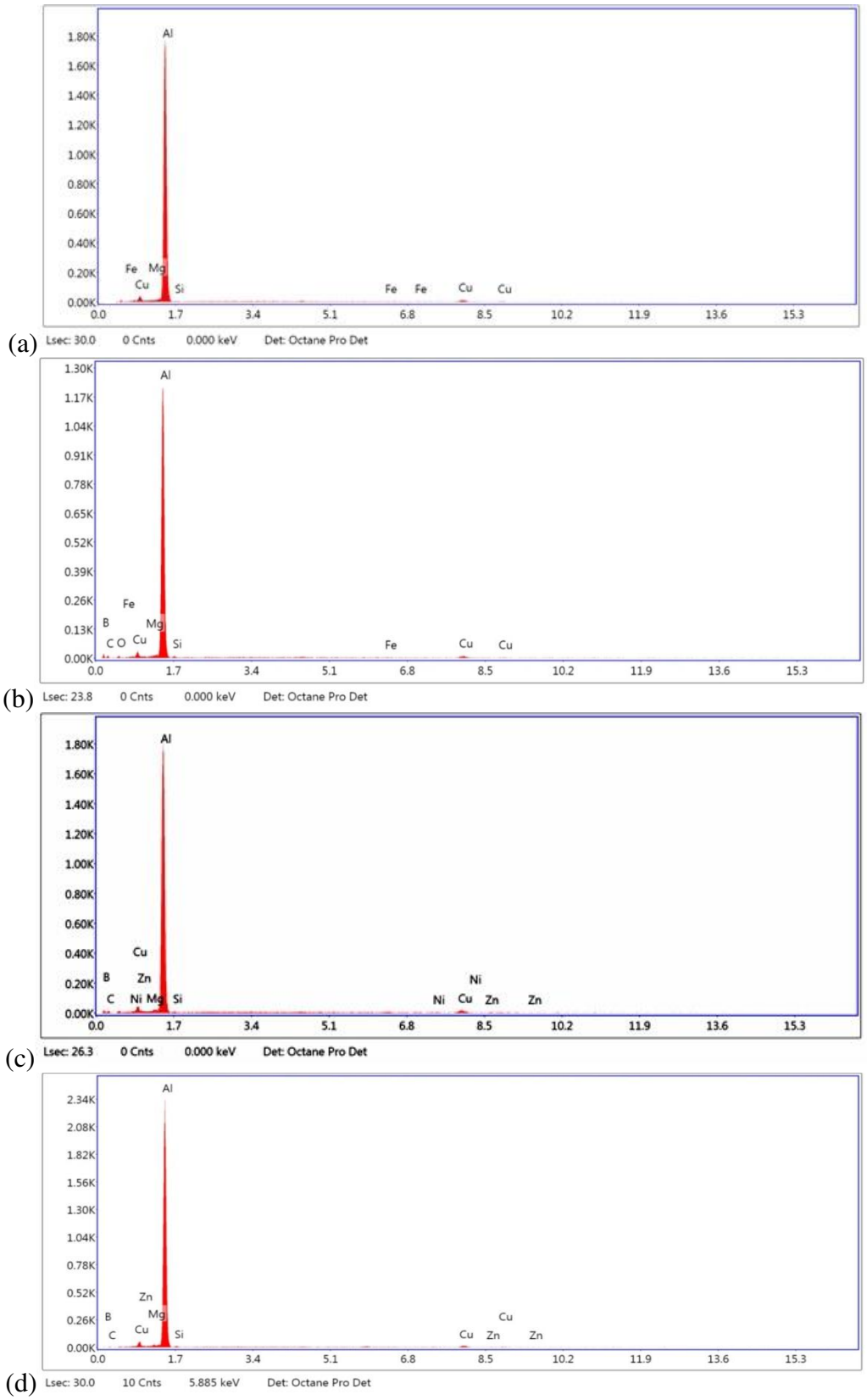

Fig. 7. EDS spectrums of (a) Al2618 alloy (b) Al2618-8 wt.% of 63 micron B_4C composites (c) Al2618-8 wt.% of 44 micron B_4C composites (d) Al2618-8 wt.% of 20 micron B_4C composites

Hardness measurements. Composites of Al2618 alloy with 4, 8, and 12 weight percent of boron carbide particles ranging in size from 63 to 44 to 20 microns are tested for hardness. As shown in Figs. 8, 9, and 10, the composites' hardness linearly increases with increasing percentages of B4C as the particle sizes are reduced. Hardness increases of around 35.8%, 62.6%, and 72.4% were seen in the case of 8 wt.% of 63, 44, and 20 micron sized B_4C reinforced composites, respectively. As a result of B_4C's incorporation into the Al2618 matrix, its hardness has increased significantly. All throughout the matrix, strengthening particles work to prevent the matrix from undergoing plastic deformation because they are stronger and more rigid than the matrix. However, the dispersal of the boron carbide particles throughout the Al2618 matrix is crucial for preventing the matrix from plastically deforming. There may be a significant difference in hardness value at different locations in composite samples if particle distribution is concentrated in one area and absent in others.

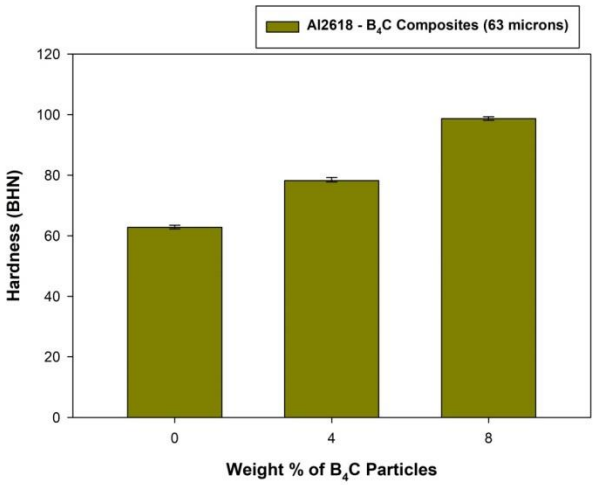

Fig. 8. Hardness of Al2618 alloy with 63 micron sized B_4C composites

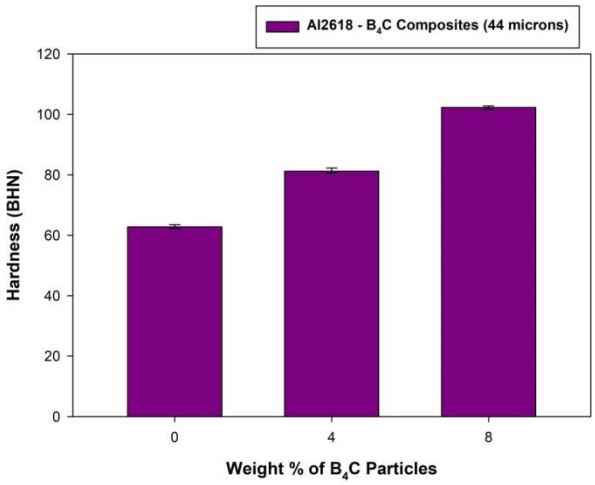

Fig. 9. Hardness of Al2618 alloy with 44 micron sized B_4C composites

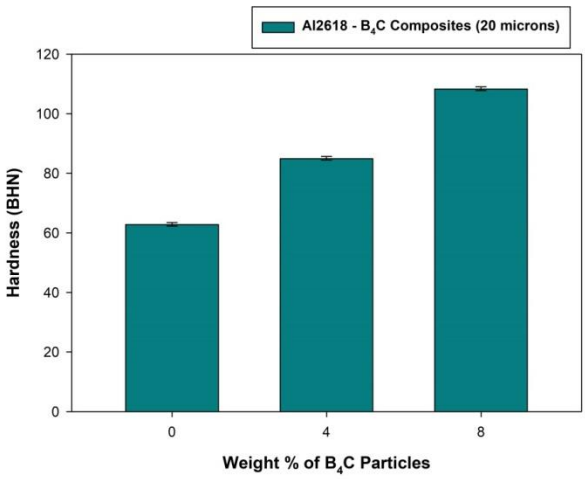

Fig. 10. Hardness of Al2618 alloy with 20 micron sized B_4C composites

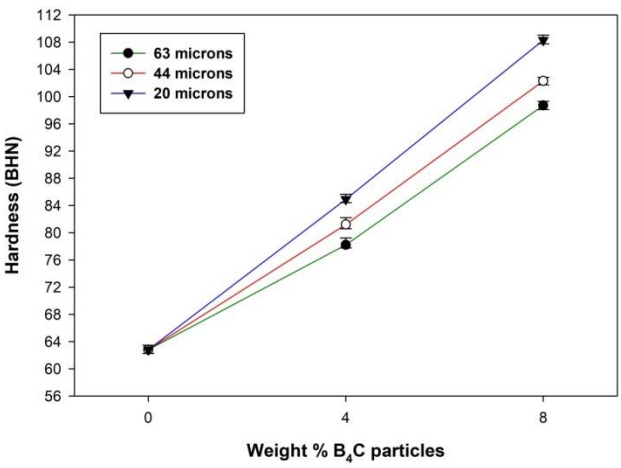

Fig. 11. Comparison of hardness of Al2618 alloy with 63, 44, and 20 micron sized B_4C composites

The hardness of Al2618-B_4C composites as a function of boron carbide weight percentage and particle size is shown in Fig. 11. Figure 11 demonstrates that the hardness of reinforced composites can be improved by decreasing particle size. It's possible to take into account a wide range of variables in situations of this kind. To begin, the smaller, 20 micron-

sized particles will have a higher interface than the larger, 63, and 44 micron-sized particles, all of which will result in increased hardness. Compared to a composite reinforced with larger size particles, the surface area of a smaller size particle is greater. As for the second, it's because the distance between particles of different sizes is roughly the same in all cases, though it's shorter for particles between 44 and 63 microns.

Wear studies

Effect of load on volumetric wear loss. Al2618 alloy and 63, 44, and 20 micron sized B_4C composites volumetric wear loss at varying loads of 10 N to 40 N at a constant speed of 2.08 m/sec for 2000 m sliding distance is shown in Figs. 12, 13, and 14.

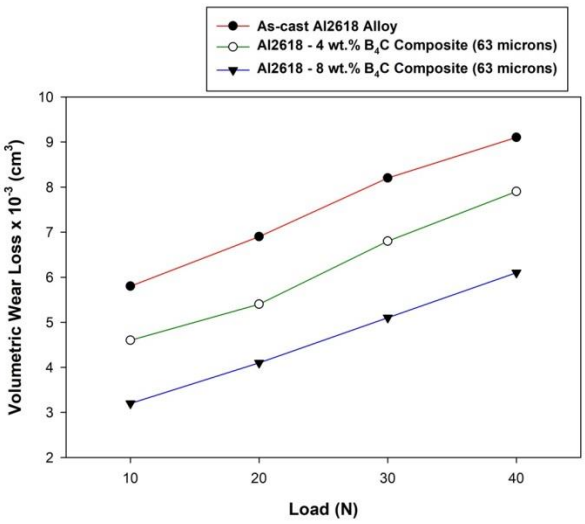

Fig. 12. Volumetric wear loss of Al2618 with 63 micron sized B_4C composites at varying loads

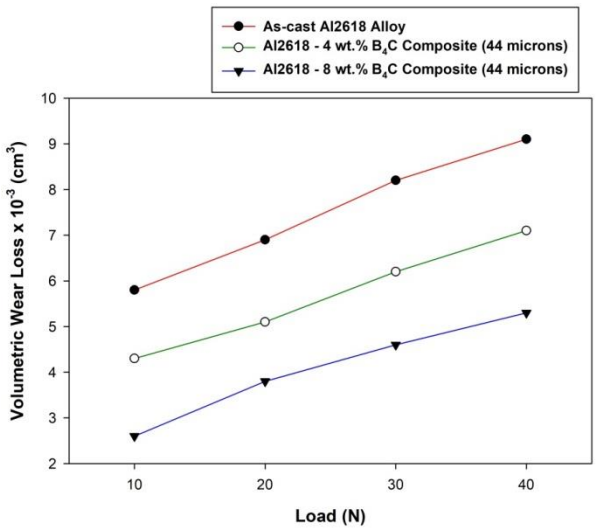

Fig. 13. Volumetric wear loss of Al2618 with 44 micron sized B_4C composites at varying loads

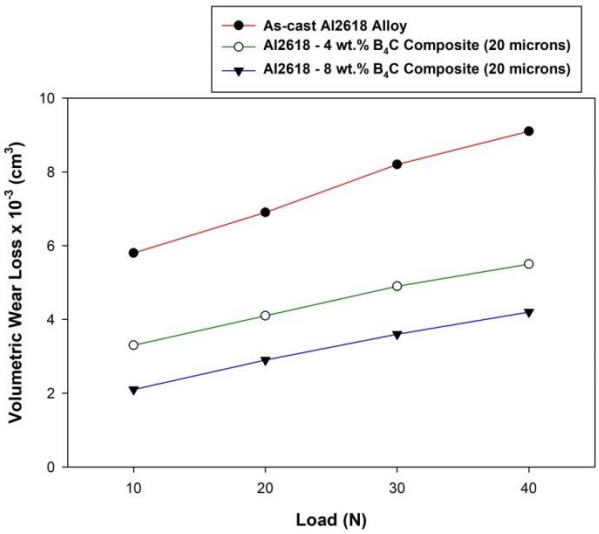

Fig. 14. Volumetric wear loss of Al2618 with 20 micron sized B_4C composites at varying loads

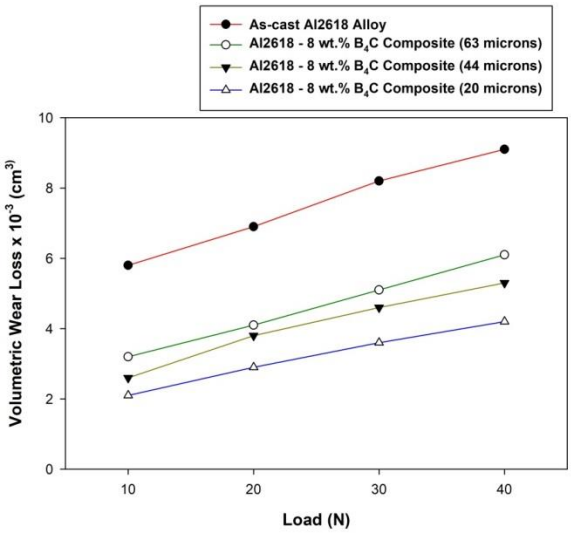

Fig. 15. Comparaison of volumetric wear loss of Al2618 with 63, 44, and 20 micron sized B_4C composites at varying loads

From Figures 12, 13, and 14 wear of Al2618 alloy increases as the load on the specimen increased from 10 N to 40 N. Highest wear of material is observed at an applied load of 40 N in all 63, 44, and 20 micron sized carbide reinforced composites. The temperature of the

sliding surface and the pin exceeds the critical value when the load is at its highest point. The matrix alloy and B_4C composites' wear loss increases as the pin's load increases. However, it has been discovered that adding 4 or 8 weight percent of B_4C reinforcements to the matrix alloy reduces the composites' wear loss. When it comes to preventing material loss from occurring in composites, boron carbide particulates serve as an effective barrier because of their high hardness [20]. Thirumalai et al. [21] investigated the wear behavior of B_4C and graphite-reinforced hybrid composites. Hybrid composites exhibited wear resistance as compared to as-cast alloy. Further, Al2618 alloy with 20 micron sized B_4C composites exhibited more wear resistance as compared to the 63 and 44 micron sized particles composites as shown in Fig. 15.

Figures 12, 13, and 14 show that up to 40 N of load, volumetric wear loss increases steadily. Al2618 and Al2618 - B_4C composites at varying particle sizes exhibit an increase in wear loss with increasing load due to a maximum amount of plastic deformation. As can be seen in Fig. 15, the volumetric wear loss in Al2618 alloy and all composites with 4 and 8 wt.% of 63, 44, and 20 micron sized B_4C particles is initially low at 10 N and high at higher load 40 N. Increased material loss occurs at maximum loads during the wear test because metals normally protected by an oxide film experience greater stress. Solid metallic layers make contact when the oxide film between them cracks.

Effect of speed on volumetric wear loss. Al2618 alloy and 63, 44, and 20 micron sized B_4C composites wear behavior at varying speeds of 0.52 m/sec to 2.08 m/sec at a constant load of 40 N for 2000 m sliding distance is shown in Figs. 16, 17, and 18.

Al2618 alloy and B_4C composites volumetric wear loss is shown in Figs. 16, 17, and 18 as a function of the sliding speed. Wear on the Ai2618 and its constituent composites increases as the sliding speed rises from 0.52 m/sec to 2.08 m/sec.

There has been delamination in Al2618 alloy, which has resulted in the transfer of pin fragments onto the disc and larger fragments being thrown out [22]. Adding B_4C to the Al2618 reduces wear loss. Wear resistance on aluminium composites is improved by B_4C particles, which form mechanically mixed layers at their interface with the steel disc.

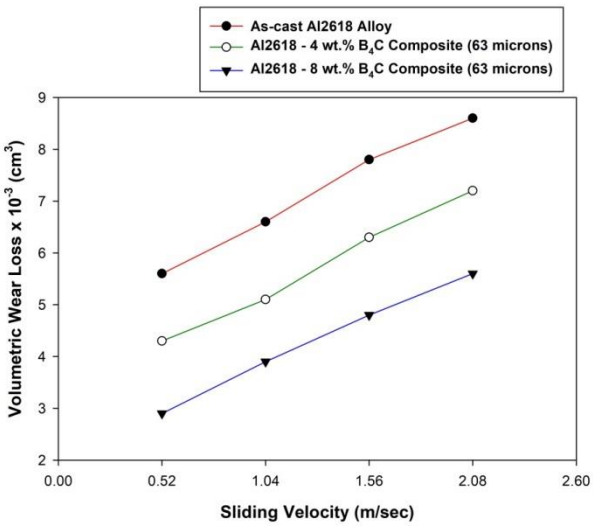

Fig. 16. Volumetric wear loss of Al2618 with 63 micron sized B_4C composites at varying speeds

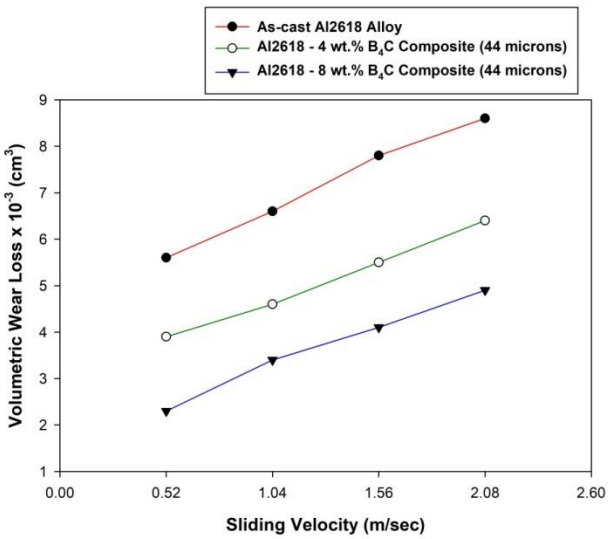

Fig. 17. Volumetric wear loss of Al2618 with 44 micron sized B_4C composites at varying speeds

Figures 16, 17, and 18 show that at lower sliding speeds of 0.52 m/sec, volumetric wear loss is mild, but at intermediate speeds of 1.04 and 1.56 m/sec, the transition from mild to severe begins, and at higher sliding speeds of 2.08 m/sec, severe wear is experienced in both

the Al2618 alloy and all produced composites. An increase in wear loss is expected for both the matrix and the composites that result from this. High strain deformation of the subsurface is the primary cause of the rise in wear loss. Fracture and asperity fragmentation areas are increased when the rate of subsurface deformation is accelerated. This results in greater volumetric wear loss and enhanced delamination.

Additionally, as the sliding speed increases, the wear loss also increases due to the softening of the composite due to rubbing action at higher temperatures. Due to higher sliding speeds, the test piece deforms as a result of the increase in temperature [23]. As a result, there is more delamination, which leads to more wear [24,25]. Further, Al2618 alloy with 20 micron sized B_4C composites exhibited more wear resistance as compared to the 63 and 44 micron sized particles composites as shown in Fig. 19.

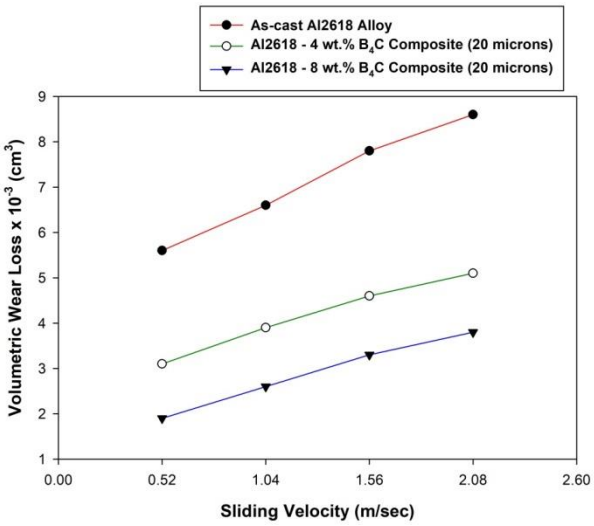

Fig. 18. Volumetric wear loss of Al2618 with 20 micron sized B_4C composites at varying speeds

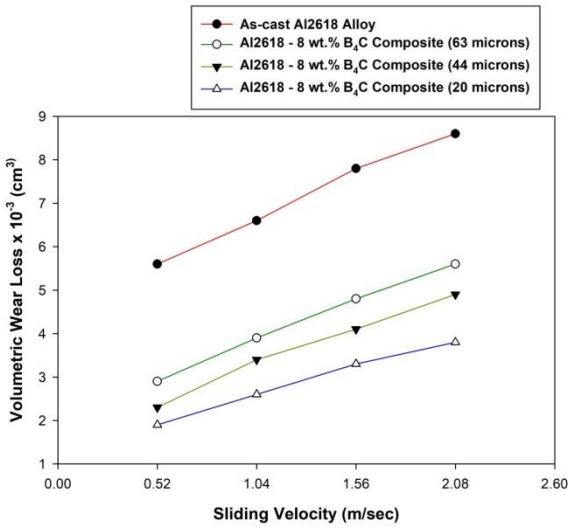

Fig. 19. Comparaison of volumetric wear loss of Al2618 with 63, 44, and 20 micron sized B_4C composites at varying speeds

Figure 19 shows the volumetric wear loss results for all composites with 63, 44, and 20 microns on different sliding speeds. The volumetric wear loss of the composite made with a fine particle is found to be lower than that of the composites made with 44 and 63 micron particles and the unreinforced alloy at all sliding speeds. Possible explanation: at a given mass fraction, a greater number of particles can fit into a given volume if the particle size is decreased. Hardening and low plastic deformation are enhanced by an increase in the number of particles or dislocation barriers [26,27].

Effect of coefficient of friction on volumetric wear loss. Figures 20 and 21 are demonstrating the effect of coefficient of friction on Al2618 alloy and 63, 44, 20 micron sized B_4C reinforced composites at varying loads and sliding speeds respectively. Figure 20 depicts the effect of coefficient friction of 4 and 8 wt. % of 63, 44, and 20 micron sized B_4C at varying loads of 10 N to 40 N, constant speed of 2.09 m/sec. The coefficient of friction is high in the case of as-cast Al2618 alloy compared to all other produced composites. Further, the coefficient of friction is increased as load increased from 10 N to 40 N for all composites with 63, 44 and 20 micron sized composites and unreinforced alloy. The increase in coefficient of friction is mainly due to the more plastic deformation of produced composites at higher loads. There is a decrease in the coefficient of friction as the particle size of the reinforcement decreases. The lowest coefficient of friction is observed in the case of Al2618 alloy with 8 wt. % of 20 micron sized B_4C reinforced composites. The smaller contributes

have more particle distribution in the base and the distance between the particles is lesser which creates more resistance to friction.

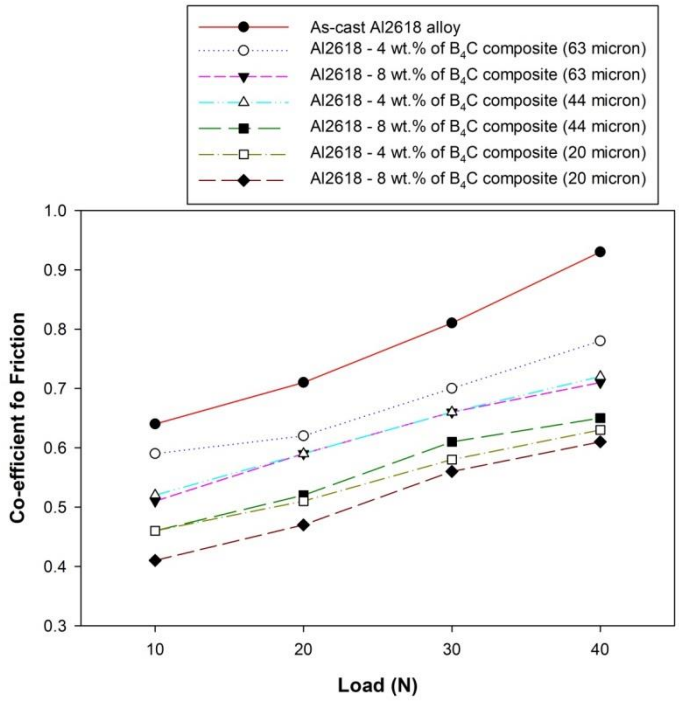

Fig. 20. Comparaison of co-efficient of friction of Al2618 with 63, 44, and 20 micron sized B_4C composites at varying loads

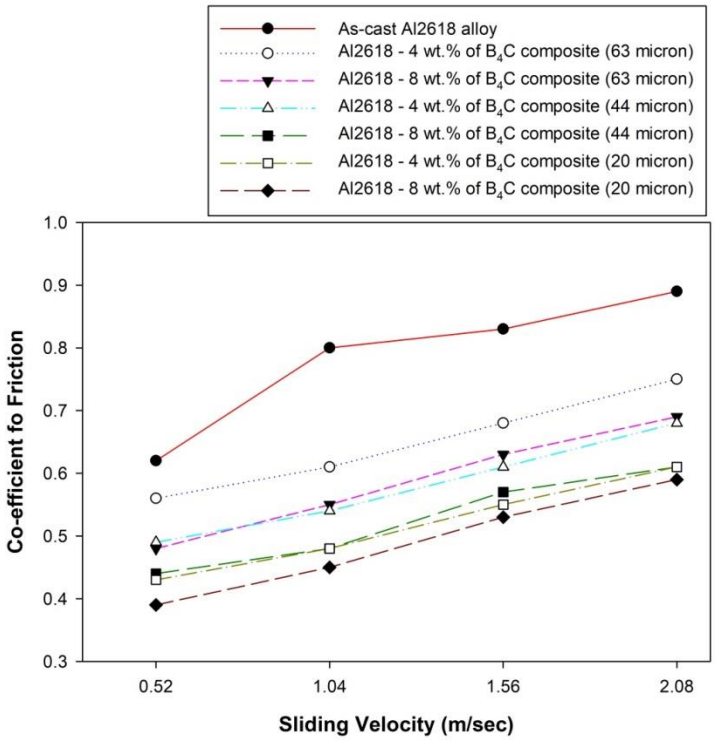

Fig. 21. Comparaison of coefficient of friction of Al2618 with 63, 44, and 20 micron sized B_4C composites at varying speeds

Figure 21 depicts the effect of coefficient friction of 4 and 8 wt. % of 63, 44, and 20 micron sized B_4C at varying sliding speeds of 0.52 m/sec to 2.08 m/sec, the constant load

of 40 N. The coefficient of friction is high in the case of as-cast Al2618 alloy compared to all other produced composites. Further, the coefficient of friction is increased as sliding speed increased from 0.52 m/sec to 2.08 m/sec for all composites with 63, 44 and 20 micron sized composites and unreinforced alloy. Further, coefficient of friction is lesser in the case of 8 wt. % of 20 micron sized particle reinforced composites.

Worn morphology. SEM microphotographs are used to examine the worn surface of Al2618 alloy and B_4C reinforced composites. Matrix Al2618 alloy (Fig. 22(a)), Al2618 with 8 wt.% of 63 B_4C composite (Fig. 22(b)), Al2618 with 8 wt.% of 44 B_4C composite and Al2618 with 8 wt.% of 20 B_4C composite tested at 40 N load and 2.08 m/sec sliding speed.

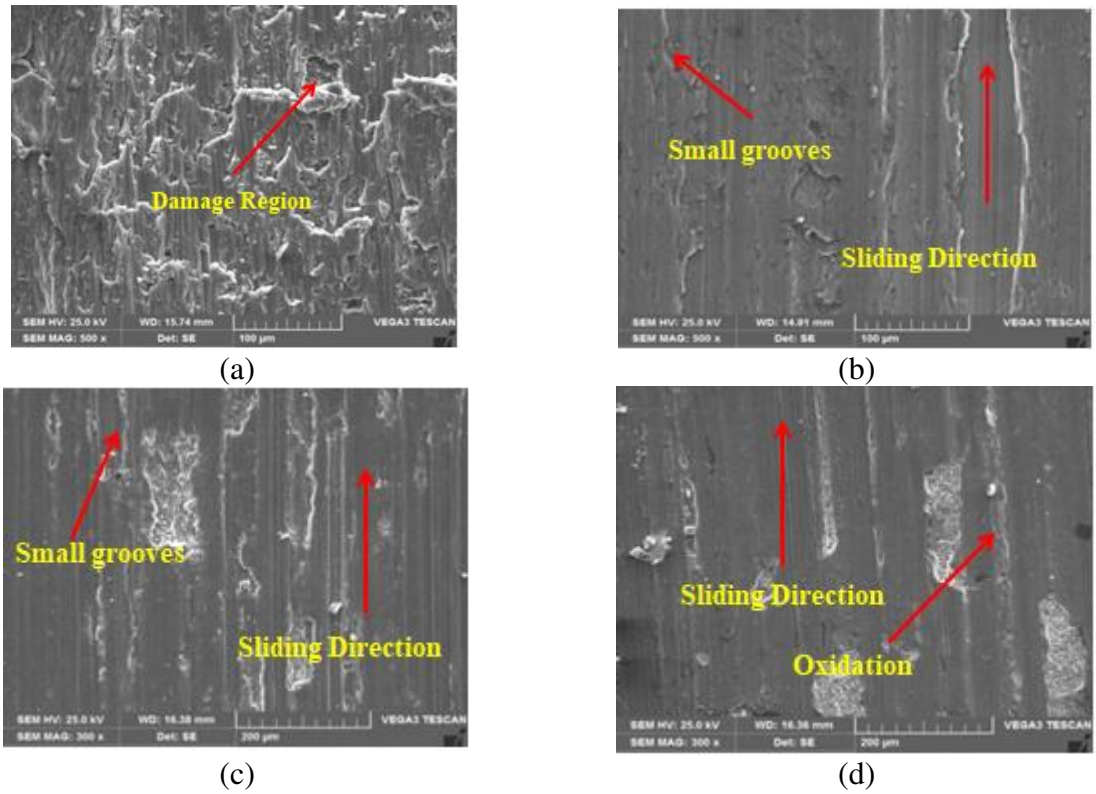

Fig. 22. Worn surfaces SEM micrographs of (a) Al2618 Alloy (b) Al2618-2 wt. % B_4C (c) Al2618-4 wt. % B_4C (d) Al2618-6 wt. % B_4C (e) Al2618-8 wt. % B_4C composites with 20 micron particles

Figure 22(a) shows the particular edges and depressions that run parallel to each other in the sliding direction. Under comparable conditions, the micrograph shows that the cracks in lattice combination Al2618 are deeper and more widespread than in micron composites. Figures 22(b), 22(c), and 22(d) show that the well-used outer surface of the Al2618-8 wt. % of B_4C composite has a break as a result of the sliding of oxide molecules in the reinforced composite. To prevent the basic matrix from coming into contact with the sliding partner, a thick layer of composites was created. This layer helps to reduce wear damage [28,29]. Since metal-metal contact is suppressed by the self-protective layer on the composites, these results in the metal-metal contact being prevented.

4. Conclusions

The stir cast route effectively produces the Al2618 alloy with 63, 44, and 20 micron sized B_4C particles MMCs with 4 and 8 wt. %. The SEM micrographs show that the B_4C particles are dispersed uniformly in the Al2618 alloy. The EDS study exposed the occurrence of B_4C particles in manufactured composites. The hardness of Al2618 alloy has increased with the

addition of 63, 44, and 20 micron sized B_4C particles. Further, the highest hardness is found in the 8 wt. % of 20 micron sized boron carbide reinforced composites. B_4C reinforced composites wear resistance increased with the addition of B_4C particles. Al2618 alloy with 20 micron sized B_4C composites exhibited greater wear resistance as compared with 63 and 44 micron sized B_4C reinforced composites. The load and sliding speed impacted the volumetric wear loss and coefficient of friction of Al2618 alloy and its 63, 44, and 20 micron sized B_4C reinforced composites. Al2618 alloy with 8 wt. % of 20 micron sized boron carbide particles reinforced composites exhibited lesser wear loss and low coefficient of friction. The various wear surface mechanisms of the base alloy Al2618 alloy and produced composites were revealed by wear surface analysis using SEM.

References

1. Madeva N, Shivananda K, Virupaxi A, Shivaputrappa K. Mechanical characterization of ceramic nano B_4C-Al2618 alloy composites synthesized by semi solid processing. *Transactions of the Indian Ceramic Society*. 2018;77(3): 1-4.
2. Siddesh Kumar NG, Shivashankar GS, Basavarajappa S, Suresh R. Some studies on mechanical and machining characteristics of Al2219/n-B_4C/MoS2 nano hybrid metal matrix composites. *Measurement*. 2017;107: 1-11.
3. Pankaj RJ, Sridhar BR, Nagaral M, Jayasheel IH. Mechanical behavior and fractography of graphite and boron carbide particulates reinforced A356 alloy hybrid metal matrix composites. *Advanced Composites and Hybrid Materials*. 2020;3: 114-119.
4. Prasad HN, Srinivas HK, Nagaral M. Characterization of tensile fractography of nano ZrO_2 reinforced copper-zinc alloy composites. *Frattura ed Integrity Strutturale (Fracture and Structural Integrity)*. 2019;48: 370-376.
5. Bharath V, Nagaral M, Auradi V. Preparation, characterization and mechanical properties of Al2O3 reinforced 6061 Al particulate MMCs. *International Journal of Engineering Research and Technology*.2012;1(6): 1-6.
6. Bharath V, Auradi V, Nagaral M, Satish BP, Ramesh S, Palanikumar K. Microstructural and wear behavior of Al2014-alumina composites with varying alumina content. *Transactions of the Indian Institute of Metals*. 2022;75(1): 133-147.
7. Veereshkumar GB. Assessment of mechanical and tribological characteristics of Silicon Nitride reinforced aluminium metal matrix composites. *Composites Part B: Engineering*. 2019;175: 107138.
8. Raj K, Deshpande RG, Gopinath B, Jayasheel H, Nagaral M, Auradi V. Mechanical Fractography and Worn Surface Analysis of Nanographite and ZrO_2-Reinforced Al7075 Alloy Aerospace Metal Composites. *Journal of Failure Analysis and Prevention*. 2021;21: 525-536.
9. Matti S, Shivakumar BP, Shashidhar S, Nagaral M. Dry sliding wear behavior of mica, fly ash and red mud particles reinforced Al7075 alloy hybrid metal matrix composites. *Indian Journal of Science and Technology*. 2021;14(4): 310-318.
10. Rajmohan T, Palanikumar K, Ranganathan S. Evaluation of mechanical and wear properties of hybrid aluminium matrix composites. *Transactions of Nonferrous Metals Society of China*. 2013;23: 2509-2517.
11. Sallahauddin A, Nagaral M, Reddappa HN, Auradi V. Effect of B_4C particulates addition on wear properties of Al7025 alloy composites. *American Journal of Materials Science*. 2015;5(3C): 53-57.
12. Bharath V, Auradi V, Nagaral M, Satish BP. Experimental investigations on mechanical and wear behaviour of 2014Al–Al_2O_3 Composites. *Journal of Bio-and Tribo-Corrosion*. 2020;45: 6.

13. Nagaral M, Auradi V, Kori SA, Veena S. Mechanical characterization and wear behavior of nano TiO2 particulates reinforced Al7075 alloy composites. *Mechanics of Advanced Composite Structures.* 2020;7(1): 71-78.
14. Harun M. Reciprocal sliding wear behaviour of B_4C particulate reinforced aluminum alloy composites. *Materials Letters*. 2010;64: 405-407.
15. Ruth GH, Nayomi P, Oscar MS. A study on tribological characterization of Al-Cu-Mg-B composites subjected to mechanical wear. *Sci Eng Compos Mater*. 2014;21(3): 333-339.
16. Suresh S, Harinath G, Deva Kumar MLS. Mechanical and wear behavior of Al 7075/Al2O3/SiC/mg metal matrix nanocomposite by liquid state process. *Advanced Composites and Hybrid Materias.* 2019;2: 530-539.
17. Nagaral M, Deshapande RG, Auradi V, Satish BP, Samuel Dd, Anilkumar MR. Mechanical and wear characterization of ceramic boron carbide-reinforced Al2024 alloy metal composites. *Journal of Bio-and Tribo-Corrosion*. 2021;7(1): 1-12.
18. Nagaral M, Auradi V, Parashivamurthy KI, Shivananda BK, Kori SA. Dry sliding wear behaviour of aluminium 6061-SiC-graphite particulates reinforced hybrid composites. *IOP Conference Series: Materials Science and Engineering*. 2018;310(1): 012156.
19. Samuel D, Satish BB, Auradi V, Nagaral M, Udaya RM. Evaluation of wear properties of heat-treated Al-AlB_2 in-situ metal matrix composites. *Journal of Bio-and Tribo-Corrosion.* 2021;(2): 1-11
20. Vinod L, Nagaral M, Suthan R, Auradi V. Microstructure and dry sliding wear behavior of Al2219-8 wt% of B_4C particulate Reinforced composites. *International Journal of Applied Engineering Research*. 2015;10.
21. Thirumalai T, Subramanian R, Dharmalingam S, Nachiappan R. Wear behavior of B_4C reinforced hybrid aluminium matrix composites. *Materials and Technologies*. 2015;49(1): 9-13.
22. Prashant SN, Nagaral M, V Auradi V. Preparation and evaluation of mechanical and wear properties of 6061 Al reinforced with graphite particulate metal matrix composite. *International Journal of Metallurgical & Materials Science and Engineering*. 2012;2(3): 85-95.
23. Nagaral M, Auradi V, Kori SA. Dry sliding wear behavior of graphite particulate reinforced Al6061 alloy composite materials. *Applied Mechanics and Materials*. 2014;592: 170-174.
24. Nagaral M, Auradi V, Parashivamurthy KI, Kori SA. Wear behavior of Al_2O_3 and graphite particulates reinforced Al6061 alloy hybrid composites. *American Journal of Materials Science*. 2015;5(3C): 25-29.
25. Nagaral M, Auradi V, Kori SA, Vijaykumar H. Investigations on mechanical and wear behavior of nano Al2O3 particulates reinforced AA7475 alloy composites. *Journal of Mechanical Engineering and Sciences*. 2019;13(1): 4623-4635.
26. Krishna UB, Vasudeva B, Auradi V, Nagaral M. Effect of percentage variation on wear behaviour of tungsten carbide and cobalt reinforced Al7075 matrix composites synthesized by melt stirring method. *Journal of Bio-and Tribo-Corrosion*. 2021;7(3): 1-8.
27. Pankaj RJ, Nagaral M, Shivakumar R, Jayasheel IH. Impact of boron carbide and graphite dual particulates addition on wear behavior of A356 alloy metal matrix composites. *Journal of Metals, Materials and Minerals.* 2020;30(4): 106-112.
28. Zeeshan A, Muthuraman V, Rathnakumar P, Gurusamy P, Nagaral M. Investigation on the tribological properties of copper alloy reinforced with Gr/ZrO_2 particulates by stir casting route. *Materials Today: Proceedings.* 2020;33: 3449-3453.
29. Kumar G, Saravanan R, Nagaral M. Dry sliding wear behavior of nano boron carbide particulates reinforced Al2214 alloy composites. To be published in *Materials Today: Proceedings.* 2021. Available from: https://doi.org/10.1016/j.matpr.2021.03.065.

THE AUTHORS

Veeresha G.
e-mail: veermech87@gmail.com

Manjunatha B.
e-mail: manjunatha.princi@gmail.com

Nagaral M.
e-mail: madev.nagaral@gmail.com
ORCID: 0000-0002-8248-7603

Auradi V.
e-mail: vsauradi@gmail.com
ORCID: 0000-0001-6549-6340

Bharath V.
e-mail: bharathv88@gmail.com

Mathematical model of extrusion in FDM 3D printing technology

O.B. Kudryashova✉, N.E. Toropkov, M.I. Lerner, A.B. Vorozhtsov

National Research Tomsk State University, 36, Lenin's Avenue, Tomsk, Russia, 634050

✉ olgakudr@inbox.ru

Abstract. We proposed a mathematical model of flow and extrusion in the 3D printing process (FDM technology). The model is based on fluid mechanics and uses conservation laws taking into account friction losses and local resistance losses. We performed a parametric study of the model. We have obtained experimental data on the rheology of compositions based on bimodal powders containing micro- and nanoparticles. The rheological properties of low-filled mixtures of powders with polymer differ from those of highly-filled mixtures of bimodal powders. These data are used as the basis for calculating the extrusion rate of compositions in FDM 3D printing of the considered compositions. The results of calculations of the extrusion rate depending on temperature, pressure, and dispersion of powders are given in the report. The search for optimal printing parameters based on mathematical modeling of the process is the goal of this work.
Keywords: extrusion, 3D printing, FDM technology, bimodal powders, mathematical mo

Acknowledgement. *The study was supported by a grant from the Russian Science Foundation (project No. 21-79-30006).*

Citation: Kudryashova OB, Toropkov NE, Lerner MI, Vorozhtsov AB. Mathematical model of extrusion in FDM 3D printing technology. *Materials Physics and Mechanics*. 2022;50(3): 388-400. DOI: 10.18149/MPM.5032022_3.

1. Introduction

The technology of layer-by-layer deposition (Fused deposition modeling, FDM) is most often used in additive technologies for creating three-dimensional objects [1]. This method is based on the application of fused fiber material to the platform, which makes it possible to design and implement new materials, including composites. Usually, a polymer thread is used as a material for creating objects, but recently there have been attempts to apply this technology for printing polymeric materials modified with various powders (steel, aluminum, wood ash, thermites, etc.) [2-5].

Commonly used additive technologies for working with metal powders are SLS (Selective Laser Sintering) and SLM (Selective Laser Melting) [5]. They involve the use of expensive and complex equipment, including a powerful laser. FDM 3D printing technology is based on the use of a relatively simple and inexpensive printer. This is the most used 3D printing technology due to the relative simplicity and availability of devices, as well as the ability to adjust operating parameters over a fairly wide range of values.

Typically, a polymer thread is used for this printer. If a polymer composition with metal powders is used instead of a thread, then the problem of using the FDM technology lies in the high viscosity of the material, which is especially high at a high concentration of particles.

The classic version of FDM technology uses thermoplastic polymers or composites based on them, which are heated in the hot part (hotend) of the print head to a molten or semi-liquid state, and then flow through the extruder die onto the platform or over previously printed layers. The thermoplasticity of the polymer thread is an essential property of this method. It allows the filaments to melt and solidify at room temperature after printing [6]. Usually, a composite filament for printing is prepared in advance, but in some cases, a mixture of filler and polymer powders is fed directly into the print head of the printer, where these powders are mixed and melted [7].

The complexity of using FDM, as well as some other additive technologies, is associated with the high viscosity of the material, which often depends non-linearly on operating parameters. To overcome the problem of high viscosity (> 1000 Pa s) and reduce friction in the printing process, for example, ultrasound inside the nozzle is used [8]. Bimodal metal powder, which exhibits high fluidity even at a high volume content in the mixture, could be a promising raw material for extrusion additive manufacturing [9].

The choice of operating parameters of the FDM printing process for working with viscous highly filled materials is an urgent task. Very few works are devoted to the theoretical study of this process. Meanwhile, mathematical modeling will reveal the main patterns of the process and the dependence of the target characteristics of printing on operating parameters.

Several theoretical works are devoted to the issues of mathematical modeling of various additive processes: Selective laser melting (SLM) [10-12]; Direct Metal Deposition (DMD) [13], and Direct ink writing (DIW) [14,15]. Meanwhile, few theoretical studies are devoted to FDM technology. The authors of [16] optimize the parameters of the FDM process using hybrid statistical methods. They take into account a number of competing process parameters, including layer thickness, build orientation, fill density, and number of loops. Recent work [7] investigated the effect of HMX solids content and particle size on the viscosity of molten TNT/HMX explosives. The authors used computational fluid dynamics methods to simulate the influence of viscosity, pressure, temperature, nozzle diameter, and particles on fluid flow inside a 3D printer nozzle.

Fluid mechanics methods allow us to identify the most significant characteristics that affect the target parameters of the printing process. However, there are no systematic works describing the features of the technology and the ongoing processes using the selected methods.

Extrusion speed is one of the most important parameters that must be controlled during the printing process. Too low or too high speed leads to deformation of the target object, associated with excessive or insufficient cooling, or poor adhesion of the layers. You can choose the optimal speed using the printer settings when printing with known polymer filament. But it will be difficult to set up printing with more viscous composite formulations without knowing the patterns of viscosity and extrusion rate changes depending on the main control parameters. The control parameters include the feed pressure of the mixture, the heating temperature, the fineness of the powder, and its concentration in the mixture.

The purpose of this work is to determine the extrusion rate of a viscous liquid containing particles and the influence of control parameters on the speed of FDM printing based on mathematical modeling and the application of fluid mechanics methods.

2. Mathematical model of the flow of a viscous liquid in a nozzle

Let us consider a mixture of polymer powder and particles that is fed into a nozzle using a piston/screw. In the heating block (hot end) of the nozzle, the mixture is heated to a predetermined temperature. The viscosity of the resulting liquid depends significantly on temperature and pressure.

From the point of view of reducing the viscosity of the material, it is better to use a lower concentration of particles [17]. Therefore, the concentration of particles is one of the most important parameters that must be optimized. As the experiment shows, the dispersion of particles also significantly affects the viscosity of the material [9].

Formulation of the problem. A mixture of polymer and powdered particles of a given volume concentration φ is placed in the nozzle heating block (Hot end). The mixture is heated to a given temperature T, greater than or equal to the melting point of the polymer; the mixture is acted upon by a piston with a given pressure P_p. Further, the viscous mixture flows inside the nozzle and outflows from it at a certain velocity V_e. It is necessary to determine this speed depending on the control parameters (T, P_p, φ), as well as the critical values of the parameters at which extrusion is impossible. The geometry of the nozzle is shown schematically in Fig. 1.

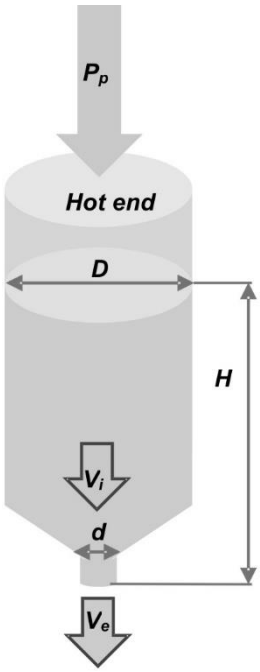

Fig. 1. Nozzle scheme

In accordance with the continuity equation the outflow velocity $V_e = V_i \frac{D^2}{d^2}$, where V_i is the velocity of the liquid inside the nozzle, D is the diameter of the wide part, d – is the diameter of the nozzle, H is the height of the extruder.

Bernoulli's equation for a viscous fluid:

$$\frac{\Delta P}{\rho g} + \frac{V_i^2}{2g} = -H + \frac{V_e^2}{2g} + h_g + h_{loc} = -H + \frac{V_i^2}{2g}\frac{D^2}{d^2} + h_g + h_{loc}, \quad (1)$$

where $\Delta P = P_p - P_{atm}$ is the extrusion pressure (relative to atmospheric), h_g is hydraulic friction losses, with the laminar flow: $h_g = \frac{64}{\mathrm{Re}}\frac{H}{D}\frac{V_i^2}{2g}$ (Darcy-Weisbach formula), $\mathrm{Re} = \frac{\rho D V_i}{\eta}$, η is the dynamic viscosity of the medium.

There is no flow at the inlet, and the velocity is equal to zero, at the bottom near the nozzle outlet is V_i. According to the conditions of the problem, friction losses due to viscosity are significant.

The nozzle is characterized by losses due to local resistance (sudden narrowing of the flow). Hydraulic losses due to local resistance are expressed by the Altshul formula [18]:

$$h_{loc} = \left(\frac{1-\varepsilon}{\varepsilon}\right)^2, \ \varepsilon = 0.57 + \frac{0.043}{1.1 - d^2/D^2}. \tag{2}$$

Since the Re number includes the V_i, we have a quadratic equation for the velocity inside the tube. It is a positive decision:

$$V_i = \frac{-b + \sqrt{b^2 - 4ac}}{2a}, \text{где } a = \frac{1 - D^2/d^2}{2g}, \ b = -\frac{32\eta}{gD^2}, \ c = H - h_{loc} + \frac{\Delta P}{\rho g}. \tag{3}$$

The first speed limit is the absence of a solution to the quadratic equation (3). It occurs when the following condition is met:

$$b^2 = 4ac, \text{ or } \left(\frac{32\eta}{gD^2}\right)^2 = 4\left(H - h_{loc} + \frac{\Delta P}{\rho g}\right)\left(\frac{1 - D^2/d^2}{2g}\right). \tag{4}$$

In this case, the rate is:

$$V_i = \frac{-b}{2a} = \frac{32\eta\left(1 - D^2/d^2\right)}{D^2}. \tag{5}$$

Simplifications. Consider the Bernoulli equation in the dimensionless form:

$$\frac{\Delta P}{\rho g H} = -1 + \frac{V_i^2}{2gH}\left(\frac{D^2}{d^2} - 1\right) + \frac{h_g}{H} + \frac{h_{loc}}{H}. \tag{6}$$

Let us estimate the value of different terms of the equation. Let us find the conditions under which one or another term can be neglected.

At high viscosity, the term of the equation responsible for the kinetic energy of the liquid can be neglected. Then the equation will take the form:

$$\frac{\Delta P}{\rho g H} = -1 + \frac{h_g}{H} + \frac{h_{loc}}{H}. \tag{7}$$

This is done if:

$$\frac{V_i^2}{2g}\left(\frac{D^2}{d^2} - 1\right) << h_g, \text{ или } \mathrm{Re} << \frac{64}{\left((D/d)^2 - 1\right)}\frac{H}{D}. \tag{8}$$

From here we get a simplified expression for the rate inside the structure:

$$\frac{\Delta P}{\rho g H} = -1 + \frac{32 V_i \eta}{g\rho D^2} + \frac{h_{loc}}{H}. \tag{9}$$

From here we get a simplified expression for the rate inside the structure:

$$V_i = \left(1 + \frac{\Delta P}{\rho g H} - \frac{h_{loc}}{H}\right) \cdot \frac{g\rho D^2}{32\eta}. \tag{10}$$

With a relatively high-pressure drop, i.e. at $\frac{\Delta P}{\rho g H} >> 1 - \frac{h_{loc}}{H}$, the expression for the velocity can be further simplified:

$$V_i \approx \frac{\Delta P D^2}{32\eta H}. \tag{11}$$

Taking into account the continuity equation, we obtain an expression for the outflow velocity: $V_e \approx \frac{\Delta P}{32\eta H}\frac{D^4}{d^2} = A_1 \frac{\Delta P}{\eta}$, (12)

where $A_1 = \frac{D^4}{32 H d^2}$ – constant characterizing the geometry of the nozzle.

Expression (12), which is correct under conditions of high fluid viscosity and sufficiently high piston pressure, makes it possible to obtain explicit dependences of the extrusion rate on the control parameters – pressure and viscosity. Viscosity, in turn, depends on temperature, pressure, and particle concentration.

Accounting for the dependence of viscosity on temperature, pressure and particle concentration. The dependence of the viscosity of thermoplastics on temperature is determined by the Frenkel-Eyring equation [19]:

$$\eta = \eta_{0T} \cdot \exp\left(-\frac{E_a}{RT}\right), \tag{13}$$

where η_{0T} is a constant having the dimension of viscosity, E_a is flow activation energy, R is the universal gas constant; R = 8.32 J/(mol·K); T is thermodynamic temperature, K.

The dependence of viscosity on pressure is also exponential:

$$\eta = \eta_{0P} \cdot \exp(\beta \Delta P), \tag{14}$$

where β is exponential pressure coefficient, η_{0P} is a constant having the dimension of viscosity.

Combining (13) and (14) we obtain the expression:

$$\eta = \eta_0 \cdot \exp\left(-\frac{E_a}{RT}\right) \cdot \exp(\beta \Delta P). \tag{15}$$

At low-pressure drops (ΔP less than 800 MPa) and temperature (ΔT less than 200 K), a linear approximation of the dependence of viscosity on these parameters can be used [20]:

$$\eta = \eta_0 \cdot (1 + \alpha_l \Delta T + \beta_l \Delta P). \tag{16}$$

In [21], the rheological properties of mixtures of poly(vinylidene fluoride) (PVDF) and polyethylene (LDPE) in the molten state were studied. Values of flow activation energy for different shear rates (τ = 3-10 s^{-1}) are obtained, which are 41.95-55.37 kJ/mol for PVDF. The corresponding PVDF melt viscosities at 190°C are 4 to 7.5 kPa·s.

According to the conditions of the problem, we have not just a polymer melt, but a melt containing particles. Einstein established the dependence of the viscosity of a solution on the concentration of suspended particles [22]:

$$\eta = \eta_0 (1 + \alpha\varphi), \tag{17}$$

where φ is volume fraction of the dispersed phase; α is coefficient depending on the particle shape. For spherical particles α = 2.5; for elongated particles α > 2.5. This equation was derived under the assumption that the particles of the dispersed phase are much larger than the matrix molecules, they are distant from each other, have the same size and shape, and do not interact.

Subsequent experiments showed [23] that formula (17) is valid only for $\varphi \le 10^{-3}$. Einstein's theory was generalized to the case of higher volume concentrations. As a result, for the effective viscosity coefficient, a relation of the form was obtained:

$$\eta = \eta_0 (1 + \alpha\varphi + k\varphi^2), \tag{18}$$

where the coefficient k ~ 6-6.25.

Influence of control parameters on blend viscosity and extrusion rate (Parametric Model Study). Below are the calculated dependences of the viscosity and extrusion rate on the control parameters in accordance with the proposed mathematical model.

The rate depends inversely on viscosity (Fig. 2). The calculation is made for D = 3 mm, H = 0.1 m, $D^2 / d^2 = 36$ (A_1 = 0.1 mm).

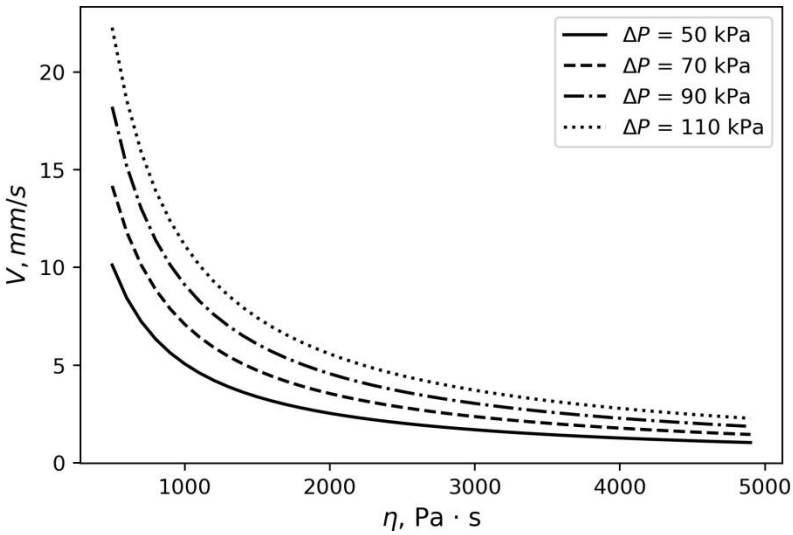

Fig. 2. Extrusion Rate vs. Viscosity

We obtained the dependence of the extrusion rate on temperature taking into account the exponential dependence of viscosity on temperature (13) and the data of work [21] (Fig. 3). The calculation is made for E_a = 60 kJ/mol, η_{0T} = 10E+10 Pa·s, A_1 = 0.1 mm.

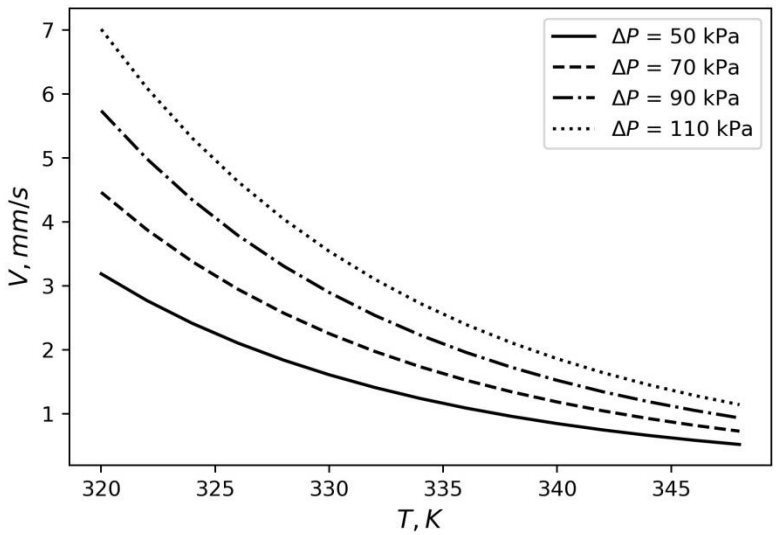

Fig. 3. Temperature dependence of extrusion rate

We calculated the dependence of the extrusion rate on pressure, taking into account the exponential dependence of viscosity on pressure (14) for given parameters E_a = 60 kJ/mol, η_{0P} = 10E+10 Pa·s, A_1 = 0.1 mm, β = 0.05 (Fig. 4).

The obtained dependencies correspond in character to those obtained in [7] using nozzle simulation in FDM technology.

The extrusion rate decreases with increasing temperature and pressure, which is not intuitively obvious. However, with increasing pressure, the velocity can not only decrease (Fig. 5, calculation at β = 0.005).

As follows from expression (12), the dependence on the geometric factor A1 is linear (Fig. 6).

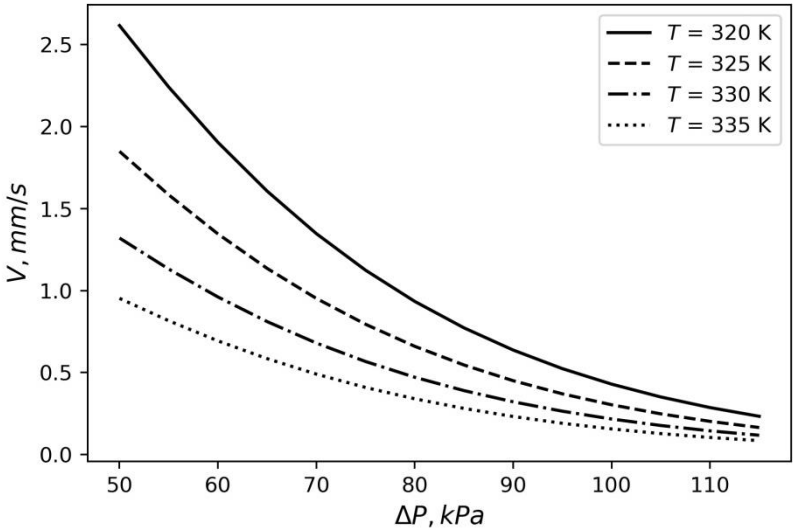

Fig. 4. Extrusion rate versus pressure (β = 0.05)

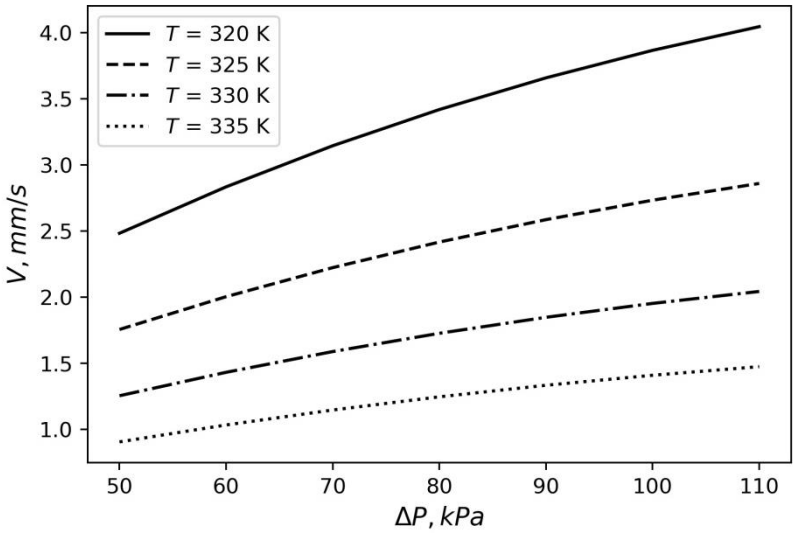

Fig. 5. Extrusion rate versus pressure (β = 0.005)

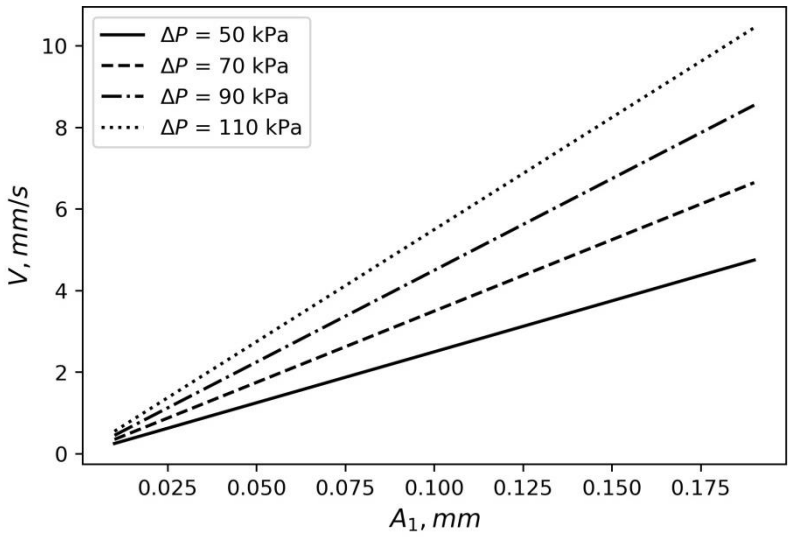

Fig. 6. Dependence of the extrusion rate on the geometric factor

The dependence on the concentration of particles in the mixture, calculated by equation (18), is shown in Fig. 7.

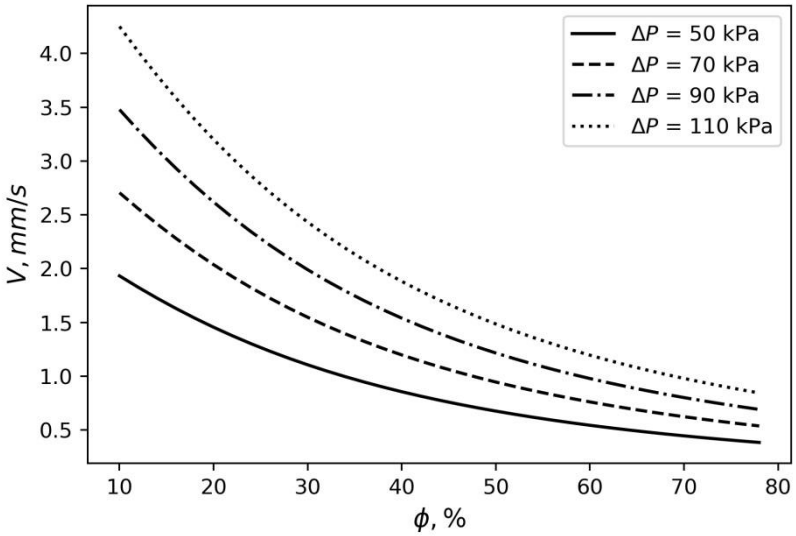

Fig. 7. The dependence of the extrusion rate on the concentration of solid particles in the mixture

The results obtained are intuitive: the smaller the proportion of particles in the polymer, the lower the viscosity of the mixture, and the higher the extrusion rate.

As can be seen, the lower the temperature of the mixture, the lower the viscosity and the higher the extrusion rate. Thus, operating the nozzle at the lowest temperature sufficient to melt the polymer is preferred.

3. Experiment

Materials and methods. A mixture of powders of micro- and nanoparticles was obtained by the method of the electrical explosion of wires (EEW) with a controlled ratio of dispersed phases in one technological process [9, 24]. Bimodal powders obtained by EEW do not require additional mixing and do not separate into fractions, like mixtures of micro- and nanopowders.

The dispersion of the obtained powders was measured using a laser diffraction particle size analyzer MASTERSIZER 2000 (Malvern Panalytical, UK).

The melt flow index (MFI) for all composites was measured with the plastometer IIRT-M (LOIP, Russia) with a load of 1-50 kg at 130-160°C. The measurement of MFI was carried out according to ISO 1133. The MFI index is related to the dynamic viscosity η [25]:

$$\eta = \frac{A \cdot \rho \cdot L}{\mathrm{MFI}}, \tag{18}$$

where the constant A = 155.709 kg·m/s^2, ρ is material density [g/cm^3], L is the load [kg], MFI is the melt flow index [g/10 min]. The load application area is S_p = 69.3626 mm, thus, pressure is $P = L/S_p$.

The binder is a ready-made mixture of polymer marked Viscowax 331 (Innospec, Germany) with the addition of 0.5% stearic acid. The binder content is 63% vol.

Rheological characteristics of bimodal powder (experimental results). Extrusion rate depending on pressure and temperature (calculation). To study the rheological characteristics, a bimodal powder of 316L stainless steel was taken, obtained at various energies of an electric explosion (32, 60, 93 J/mm2, further indicated by the corresponding

numbers) with different dispersity, as well as a powder with a characteristic particle size of the order of tens of micrometers (designated "micron") (Table 1).

Table 1. Median values of powder dispersion

Sample	10% *D* (μm)	50% *D* (μm)	90% *D* (μm)
32	0.157	1.777	3.421
60	0.123	1.209	2.561
93	0.102	1.112	2.145
Micron	10.965	17.357	29.777

Figure 8 shows the experimental dependence of viscosity on temperature, and Fig. 9 shows the experimental dependence of viscosity on pressure for these powders.

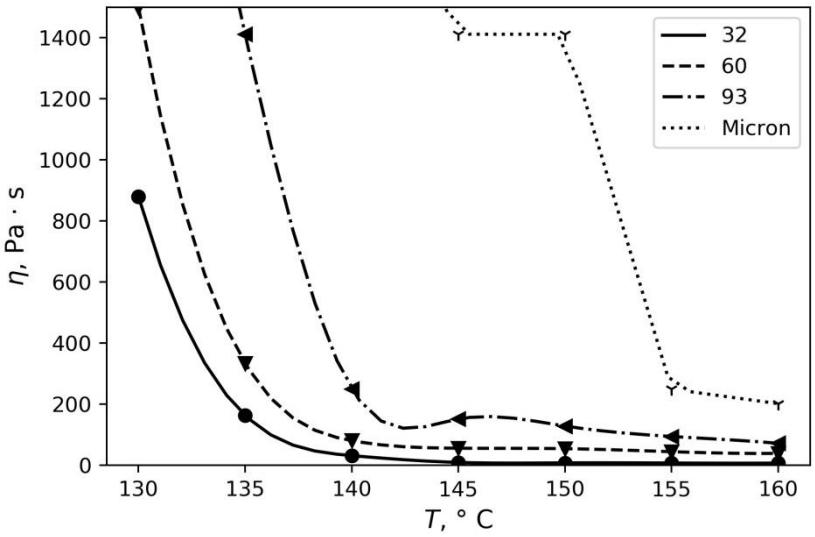

Fig. 8. Temperature dependence of viscosity obtained experimentally for four powders of different dispersion

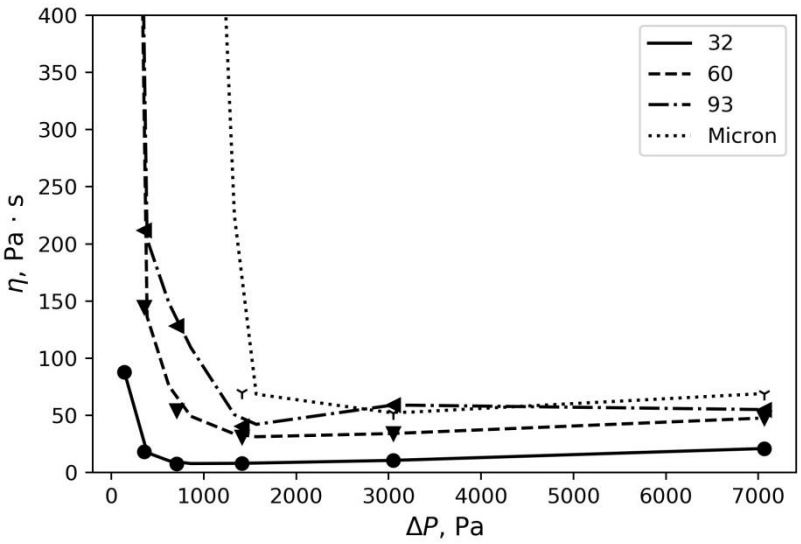

Fig. 9. Pressure dependence of viscosity obtained experimentally for four powders of different dispersion

The flow of the mixture, as follows from the obtained data, has a pronounced threshold character: at a pressure below a certain value, the viscosity is very high, then at a pressure of

about 1-1.5 MPa, the viscosity becomes minimal. Then it gradually grows linearly. At temperatures below ~140-145°C, the viscosity is also very high, then it drops sharply, and then decreases with temperature in accordance with a linear law.

The lowest viscosity in the experiment was obtained for the powder obtained at explosion energy of 32.5 J/mm2, which has a relatively large fraction of micron-sized particles. On the other hand, a powder with only micron-sized particles, without nanoparticles, has the highest viscosity. Substituting the experimental dependences of viscosity on temperature and pressure into formula (12), we obtain the dependence of the extrusion rate on temperature (Fig. 10) and pressure (Fig. 11).

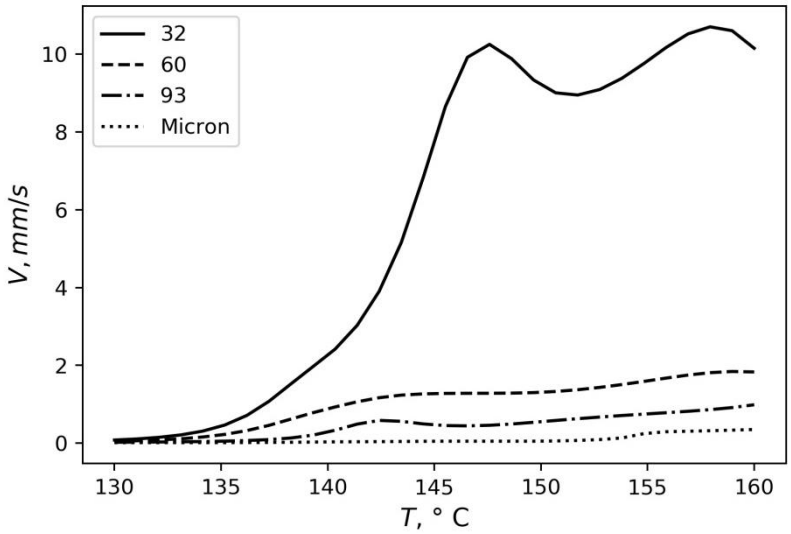

Fig. 10. Dependence of the extrusion rate on temperature, taking into account the experimental dependence of viscosity on temperature for four powders of different dispersion

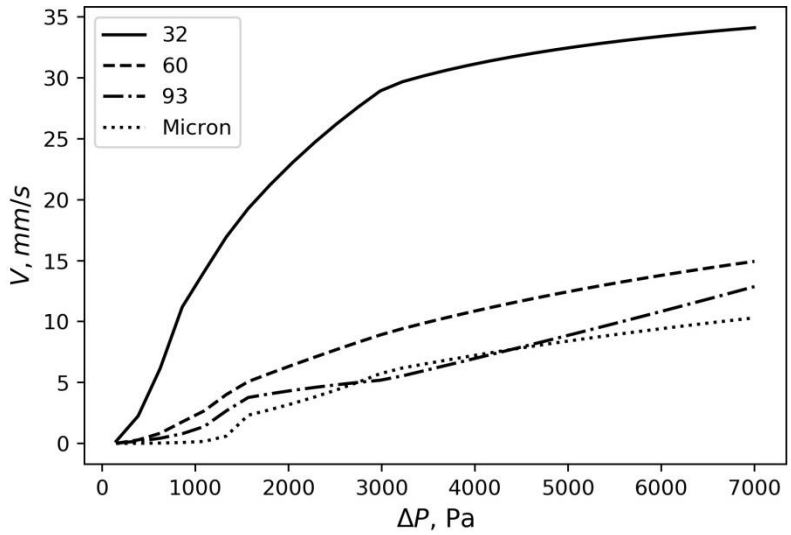

Fig. 11. Dependence of the extrusion rate on pressure, taking into account the experimental dependence of viscosity on pressure for four powders of different dispersion

The extrusion rate grows weakly with temperature and pressure for all powders, except for powder "32" with the most pronounced bimodality. Nanoparticles in a bimodal powder play the role of liquid molecules, with micron-sized particles suspended there. Such a pseudo-liquid, as shown by the experiment, has a lower viscosity than highly filled thermoplastic mixtures with particles of the same size.

4. Conclusion

The paper proposes a mathematical model of the 3D printing process (FDM technology) of materials based on polymer binders and powders. The model is based on the integral equations of continuum mechanics. Reasonable simplifications adequate to the case under consideration are carried out. A simple relation (12) is obtained, which relates the extrusion rate to the control parameters of the system: pressure, geometrical characteristics of the nozzle, and mixture viscosity. The dependences of the viscosity of the mixture on pressure, temperature, and the content of the dispersed phase are considered. A parametric study of the model was carried out. The obtained dependences correspond to the data of other researchers for similar materials and FDM technology.

The rheological properties of low-filled mixtures of powders with polymer differ from those of highly-filled mixtures of bimodal powders. The paper presents experimental data on the rheological properties of mixtures containing bimodal powders, depending on pressure, temperature, and dispersion composition. A threshold dependence was found: at pressure and temperature below a certain value (1-1.5 MPa, 140-145°C), the viscosity is very high, which makes it impossible or difficult to flow. After this threshold, the viscosity decreases slightly with temperature and slightly increases with pressure. Estimates of the extrusion rate of this starting material were carried out, based on the proposed model and the experimental results obtained.

References

1. Camargo JC, Machado ÁR, Almeida EC, Silva EF MS. Mechanical properties of PLA-graphene filament for FDM 3D printing. *The International Journal of Advanced Manufacturing Technology.* 2019;103(5): 2423-2443.
2. Dudek P. FDM 3D printing technology in manufacturing composite elements. *Archives of metallurgy and materials.* 2013;58(4): 1415-1418.
3. Ramazani H, Kami A. Metal FDM, a new extrusion-based additive manufacturing technology for manufacturing of metallic parts: a review. *Progress in Additive Manufacturing*. 2022;7: 609–626.
4. Gonzalez-Gutierez J, Godec D, Guráň R, Spoerk M, Kukla C, Holzer C. 3D printing conditions determination for feedstock used in fused filament fabrication (FFF) of 17-4PH stainless steel parts. *Metalurgija*. 2018;57(1-2): 117-120.
5. Mazurchevici AD, Nedelcu D, Popa R. Additive manufacturing of composite materials by FDM technology: A review. *Indian Journal of Engineering and Materials Sciences (IJEMS).* 2021;27(2): 179-192.
6. Ngo TD, Kashani A, Imbalzano G, Nguyen KT, Hui D. Additive manufacturing (3D printing): A review of materials, methods, applications and challenges. *Composites Part B: Engineering*. 2018;143: 172-196.
7. Zong H, Cong Q, Zhang T, Hao Y, Xiao L, Hao G et al. Simulation of Printer Nozzle for 3D Printing TNT/HMX Based Melt-Cast Explosive. *The International Journal of Advanced Manufacturing Technology.* 2022;119: 3105-3117.
8. Gunduz IE, McClain MS, Cattani P, Chiu GC, Rhoads JF, Son SF. 3D printing of extremely viscous materials using ultrasonic vibrations. *Additive manufacturing.* 2018;22: 98-103.
9. Pervikov A, Toropkov N, Kazantsev S, Bakina OV, Glazkova E, Lerner M. Preparation of Nano/Micro Bimodal Aluminum Powder by Electrical Explosion of Wires. *Materials.* 2021;14(21): 6602.
10. Ökten K, Biyikoğlu A. Development of thermal model for the determination of SLM process parameters. *Optics & Laser Technology.* 2021;137: 106825.

11. Ansari MJ, Nguyen DS, Park HS Investigation of SLM process in terms of temperature distribution and melting pool size: modeling and experimental approaches. *Materials.* 2019;12(8): 1272.
12. Estrada-Díaz JA, Elías-Zúñiga A, Martínez-Romero O, Olvera-Trejo D. Enhanced Mathematical Model for Producing Highly Dense Metallic Components through Selective Laser Melting. *Materials.* 2021;14(6): 1571.
13. Choi J, Han L, Hua Y. Modeling and Experiments of Laser Cladding With Droplet Injection. *ASME. J. Heat Transfer.* 2005;127(9): 978-986.
14. Zhang B, Nguyen AK, Narayan RJ, Huang J Direct ink writing of vancomycin loaded polycaprolactone/polyethylene oxide/hydroxyapatite 3D scaffolds. *Journal of the American Ceramic Society.* 2021;105(3): 1821-1840.
15. Buj-Corral I, Domínguez-Fernández A, Gómez-Gejo A. Effect of printing parameters on dimensional error and surface roughness obtained in direct ink writing (DIW) processes. *Materials.* 2020;13(9): 2157.
16. Deswal S, Narang R, Chhabra D. Modeling and parametric optimization of FDM 3D printing process using hybrid techniques for enhancing dimensional preciseness. *International Journal on Interactive Design and Manufacturing (IJIDeM).* 2019;13(3): 1197-1214.
17. Knott MC, Craig AW, Shankar R, Morgan SE, Iacono ST, Mates JE, McCollum JM. Balancing processing ease with combustion performancein aluminum/PVDF energetic filaments. *Journal of Materials Research.* 2021;36(1): 203-210.
18. Altshul AD. *Hydraulic resistances.* Moscow: Nedra; 1970.
19. Frenke YI. *Kinetic Theory of Liquids.* M-L.:Akad. Nauk SSSR; 1945. (In Russian)
20. Kerber ML et al. *Technology of polymer processing. Physical and chemical processes*. Moscow: URITE; 2018. (In Russian)
21. Kaseem M, Hamad K, Yang HW, Lee YH, Deri F, Ko YG. Melt rheology of poly (vinylidene fluoride)(PVDF)/low density polyethylene (LDPE) blends. *Polymer Science Series A.* 2015;57(2): 233-238.
22. Sherman P. *Rheology of emulsions.* Oxford: Pergamon Press; 1963.
23. Rudyak VY. *Statistical aerohydromechanics of homogeneous and heterogeneous media*. Novosibirsk: NSUACE (Sibstrin); 2005. (In Russian)
24. Krinitcyn M, Toropkov N, Pervikov A, Glazkova E, Lerner M. Characterization of nano/micro bimodal 316L SS powder obtained by electrical explosion of wire for feedstock application in powder injection molding. *Powder Technology.* 2021;394: 225-233.
25. Shenoy AV, Saini DR, Nadkarni VM. Melt rheology of polymer blends from melt flow index. *International Journal of Polymeric Materials.* 1984;10(3): 213-235.

THE AUTHORS

Kudryashova O.B.
e-mail: olgakudr@inbox.ru
ORCID: 0000-0002-0404-8736

Toropkov N.E.
e-mail: zerogooff@gmail.com
ORCID: 000-0003-3146-3043

Lerner M.I.
e-mail: lerner@ispms.tsc.ru
ORCID: 0000-0001-8565-1344

Vorozhtsov A.B.
e-mail: abv@mail.tomsknet.ru
ORCID: 0000-0003-2080-9942

Materials Physics and Mechanics. 2022;50(4): 401-409
Research article
http://dx.doi.org/10.18149/MPM.5032022_4

Submitted: July 18, 2022
Approved: September 19, 2022
Accepted: November 23, 2022

The void evolution kinetics driven by residual stress in icosahedral particles

A.S. Khramov[1], S.A. Krasnitckii[2*], A.M. Smirnov[1,3], M. Yu. Gutkin[1,3,4]

[1]ITMO University, St. Petersburg, 197101, Russia

[2]St. Petersburg State University, St. Petersburg, 199034, Russia

[3]Peter the Great St. Petersburg Polytechnic University, St. Petersburg, 195251, Russia

[4]Institute for Problems in Mechanical Engineering, Russian Academy of Sciences, St. Petersburg, Russia

*krasnitsky@inbox.ru

Abstract. A kinetic model of vacancy diffusion induced by both the Gibbs-Thompson curvature effect and stress state of the Marks-Ioffe stereo-disclination in a hollow spherical particle is suggested to investigate the void evolution in hollow icosahedral particles. The obtained analytically vacancy concentration profile inside the hollow icosahedral particle is employed to derive numerically the evolution equation of void kinetics. It is shown that the scenario of void evolution in icosahedral particles strongly depends on the inner-to-outer radius ratio at the initial moment of time and on the value of dimensionless parameter α reflecting the contribution of a pressure-induced (drift) vacancy flux between the external and internal particle surfaces.

Keywords: Icosahedral small particles, residual stress, stress relaxation, disclination, hollow particles, spherical pore, pressure-induced diffusion

Acknowledgements. *Acknowledgements. This work was supported by the Russian Science Foundation (grant No. 22-11-00087, https://rscf.ru/en/project/22-11-00087/).*

Citation: Khramov AS, Krasnitckii SA, Smirnov AM, Gutkin MY. The void evolution kinetics driven by residual stress in icosahedral particles. *Materials Physics and Mechanics*. 2022;50(3): 401-409. DOI: 10.18149/MPM.5032022_4.

Introduction

Hollow and porous nanostructures have aroused a keen interest due to their higher performance in the various fields as plasmonics [1], nanosensing [2], energy storing [3], catalysis [4] and medicine [5] than their solid counterparts. By now, a large number of reviews (see, for example, [6-9]) has been devoted to different aspects of synthesis of hollow nanostructures as well as the influence of hollows on the functional properties of the devices based on these nanostructures. However, the theoretical aspects of void evolution are still of great concern being limited by following issues [10]: void shrinkage due to the Gibbs-Thompson curvature effect in single-crystalline (SCPs) and polycrystalline (PCPs) particles of pure elements [11-16], void growth due to the nanoscale Kirkendall effect in bi-metallic [12,17-19] and oxidated [20-22] particles, void formation as a residual stress relaxation mechanism in multiply twinned particles (MTPs) [23-28]. The latter phenomenon was effectively investigated by quasi-equilibrium energetic approach in pentagonal whiskers (PWs), icosahedral (IcPs) [25] and decahedral particles (DhPs) [28] with respect to the disclination concept.

According to the disclination concept [29-31], the residual stress in an IcP can be described in terms of Marks-Ioffe stereo disclination (SD) with strength $\chi \approx 0.0613$ sr spread

© A.S. Khramov, S.A. Krasnitckii, A.M. Smirnov, M. Yu. Gutkin, 2022.
Publisher: Peter the Great St. Petersburg Polytechnic University
This is an open access article under the CC BY-NC 4.0 license (https://creativecommons.org/li-censes/by-nc/4.0/)

over the volume of the elastic sphere [32]. Whitin this model, the interior region of IcP is subject to hydrostatical compression while the periphery region is subject to hydrostatical tension. This residual stress state induces the generation of vacancies on external particle surface and their subsequent migration to IcP central region. The vacancy saturation in particle central region can cause the void formation. From the energetical point of view, the void formation should decrease the stored strain energy and it seems to be an effective channel of residual stress relaxation in IcPs.

The void formation in IcPs was experimentally investigated by electron microscopy in [33-35]. Yasnikov and Vikarchuk in [33] employed chemical etching to examine porous structures in Cu IcPs produced by electrodeposition method. The voids were revealed in relatively big IcPs (with outer diameter more than ~1 μm) while relatively small IcPs (with outer diameter less than ~1 μm) were void-free. Besides, Huang *et al.* [35] investigated the influence of residual stress on the void formation and growth in bimetallic particles with icosahedral and octahedral shapes. It was shown that heating of a mixture of solid strained icosahedral Pd particles in Cu solution can be employed to synthesize hollow Pd-Cu alloyed particles, while heating of a mixture of strain-free solid octahedral Pd particles in the Cu solution did not lead to void formation and, on the contrary, the solid Pd/Cu core-shell particles were performed. This means that the void occurrence in particles strongly depends on the residual stress induced by multiply cycling twinning.

The aforementioned quasi-equilibrium energetic models [25,28] have not taken into account the influence of the vacancy diffusion on the void formation process in MTPs. An attempt to overcome this limitation was made in [24,26] for PWs and [27] for IcPs. Vlasov and Fedik [26] applied the bulk diffusion theory to investigate the initial-stage kinetics of void nucleation in PWs via the migration of vacancies under the stress state induced by a positive partial wedge disclination (WD). It was shown that the void growth rate at the initial stages in PWs obeys the parabolic low. Romanov and Samsonidze [24] considered the diffusion value problem in cylinder subjected to an elastic field of a WD with regard to presence of vacancy sinks/sources. The boundary conditions for vacancy concentration were prescribed by the WD stress field. Tsagrakis *et al.* [27] were the first who figured out the stress field of Mark-Ioffe SD in terms of strain-gradient elasticity. The obtained nonsingular analytical expression of the SD hydrostatic stress was employed to determine the vacancy concentration in IcPs in terms of diffusion associated theory. The main drawback of the discussed above kinetic models of void evolution in MTPs, however, is the fact that they have not taken into consideration the vacancy concentration gradient induced by the Gibbs-Thomson curvature effect on external and internal particle surfaces, although it is well known that this effect is responsible for void shrinking process observed experimentally [36,37] and within computer simulations [38-40].

This work aims at investigating the void evolution kinetics in IcPs in terms of counteraction of the Gibbs-Thomson curvature effect [11] and the relaxation of residual stress [32]. In order to do this, an analytical solution of the boundary value problem of bulk diffusion of vacancies in the spherical shell with respect to both the Gibbs-Thompson surfaces conditions and the stress state of Marks-Ioffe SD is obtained. This solution is employed to elucidate the scenarios of void evolution kinetics in hollow IcPs.

Model

We consider a bulk diffusion kinetics of the vacancies in a single element isotropic spherical shell with inner and outer radii a_p and a subjected to stress state of a Marks-Ioffe SD with strength $\chi \approx 0.0613$ (see Fig.1). The total vacancy flux density [$m^{-2}s^{-1}$] inside the shell can be presented as a sum:

$$\mathbf{j}_v = \mathbf{j}_c + \mathbf{j}_\sigma , \quad (1)$$

where

$$\mathbf{j}_c = -\frac{D}{\Omega}\nabla C\,, \tag{2}$$

is the outward vacancy flux density corresponding to vacancy concentration gradient between the internal and external spherical shell surfaces, and

$$\mathbf{j}_\sigma = -\frac{D\,\delta v}{kT\,\Omega}C\nabla\sigma_\chi\,, \tag{3}$$

is the inward vacancy flux density corresponding to residual stress state of the IcP, D is the vacancy diffusion coefficient [m^2/s], $C = C(\boldsymbol{R}, t)$ is the dimensionless relative concentration of vacancies, $\boldsymbol{R}$ is the position-vector, t is the time, Ω is the atomic volume corresponding to the vacancy, δv is the vacancy relaxation volume, σ_χ is the hydrostatic stress induced by the Marks-Ioffe stereo disclination, kT has its usual meaning, and ∇ is the nabla operator. The void evolution scenario is defined by the contribution of each term in Eq.1: (i) shrinkage if $|\mathbf{j}_c| > |\mathbf{j}_\sigma|$, (ii) growth if $|\mathbf{j}_\sigma| > |\mathbf{j}_c|$, and (iii) equilibrium if $|\mathbf{j}_\sigma| = |\mathbf{j}_c|$.

The rate of vacancy concentration inside the shell is goverend by the mass conservation law

$$\frac{\partial C}{\partial t} + \nabla\cdot(\Omega\,\mathbf{j}_v) = 0\,. \tag{4}$$

Substituting Eqs.1-3 in Eq.4 and taken into consideration the steady state process assumption ($\partial C/\partial t \approx 0$) one can obtain the Fick second law in the following form:

$$\nabla^2 C + \frac{\delta v}{kT}\nabla\cdot(C\nabla\sigma_\chi) = 0 \tag{5}$$

According to the classical Gibbs-Thomson effect in hollow SCPs, vacancies tend to migrate from the internal surface to the external surface causing the void shrinkage with subsequent void collapse. The influence of this phenomenon on the void evolution kinetics in hollow particles can be introduced in terms of the boundary condition for Eq.5 at the internal and external shell surfaces in the linear form of the Gibbs-Thompson conditions [11]:

$$C(a_p) = C_0\left(1 + \frac{\beta}{a_p}\right),\quad C(a) = C_0\left(1 - \frac{\beta}{a}\right), \tag{6a,b}$$

where C_0 is the equilibrium vacancy concentration in vicinity of a planar surface, $\beta = 2\gamma\,\Omega/kT$, and γ is the specific surface energy.

The pressure-induced (drift) vacancy flux from the external IcP surface to the internal one is determined by the hydrostatic component of the SD stress tensor ($\sigma_\chi = -1/3\ \mathrm{tr}\,\boldsymbol{\sigma}$). In accordance with the continuum model of a hollow IcP [32], the hydrostatic stress can be written as

$$\sigma_\chi = \frac{4G\chi(1+\nu)}{3(1-\nu)}\left[\frac{1}{3} + \ln\frac{R}{a} + \frac{a_p^3}{a^3 - a_p^3}\ln\frac{a_p}{a}\right], \tag{7}$$

where G is the shear modulus, ν is the Poisson ratio, and $R = |\mathbf{R}|$. The gradient of the hydrostatic stress is given by

$$\nabla\sigma_\chi = \frac{4G\chi(1+\nu)}{3(1-\nu)}\frac{\mathbf{R}}{R^2}\,. \tag{8}$$

Then the equation of the Fick second law in spherical coordinate systems for a hollow particle subjected to the SD stress fields in the steady-state process assumption reads

$$\frac{d^2C}{dR^2} + \frac{2-\alpha}{R}\frac{dC}{dR} - \frac{\alpha C}{R^2} = 0\,, \tag{9}$$

where

$$\alpha = \frac{G\chi}{3}\frac{1+\nu}{1-\nu}\frac{\delta v}{kT}\,. \tag{10}$$

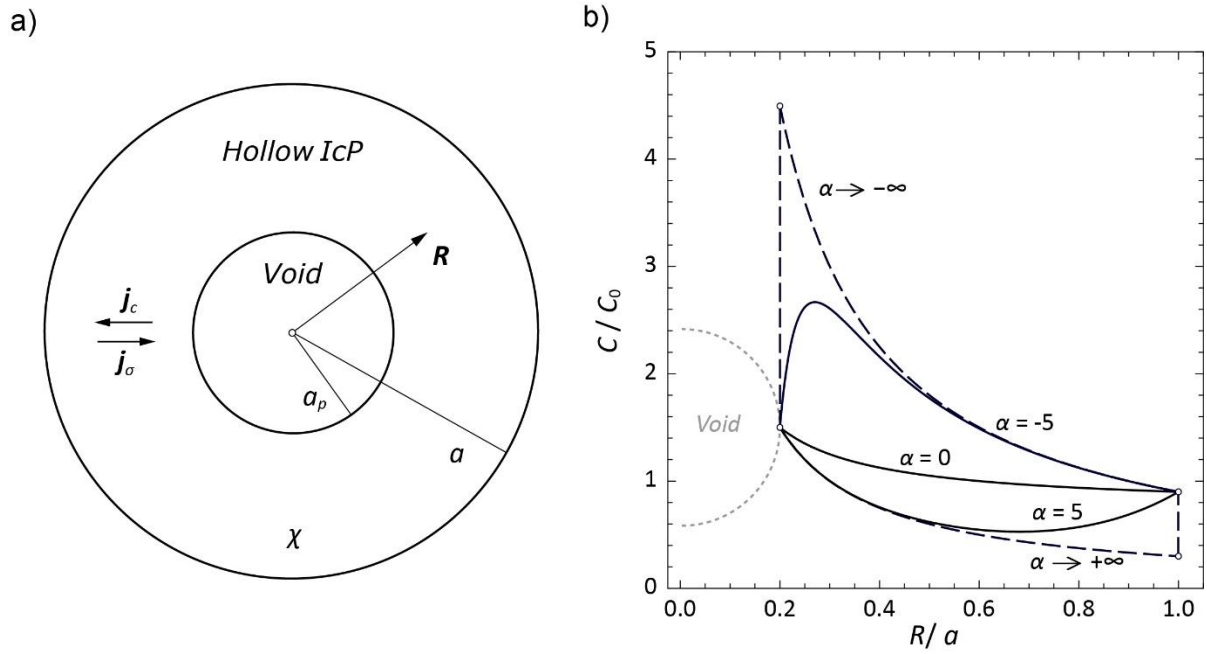

Fig. 1. a) The continuum model of an IcP containing a central spherical void. b) The dependences of normalized vacancy concentration on dimensionless radial coordinate R/a in the IcP with $a_p/a = 0.2$ and $\beta/a = 0.1$ given for different values of parameter $\alpha = 0, \pm 5$ and for $\alpha \to \pm\infty$

Thus, the vacancy diffusion in hollow IcPs can be described by Eq.9 under the boundary condition given by Eq.6.

Results

One can obtain the analytical solution of Eq.9 under the boundary conditions (Eqs.6a,b) on the internal and external surfaces in the following form

$$C = C_0 \frac{(a_p + \beta)(a^{1+\alpha} - R^{1+\alpha}) + (a - \beta)(R^{1+\alpha} - a_p^{1+\alpha})}{(a^{1+\alpha} - a_p^{1+\alpha})R}. \tag{11}$$

In the case of $\alpha \to 0$, Eq.11 transforms to the expression obtained in work [11] for stress-free hollow SCPs.

Fig. 1b demonstrates the vacancy concentration profiles in a hollow IcP with the ratio of inner to outer radii $a_p/a = 0.2$, calculated from Eq.11 for $\beta/a = 0.1$ and different values of α. As is seen from Fig.1b, the presence of the SD stress state ($\alpha < 0$) induces a local increase of vacancy concentration in vicinity of the internal particle surface. In the limiting case of $\alpha \to -\infty$, the contribution of concentration flux is negligible small (the vacancy flux is completely determined by the drift term), and the vacancy concentration reaches the highest value ~$4.5C_0$ at the internal surface ($R = a_p$). It is worth noting that diffusion of impurities (here we mean interstitial atoms or substitutional impurity atoms of radius greater than the radius of the parent atoms) in IcPs can be described by positive values of α. Fig.1b shows that the values of impurity concentration in hollow IcPs always less than those in SCPs. Besides, the minimum value of impurity concentration tends to move to the external surface with an increase in α. In the limiting case of $\alpha \to +\infty$, the impurity concentration takes a constant value ~$0.3C_0$ at the outer surface of the hollow IcP.

Turn now to the void evolution kinetics in IcPs. The rate of the inner surface can be determined by vacancy flux at the void surface from Eqs.1-3 in the following form

$$\frac{da_p}{dt} = -\Omega \frac{\mathbf{j}_v \cdot \mathbf{R}}{R}\bigg|_{R=a_p} = \frac{(1+\alpha)C_0 D}{a_p^2} \frac{(a_p+\beta)a^{1+\alpha} - (a-\beta)a_p^{1+\alpha}}{a^{1+\alpha} - a_p^{1+\alpha}}. \tag{12}$$

Let us rewrite Eq.12 as

$$\frac{dp}{d\tau} = -\frac{(1+\alpha)\Delta^5}{bp^2} \frac{(p+b\Delta)-(1-b\Delta)p^{1+\alpha}}{1-p^{1+\alpha}}, \tag{13}$$

where the following dimensionless variables are introduced

$$p = \frac{a_p}{a}, \qquad \tau = \frac{C_0 D\beta t}{a_0^3}, \qquad \Delta = (1-p^3)^{1/3}, \qquad b = \frac{\beta}{a_0}, \tag{14a-d}$$

where a_0 is the radius of a void-free particle

$$a_0 = (a^3 - a_p^3)^{1/3}. \tag{15}$$

Eq.15 claims that the particle remains unchanged during the void evolution processes.

The solution of Eq.13 was obtained by numerical integration and illustrated in Fig.2a. The curves $p(\tau)$ are shown for different values of α and initial normalized void radius $p_0 = a_{p,0}/a$. As is seen from Fig.2a, the scenario of void evolution in IcPs is strongly determined by the initial void radius and the value of α. In the case of $\alpha = 0$, for any values of p_0, the void tends to shrinkage and finally collapses at the time $\tau = \tau_f$ as it was shown in [12,13]. For $\alpha = -0.5$, the void tends to reach some equilibrium size $p_{eq} = a_{p,eq}/a$ via growing (when $p_0 < p_{eq}$) or shrinking (when $p_0 > p_{eq}$). It is worth noting that, for relatively small values of $\alpha < -1$, solid IcPs could be transformed into thin spherical shells (see, for example, the curve for $\alpha = -2$) as it was observed experimentally in [33].

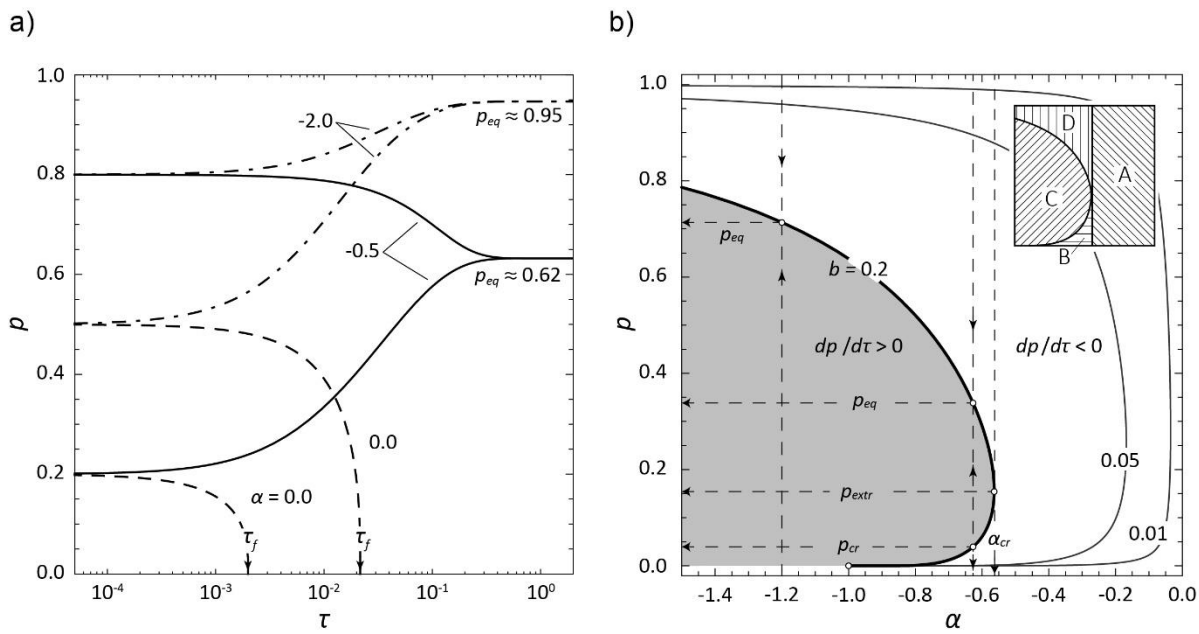

Fig. 2. a) Dependence of the normalized void radius $p = a_p / a$ on the dimensionless time τ at $b = 0.1$ for different values of the initial IcP radii ratio $p_0 = 0.2$, 0.5, and 0.8, and $\alpha = 0.0$ (dashed curves), –0.5 (solid curves), –2.0 (dashed-and-dotted curves). b) The curves $dp/d\tau = 0$ in dependence on the normalized void radius p and the parameter α for different values of $b = 0.01$, 0.05, 0.2. The inset in the upper right corner demonstrates the regions A, B, C and D corresponding to different pathways of the void evolution

The void growth or shrinkage scenarios are determined by the sign of $dp/d\tau$ in Eq.13. In order to analyze possible pathways of void evolution in IcPs, the condition $dp/d\tau = 0$ was considered. Then from Eq.13 one gets

$$1+\alpha = \log_p \frac{p+b\Delta}{1-b\Delta}. \tag{16}$$

In Fig.2b, the curves $f(\alpha, p)$ satisfying Eq.16 for different values of b are shown. As is seen from Fig.2b, the void tends to grow if p_0 and α values are in the area $dp/d\tau > 0$; in contrast, the void tends to shrink if p_0 and α values are in the area $dp/d\tau < 0$. Therefore, one can define the regions in Fig.2b according to the following void evolution scenarios: A) the void tends to shrink with collapse for any values of the initial void ratio if α exceeds some critical value α_{cr} ($\alpha > \alpha_{cr}$, $0 < p_0 < 1$). Besides, the critical parameter $\alpha_{cr} \to 0$ if b decreases; B) there is a critical value of the normalized void radius, p_{cr}, bellow which the void nucleus shrinks to collapse ($-1 < \alpha < \alpha_{cr}$, $0 < p_0 < p_{cr}$); C) for ($-1 < \alpha < \alpha_{cr}$, $p_{cr} \le p_0 < p_{eq}$) or ($\alpha < -1$, $0 < p_0 < p_{eq}$), the void grows to get the optimal (equilibrium) normalized radius p_{eq}; D) for ($\alpha < \alpha_{cr}$, $p_0 > p_{eq}$), the void shrinks to get the optimal normalized radius p_{eq}.

Thus, the void is unstable in regions A and B – here a hollow IcP has a tendency to transform in a compact particle with radius a_0. On the contrary, the void has an optimal size in regions C and D – the void in an IcP has a tendency to change its volume until reaching the equilibrium radius $a_{p,eq}$.

Conclusions

In summary, we have considered the vacancy diffusion in hollow IcPs to analyze the void evolution kinetics. The vacancy flux is defined by concentration gradient and pressure-induced (drift) terms. The first term is caused by the difference between vacancy concentrations at the inner and outer particle surfaces due to the Gibbs-Thompson curvature effect. The second term is determined by the residual stress state and described by the Marks-Ioffe SD elastic model of a hollow IcP. The contribution of each term in vacancy diffusion is defined by a dimensionless parameter α: the drift diffusion prevails over the concentration one if $\alpha \ll -1$, vice versa if $\alpha \to 0$, and the contributions of both the terms are comparable if $\alpha \approx 0$. An analytical solution of the corresponding boundary value problem of bulk diffusion is given for the radial dependence of vacancy concentration. It is demonstrated that in IcPs, a local vacancy saturation is observed in vicinity of the void surface. The analytical expression for vacancy profile is employed to obtain the equation of void evolution. It is shown that the scenario of void evolution in IcPs strongly depends on the initial void radius $a_{p,0}$ as well as the value of parameter α. There is such a critical parameter α_{cr} that, for $\alpha > \alpha_{cr}$, the void has a tendency to shrink with subsequent collapse for any initial void radius $a_{p,0}$. When $\alpha < \alpha_{cr}$, the following processes can occur: (i) the void shrinkage with subsequent collapse, if the initial void radius is less than its critical value, $a_{p,0} < a_{p,cr}$; (ii) the void shrinkage until reaching its optimal size, if the initial void radius is larger than its equilibrium value, $a_{p,0} > a_{p,eq}$; and (iii) the void growth until reaching its optimal size, if the initial void radius is in the interval $a_{p,cr} < a_{p,0} < a_{p,eq}$.

References

1. Genç A, Patarroyo J, Sancho-Parramon J, Bastús NG, Puntes V, Arbiol J. Hollow metal nanostructures for enhanced plasmonics: synthesis, local plasmonic properties and applications. *Nanophotonics*. 2017;6(1): 193-213.

2. Wang T, Kou X, Zhao L, Sun P, Liu C, Wang Y, Shimanoe K, Yamazoe N, Lu G. Flower-like ZnO hollow microspheres loaded with CdO nanoparticles as high performance sensing material for gas sensors. *Sensors and Actuators B: Chemical*. 2017;250: 692-702.

3. Zhu C, Wang H, Guan C. Recent progress on hollow array architectures and their applications in electrochemical energy storage. *Nanoscale Horizons*. 2020;5(8): 1188-1199.
4. Fu J, Detsi E, De Hosson JTM. Recent advances in nanoporous materials for renewable energy resources conversion into fuels. *Surface and Coatings Technology*. 2018;347: 320-336.
5. Yasun E, Gandhi S, Choudhury S, Mohammadinejad R, Benyettou F, Gozubenli N, Arami H. Hollow Micro and Nanostructures for Therapeutic and Imaging Applications. *Journal of Drug Delivery Science and Technology*. 2020;60: 102094.
6. Anderson BD, Tracy JB. Nanoparticle conversion chemistry: Kirkendall effect, galvanic exchange, and anion exchange. *Nanoscale*. 2014;6(21): 12195-12216.
7. Wang X, Feng JI, Bai Y, Zhang Q, Yin Y. Synthesis, properties, and applications of hollow micro-/nanostructures. *Chemical Reviews*. 2016;116(18): 10983-11060.
8. Yu L, Yu XY, Lou XW. The Design and Synthesis of Hollow Micro-/Nanostructures: Present and Future Trends. *Advanced Materials*. 2018;30(38): 1800939.
9. Zhu M, Tang J, Wei W, Li S. Recent progress in the syntheses and applications of multishelled hollow nanostructures. *Materials Chemistry Frontiers*. 2020;4(4): 1105-1149.
10. Krasnitckii SA, Gutkin MY. Review on theoretical models of void evolution in crystalline particles. *Reviews on Advanced Materials and Technologies*. 2021;3(1): 96-126.
11. Tu KT, Gösele U. Hollow nanostructures based on the Kirkendall effect: design and stability considerations. *Applied Physics Letters*. 2005;86(9): 093111.
12. Gusak AM, Zaporozhets TV, Tu KT, Gösele U. Kinetic analysis of the instability of hollow nanoparticles. *Philosophical Magazine*. 2005;85(36): 4445-4464.
13. Evteev AV, Levchenko EV, Belova IV, Murch GE. Shrinking kinetics by vacancy diffusion of a pure element hollow nanosphere. *Philosophical Magazine*. 2007;87(25): 3787-3796.
14. Fischer FD, Svoboda J. High temperature instability of hollow nanoparticles. *Journal of Nanoparticle Research*. 2008;10(2): 255-261.
15. Yanovsky VV, Kopp MI, Ratner MA. Gas-filled pore in bounded particle. *Arxiv*. [Preprint] 2019. Available from: https://doi.org/10.48550/arXiv.1910.13956.
16. Klinger L, Murch GE, Belova IV, Rabkin E. Pores shrinkage and growth in polycrystalline hollow nanoparticles and nanotubes. *Scripta Materialia*. 2020;180: 93-96.
17. Evteev AV, Levchenko EV, Belova IV, Murch GE. Formation of a hollow binary alloy nanosphere: a kinetic Monte Carlo study. *Journal of Nano Research*. 2009;7: 11-17.
18. Yu HC, Yeon DH, Li X, Thornton K. Continuum simulations of the formation of Kirkendall-effect-induced hollow cylinders in a binary substitutional alloy. *Acta Materialia*. 2009;57(18): 5348-5360.
19. Jana S, Chang JW, Rioux RM. Synthesis and modeling of hollow intermetallic Ni–Zn nanoparticles formed by the Kirkendall effect. *Nano Letters*. 2013;13(8): 3618-3625.
20. Fischer FD, Svoboda J. Modelling of reaction of metallic nanospheres with gas. *Solid State Phenomena*. 2011;172: 1028-1037.
21. Levitas VI, Attariani H. Mechanochemical continuum modeling of nanovoid nucleation and growth in reacting nanoparticles. *The Journal of Physical Chemistry C*. 2012;116(1): 54-62.
22. Klinger L, Kraft O, Rabkin E. A model of Kirkendall hollowing of core-shell nanowires and nanoparticles controlled by short-circuit diffusion. *Acta Materialia*. 2015;83: 180-186.
23. Mikhailin AI, Romanov AE. Amorphization of disclination core. *Sov. Physics of the Solid State*. 1986; 28(2): 601–603.
24. Romanov AE, Samsonidze GG. Diffusion in the elastic field of a wedge disclination. *Sov. Technical Physics Letters*. 1988;14(14): 585-586.
25. Romanov AE, Polonsky IA, Gryaznov VG, Nepijko SA, Junghanns T, Vitrykhovski NJ. Voids and channels in pentagonal crystals. *Journal of Crystal Growth*. 1993;129: 691-698.
26. Vlasov NM, Fedik II. Diffusion-induced relaxation of residual stresses. *Doklady Physics*. 2000;45(11): 623-626.

27. Tsagrakis I, Yasnikov IS, Aifantis EC. Gradient elasticity for disclinated micro crystals. *Mechanics Research Communications.* 2018;93: 159-162.
28. Krasnitckii SA, Gutkin MY, Kolesnikova AL, Romanov AE. Formation of a pore as stress relaxation mechanism in decahedral small particles. *Letters on Materials*. 2022;12(2): 137-141.
29. Wit RDe. Partial disclinations. *Journal of Physics. C. Solid State Physics*. 1972;5: 529-534.
30. Romanov AE, Kolesnikova AL. Application of disclination concept to solid structures. *Progress in Material Science*. 2009;54: 740–769.
31. Romanov AE, Kolesnikova AL. Elasticity Boundary-Value Problems for Straight Wedge Disclinations. A Review on Methods and Results. *Reviews on Advanced Materials and Technologies.* 2021;3(1): 55-95.
32. Howie A, Marks LD. Elastic strains and the energy balance for multiply twinned particles. *Philosophical Magazine A*. 1984;49(1): 95-109.
33. Yasnikov IS, Vikarchuk AA. Voids in icosahedral small particles of an electrolytic metal. *Journal of Experimental and Theoretical Physics Letters*. 2006;83(1): 42-45.
34. Wang X, Figueroa-Cosme L, Yang X, Luo M, Liu J, Xie Z, Xia Y. Pt-based icosahedral nanocages: using a combination of {111} facets, twin defects, and ultrathin walls to greatly enhance their activity toward oxygen reduction. *Nano Letters*. 2016;16(2): 1467-1471.
35. Huang J,.Yan Y, Li X, Qiao X, Wu X, Li J, Zhang H. Unexpected Kirkendall effect in twinned icosahedral nanocrystals driven by strain gradient. *Nano Research*. 2020;13(10): 2641-2649.
36. Nakamura R, Tokozakura D, Lee JG, Mori H, Nakajima H. Shrinking of hollow Cu_2O and NiO nanoparticles at high temperatures. *Acta Materialia*. 2008;56(18): 5276-5284.
37. Glodán G, Cserháti C, Beke DL. Temperature-dependent formation and shrinkage of hollow shells in hemispherical Ag/Pd nanoparticles. *Philosophical Magazine*. 2012;92(31): 3806-3812.
38. Wang Y, Liu Q, Sun Y, Wang R. Magnetic field modulated SERS enhancement of CoPt hollow nanoparticles with sizes below 10 nm. *Nanoscale*. 2018;10(26): 12650-12656.
39. Valencia FJ, Ramírez M, Varas A, Rogan J. Understanding the stability of hollow nanoparticles with polycrystalline shells. *The Journal of Physical Chemistry C*. 2020;124(18): 10143-10149.
40. Jiang C, Mo Y, Wang H, Li R, Huang M, Jiang S. Molecular dynamics simulation of the production of hollow silver nanoparticles under ultrafast laser irradiation. *Computational Materials Science.* 2021;196: 110545.

THE AUTHORS

Khramov A.S.
e-mail: 242531@niuitmo.ru
ORCID: 0000-0002-3895-0728

Krasnitckii S.A.
e-mail: Krasnitsky@inbox.ru
ORCID: 0000-0003-4363-8242

Smirnov A.M.
e-mail: andrei.smirnov@niuitmo.ru
ORCID: 0000-0002-7962-6481

Gutkin M. Yu.
e-mail: m.y.gutkin@gmail.com
ORCID: 0000-0003-0727-6352

Materials Physics and Mechanics. 2022;50(3): 410-419
Research article
http://dx.doi.org/10.18149/MPM.5032022_5

Submitted: August 22, 2022
Approved: September 9, 2022
Accepted: October 19, 2022

Bearing capacity of spherical thick-walled shell taking into account compressibility and nonlinear plasticity

I.K. Andrianov✉, S.I. Feoktistov

Federal State-Financed Educational Institution of Higher Learning "Komsomolsk-na-Amure State University",

Russia, 681013, Khabarovsk Krai, Komsomolsk-on-Amur, Lenin Avenue, 27

✉ ivan_andrianov_90@mail.ru

Abstract. The stress-strain state of a thick-walled spherical shell is considered under the conditions of compressibility of the material and the nonlinear law of hardening. Using the equations of the relationship between stresses and deformations according to the method of variable elasticity parameters, an integral equation of compatibility of logarithmic deformations is obtained. When performing numerical calculations using the method of simple iterations, the moment of unstable deformation of the spherical shell is determined. The dependences of the relative pressure on the radial displacement of the points of the outer surface of the spherical shell are obtained, taking into account the compressibility of the material and without taking into account the compressibility for an ideal elastic-plastic material and for an elastic-plastic material with nonlinear hardening. According to the results of numerical calculation, failure to account for compressibility introduces a significant error in the calculation of radial displacements of the outer surface. The results of the study will allow us to determine the maximum permissible load of a thick-walled spherical shell corresponding to stable deformation.
Keywords: thick-walled shell, sphere, compressibility of the material, physical nonlinearity, stress-strain state, variable elasticity parameters, shaping

Acknowledgements. *The research was carried out with the financial support of the "Council for Grants of the President of the Russian Federation for state support of young Russian scientists and state support of leading scientific schools of the Russian Federation" within the framework of a scholarship under the project SP-2200.2022.5 "Development of models and algorithms for calculating plastic shaping of blanks of stamping production".*

Citation: Andrianov IK, Feoktistov SI. Bearing capacity of spherical thick-walled shell taking into account compressibility and nonlinear plasticity. *Materials Physics and Mechanics*. 2022;50(3): 410-419. DOI: 10.18149/MPM.5032022_5.

1. Introduction

Thick-walled axisymmetric shells are currently widely used in various engineering structures. These are high–pressure vessels, ring foundations, pressure pipes, tunnels, and others. Stresses in such structures are distributed unevenly across the thickness, which must be taken into account when calculating strength. The issues of modeling the stress-strain state of shells of various types were considered in [1-7] under conditions of incompressibility of the material, linear hardening, and ideal plasticity.

© I.K. Andrianov, S.I. Feoktistov, 2022.
Publisher: Peter the Great St. Petersburg Polytechnic University
This is an open access article under the CC BY-NC 4.0 license (https://creativecommons.org/li-censes/by-nc/4.0/)

When conducting a literature review on the subject of the study, one of the little-studied aspects is taking into account the compressibility of the material in the process of elastic-plastic deformation. In addition, it should be noted that the issues of assessing the stress-strain state of shells were considered in the works [8-10]. The analysis of radial and circumferential stresses in a spherical shell was considered in the works [11,12]. The physical nonlinearity of materials manifested in the nonlinear relationship between stresses and deformations under various types of deformation was considered in the works [13-15]. The features of working with the deformation diagram when assessing the stress-strain state were considered in the article [16]. The problem of solving elastic-plastic problems under various hardening laws, and the evaluation of the methods of the solution was considered in the works [17-21]. Aspects of finite element modeling of stamping and shaping problems were investigated in the works [22,23]. The application of the method of variable elasticity parameters in finite element analysis was considered in the work [24]. The issues of modeling and optimization in the field of metallurgy, and mechanical engineering were studied in articles [25-33].

2. Methods

The main equations for calculations beyond the limits of elasticity according to the deformation theory are differential equations of equilibrium, conditions for the compatibility of deformations, the relationship between deformations and stresses, and boundary conditions. When determining the stress-strain state of thick-walled shells, it is also necessary to take into account the physical nonlinearity of the material – the law of hardening during plastic deformation.

The deformation diagram of a material, as a relationship between the intensity of stresses and the intensity of logarithmic deformations, is given by a linear power function [5]:

$$\sigma_i = \begin{cases} 3G\, e_i & , e_i \le e_{i\text{т}} \\ A\, e_i^n & , e_i > e_{i\text{т}} \end{cases}, \tag{1}$$

where $G = E/2(1+\mu)$ – modulus of elasticity of the second kind, $e_i -$ intensity of logarithmic strains, $e_{i\text{т}} -$ intensity of logarithmic strains corresponding to the yield strength, $A,\ n -$ approximating coefficients of the power function, $E -$ Young's module, $\mu -$ Poisson's ratio.

Consider the problem of determining the bearing capacity of a spherical thick-walled shell, taking into account compressibility and nonlinear plasticity. We will solve the problem using the method of variable elasticity parameters. This method is quite universal since it allows solving elastic problems, elastic-plastic, and purely plastic problems in a single formulation.

Consider the stress-strain state of a thick-walled spherical shell under the conditions of compressibility of the material and the nonlinear law of hardening. For a volumetric axisymmetric stress state in a spherical coordinate system ρ, θ, φ at uniform pressure inside the sphere, there are no tangential stresses, derivatives with respect to φ are zero, and the equilibrium conditions have the form:

$$\frac{\partial \sigma_\rho}{\partial \rho} + \frac{1}{\rho}\left[2\sigma_\rho - \left(\sigma_\varphi + \sigma_\theta\right)\right] = 0;$$

$$\sigma_\varphi = \sigma_\theta$$

or

$$\frac{d\sigma_\rho}{d\rho} = \frac{2(\sigma_\theta - \sigma_\rho)}{\rho}, \tag{2}$$

where σ_ρ, σ_θ , σ_φ – radial, tangential (circumferential) and meridional stresses.

Integrating equation (2), we obtain the integral equation of equilibrium in the form:

$$\sigma_\rho = \int_R^\rho \frac{2(\sigma_\theta - \sigma_\rho)}{\rho} d\rho + \sigma_{\rho R}\,, \tag{3}$$

where R – radius of the outer surface of the sphere, $\sigma_{\rho R}$ – radial stress on the outer surface of the sphere.

The conditions for the compatibility of logarithmic strains in the case of central symmetry are represented as [6]:

$$\frac{de_\theta}{d\rho} = \frac{1-\exp(e_\theta - e_\rho)}{\rho}; \tag{4}$$
$$e_\varphi = e_\theta.$$

The equations of the relationship between stresses and deformations, in accordance with the method of variable elasticity parameters, have the form:

$$\left.\begin{aligned} e_\rho &= \frac{1}{E^*}\left[\sigma_\rho - 2\mu^*\sigma_\theta\right]; \\ e_\theta &= \frac{1}{E^*}\left[\sigma_\theta - \mu^*(\sigma_\theta + \sigma_\rho)\right]. \end{aligned}\right\}, \tag{5}$$

where E^* and μ^* – variable elasticity parameters.

In the equation of compatibility of logarithmic deformations (4), we will replace:

$$\frac{de_\theta}{d\rho} = \frac{1}{\exp(e_\theta)}\frac{d(\exp(e_\theta))}{d\rho},$$

we write this equation in the form:

$$\frac{d(\exp(e_\theta))}{d\rho} = \frac{1}{\rho}\exp(e_\theta) - \frac{1}{\rho}\exp(2e_\theta - e_\rho). \tag{6}$$

Considering equation (6) as a nonlinear differential equation of the first degree of the form and solving it by the Bernoulli method, we obtain a general solution:

$$\exp(e_\theta) = -\rho\int\frac{1}{\rho^2}\exp(2e_\theta - e_\rho)\,d\rho + C\rho\,.$$

Given the boundary conditions: $\rho = R$, $e_\theta = e_{\theta R} = \ln(R/R_0)$, then:

$$e_\theta = \ln\left(-\rho\int_R^\rho \frac{1}{\rho^2}\exp(2e_\theta - e_\rho)d\rho + \rho/R_0\right).$$

Using the equations of the relationship between stresses and deformations (5), we obtain an integral equation of the compatibility of logarithmic strains in stresses:

$$\sigma_\theta = \frac{\mu^*}{(1-\mu^*)}\sigma_\rho + \frac{E^*}{(1-\mu^*)}\ln\left(-\rho\int_R^\rho \frac{1}{\rho^2}\exp\left(\frac{2\sigma_\theta}{E^*} - \frac{(1+2\mu^*)}{E^*}\sigma_\rho\right)d\rho + \rho/R_0\right). \tag{7}$$

The solution for determining the stress-strain state of a spherical shell, in accordance with the method of variable elasticity parameters, is carried out by the method of successive approximations according to a recurrent scheme using equations (3) and (7) for given boundary conditions, that is, with a known position of the outer edge of the sphere R and radial stress on the outer edge $\sigma_{\rho R} = 0$:

$$\sigma_\theta{}^{(k+1)} = \frac{\mu^{*(k)}}{\left(1-\mu^{*(k)}\right)}\sigma_\rho{}^{(k)} +$$
$$+\frac{E^{*(k)}}{\left(1-\mu^{*(k)}\right)}\ln\left(-\rho\int_R^\rho \frac{1}{\rho^2}\exp\left(\frac{2\sigma_\theta{}^{(k)}}{E^{*(k)}} - \frac{\left(1+2\mu^{*(k)}\right)}{E^{*(k)}}\sigma_\rho{}^{(k)}\right)d\rho + \rho/R_0\right);$$

$$\sigma_\rho{}^{(k+1)} = \int_R^\rho \frac{2\left(\sigma_\theta{}^{(k+1)} - \sigma_\rho{}^{(k)}\right)}{\rho}d\rho\,,$$

where are the values with the index (*k*) и (*k+1*) denote, respectively, their values in the *k*-th and *(k+1)*-th approximations. Numerical integration is carried out from R to $r^{(j)}$, where $r^{(j)}$ – the inner radius of the pipe in the process of deformation. In the zero approximation, for $j = 0$, we assume that $r^{(j)} = r_0$, where r_0 is the inner radius of the pipe in the initial state without load

As calculations have shown, the results of calculations do not depend on the choice of the values of the initial approximation for σ_ρ, σ_θ, и σ_φ, therefore, in the initial approximation we take:

$\sigma_\rho{}^{(0)} = 0;\ \sigma_\theta{}^{(0)} = 0;\ \sigma_\varphi{}^{(0)} = 0;\ E^{*(0)} = E;\ \mu^{*(0)} = \mu,$

where E – modulus of elasticity of the material from which the sphere is made, μ – Poisson's ratio.

The deformed state in the *(k+1)*-th approximation is determined by:

$$e_\rho{}^{(k+1)} = \frac{1}{E^{*(k)}}\left[\sigma_\rho{}^{(k+1)} - 2\mu^{*(k)}\sigma_\theta{}^{(k+1)}\right];$$

$$e_\theta{}^{(k+1)} = \frac{1}{E^{*(k)}}\left[\sigma_\theta{}^{(k+1)} - \mu^{*(k)}\left(\sigma_\theta{}^{(k+1)} + \sigma_\rho{}^{(k+1)}\right)\right].$$

In the case of the transition of the material to the plasticity zone, the secant modulus in *(k+1)*-th approximations is determined by:

$$E_{sec}{}^{(k+1)} = \frac{A\left(e_i{}^{(k+1)}\right)^n}{e_i{}^{(k+1)}},$$

where the strain intensity is determined in the (k+1)-th approximation:

$$e_i{}^{(k+1)} = \frac{2}{3}\left(e_\rho{}^{(k+1)} - e_\theta{}^{(k+1)}\right).$$

Then the value of the variable elasticity parameters is specified:

$$E^{*(k+1)} = \frac{E_{sec}{}^{(k+1)}}{1 + \frac{1-2\mu}{3E}E_{\sec}{}^{(k+1)}};\quad \mu^{*(k+1)} = \frac{\frac{1}{2} - \frac{1-2\mu}{3E}E_{\sec}{}^{(k+1)}}{1 + \frac{1-2\mu}{3E}E_{\sec}{}^{(k+1)}}.$$

To control the convergence of the process, the values of stress intensities are compared:

$$\frac{\sigma_i{}^{(k+1)} - \sigma_i{}^{(k)}}{\sigma_i{}^{(k+1)}}100\% \le \Delta\sigma_i\%\,.$$

The calculation is continued until the specified percentage accuracy is reached. After achieving the specified accuracy of the calculation of the stress-strain state, the position of the inner surface of the spherical shell is clarified:

$$r^{(j+1)} = r_0\, exp\left(e_{\theta r}{}^{(j)}\right),$$

where $e_{\theta r}{}^{(j)}$ – the value of the tangential logarithmic deformation at the upper bound of the numerical integration, that is, when $\rho = r^{(j)}$.

After clarifying the inner radius during deformation and changing the upper limit of numerical integration, the calculation of the stress-strain state is repeated until the specified accuracy of determining the inner radius is reached:

$$\frac{r^{(j+1)} - r^{(j)}}{r^{(j+1)}}100\% \le \Delta r\%.$$

After the final determination of the stress-strain state, it is possible to determine the internal pressure in the sphere at which a given increase in the outer radius occurred:

$$p = -\sigma_{\rho r},$$

where $\sigma_{\rho r}$ – the value of the radial stress on the inner surface of the pipe in the conclusion of all calculations.

To determine the bearing capacity of a thick-walled shell, it is necessary to determine when the pressure reaches the point of the extremum. To do this, the condition must be met:

$p = P_{max}$ by $dp = 0$.

Thus, the value of P_{max} determines the bearing capacity of the sphere. By changing the outer radius R with a certain step and determining the pressure p at each step, it is possible to plot the dependence of p on R. Analyzing the resulting graph, it is possible to determine the moment when, with an increase in the outer radius, the deformation pressure begins to fall, that is, the pressure reaches a maximum and the pressure increment with an increase in the radius becomes less than zero:

$dp < 0$.

This indicates that the moment of unstable deformation of the shell with subsequent destruction has come. The value of the maximum pressure in this case determines the bearing capacity of the spherical shell.

3. Results and Discussion

Let us compare the results of calculations obtained on the example of a thick-walled spherical shell, performed taking into account the compressibility of the material and in the case of an incompressible material, for an ideal elastic-plastic material and for an elastic-plastic material with nonlinear hardening. The inner radius of the shell $r_0 = 50$ mm, outer radius $R_0 = 100$ mm.

In the case of an ideal elastic-plastic material, the deformation diagram of the material is given by the equation:

$$\sigma_i = \begin{cases} 3G \ \ by \ \ e_i \le e_{i\text{т}} \\ \sigma_T \ \ by \ e_i > e_{i\text{т}} \end{cases}.$$

Figures 1 and 2 show the results of changes in relative internal pressure ($\bar{p} = p/\sigma_T \ or \ \bar{p} = p/\sigma_{0.2}$) from the radial displacement of the points of the outer surface of the spherical shell ($U_R = R - R_0$).

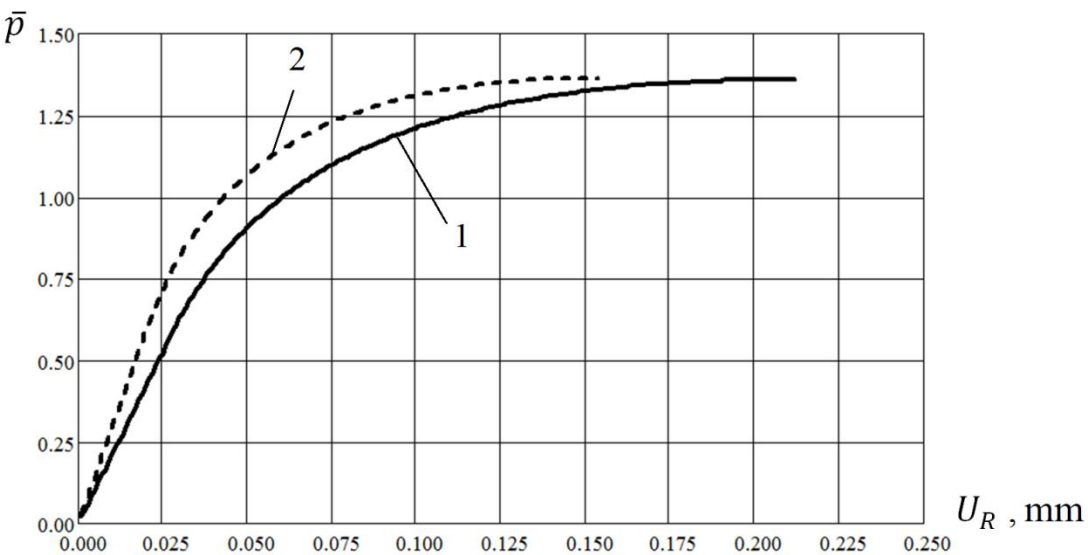

Fig. 1. Graph of the relative pressure dependence on the radial displacement of the points of the outer surface of the spherical shell.

1 – taking into account the compressibility of the material ($\mu = 0.3$);

2 – without taking into account the compressibility of the material ($\mu = 0.5$)

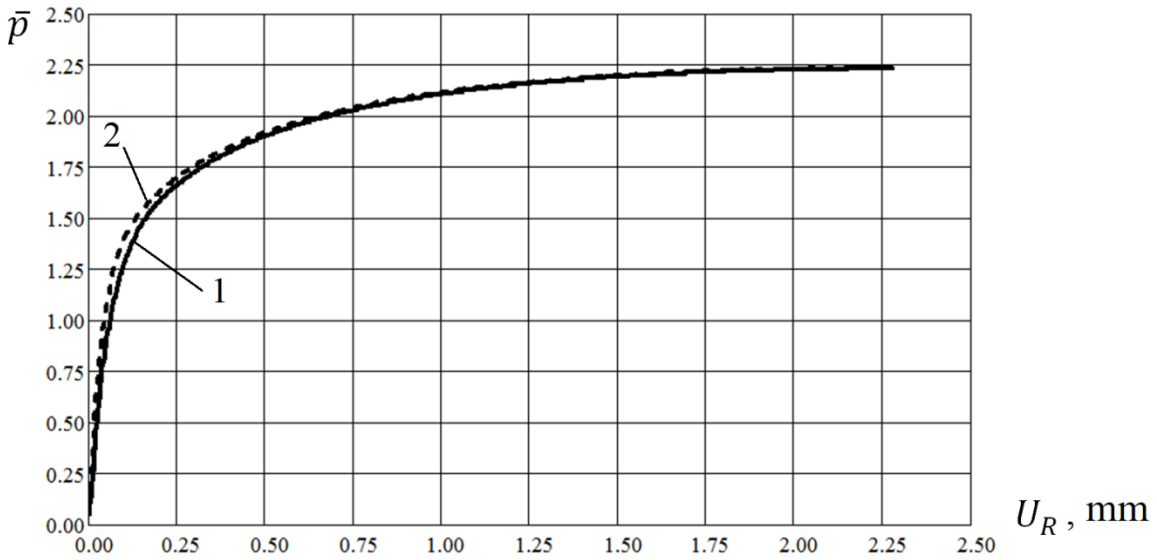

Fig. 2. Graph of the relative pressure dependence on the radial displacement of the points of the outer surface of the spherical shell
(elastic-plastic material with nonlinear hardening E=71000 MPa, $\sigma_{0,2}$=224 MPa, σ_{B}=400 MPa, $\delta\% = 15$)
1 – taking into account the compressibility of the material ($\mu = 0.3$);
2 – without taking into account the compressibility of the material ($\mu = 0.5$)

As follows from the comparison of curves 2 with curves 1 (see Figs. 1 and 2), the assumption of incompressibility of the material gives a very small error in determining the bearing capacity of a thick-walled spherical shell. Thus, calculations show that for an ideal elastic-plastic material, this error is 0.35%, and for an elastic-plastic material with nonlinear hardening – 0.013%.

A significant error is obtained when calculating radial displacements. Thus, for an ideal elastic-plastic material, this error for radial displacements of the outer surface of the sphere during destruction is 40%, and for an elastic-plastic material with nonlinear hardening – 7%.

A deeper analysis of the results obtained for an ideal elastic-plastic material showed that they agree very well with the analytical solution for a constrained thick-walled pipe presented in books [2,7]. As with the analytical solution, it can be shown that curve 1 in Fig. 1 can be obtained from curve 2 by multiplying the radial displacement value by $2(1-\mu)$.

This analysis proves the adequacy of the proposed mathematical model and the reliability of the results obtained in this article.

Figures 3 and 4 show the results of changing the effect of the compressibility of the material on the calculated value of internal pressure depending on the radial displacement of the points of the outer surface of the spherical shell.

The effect of compressibility was estimated as a percentage of the design pressure in the case of compressible material according to the formula

$$\Delta p\% = \frac{(p^* - p_*)}{p_*} 100\%,$$

where p_* – pressure under the condition of compressibility of the material, p^* –pressure under the condition of incompressibility of the material

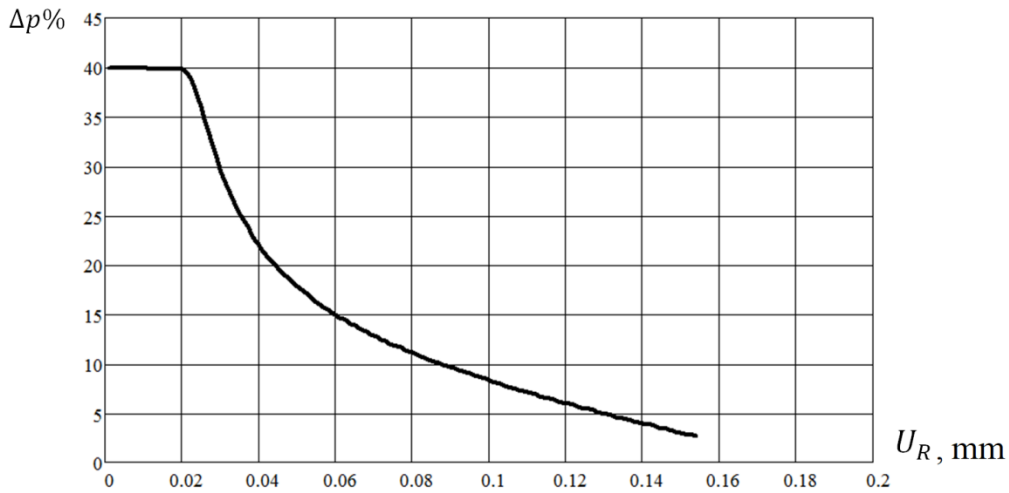

Fig. 3. Graph of the change in the effect of compressibility of the material on the calculated value of internal pressure depending on the radial displacement of the points of the outer surface of the spherical shell (ideal elastic-plastic material)

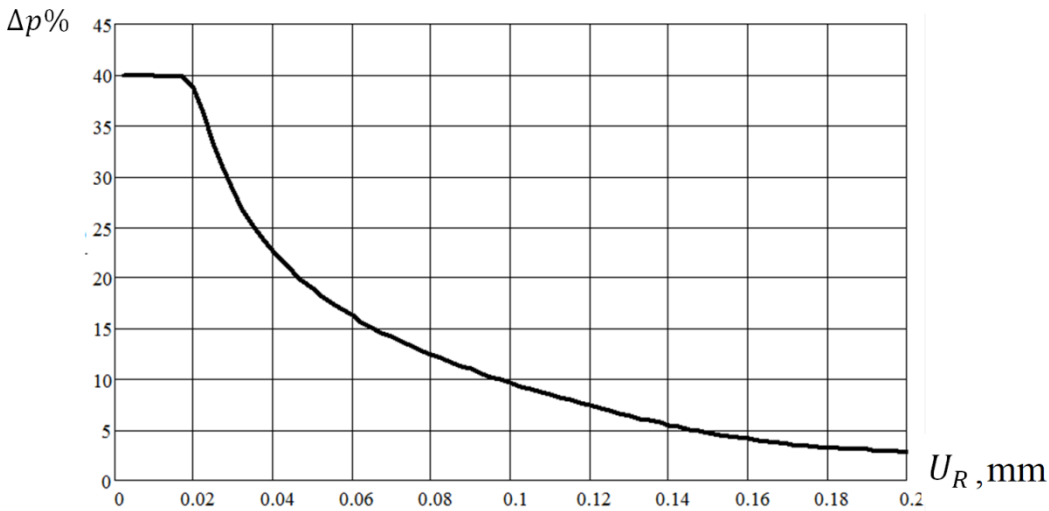

Fig. 4. Graph of changes in the effect of compressibility of the material on the calculated value of internal pressure depending on the radial displacement of the points of the outer surface of the spherical shell (elastic-plastic material with nonlinear hardening)

The analysis of the graphs presented in Figs. 3 and 4 show that the compressibility of the material has the maximum effect on the calculated value of the internal pressure during elastic deformation. As soon as the radial displacements exceed a certain value at which plastic deformations occur in the walls of the spherical shell, the compressibility effect decreases sharply, asymptotically approaching zero. Moreover, the nature of the change in the influence of compressibility practically does not depend on hardening, but depends only on the intensity of deformations and repeats the nature of the change in the variable elasticity parameter μ^*.

It can be shown that the maximum value of $\Delta p\%max$ explicitly depends on the Poisson's ratio and is defined by the expression $\Delta p\%\max = (1 - 2\mu)100\%$.

4. Conclusion

Thus, these studies have shown the effectiveness and universality of the application of the method of variable elasticity parameters for solving complex elastic-plastic problems, taking

into account the compressibility and nonlinear plasticity of the material. According to the presented ratios, the bearing capacity of the sphere is determined by the maximum load that the sphere can withstand without destruction. Since the load and the radial stress at the inner boundary of the sphere are equal in modulus, the maximum pressure is determined primarily by the radial stress, which practically does not depend on the coefficient μ. As a result, the compressibility of the material affects the amount of deformation of the neck formation but does not affect the bearing capacity.

References

1. Storozhev MV, Popov EA. *Theory of metal processing by pressure.* Moscow: Mechanical Engineering; 1977. (In Russian)
2. Malinin NN. *Applied theory of plasticity and creep*. Moscow: Mechanical Engineering; 1975. (In Russian)
3. Birger IA. *Round plates and shells of rotation.* Moscow: Mechanical Engineering; 1961. (In Russian)
4. Chumadin AS. *Theory and calculations of sheet stamping processes*. Moscow: MAI; 2014. (In Russian)
5. Feoktistov SI, Andrianov IK, Lin H. Modeling of the stress-strain state of thick-walled cylindrical shells taking into account the physical nonlinearity of the material. *Scientific notes of Komsomolsk-on-Amur State Technical University*. 2022;3(59): 12-20.
6. Feoktistov SI, Andrianov IK. Equations of compatibility of logarithmic deformations in Euler coordinates for solving axisymmetric processes of metal processing by pressure. *Scientific notes of Komsomolsk-on-Amur State Technical University*. 2021;VII-1(55): 26-30.
7. Prager V, Hodge FG. *Theory of ideally plastic bodies*. Moscow: Publishing House of Foreign lit; 1956.
8. Borjalilou V, Asghari M. Mathematical Modeling of Anisotropic Hyperelastic Cylindrical Thick Shells by Incorporating Thickness Deformation and Compressibility with Application to Arterial Walls. *International Journal of Structural Stability and Dynamics*. 2022;22: 1.
9. Thakur P, Pathania DS, Sajic JL, Verma G. Non-homogeneity effect in the spherical shell by using Seth's theory. *Structural Integrity and Life*. 2017;17(3): 177-182.
10. Shein A, Chumanov A. Modified method of variable elasticity parameters for solving problems of dynamics of rod systems taking into account physical and geometric nonlinearities. *IOP Conference Series: Materials Science and Engineering*. 2020;960: 042066.
11. Arbanil J, Panotopoulos G. Tidal deformability and radial oscillations of anisotropic polytropic spheres. *Physical Review*. 2022;105: 1.
12. Tertel E, Piotr K, Papacz W. The Stress State in the Three-layer Open Conical Shell During Stability Loss. *Acta Mechanica Slovaca*. 2015;19: 38-44.
13. Bharatha S, Levinson M. On physically nonlinear elasticity. *Journal of Elasticity*. 1977;7: 307–324.
14. Artamonova N, Sheshenin S. Geometrically and physically nonlinear coupled consolidation problem. *PAMM*. 2021;21: 1.
15. Krysko AV, Awrejcewicz J, Zhigalov M, Bodyagina K, Krysko VA. On 3D and 1D mathematical modeling of physically nonlinear beams. *International Journal of Non-Linear Mechanics.* 2021;134: 103734
16. Temis YM, Fakeev AI. Modeling the non-isothermal cyclic deformation curve. *Problems of Strength and Plasticity*. 2013;75: 5-10.
17. Nguyen VT, Kolesnikova AL, Romanov AE. Elasticity of thin dilatational disk in an isotropic half-space. *Materials Physics and Mechanics*. 2022;48(1): 44-60.

18. Nikonov AY, Bibko AA, Lychagin DV. Calculation of the stress level in modeling the inter-dislocation interaction of aluminum bronze. *Materials Physics and Mechanics*. 2022;48(3): 443-451.
19. Bormotin K, Burenin A, Krivenok A. On the optimization of the kinematic scheme for shaping thin elastoplastic coverings. *Mechanics of Solids*. 2022;57: 1.
20. Mir-Salim-zade M. Elastic-Plastic Problem for a Stringer Plate with a Circular Hole. *Journal of Mechanical Engineering*. 2021;24: 61-69
21. Svirskii Y, Bautin A, Luk'yanchuk A, Basov V. Approximate method for local elastic-plastic problems solving. *Vestnik Moskovskogo aviatsionnogo instituta*. 2020;27: 61-70. (In Russian)
22. Marchuk O, Il'Chenko Y, Gnedash S. Analyzing the stress-strain state of thick cylindrical shells. *International Applied Mechanics*. 2011;47: 1.
23. Gaidaichuk V, Kotenko K. Stress-strain state of a three-layer cylindrical shell under internal axisymmetric pulse load. *Strength of Materials and Theory of Structures*. 2020;105: 145-151.
24. Kruglov V, Iurchenko V. Calculation of Reinforced Concrete Prismatic Shells by the Finite Element Method Using Variable Elasticity Parameters. *Materials Science Forum*. 2019;945: 969-974.
25. Bormotin K. Modeling and Optimization of Forming Processes of Aircraft Engineering Thin-Wall Structures. *Current Problems and Ways of Industry Development: Equipment and Technologies.* 2021;1: 10-17.
26. Kozin O, Papkovskaya O. Analysis of stress-strain state of the spherical shallow shell with inclusion. *Odes'kyi Politechnichnyi Universytet. Pratsi*. 2016;1: 30-40.
27. Lugovyi P, Gaidaichuk V, Skosarenko Y, Kotenko K. Stress–Strain State of Three-Layer Cylindrical Shells with Reinforced Light Core Under Nonstationary Loading. *International Applied Mechanics.* 2021;57: 1-10.
28. Arkov D, Kochetkova O, Gureeva N, Matveyev A, Shiryaeva E. Simulation of the stress-strain state of shells under internal pressure using the mixed finite element method, taking into account physical nonlinearity. *IOP Conference Series: Materials Science and Engineering*. 2020;873: 012032.
29. Kosytsyn S, Akulich V. Stress-Strain State of a Cylindrical Shell of a Tunnel Using Construction Stage Analysis. *Communications - Scientific letters of the University of Zilina*. 2019;21: 72-76.
30. Andreev V, Polyakova L. Numerical Methods for Solving Physically Nonlinear Problems for Inhomogeneous Thick-Walled Shells. *Applied Mechanics and Materials*. 2017;865: 325-330.
31. Maslov B, Zhukov V, Pogrebnyak A. Method of Stressed State Analysis of Thick-Walled GTE Shells from Composite Materials. *Strength of Materials*. 2003;35: 376-382.
32. Andreev V, Potekhin I. Calculation of Equal Strength Thick-Walled Concrete Cylinder with Free Ends. *IOP Conference Series: Materials Science and Engineering*. 2019;661: 012023.
33. Shinkin V. Analytical description of metal plasticity at shift. *CIS Iron and Steel Review*. 2020;1: 66-70.

THE AUTHORS

Andrianov I.K.
e-mail: ivan_andrianov_90@mail.ru
ORCID: 0000-0001-8732-9615

Feoktistov S.I.
e-mail: serg_feo@mail.ru

Materials Physics and Mechanics. 2022;50(3): 420-430
Research article
http://dx.doi.org/10.18149/MPM.5022022_6

Submitted: July 5, 2022
Approved: October 6, 2022
Accepted: October 25, 2022

Flexible microwave absorbers based on powdered activated coconut charcoal and moisture-containing ceramsite

O.V. Boiprav✉, S.E. Savanovich, E.S. Belousova

Educational Establishment "Belarusian State University of Informatics and Radioelectronics", Minsk, Belarus

✉ smu@bsuir.by

Abstract. The article presents the results of the development of the technology for manufacturing flexible microwave absorbers, the fillers of which are powdered activated coconut charcoal and moisture-containing ceramsite, and the matrix for these materials' particles holding is polyurethane mastic. The results of the study of the regularities of the electromagnetic radiation interaction in the frequency range of 0.7-17.0 GHz with absorbers, manufactured according to the developed technology, depending on the size of the ceramsite particles contained in them, are presented. On the basis of these results, it was found that the studied absorbers, in comparison with absorbers, filled with moisture-containing ceramsite, are characterized by lower values of the electromagnetic radiation reflection coefficient in the frequency range of 0.7-17.0 GHz, reaching a value of -20.0 dB. In this case, the values of their electromagnetic radiation transmission coefficient in the indicated frequency range reach the value of -43.0 dB. Microwave absorbers, manufactured according to the developed technology, are promising for use in order to solve problems related to ensuring the functional reliability of radio electronic equipment, as well as ensuring environmental safety and information security.

Keywords: activated coconut charcoal, ceramsite, microwave absorber, reflection coefficient, transmission coefficient

Acknowledgements. *The research was carried out within the framework of research and development work "Development of electromagnetic radiation absorbers based on charcoal-containing and foiled materials for information and environmental security systems. Development of devices for interference suppression in the circuits of radio electronic and electrical equipment" under task 32 "Develop new materials, coatings and systems for the protection of radio electronic, optoelectronic and information equipment, biological objects from external energy impacts, ensuring their environmental and information safety, high functional reliability and efficiency" of subprogram 2 "Mastering new and high technologies in production" of the State Program of the Republic of Belarus "High technologies and equipment" for 2021-2025.*

Citation: Boiprav OV, Savanovich SE, Belousova ES. Flexible microwave absorbers based on powdered activated coconut charcoal and moisture-containing ceramsite. *Materials Physics and Mechanics*. 2022;50(3): 420-430. DOI: 10.18149/MPM.5032022_6.

© O.V. Boiprav, S.E. Savanovich, E.S. Belousova, 2022.
Publisher: Peter the Great St. Petersburg Polytechnic University
This is an open access article under the CC BY-NC 4.0 license (https://creativecommons.org/li-censes/by-nc/4.0/)

1. Introduction

Microwave absorbers are used to solve a number of technical problems associated with the operation of radio electronic equipment. These tasks can be roughly divided into three groups:

1) ensuring the functional reliability of radio electronic equipment [1,2];
2) ensuring environmental safety [3,4];
3) ensuring information security [5,6].

The solution to the problems of the first indicated group is aimed at radio electronic equipment protection from accidental exposure to electromagnetic interference (including ensuring the electromagnetic compatibility of radio electronic equipment). The solution is based on the use of the following products, made with microwave absorbers:

- covers for radio-electronic equipment housings;
- partitions for zonal division of space in the rooms, where radio electronic equipment is located;
- panels for cladding the walls of rooms, where radio electronic equipment is located.

The solution to the problems of the second indicated group is aimed at reducing the degree of electromagnetic radiation's influence on a person. The solution is based on the use of workwear or panels, made with microwave absorbers for cladding the walls of rooms, where people work.

The solution to the problems of the third indicated group is aimed to:

- information protection from leakage via the channel of spurious electromagnetic radiation and pickups;
- protection of information processing devices from deliberate electromagnetic interference;
- protection objects from detection by radar reconnaissance.

The solution is based on the use of the following products, made with microwave absorbers:

- cases for information processing devices;
- partitions for zonal division of space in rooms, where information processing devices are located;
- panels for cladding the walls of rooms, where information processing devices are located;
- camouflage coatings for the hulls of the objects, that may be targets of radar reconnaissance.

As a rule, the following requirements are imposed on the absorbers, which are currently used for the making of the listed products:

1) flexibility [7];
2) wide operating frequency range [8];
3) low ($\leq$ -5.0 dB) values of the electromagnetic radiation reflection coefficient;
4) low ($\leq$ -20.0 dB) values of the electromagnetic radiation transmission coefficient [8,9].

The first of these requirements is due to the fact that the products, the use of which is based on the solutions of the indicated technical problems, either characterized by a complex shape or intended to fixing on surfaces characterized by the presence of corners or kinks. The second of these requirements is due to the fact that the currently used radio electronic equipment (including information processing devices) is a source of electromagnetic radiation of a wide frequency range. The third and fourth of these requirements are due to the fact that high values of the electromagnetic radiation reflection coefficient of the listed products can cause passive electromagnetic interference. Such interference is formed due to the re-reflection of electromagnetic radiation from radio electronic equipment. It may affect the functional reliability of such equipment.

In connection with the foregoing, it can be stated that studies aimed at improving the existing microwave absorbers in order to ensure their compliance with the requirements presented are relevant.

The study, the results of which are presented in the article, was the development of the research work aimed at obtaining and improving microwave absorbers based on moisture-containing ceramsite. The advantages of the moisture-containing ceramsite used for the manufacture of microwave absorbers, characterized by the wide operating frequency range, are presented in [10,11]. The main of these advantages lies in the low cost of the ceramsite. The indicated advantage makes it possible to manufacture on the base of ceramsite the microwave absorbers, characterized by the corresponding property (including flexible ones [12]).

The aim of the study, the results of which are presented in the article, was to theoretically substantiate and experimentally confirm the technology for manufacturing microwave absorbers based on moisture-containing ceramsite, which are characterized by the flexibility property and lower values of the electromagnetic radiation reflection coefficient, in comparison with the absorbers, considered in [12]. In the course of the aim achieving, the following four scientific tasks have been solved:

1) selection and justification of methods for developing the technology for manufacturing microwave absorbers, that meet the requirement presented in the aim, and determining the procedure for the technology implementation;

2) laboratory implementation of the technology, using various types of the ceramsite (each type corresponds to a certain particle size of the ceramsite), as well as components, selected and justified as a result of the first task solving;

3) study of the regularities of the electromagnetic radiation interaction with absorbers, obtained as a result of the second scientific task solving, depending on the particle size of the ceramsite, contained in them;

4) comparative analysis of the electromagnetic radiation reflection coefficient values of the absorbers, obtained as a result of the second scientific task solving, with similar values, characterizing the absorbers presented in [12].

2. Materials and methods

In the course of solving the first scientific task, set to achieve the aim, a hypothesis has been put forward. According to this task, in order to decrease the electromagnetic radiation reflection coefficient values of the absorbers based on moisture-containing ceramsite, it is advisable to modify the outer structure of such material particles by forming on their surfaces the inhomogeneities. The size of these inhomogeneities should be comparable with the pore diameter of these particles. The hypothesis was based on information about the phenomena of microwave radiation propagation at the interfaces between media characterized by different wave impedance [13-15]. One such phenomenon is radiation scattering on the geometric inhomogeneities of these boundaries. The energy of radiation, scattered by the geometric inhomogeneities of the interfaces between media, characterized by different wave impedance, determines the energy of the radiation reflected from these boundaries: if the first one is higher, the second one is lower (and, therefore, the lower the values the electromagnetic radiation reflection coefficient, registered on the named boundaries) [15].

Forming of the inhomogeneities on the surfaces of materials (including powdered ones) can be implemented by using one of the following methods:

1) doping [16,17];

2) selective metallization [18,19];

3) 3D printing [20-22];

4) agglomeration of the particles with binders on surfaces [22,23].

For the formation of the inhomogeneities on the surfaces of the ceramsite particles, the fourth of the presented methods has been chosen. This is due to the fact, that it does not involve the use of special technological equipment. As a result, this method is characterized by the least time and financial costs for implementation. The particles of the powdered activated coconut charcoal have been selected for agglomeration with a binder on the ceramsite particles' surfaces. This choice was due to the following three reasons.

1. Powdered activated charcoal is characterized by high porosity (~ 95%). Therefore, it is characterized by high adhesion to binders [24].

2. The particle size of the powdered activated coconut charcoal is from 0.4 to 0.85 mm. Such size is comparable to the pore size of the ceramsite particles. This is the condition for strong adhesion of the first ones to the surfaces of the second ones [25].

3. The cost of 1 kg of powdered activated coconut charcoal is comparable to the cost of 1 kg of ceramsite. Therefore, the use of powdered activated coconut charcoal to modify the outer structure of the ceramsite particles will slightly increase the cost of the microwave absorber, based on them [26].

The developed technology is based on the technology for manufacturing the absorbers, considered in [12]. The procedure of the developed technology implementation includes the following steps.

Step 1. Solution preparation by mixing the sodium carboxymethyl cellulose aqueous solution with 20 % sodium chloride aqueous solution. The concentration of the sodium carboxymethyl cellulose aqueous solution, as well as the ratio, in which this solution should be mixed with 20 % sodium chloride aqueous solution, should be chosen such, that the dynamic viscosity of the solution, prepared from them, is 77.5 mPa·s at an ambient temperature of 20±3°C.

Step 2. Immersion wetting of the ceramsite particles, the size of which is at least 10.0 mm, with the prepared solution at atmospheric pressure of 101.3 kPa and an ambient temperature of 20±3°C.

Step 3. Preparation of the water-containing binder by mixing the sodium carboxymethyl cellulose aqueous solution with 40 % calcium chloride aqueous solution. The concentration of the sodium carboxymethyl cellulose aqueous solution, as well as the ratio, in which this solution is to be mixed with a 40 % calcium chloride aqueous solution, should be chosen such, that the dynamic viscosity of the water-containing binder, prepared from them, is 237.5 mPa·s at the ambient temperature of 20±3°C.

Step 4. Treatment of the ceramsite particles (step 2), with the prepared water-containing binder.

Step 5. Agglomeration of the powdered activated coconut charcoal particles on the surfaces of the ceramsite particles (step 4), by uniform mechanical mixing of the first ones with the second ones. The indicated components ratio should be that to create conditions for agglomeration of all particles of the powdered activated coconut charcoal on the surfaces of the ceramsite particles.

Step 6. Cutting two fragments from the fiberglass fabric, the shape and size of which are determined by the requirements for the shape, and size of the manufactured absorber.

Step 7. Cutting one fragment from a roll of a foiled polymer film, the shape, and size of which are determined by the requirements for the shape and size of the manufactured absorber.

Step 8. Fixing on the surface of one of the fiberglass fabric fragments (step 6) and the film fragment (step 7) using sprayed glue or double-sided adhesive tape. When fixing, the boundaries of the first of these fragments coincide with the boundaries of the second of specified fragments.

Step 9. Applying polyurethane mastic to the surface of the film fragment (step 7) with a layer of 6.0 mm thickness.

Step 10. Uniform distribution of the ceramsite particles (step 5) over the surface of the polyurethane mastic layer (step 9) on the surface of the film fragment.

Step 11. Applying polyurethane mastic to the surface of the second of the fiberglass fabric fragments, was obtained as a result of the step 6 implementation, with a layer of 4.0 mm thickness.

Step 12. Connecting the structure (steps 1-10) with the structure (step 11). When connecting, the first of these structures is oriented relative to the second one by the surface, on which the ceramsite particles are distributed. Also when connecting, the second of these structures is oriented relative to the first one by the surface, on which the polyurethane mastic is applied.

Step 13. Keeping under pressure the structure (steps 1-12).

As a result of solving the second scientific task, set to achieve the aim, according to the developed technology, two groups of microwave absorbers have been manufactured. Manufactured absorbers differed in the particle size of the ceramsite, included in their composition. Absorbers of group 1 included commercially produced ceramsite sand with a particle size of 1.0 to 2.0 mm. Absorbers of group 2 included ceramsite gravel with a particle size of 10.0 to 20.0 mm. Figure 1 shows the appearance of the particles of ceramsite sand and ceramsite gravel.

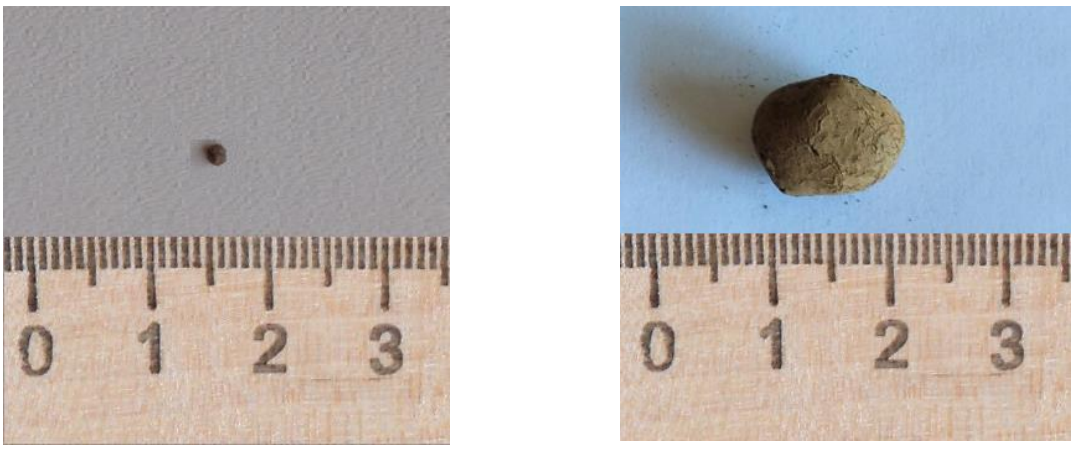

a) b)

Fig. 1. The appearance of the ceramsite sand particle (a) and ceramsite gravel particle (b)

Also, in the course of solving the second scientific task, set to achieve the aim, was determined the following. All particles of powdered activated coconut charcoal, when uniformly mechanically mixed with the ceramsite particles, treated with the water-containing binder, agglomerate on the surfaces of these particles, if the mass ratio of the powdered activated coconut charcoal particles and the ceramsite particles, treated with the water-containing binder, -7:10.

Figure 2 shows the appearance of the ceramsite sand and ceramsite gravel particles, treated with the water-containing binder, on the surfaces of which the powdered activated coconut charcoal particles are agglomerated.

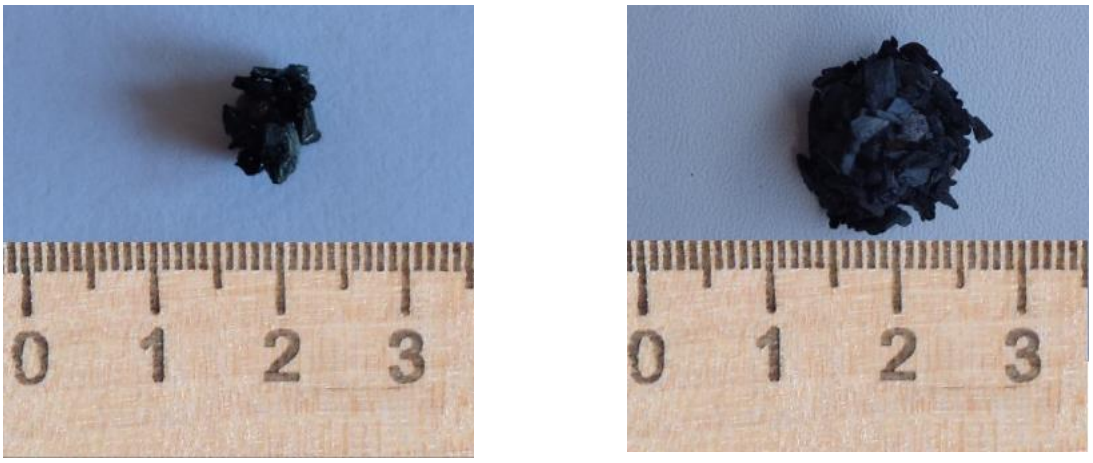

a) b)

Fig. 2. The appearance of the ceramsite sand (a) and ceramsite gravel (b) particles, treated with the water-containing binder, on the surfaces of which the powdered activated coconut charcoal particles are agglomerated

To solve the third scientific task, set to achieve the aim, measurements of the electromagnetic radiation reflection (S_{11}) and transmission (S_{21}) coefficient values of the manufactured absorbers were performed. In this case, a panoramic meter of reflection and transmission coefficients SNA 0.01-18 was used. The measurements were carried out in the frequency range of 0.7-17.0 GHz according to the technique, described in [27]. The choice of the frequency range for the measurements performing was due to the fact, that it corresponds to the most high-amplitude components of the electromagnetic radiation spectrum of modern radio electronic equipment [28].

Based on the measurement results, the frequency dependences of the electromagnetic radiation reflection and transmission coefficients of the manufactured absorbers have been plotted.

3. Results and Discussion

Frequency dependences of the electromagnetic radiation reflection coefficient in the range of 0.7-17.0 GHz of the absorbers, manufactured according to the developed technology, are shown in Fig. 3.

It follows from Fig. 3, that the electromagnetic radiation reflection coefficient values in the frequency range of 0.7-3.0 GHz of absorbers of group 1 vary from -1.0 to -20.0 dB, and absorbers of group 2 – from -1.0 to -15.0 dB. In the frequency range of 3.0-17.0 GHz, the electromagnetic radiation reflection coefficient values of these absorbers vary accordingly within the following limits: from -1.0 to -15.0 dB and from -3.0 to -17.0 dB. At the same time, it should be noted, that the average value of the electromagnetic radiation reflection coefficient in the frequency range of 0.7-3.0 GHz for the absorbers of group 1 is -5.9 dB, and for the absorbers of group 2 is -7.2 dB. In the frequency range of 3.0-17.0 GHz, the indicated parameter values for the absorbers are practically equivalent and amount to -9.0 dB and -8.0 dB, respectively. Absorbers of group 1 are characterized by a higher average value of the electromagnetic radiation reflection coefficient in the frequency range of 0.7-3.0 GHz, in comparison with the absorbers of group 2 due to the following set of these absorbers features.

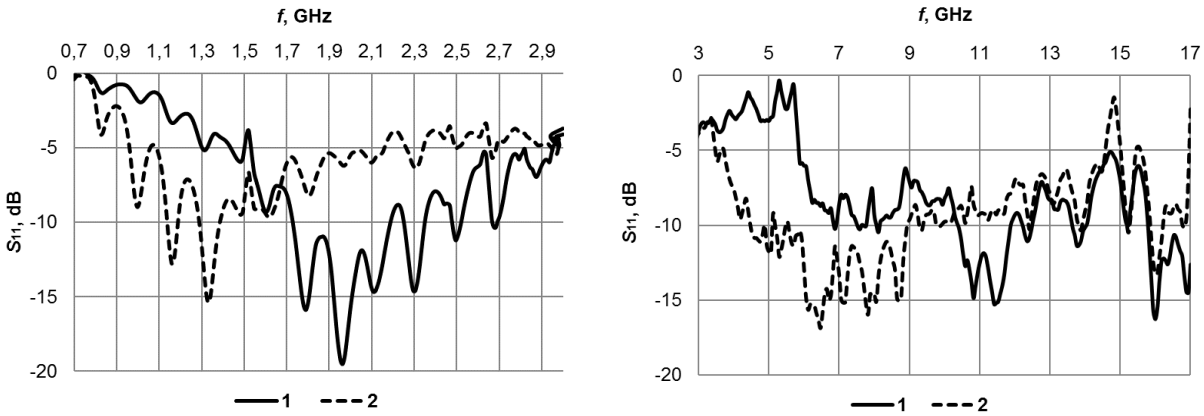

a) b)

Fig. 3. Frequency dependences of the electromagnetic radiation reflection coefficient in the range of 0.7-3.0 GHz (a) and 3.0-17.0 GHz (b) of the absorbers of group 1 (curves 1) and the absorbers of group 2 (curves 2)

1. The mass of the ceramsite particles, included in a unit volume of absorbers of group 1, exceeds the mass of the ceramsite particles, included in a unit volume of absorbers of group 2. This is due to the fact, that the bulk density of the ceramsite particles, on the basis of which the absorbers of group 1 are made, is higher than the bulk density of the ceramsite particles, on the basis of which the absorbers of group 2 are made.

2. In connection with the first indicated feature, absorbers of group 1 contain more powdered activated coconut charcoal than absorbers of group 2.

3. In connection with the second indicated feature, the electrical conductivity of absorbers of group 1 is higher than the electrical conductivity of absorbers of group 2.

The frequency bands, in which the electromagnetic radiation reflection coefficient values of the absorbers of group 1 are less than -5.0 dB are from 1.5 to 2.9 GHz and from 10.0 to 17.0 GHz. Similar frequency bands specific to the absorbers of group 2 are from 1.0 to 2.2 GHz, from 4.0 to 14.0 GHz, and from 15.0 to 17.0 GHz. Thus, electromagnetic radiation absorbers, manufactured according to the developed technology, are characterized by a wide operating frequency range. At the same time, it should be noted that the total bandwidth, in which the electromagnetic radiation reflection coefficient values of the absorbers of group 2 are less than -5.0 dB, exceeds the total width of the frequency bands, in which the electromagnetic radiation reflection coefficient values of the absorbers of group 1 are less than -5.0 dB This may be due to the following set of these absorbers features.

1. The ceramsite, on the basis of which the absorbers of group 2 are made, is characterized by a wider granulometric composition, in comparison with ceramsite, on the basis of which the absorbers of group 1 are made.

2. In connection with the first indicated feature, the number of wavelengths in the frequency range of 0.7-17.0 GHz, comparable to the particle sizes, which are parts of the absorbers of group 2, exceeds the number of wavelengths in the specified frequency range, comparable to the particle sizes, which are part of the absorbers of group 1.

The frequency dependences of the electromagnetic radiation transmission coefficient in the range of 0.7-17.0 GHz of the absorbers, manufactured according to the developed technology, are shown in Fig. 4.

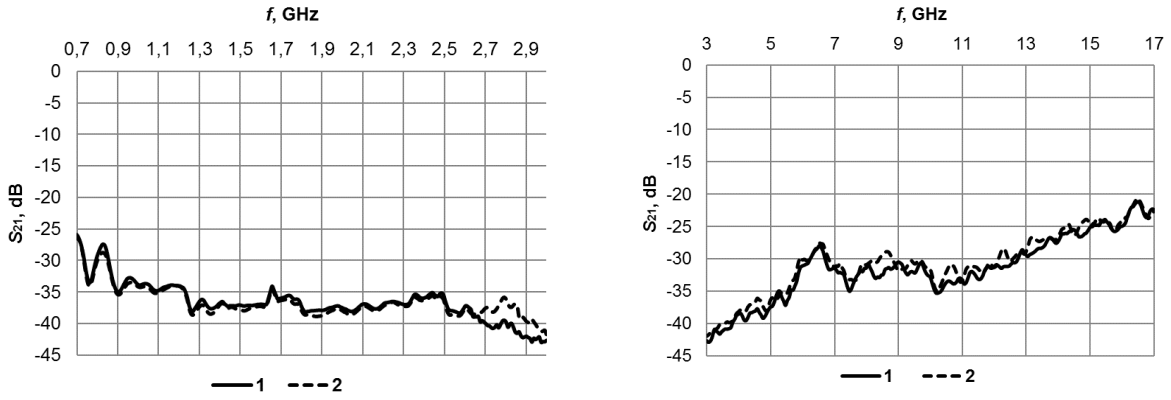

a) b)

Fig. 4. Frequency dependences of the electromagnetic radiation transmission coefficient in the range of 0.7-3.0 GHz (a) and 3.0-17.0 GHz (b) of the absorbers of group 1 (curves 1) and the absorbers of group 2 (curves 2)

It follows from Fig. 4, that the electromagnetic radiation transmission coefficient values in the frequency range of 0.7-17.0 GHz of the absorbers of group 1 vary from -20.0 to -43.0 dB and are practically equivalent to the similar parameter values, characterizing the absorbers of group 2. This is due to the fact, that the foiled polymer film, which is part of the studied absorbers, makes a greater contribution to the electromagnetic radiation energy weakening, provided by them, than particles of the ceramsite, treated by the water-containing binder, and powdered activated coconut charcoal.

In the course of solving the fourth scientific task, set to achieve the aim, it was found that the electromagnetic radiation reflection coefficient values in the frequency range of 0.7-17.0 GHz of the absorbers, manufactured according to the developed technology, are lower on average 5.0 dB, than the similar parameter values, characterizing the absorbers presented in [12].

4 .Conclusion

Thus, microwave absorbers, manufactured according to the developed technology, are characterized by:

- the flexibility property (due to the fact that, according to the developed technology, the matrix for holding the ceramsite particles with powdered activated coconut charcoal particles, agglomerated on their surface, is made on the basis of polyurethane mastic);
- the wide operating frequency range (due to the fact that the composition of the absorbers, manufactured according to the developed technology, includes particles, whose sizes are comparable to a large number of microwave wavelengths);
- the electromagnetic radiation reflection and transmission coefficients values in the frequency range of 0.7-17.0 GHz, reaching values of -20.0 dB and -43.0 dB, respectively (due to the fact, that absorbers, manufactured according to the developed technology, include the particles, that provide the scattering of the electromagnetic radiation of the specified frequency range, and also includes a foiled polymer film);
- lower values of the electromagnetic radiation reflection coefficient in the frequency range of 0.7-17.0 GHz, in comparison with absorbers, considered in [12] (due to the fact that on the surface of the ceramsite particles, which are the part of the absorbers, manufactured according to the developed technology, the powdered activated coconut charcoal particles are agglomerated and provide additional scattering of electromagnetic radiation, interacting with such absorbers).

In connection with the foregoing, we can conclude, that the aim of the study, the results of which are presented in the article, has been achieved, and the hypothesis put forward in the course of solving the first scientific task, set to achieve the aim, has been confirmed.

Microwave absorbers, manufactured according to the developed technology, seem promising for use in order to ensure the functional reliability of radio electronic equipment, as well as to ensure environmental safety and information security. At the same time, on the basis of these absorbers, it is most expedient to manufacture the following products, respectively:

- partitions for zonal division of space in the rooms, where radio electronic equipment is located;
- panels for cladding the walls of the rooms, where people work;
- modules, designed to be fixed or placed on the hulls of the objects, that may be targets of radar reconnaissance.

References

1. Liang C, Gu Z, Zhang Y, Ma Z, Qiu H, Gu J. Structural Design Strategies of Polymer Matrix Composites for Electromagnetic Interference Shielding: A Review. *Nano-Micro Letters*. 2021;13: 181.
2. Abbasi H, Antunes M, Velasco JI. Recent advances in carbon-based polymer nanocomposites for electromagnetic interference shielding. *Progress in Material Science*. 2019;103: 319-373.
3. González M, Pozuelo J, Baselga J. Electromagnetic Shielding Materials in GHz Range. *The Chemical Record*. 2018:18(7-8): 1000-1009.
4. Wang X-Y, Liao S-Y, Wan Y-J, Zhu P-L, Hu Y-G, Zhao T, Sun R, Wong C-P. Electromagnetic interference shielding materials: recent progress, structure design, and future perspective. *Journals of Materials Chemistry C*. 2022;10(1): 44-72.
5. Hayashi Y-I, Homma N. Introduction to Electromagnetic Information Security. *IEICE Transactions on Communications*. 2019;1: 40-50.
6. Inigo C. An introduction to cybersecurity at physical layer: Obstacles at radio channel to mitigate hackers' chance. *Elektronika ir Elektrotechnika*. 2020;26(6): 58-65.
7. Cheng J, Li C, Xiong Y, Zhang H, Raza H, Ullah S, Wu J, Zheng G, Cao Q, Zhang D, Zheng Q, Che R. Recent Advances in Design Strategies and Multifunctionality of Flexible Electromagnetic Interference Shielding Materials. *Nano-Micro Letters*. 2022;14: 80.
8. Majidzadeh M, Ghobadi C, Nourinia J. Ultra Wide Band Electromagnetic Shielding Through a Simple Single Layer Frequency Selective Surface. *Wireless Personal Communications*. 2017;95: 2769-2783.
9. Afilipoaei C, Teodorescu-Draghicescu H. A Review over Electromagnetic Shielding Effectiveness of Composite Materials. *Proceedings*. 2020;63(1): 23;
10. Savanovich SE, Borbotko TV. Effect of Viscosity of Aqueous Sodium Chloride Solution, Introduced Into Pores Of Expanded Clay, On Its Radioabsorbing Properties. *Vestsi Natsyyanal'nai akademii navuk Belarusi. Seryya fizika-technichnych navuk.* 2016;2: 115-119. (In Russian)
11. Borbotko TV, Savanovich SE. Influence of water content of expanded clay on the reflection coefficient of electromagnetic shield. *Vestsi Natsyyanal'nai akademii navuk Belarusi. Seryya fizika-technichnych navuk.* 2020;66(1): 93-100. (In Russian)
12. Savanovich SE, Borbotko TV. Electromagnetic shield design based on pseudooval scattering elements for information protection from leakage via the electromagnetic channel. *Vestsi Natsyyanal'nai akademii navuk Belarusi. Seryya fizika-technichnych navuk*. 2022;67(2): 214-221.

13. Peña O, Pal U. Scattering of Electromagnetic Radiation by a Multilayered Sphere. *Computer Physics Communications*. 2009;180(11): 2348-2354.
14. Brath M, Ekelund R, Eriksson P, Lemke O, Buehler SA. Microwave and Submillimeter Wave Scattering of Oriented Ice Particles. *Atmospheric Measurement Techniques*. 2020;13: 2309-2333.
15. Fung AK, Chen KS. *Microwave Scattering and Emission Models for Users*. Artech House; 2009.
16. Cojocaru B, Avram D, Kessler V, Parvulescu V, Seisenbaeva G, Tiseanu C. Nanoscale insights into doping behavior, particle size and surface effects in trivalent metal doped SnO_2. *Scientific Reports*. 2017;7: 9598.
17. Hasan F, Kim J, Song H, Sung JH, Kim J, Yoo H. Effect of Particle Size and Doping on the Electrochemical Characteristics of Ca-doped $LiCoO_2$ Cathodes. *Journal of Electrochemical Science and Technology*. 2022;11(4): 352-360.
18. Camargo MK, Uebel M, Kurniawan M, Ziegler KF, Seiler M, Grieseler R, Schmidt U, Barz A, Bliedtner J, Bund A. Selective Metallization of Polymers: Surface Activation of Polybutylene Terephthalate (PBT) Assisted by Picosecond Laser Pulses. *Advanced Engineering Materials*. 2022;24(4): 2100933.
19. Jo S, Akin S, Park MS, Jun MBG. Selective metallization on glass surface by laser direct writing combined with supersonic particle deposition. 2022;31: 64-68.
20. Lores A, Azurmendi N, Agote I, Zuza E. A Review on Recent Developments in Binder Jetting Metal Additive Manufacturing: Materials and Process Characteristics. *Powder Metallurgy*. 2019;62(5): 267-296.
21. Bai Y, Wagner G, Williams C. Effect of Particle Size Distribution on Powder Packing and Sintering in Binder Jetting Additive Manufacturing of Metals. *Journal of Manufacturing Science and Engineering*. 2017;139(8); 2017.
22. Alsaqoor S, Borowski G, Alahmer A, Beithou N. Using of Adhesives and Binders for Agglomeration of Particle Waste Resources. *Advances in Science and Technology – Research Journal*. 2022;16(3): 124-135.
23. Van Netten K, Borrow DJ, Galvin KP. Fast Agglomeration of Ultrafine Hydrophobic Particles Using a High-Internal-Phase Emulsion Binder Comprising Permeable Hydrophobic Films. *Industrial & Engineering Chemistry Process Design and Development*. 2017;56(38): 10658-10666.
24. Mohd Iqbaldin MN, Khudzir I, Mohd Azlan MI, Zaidi AG, Surani B, Zubr Z. Properties of Coconut Shell Activated Carbon. *Journal of Tropical Forest Science*. 2013;25(4): 497-503.
25. Leman AS, Shahidan S, Senin MS, Hannan NIRR. A Preliminary Study on Chemical and Physical Properties of Coconut Shell Powder as a Filler in Concrete. *IOP Conference Series: Materials Science and Engineering*. 2016;160: 012059.
26. Chopngam K, Luengchavanon M, Khangkhamano M, Chetpattananondh K, Limbut W. Coating Activated Carbon from Coconut Shells with Co_3O_4/CeO_2 for High-Performance Supercapacitor Applications: an Experimental Study. *BioResources*. 2021;16(4): 8022-8037.
27. Boiprav OV, Grinchik NN, Pukhir GA. Experimental Substantiation of the Possibility of Hydrolytic Lignin Using in the Architectural Electromagnetic Shielding Systems. *Materials Physics and Mechanics*. 2022;48(1): 124-135.
28. Abdul-Al M, Amar ASI, Elfergani I, Littlehales R, Parchin NO, Al-Yasir Y, See CH, Zhou D, Abidin ZZ, Alibakhshikenari M, Zebiri C, Elmegri F, Abusitta M, Ullah A, Abdussalam FMA, Rodriguez J, McEwan NJ, Noras JM, Hodgetts R, Abd-Alhameed RA. Wireless Electromagnetic Radiation Assessment Based on the Specific Absorption Rate (SAR): A Review Case Study. *Electronics*. 2022;11(4): 511.

THE AUTHORS

Boiprav O.V.
e-mail: smu@bsuir.by
ORCID: 0000-0002-9987-8109

Savanovich S.E.
e-mail: svetasav@bsuir.by
ORCID: 0000-0001-7977-8031

Belousova E.S.
e-mail: belousova@bsuir.by
ORCID: 0000-0001-9834-6074

Materials Physics and Mechanics. 2022;50(3): 431-438
Research article
http://dx.doi.org/10.18149/MPM.5032022_7

Submitted: October 17, 2022
Approved: October 31, 2022
Accepted: November 18, 2022

Grain-boundary nanoprecipitates-mediated mechanism of strengthening in Al-Cu-Zr alloy structured by high-pressure torsion

M.Yu. Gutkin[1], N.V. Skiba[2]✉, T.S. Orlova[2]

[1]Institute for Problems of Mechanical Engineering RAS, St. Petersburg, Russia

[2]Ioffe Institute, St. Petersburg, Russia

✉ nikolay.skiba@gmail.com

Abstract. The theoretical model is suggested which describes a new micromechanism of strengthening in the ultrafine-grained Al-Cu-Zr alloy subjected to severe plastic deformation. The departure point in this theoretical model is the assumption that the key role in the plastic deformation of high-pressure torsion processed ultrafine grained Al is played by extrinsic grain boundary dislocations (EGBDs) gliding along non-equilibrium grain boundaries and forming dislocation pile-ups at triple junctions of the grain boundaries. Within the model, nanoprecipitates of Al_2Cu at grain boundaries act as obstacles for the slip of extrinsic grain-boundary dislocations (EGBDs) that leads to a significant increase in the strength of the Al-Cu-Zr alloy. The plastic deformation occurs through the emission of lattice dislocations from the pile-up of EGBDs pressed to a triple junction of grain boundaries. It is shown that the division of gliding EGBDs into separate pile-ups by nanoprecipitates can provide substantial additional hardening of the alloy. The proposed model is in good quantitative agreement with available experimental results.

Keywords: ultrafine-grained aluminum alloys; grain boundary defects; precipitation; dislocations; plastic deformation

Acknowledgements. *Grant of the Russian Science Foundation (grant №22-19-00292).*

Citation: Gutkin MYu, Skiba NV, Orlova TS. Grain-boundary nanoprecipitates-mediated mechanism of strengthening in Al-Cu-Zr alloy structured by high-pressure torsion. Materials Physics and Mechanics. 2022;50(3): 431-438. DOI: 10.18149/MPM.5032022_7.

1. Introduction

Aluminum-based alloys exhibit high electrical conductivity and corrosion resistance. However, the modern practical applications of aluminum-based alloys also require high mechanical strength. One of the ways to substantially increase the strength of aluminum and Al-based alloys is the formation of ultrafine-grained or nanocrystalline structures through processing by severe plastic deformation (SPD) [1-4]. Alloying of aluminum with different doping elements such as copper (Cu) [5,6], magnesium (Mg) [7], zirconium (Zr) [8,9], etc also contributes to strength increase. It is well known that doping with copper leads to a refinement of the grain structure [10-12] and an increase in the strength [4,10] of aluminum-based alloys subjected to severe plastic deformation (SPD). For example, in a recent work [13], it is shown that Al-Cu-Zr alloy

© M.Yu. Gutkin, N.V. Skiba, T.S. Orlova, 2022. Publisher: Peter the Great St. Petersburg Polytechnic University
This is an open access article under the CC BY-NC 4.0 license (https://creativecommons.org/li-censes/by-nc/4.0/)

structured by high-pressure torsion (HPT) demonstrates a significant increase in the strength characteristics while maintaining functional ductility and good electrical conductivity. The authors [13,14] observed the formation of individual Cu-containing nanosized precipitates – nanoprecipitates of the Al_2Cu secondary phase (Al_2Cu-NPs) with sizes of 20–40 nm at grain boundaries (GBs) as a result of HPT processing of Al-Cu-Zr alloy. According to [13], the formation of such Al_2Cu-NPs at GBs contributes to a significant increase in the strength of the Al-Cu-Zr alloy, which is hard to explain by known strengthening mechanisms. As was shown in [13], the value of such additional strengthening related to the Al_2Cu-NPs at GBs is about 130 MPa which is comparable with the contribution from GB strengthening to the total strength of this alloy.

The main aim of this work is to develop a theoretical model which would describe the strengthening mechanism in the Al-Cu-Zr alloy due to the Al_2Cu-NPs at GBs. In doing so, the departure point in this modeling is the assumption [15-18] that the key role in the plastic deformation of HPT processed ultrafine-grained (UFG) Al is played by extrinsic grain boundary dislocations (EGBDs) gliding along non-equilibrium GBs and forming dislocation pile-ups at triple junctions of the GBs. The critical stress required for the emission of lattice dislocations from the heads of such pile-ups to the bulk of neighboring grains was considered the flow stress of the UFG material [15-17]. With this assumption, some theoretical models were developed to explain the experimentally revealed effects of annealing-induced hardening [15,16] and deformation-induced softening [15,17] in HPT treated UFG Al, as well as the suppression of the annealing-induced hardening effect in it at low-temperature mechanical testing [18]. Since in the Al-Cu-Zr alloy structured in a similar HPT route, new important elements of the non-equilibrium GB structure – Al_2Cu-NPs – appear, one can expect their strong interaction with EGBDs and new significant features in the behavior of the latter. In the following section, we suggest a new theoretical model which reflects the interplay of EGBDs and Al_2Cu-NPs and allows us to estimate the contribution of Al_2Cu-NPs to the strengthening of the UFG Al-Cu-Zr alloy.

Model

Consider a single GB with an initial defect structure characterized by a pile-up of the EGBDs pressed by external shear stress τ to a triple junction of GBs (Fig. 1(a)). It is well known that such dislocation pile-up can emit lattice dislocations from the triple junction into the adjacent grain. Let an edge lattice dislocation with the Burgers vector $\mathbf{b}$ (hereinafter called b-dislocation) be emitted from the head of the dislocation pile-up under the action of the external shear stress τ and glide along a crystallographic plane that makes the angle α with the GB plane. In terms of the continuum approach, the emission of the b-dislocation can be represented as the formation of a dipole of the lattice dislocations with Burgers vectors $\pm\mathbf{b}$ (Fig. 1(a)).

According to our new model, the aforementioned Al_2Cu-NPs act as obstacles to the slip of the EGBDs. Thus, the appearance of the Al_2Cu-NPs in Al-Cu-Zr alloy structured by HPT leads to the formation of a new defect structure in the GB, which is characterized by N Al_2Cu-NPs periodically distributed along the GB with a period l, and $(N+1)$ identical pile-ups of EGBDs pressed by external shear stress τ to the NPs and to the triple junction of the GBs (Fig. 1(b)). For the sake of simplicity, the dislocation pile-ups at the NPs are modeled by edge superdislocations with Burgers vector $\mathbf{B}$ (hereinafter we call them B-superdislocations). The magnitudes of the superdislocation Burgers vectors are supposed to be the same, $B = nb_{gb}$, where n is the number of the EGBDs in each dislocation pile-up (Fig. 1(b)), and b_{gb} is the magnitude of the Burgers vector of an EGBD.

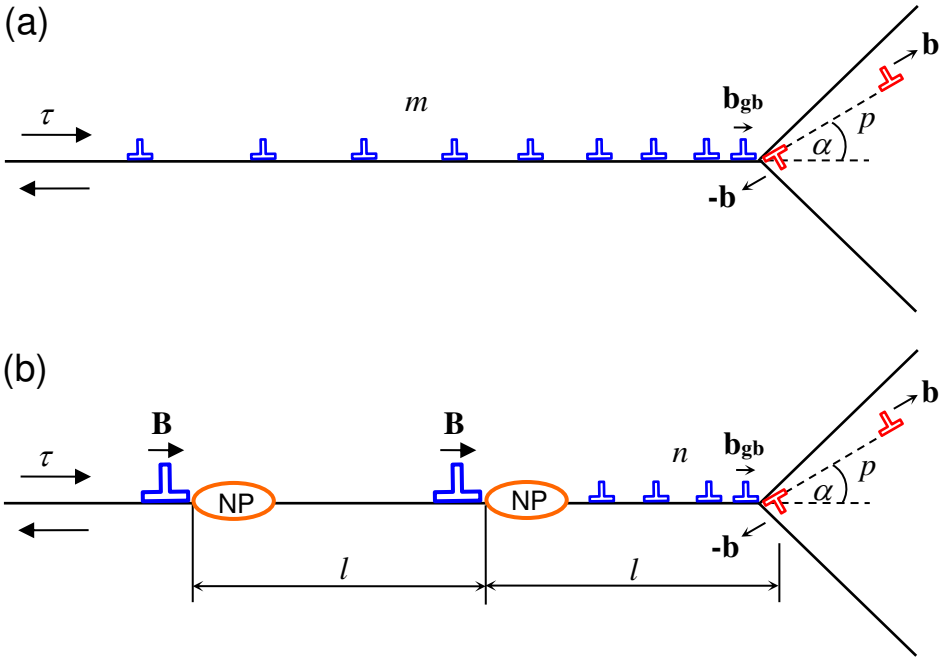

Fig. 1. Models of the lattice dislocation emission from the head of the pile-up of the EGBDs when (a) there are no NPs in the GB and (b) there are two NPs in the GB

Within the model, the combined action of the external shear stress τ and the shear stress field created by the superdislocations at the NPs leads to the emission of the lattice b-dislocation from the triple junction of the GBs. The emission event can be modeled as the formation of the corresponding $\pm b$-dislocation dipole (Fig. 1(b)).

Consider now the energy characteristics of the dislocation emission event illustrated in Fig. 1(b), and compare them with the energy characteristics of the dislocation emission from the head of the initial dislocation pile-up (Fig. 1(a)). In doing so, we will calculate the difference between the total energies characterizing the structure after and before the dislocation emission in the case shown in Fig. 1(b). The considered transformation of the defect system is energetically favorable if the total energy of the defect system decreases and energetically unfavorable if not.

The dislocation emission process is specified by the energy difference, $\Delta W = W_2 - W_1$, where W_1 is the energy of the initial state of the system before the dislocation emission and W_2 is the energy of the system after the dislocation emission (Fig. 1(b)). Such a transformation of the defect system is energetically favorable if $\Delta W < 0$.

The energy difference ΔW is determined by the expression:

$$\Delta W = E_{self}^{bb} + E_{\text{int}}^{B-bb} + E_{\text{int}}^{pu-bb} + E_{\text{int}}^{\tau}, \quad (1)$$

where E_{self}^{bb} denotes the self-energy of the $\pm b$-dislocation dipole, E_{int}^{B-bb} is the sum interaction energy of the B-superdislocations at the NPs, and the $\pm b$-dislocation dipole, E_{int}^{pu-bb} is the sum interaction energy between n EGBDs in the pile-up at the triple junction of the GDs and the $\pm b$-dislocation dipole, and E_{int}^{τ} denotes the interaction energy of the applied shear stress τ with the $\pm b$-dislocation dipole.

The self-energy E_{self}^{bb} of a dipole of $\pm b$-dislocations is given by the well-known formula [19]:

$$E_{self}^{bb} = Db^2\left(\ln\frac{p-r_c}{r_c}+1\right), \tag{2}$$

where $D = G/[2\pi(1-\nu)]$, G is the shear modulus, ν is the Poisson ratio, p is the dipole arm (in other words, it is the path moved by the emitted b-dislocation), and $r_c \approx b$ is the cut-off radius of the stress fields of the $\pm b$-dislocations.

To calculate the interaction energy between deferent defects, the standard procedure of calculating the work spent to nucleate a defect (or a group of defects) in the stress field of another defect (see, for example, [19] for details) was used. In doing so, according to Mura's method [20], the sum interaction energies E_{int}^{B-bb} and E_{int}^{p-bb} can be found using the following formulas, respectively:

$$E_{\text{int}}^{B-bb} = -\frac{DBb}{2}\sum_{i=1}^{N}\left(\cos\alpha\ln\frac{l_i^2+p^2+2l_i^2 p\cos\alpha}{l_i^2} - \frac{2l_i p\sin^2\alpha}{l_i^2+p^2+2l_i p\cos\alpha}\right), \tag{3}$$

$$E_{\text{int}}^{pu-bb} = -\frac{Db_{gb}b}{2}\sum_{i=1}^{n}\left(\cos\alpha\ln\frac{x_i^2+p^2+2x_i^2 p\cos\alpha}{x_i^2} - \frac{2x_i p\sin^2\alpha}{x_i^2+p^2+2x_i p\cos\alpha}\right), \tag{4}$$

where $l_i = il$, x_i are the positions of the EGBDs within the pile-up at the triple junction of the GBs (they are calculated as the roots of the first derivative of the Laguerre polynomial [21] within a special numerical iteration procedure described briefly below).

To determine the positions x_i of the EGBDs with taking into account the stress field of the B-superdislocations, the following numerical calculation algorithm was used. At first, the equilibrium positions of the EGBDs under the action of constant external shear stress τ only were calculated. Then they were recalculated with the account for the B-superdislocation stress effect. These corrected values of x_i were then used to find newly corrected values of the EGBD positions in the next iteration, and so on. This iteration procedure of subsequent corrections was performed until the values of x_i converge to some constant values.

The energy that specifies the interaction of the external shear stress τ with the lattice $\pm b$-dislocations is given by

$$E_{\text{int}}^{\tau} = -b\tau\, p\cos 2\alpha\ . \tag{5}$$

Results and Discussion

Let us analyze the dependences of the energy change ΔW on the characteristics of the system under consideration in the exemplary case of the UFG Al-Cu-Zr alloy with the average grain size $d \approx 300\,\text{nm}$ [13]. First, the dependences of ΔW on the distance p moved by the b-dislocation in the grain interior were calculated for different values of the external shear stress τ at the following typical values of the system parameters [22,23]: $G = 27\,\text{GPa}$, $\nu = 0.33$, $a = 0.405\,\text{nm}$, $b = a\sqrt{2}/2$, $b_{gb} = 0.1\,\text{nm}$, and $l = d/(N+1)$. The emission angle α was chosen as the average angle $\alpha = 22°$ between 0° and 45° that corresponds to the maximum and minimum levels of the external shear stress τ, respectively. The total number of EGBDs in all the cases under investigation is taken as $m = (N+1)n = 36$. This value well corresponds to the typical length of GBs in experiments [23,24] and allowed us to obtain the results that well meet the levels of the flow stress measured in [13]. The shear stress τ is related to the flow stress σ as follows: $\sigma = 2\tau/\cos 2\alpha$. The curves $\Delta W(p)$ are shown in Fig. 2 for different values of the flow stress σ at $n = 36$, 18, and 12 in the cases of no NPs ($N = 0$, Fig. 2(a)), one NP ($N = 1$, Fig. 2(b)), and two NPs ($N = 2$, Fig. 2(c)), respectively, in the GB that corresponds to direct experimental observations of Al_2Cu-NPs in [13].

In the case of no NPs ($N=0$, see Fig. 1a), the critical value of the flow stress $\sigma=\sigma_c$, under which the dislocation emission becomes energetically favorable ($\Delta W=0$ at $p=1$ nm and $\partial\Delta W/\partial p<0$ at $p>1$ nm), is equal to 320 MPa (see the red curve in Fig. 2(a)). Indeed, for $\sigma<\sigma_c$, there is an energy barrier for the emission (here it is ~1 eV/nm for $\sigma=220$ MPa, see Fig. 2(a)), while for $\sigma>\sigma_c$, there is no energy barrier and, moreover, $\Delta W<0$ and $\partial\Delta W/\partial p<0$ at $p\geq 1$ nm (see here the curve for $\sigma=420$ MPa in Fig. 2(a)).

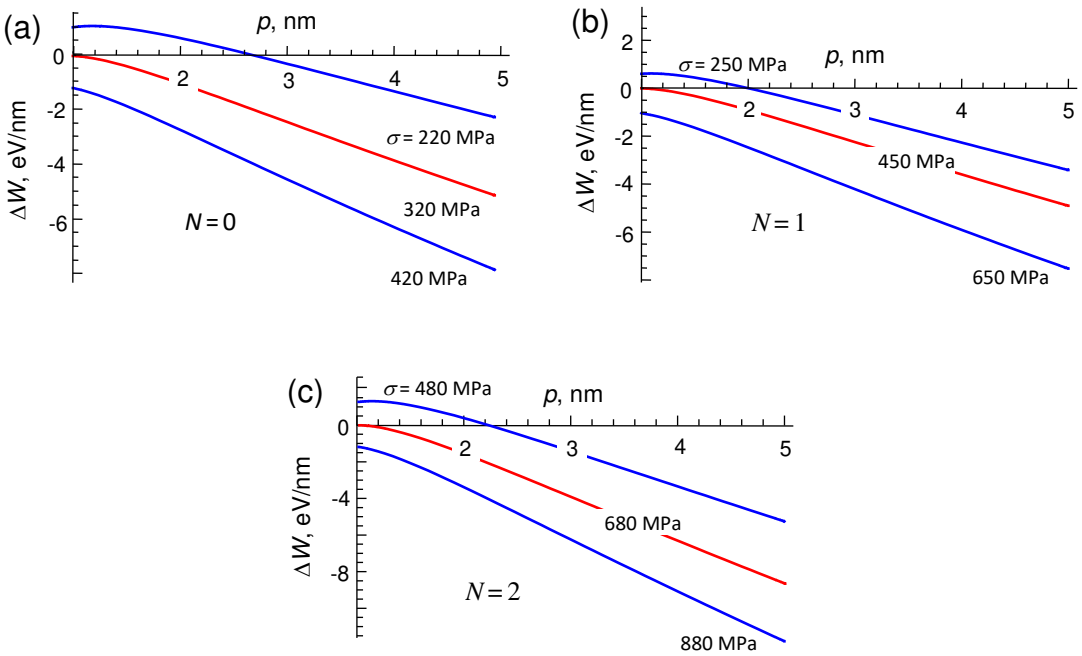

Fig. 2. Dependences of the energy difference ΔW on the distance p for different values of the flow stress σ and the number of the EGBDs in the pile-ups: (a) n=36, (b) 18, and (c) 12 in the cases of N=0, 1, and 2, respectively. The red curves correspond to the critical values of the flow stress under which the dislocation emission becomes energetically favorable

In the cases of one and two NPs ($N=1$ and 2, see Figs. 2(b,c)), the emission of lattice dislocations becomes energetically favorable at $\sigma\geq\sigma_c=450$ MPa and 680 MPa, respectively. To explain these results, we calculated the sum shear stress τ_{sum} in front of the pile-up, at $\alpha=0$ and at the distance 1 nm from the head EGBD – just in the emission region – for the three cases: (i) $N=0$, $\sigma=320$ MPa, (ii) $N=1$, $\sigma=450$ MPa, and (iii) $N=2$, $\sigma=680$ MPa. The results are $\tau_{sum}\approx 2.83$ GPa in case (i), 2.78 GPa in case (ii), and 2.79 GPa in case (iii) which is roughly 2.8 GPa in all three cases. This value is approximately equal to $G/10$ that is of the order of magnitude of the theoretical shear strength.

The dependence of the critical flow stress σ_c on the number N of the NPs in the GB is shown in Fig. 3. As is seen, σ_c noticeably increases with N and the discrete dependence $\sigma_c(N)$ is very close to linear. To determine the best-fitting line approximating our calculated points, we used the method of least squares. In the framework of this method, the equation of the best-fitting line for the dependence $\sigma_c(N)$ is given in units of GPa as follows:

$$\sigma_c\approx 0.255+0.235N. \quad (6)$$

The corresponding linear dependence $\sigma_c(N)$ is shown by the solid line in Fig. 3. This result can be used for rough estimates of the expected yield stress of the UFG Al-Cu-Zr alloy with Al_2Cu-NPs in GBs, depending on the average number of nanoprecipitates at the boundary.

Thus, it is shown that, in the case of no NPs in GBs, the critical flow stress is about 320 MPa. It corresponds well to the value of the yield stress $\sigma_{0.2}$ estimated on the basis of experimentally determined microstructural parameters as the sum of contributions from known strengthening mechanisms, such as the Peierls-Nabarro hardening, the solid solution hardening, the strain hardening, the GB hardening and the dispersion hardening [13]. In contrast, in the case with one Al_2Cu-NP in a GB, it is about 450 MPa in accordance with measurements in Ref. 13. Therefore, the difference in 130 MPa can be attributed to the role of Al_2Cu-NPs as obstacles for the glide of EGBDs in non-equilibrium GBs typical for HPT processed metals and alloys. This difference characterizes the value of the additional hardening of the UFG Al-Cu-Zr alloy structured by HPT and demonstrates good agreement with experimental data [13]. It should be noted that in the HPT processed Al-Zr alloy, in which GBs did not contain any precipitates of secondary phase, the theoretically calculated value of $\sigma_{0.2}$ as the sum of known strengthening mechanisms well corresponds to the experimental value of the yield stress [24].

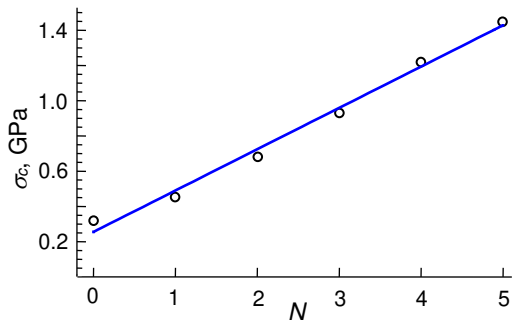

Fig. 3. Dependence of the critical flow stress σ_c on the number N of the NPs. The calculated points (open circles) are approximated by the best-fitting straight line

Summary and Conclusions

Thus, a theoretical model of a new micromechanism of strengthening in the UFG Al-Cu-Zr alloy is developed. In the model, the formation of Al_2Cu-NPs at GBs, which act as obstacles for EGBD slip, leads to a significant increase in the strength of the Al-Cu-Zr alloy. The deformation mechanism realizes through the emission of lattice dislocations from the heads of the pile-ups of the EGBDs near the triple junctions of the GBs. It is shown that the division of gliding EGBDs into separate pile-ups by Al_2Cu-NPs can provide additional hardening of the UFG Al-Cu-Zr alloy structured by HPT, the value of which well corresponds to experimental measurements [13].

References

1. Edalati K, Bachmaier A, Beloshenko VA, Beygelzimer Y, Blank V et al. Nanomaterials by severe plastic deformation: review of historical developments and recent advances. *Materials Research Letters*. 2022;10(4): 163-256.
2. Vu VQ, Toth LS, Beygelzimer Y, Zhao Y. Microstructure, texture and mechanical properties in aluminum produced by friction-assisted lateral extrusion. *Materials*. 2021;14(9): 246.
3. Horita Z, Tang Y, Masuda T, Takizawa Y. Severe plastic deformation under high pressure: upsizing sample dimensions. *Materials Transactions*. 2020;61(7): 1177-1190.
4. Xu W., Liu XC, Lu K. Strain-induced microstructure refinement in pure Al below 100 nm in size. *Acta Materialia*. 2018;152: 138-147.

5. Jia H, Bjørge R, Cao L, Song H, Marthinsen K, Li Y. Quantifying the grain boundary segregation strengthening induced by post-ECAP aging in an Al-5Cu alloy. *Acta Materialia*. 2018;155: 199-213.
6. Shuai LF, Huang TL, Wu GL, Hansen N, Huang X. Characterization of Cu Distribution in an Al-0.3%Cu Alloy Cold Rolled to 98%. *IOP Conf. Series: Materials Science and Engineering*. 2017;219: 012038.
7. Liu Y, Liu M, Chen X, Cao Y, Roven HJ, Murashkin M, Valiev RZ, Zhou H. Effect of Mg on microstructure and mechanical properties of Al-Mg alloys produced by high pressure torsion. *Scripta Materialia*. 2019;159: 137-148.
8. Belov NA, Alabin AN, Matveeva IA, Eskin DG. Effect of Zr additions and annealing temperature on electrical conductivity and hardness of hot rolled Al sheets. *Transactions of Nonferrous Metals Society of China*. 2015;25: 2817-2826.
9. Jiang SY, Wang RH. Manipulating nanostructure to simultaneously improve the electrical conductivity and strength in microalloyed Al-Zr conductors. *Scientific Reports*. 2018;8: 6202.
10. Mavlyutov AM, Orlova TS, Yapparova EKh. The effect of annealing and additional deformation on the mechanical properties of ultrafine-grained Al-1.5Cu alloy. *Technical Physics Letters.* 2020;46: 916-920.
11. Sitdikov VD, Murashkin MY, Valiev RZ, Full-scale use of X-ray scattering techniques to characterize aged Al-2wt.%Cu alloy. *Journal of Alloys and Compounds.* 2018;735: 1792-1798.
12. Nasedkina Y, Sauvage X, Bobruk EV, Murashkin MY, Valiev RZ, Enikeev NA, Mechanisms of precipitation induced by large strains in the Al-Cu system. *Journal of Alloys and Compounds.* 2017;710: 736-747.
13. Orlova TS, Sadykov DI, Murashkin MY, Enikeev NA. Peculiarities of strengthening of Al-Cu-Zr alloy structured by severe plastic deformation. *Physics of the Solid State*. 2021;63: 1744-1756.
14. Orlova TS, Sadykov DI, Danilov DV, Enikeev NA, Murashkin MY. Ultrafine-grained Al-Cu-Zr alloy with high-strength and enhanced plasticity. *Material Letters*. 2021;303: 130490.
15. Orlova TS, Skiba NV, Mavlyutov AM, Murashkin MY, Valiev RZ, Gutkin MY. Hardening by annealing and implementation of high ductility of ultra-fine grained aluminum: experiment and theory. *Reviews on Advanced Materials Science*. 2018;57: 224-240.
16. Gutkin MY, Latynina TA, Orlova TS, Skiba NV. Mechanism of hardening of ultrafine-grained aluminum after annealing. *Physics of the Solid State*. 2019;61: 1790-1799.
17. Skiba NV, Orlova TS, Gutkin MYu. Mechanism of implementation of high ductility in ultrafine-grained aluminum after annealing and subsequent deformation. *Physics of the Solid State*. 2020;62: 2094-2100.
18. Orlova TS, Mavlyutov AM, Gutkin MY. Suppression of the annealing-induced hardening effect in ultrafine-grained Al at low temperatures. *Materials Science Engineering A*. 2021;802: 140588.
19. Gutkin MY, Ovid'ko IA, Skiba NV. Crack-stimulated generation of deformation twins in nanocrystalline metals and ceramics. *Philosophical Magazine*. 2008;88: 1137-1151.
20. Mura T. The continuum theory of dislocations. In: Herman H. (ed.) *Advances in Material Research*. New York: Interscience; 1968. p.1-108.
21. Eshelby JD, Frank FC, Nabarro FRN. XLI. The equilibrium of linear arrays of dislocations. *Philosophical Magazine*. 1951;42: 351-364.
22. Hirth JP, Lothe J. *Theory of Dislocations*. New York: Wiley; 1982.
23. Smithells CJ, Brands EA. *Metals Reference Book*. London: Butterworths, London; 1976.
24. Orlova TS, Latynina TA, Mavlyutov AM, Murashkin MY, Valiev RZ. Effect of annealing on microstructure, strength and electrical conductivity of the pre-aged and HPT-processed Al-0.4Zr alloy. *Journal of Alloys and Compounds.* 2019;784: 41-48.

THE AUTHORS

Skiba N.V.
e-mail: nikolay.skiba@gmail.com
ORCID: 0000-0003-2192-0386

Gutkin M.Yu.
e-mail: m.y.gutkin@gmail.com
ORCID: 0000-0003-0727-6352

Orlova T.S.
e-mail: orlova.t@mail.ioffe.ru
ORCID: 0000-0001-8986-2624

Materials Physics and Mechanics. 2022;50(3): 439-458
Research article
http://dx.doi.org/10.18149/MPM.5032022_8

Submitted: August 30, 2022
Approved: September 20, 2022
Accepted: October 18, 2022

Effect of reinforcements on mechanical and tribological behavior of magnesium-based composites: a review

Dinesh Kumar✉, Satnam Singh, Surjit Angra

Department of Mechanical Engineering, National Institute of Technology Kurukshetra-136119, Haryana, India

✉ dinesh_61900120@nitkkr.ac.in

Abstract. The challenges faced in the development of light materials, motivate researchers to produce materials with improved characteristics, which have wide applications in the biomedical, automotive, defense, and aviation industries. The limited availability of monolithic or natural materials on the earth can be another reason to develop a newer version of metals, alloys, and composites. These developed materials should have enhanced physical, mechanical, and tribological properties. The present article discusses the effect of numerous reinforcements with different weight/volume percentages on the hardness, tensile strength, corrosion, and wear resistance of Mg-based metal matrix composites (Mg-MMCs). It has been observed that the hardness and tensile strength of Mg-MMCs range from 34-152.7 HV and 45-240 MPa, respectively, and its corrosion current density reduces from 549.21-1.923 μA cm^{-2}. This research paper also focused on the effect of various wear and friction process parameters such as applied load (10-80 N), sliding distance (100-2000 m), sliding velocity (1-3 m/s), sliding time (5-30 minutes), and the effect of different weight/volume reinforcement percentages (0-25%) on the performance of Mg-MMCs during wear and friction phenomenon. The material loss during wear measurement and coefficient of friction (COF) of Mg-MMCs ranges from 0.0174 -0.09 g and 0.90-0.0234, respectively.
Keywords: MMC, magnesium, bio-medical, tensile strength, hardness, corrosion, wear, friction

Acknowledgements. *No external funding was received for this study.*

Citation: Kumar D, Singh S, Angra S. Effect of reinforcements on mechanical and tribological behavior of magnesium-based composites: a review. *Materials Physics and Mechanics*. 2022;50(3): 439-458. DOI: 10.18149/MPM.5032022_8.

1. Introduction

Over the recent years, rapid transformation in social inevitabilities and requirements contributes to the various progressive genera of materials through enhanced properties achieved from alloys, metals, and non-metals [1]. Material adoption is a vital part of our everyday needs and in the advancement of every nation [2]. As of now, how materials are being utilized for the betterment of our daily needs is genuinely enough to know the significance of designing that material in our life [3].

New materials have to create with quick production and assembly needs among worldwide industries [4]. The evolved material should have improved properties over monolithic materials [5]. The necessity for enhanced properties can be fulfilled with

© Dinesh Kumar, Satnam Singh, Surjit Angra, 2022.
Publisher: Peter the Great St. Petersburg Polytechnic University
This is an open access article under the CC BY-NC 4.0 license (https://creativecommons.org/li-censes/by-nc/4.0/)

composites [6]. The combination of two or more materials is identified as a composite. Matrix and reinforcements can be called two portions of the composites. The matrix material should be metal, whereas reinforcement can be metal or non-metal [7]. When the metal and its alloy are used as matrix material, then the fabricated composite is known as metal matrix composite (MMC). Metal matrix composites have mostly improved properties by adding some reinforcement weight/volume percentage [8]. The types of composites are represented in Fig. 1. The pictorial view of the constituents of the hybrid metal matrix composite is shown in Fig. 2.

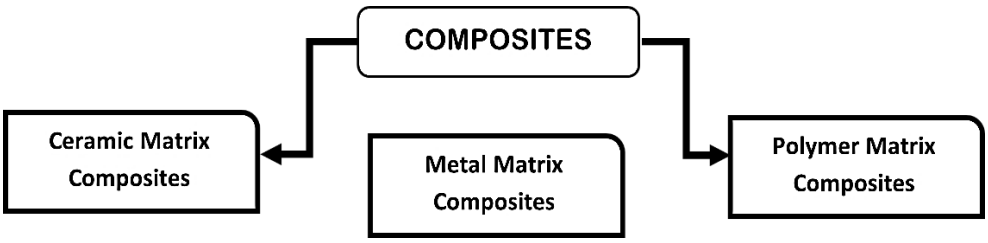

Fig. 1. Classification of composite materials

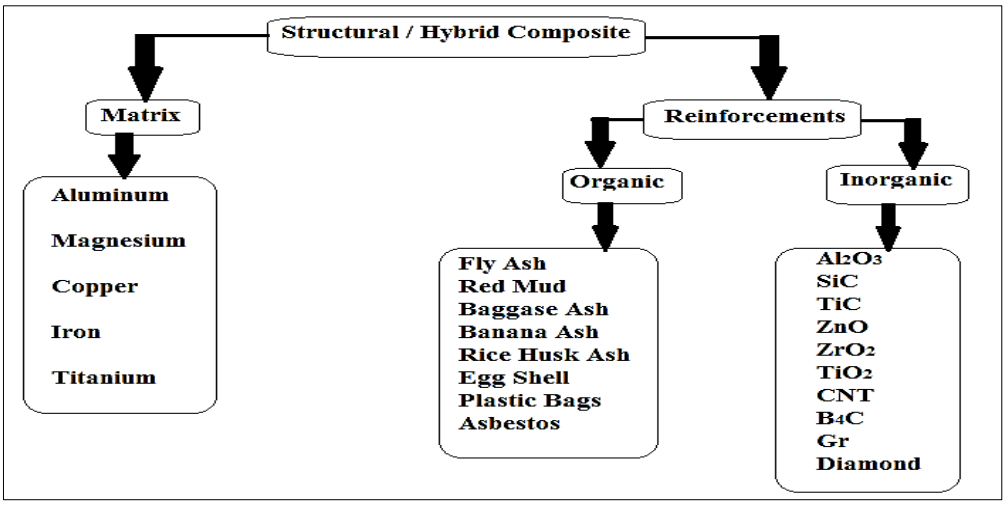

Fig. 2. Constituents of hybrid composites [9]

Iron (Fe), zinc (Zn), aluminum (Al), copper (Cu), titanium (Ti), and magnesium (Mg) are being utilized as matrix materials in MMCs. Each metal matrix has its importance regarding its application. Mg is the most used lightweight material for various applications. It is the eighth most abundant material in the earth's crust and one-third and one-sixth lighter than aluminum and titanium, respectively [10]. The Mg applications include biomedical (such as orthopedic, cardiovascular, and other transplants) [11], automotive (like gearbox, steering column, seat frames, drivers' airbags, and fuel tank covers) [12], and other (laptops, cameras, luggage storage products, power tools, and household) [13]. The Mg-MMC's demand consistently increases due to artificial implants. To fulfill this demand for patients with bone injuries and degeneration caused by the normal process of aging, injuries, and accident, we required biomedical materials to bring back into the functionality of the part [14-16].

Mg-MMCs have shown tremendous potential in orthopedic and other implant applications to address the problems. The elastic moduli of Mg-MMCs closer to natural bone is also the main reason for its adaptation in bio-medical industries [17]. The Mg-MMCs also have enhanced mechanical properties (like hardness, tensile strength, compressive strength, flexural strength, etc.) and tribological properties (Corrosion, friction, and wear) compared to base Mg and it's alloy [17-19]. The high strength stiffness and light-in-weight makes Mg an

important material for use in aviation and automotive applications [20], however, its high manufacturing cost restricts the use of Mg as a matrix material. To overcome these factors, homogeneity and reinforcement are used and tried to make an inexpensive using fast dispersion process to manufacture Mg-MMCs composites. Metal and ceramic particulates are among the furthermost traditionally used reinforcements in composites [21,22].

2. Material used and methods of fabrication

The study focuses on magnesium and its alloy used as a matrix material for the fabrication of composites. Due to the high damping and vibration coefficient, low density, and high strength of the magnesium, the Mg-based composites have great potential to use in structural elements in automotive, aerospace, and bio-medical industries [23]. The various kinds of reinforcements in different proportions can be added during the synthesis of Mg-MMCs [24]. The commonly used composite fabrication methods are:

1. Stir Casting
2. Powder Metallurgy (PM)
3. Friction stirs processing (FSP)

Stir casting. The fabrication of discontinuous particle reinforced MMCs use the stir casting technique. The process is affected by many influencing parameters on which the mechanical and microstructure of the composite depends. The two-step stir casting technique was used to produce a composite of aluminum alloy and alumina oxide by Alaname et al. The Al6063 was preheated at 250°C, then the preheated form of matrix material is put into a graphite furnace and heated up to 750°C to convert into a molten state. Then the stirrer with 300 rpm for 10 minutes was used for uniform dispersion of the reinforcement into the molten matrix. After that, the molten metal was poured into a sand mould for solidification [25]. Figure 3 describes the stir casting setup.

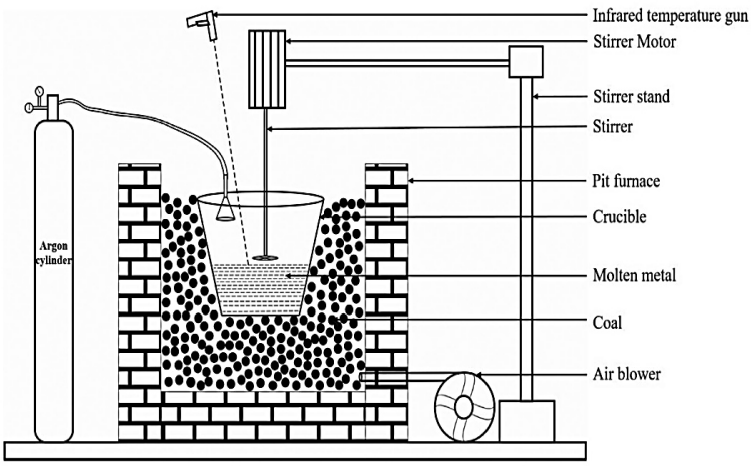

Fig. 3. Stir Casting Setup [26]

Meher et al. adopted a stir casting process to fabricate the magnesium composite for manufacturing the components of the automotive and aerospace sectors. The 4, 6, and 8 weight percentage of TiB_2 was added to the RZ5 magnesium alloy. The mechanical properties were enhanced with TiB_2 at 8 weight percentage addition in the base metal [26]. Kumar and Sozhamannan discuss the characterization of magnesium-based matrix composites in the study. The stir cast samples of graphene 0.5, 1 and 1.5 wt.% and magnesium alloy were prepared. The preheating of the die was done at 300ºC and the stirrer speed was used at 450-500 rpm to avoid the casting defects in the samples. The strong interfacing between graphene and magnesium alloy was observed during microstructure analysis [27].

Powder metallurgy. Sintering, blending, and compacting are the three steps involved in powder metallurgy. First of all the base metal or compound powders are blended appropriately then afterward passed through the high-pressure die then at high temperature it was sintered for the legitimate holding of particles [28]. Singh et al. concluded in their study that the heating of the magnesium powder and Sic powder was done at 400ºC thereafter desired shape was given by passing the material through the die and punch for 60 minutes at 150 rpm, then room temperature was maintained at the molten metal [29]. The extruded rods were cut into a length of 150 mm and after that using a muffle furnace the internal stress was released from the prepared rods. Ghasali et al. observed the higher bending strength and microhardness of the sintered magnesium/ B_4C composites [30]. Kumar et al. studied the influence of sintering temperature, milling time, and compaction pressure on magnesium-based composite during powder metallurgy processing technique. The improvement was noticed in the hardness and density of the composite [31]. The graphical representation of powder metallurgy process is mentioned in Fig. 4.

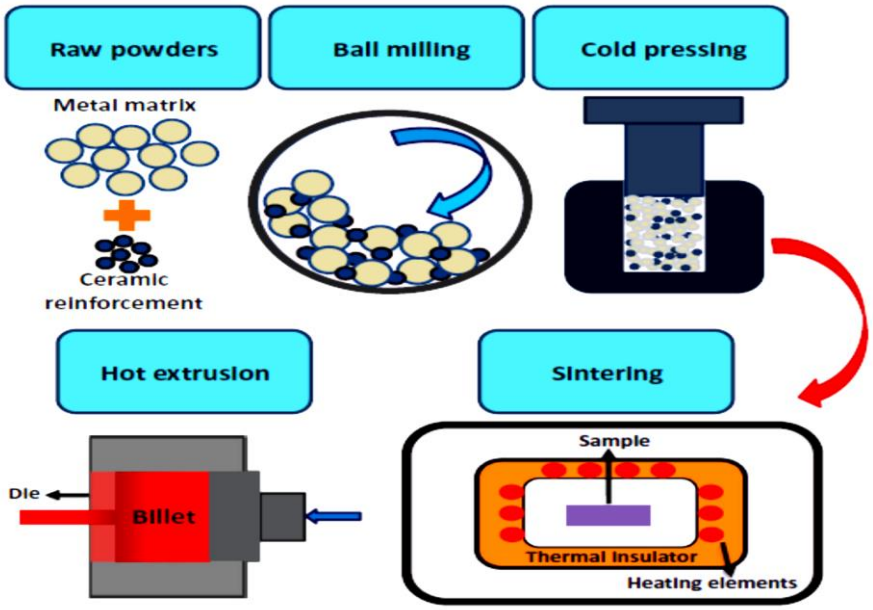

Fig. 4. Powder Metallurgy [32]

Friction stir processing. When the modification in surface property is required during the manufacturing of metal matrix then the friction stir technique is utilized. The structural advancement by plastically deformation during the advancement of non-consumable apparatus into the work-piece is done by this process [33,34]. During the progression, a turning or rotating pin type of tool is progressed on the surface of the work-piece. Due to frictional resistance, heat is generated which is the main reason for plastic deformation between the surface of the work-piece and tool pin [35]. Dinaharan et al. utilized FSP to fabricate Mg MMC's of AZ31/Ti-6Al-4V. The H13 steel material cylindrical shaped tool of diameter 24 mm was used in the processing of composite fabrication. The height of the tool tip was 5.7 mm with the threaded profile. The effect of transverse speed, tilt angle, and tool rotation speed was studied on the mechanical properties of the composite [36].

Pandey et al. studied the influence of FSP on the strength and wear of magnesium and SiC nano-composites. The enrichment was seen in the mechanical and metallurgical properties of the produced nano-composite. The homogenous mixture of the SiC was observed in SEM analysis [37]. The 19.72% and 77.5% increment was noticed for the micro-hardness and compressive strength of the AZ31/graphene/MWCNT composites.

The MWCNT with 1.6 vol.% and 0.3 vol.% of graphene was found optimized at the rotation speed of 1400 rpm [38]. Figure 5 shows the process parameters and response parameter of friction stir processing.

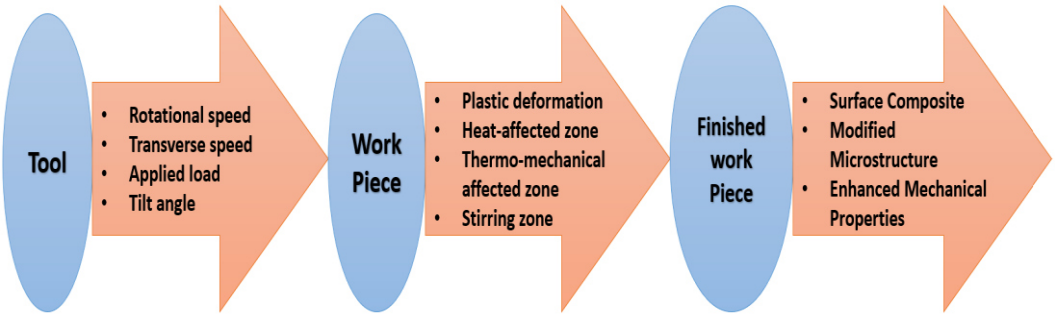

Fig. 5. Friction stir process [10]

3. Effects of different reinforcements on mechanical properties of Mg-MMCs

Effect on hardness. The resistance to indentation and abrasion of the material is called hardness. The Brinnel, Rockwell, and Vickers are commonly used machines for testing hardness. The experimental work concluded that increment in the hardness of Mg-MMCs of 10 wt.% titanium carbide (TiC) when reinforced in the matrix of RZ5 magnesium alloy, fabricated using the self-propagating high-temperature technique [39]. Authors have produced Mg-MMCs with reinforcement of 0.5 wt. % of Al_2O_3 and 8 wt. % of Tio_2 with AZ61 Mg alloy using laser cladding (LC). It has been observed that hardness increases as wt.% of reinforcements increases due to the particle grain size refinement of Al_2O_3 and Tio_2 in matrix material [40].

The research work concluded that the increase in value of Vickers hardness (HV) for Mg alloy AZ91 fabricated using stir casting technique when reinforced with TiO_2 having 2 wt.% and graphene 0.5 wt.%. The increment in hardness of Mg-MMCs was due to the solid lubrication behavior of graphene for consistent mixing in a matrix material [41]. In this work, the effect of calcium reinforcement (0.2 Vol.%) in Mg alloy matrix when fabricated with friction stir processing (FSP) was studied. It was also noticed that the hardness increased to 73.7 ± 9.9 HV from 60.98 ± 5.3 HV. The grain refinement and texture effect are the main reasons behind the hardness value increment [42].

The value of Vickers hardness increased to 106 from 34 when pure magnesium is reinforced with SiC using FSP at tool pin rpm of 1300 was observed. The reason behind that was reduced grain size and low dislocation movement. The SiC has hard particles, which increases the high load-bearing capability of the composite [43]. The fabrication of Mg-MMCs when reinforced with 5wt.% $Al_2O_3$and 8 wt.% SiC particles in AZ31 Mg alloy. The hardness value was reported to increment 75.16 HV from 64.53 HV, which principally increases the load-bearing capability due to SiC particles present in the Mg-MMCs [44]. Figure 6 shows the comparison of different Mg-MMCs.

When matrix metal AZ91 was reinforced with 10 wt% Al_2O_3 and 5 wt.% SiC, the hardness value expanded by 25% compared to without reinforcement, the Mg-MMC was fabricated using the powder metallurgy (PM) technique. The increment in hardness was observed from 36.3 HV to 45.39HV, as reported in this work [45]. The authors observed the increase in hardness when ZrO_2 was reinforced in the matrix of Mg alloy AZ91D. The authors concluded that hardness increased to 31% compared to Mg alloy due to uniform strain deformation and proper distribution of reinforcement particles [46]. The 28% improvement in the hardness was noticed when stir-cast Mg-MMCs reinforced with zinc oxide (0-5 wt.% ZnO) to Mg alloy [6]. 143.6 HV was reported in Mg-MMC and 112.3 HV in

Mg alloy [47]. Table 1 shows the summary sheet for the hardness of some researchers for magnesium-based composites.

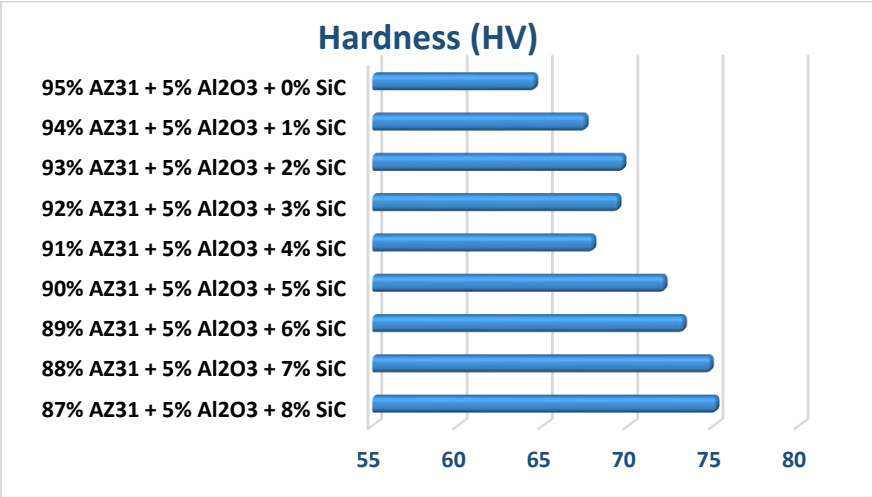

Fig. 6. Hardness of different Mg-MMCs [44]

Table 1. Hardness summarized sheet of Mg-MMCs

S No	Reinforcement	Method	Hardness		Ref.
			Mg Alloy	Mg-MMC	
1	Nano Y_2O_3 0.7 Wt. %	Microwave Sintered	35 HV	45 HV	[21]
2	B_4C 9 Wt.%	Stir Casting	42 HR	78 HR	[48]
3	Nano BN 2.5 Wt. %	Microwave Sintered	48±1 HV	57±2 HV	[49]
4	B_4C 5 Wt. %	Stir Casting	88±10 HV	61±11 HV	[32]
5	Nano CNT 0.1 Wt. %	Microwave Sintered	48±1 HV	61.8±8.6 HV	[50]
6	TiO_2 15 Wt. %	Stir Casting	55.9 BHN	72.4 BHN	[51]
7	$Niti_p$ 10 Vol. %	Friction Stir Processing	35±5 HV	152.7 HV	[52]

Effect on tensile strength. In industries, mechanical testing has great importance before producing or developing any material. The testing also leads to cost reduction without comprising the quality during production. The tensile strength concludes the functionality of the manufactured products. Jayabharthy et al. and Mehra et al. also reported the enhancement of tensile strength increment in the stir-casted Mg-MMCs. The values of Tensile strength of Mg-MMCs were 149.1 MPa and 195 MPa as compared to Mg alloy (84.3 MPa and 179 MPa respectively) [39,41]

The microwave sintering process was used to produce a composite with 2 wt.% of nano Y_2O_3 reinforcement in the Mg alloy matrix. The study reported that tensile strength was increased to 85% (130 MPa to 240 MPa) with 2 wt.% nano Y_2O_3 in the matrix material. The enhancement of tensile strength was attributed to uniform particle dispersion, grain refinement, and increment in extrusion ratio [21]. The effect of variation with B_4C particles in pure Mg on tensile strength was studied by fabricating samples of Mg-MMCs using the stir casting technique. The authors observed that tensile strength increased from 45 MPa to

84 MPa with an increment of reinforcement in Mg matrix. The decrement in porosity, grain size, and nearly uniform distribution of B_4C particles can be the reason for the increment in the tensile strength of MMC's[48].

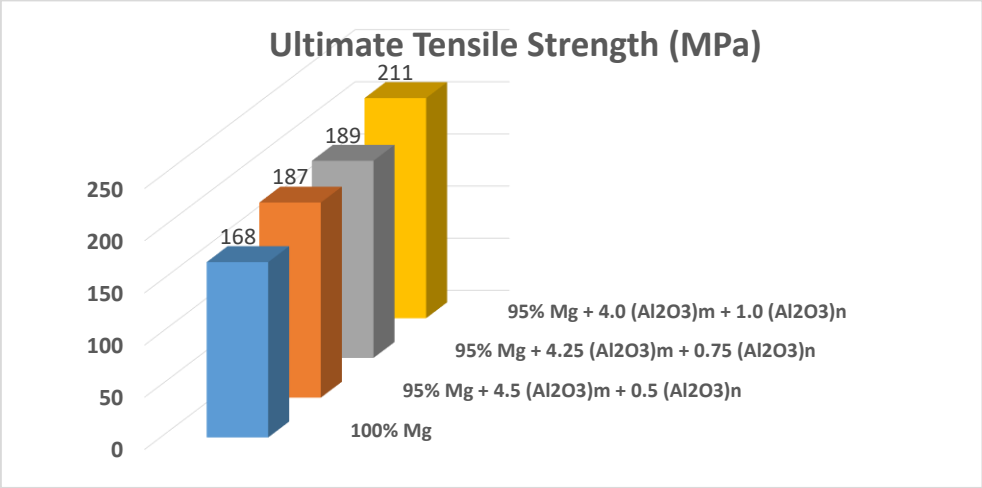

Fig. 7. Ultimate tensile strength of Mg-MMCs at different Reinforcements [53]

The fabrication of MMC's was completed using SiC (0.5 vol.% and 1 vol.%) in pure Mg by powder metallurgy. The maximum tensile strength was reported at 1 vol.% of SiC particles in Mg-MMC. The increment in tensile strength was 18% (172 MPa to 203 MPa) compared to monolithic magnesium. The smaller size and lower volume fraction of reinforcement in the MMC are attributed to the enhancement of tensile strength [54]. The powder metallurgy technique was utilized for the fabrication of MMC's by submicron and nano Al_2O_3 (4 to 4.5 vol.% and 0.5 to 1 vol.% respectively) in pure Mg using the powder metallurgy technique. The increment in tensile strength was observed to be 26% (168 MPa to 211 MPa) as compared to pure magnesium (as shown in Fig. 7) [53]. Table 2 shows the summary sheet for the tensile strength of some researchers for magnesium-based composites.

Table 2. Tensile strength summarized sheet of Mg-MMCs

S. No	Reinforcement Percentage	Method	Tensile Strength (MPa)		Ref.
			Mg Alloy	Mg-MMC	
1	2 Y_2O_3	Microwave sintered	130	240	[21]
2	5 B_4C	Microwave sintered	65	112	[30]
3	5 B_4C	Spark plasma sintered	65	191	[30]
4	10 Tic	Stir casting	179	195	[39]
5	1 TiO_2 + 0.5 Gr 2 TiO_2+ 0.5 Gr	Stir casting	84.3	149.1	[41]
6	B_4C	Stir casting	45	84	[48]
7	0.5 SiC 1 SiC	Powder metallurgy	172	203	[54]
8	4 $(Al_2O_3)_m$ + 0.5 $(Al_2O_3)_n$	Powder metallurgy	168	211	[55]
9	0.66 TiO_2	Powder metallurgy	194	197	[56]
10	0.7 Y_2O_3 + 0.3 nano Cu	Microwave sintered	244	270	[57]
11	0.7 SiC + 0.3 nano CNT	Powder metallurgy	155.8	195.4	[58]
12	1 CNT + 1.5 TiB_2	Stir casting	213.96	389.67	[59]

The Mg-MMCs with 5 vol.% of B_4C reinforcement in magnesium matrix using microwave sintering (MS) and spark plasma sintering (SPS) process were prepared. The comparative analysis for tensile strength reported that 191 MPa tensile strength was observed in SPS process and 112 MPa in MS process. The study also shows that a 71% increment of tensile strength was reported using SPS process as compared to MS process. The presence of pores and microcracks formation decreases the tensile strength of microwave-sintered Mg-MMCs [30]. Hassan et al. used the powder metallurgy method to fabricate the Mg-MMCs of nano TiO_2 (0, 0.58, and 0.66 Vol.%) reinforcement in pure magnesium powder. The tensile test samples were prepared according to ASTM E8M-15a standard. Results reported that 2% (194 MPa to 197 MPa) increment of tensile strength by adding 0.66 vol.% nano TiO_2 in the Mg matrix material [56]. Authors reported the effect on tensile strength of reinforcements (Y_2O_3 0.7 Wt.% Nano Cu 0.3 Wt.%) hybrid microwave sintered in Mg powder at different temperatures. The 270 MPa value of ultimate tensile strength was achieved at 25ºC in (Mg/0.7 Y_2O_3/0.3 Cu) MMC [57]. The powder metallurgy technique was used to produce Mg-MMCs with reinforcements of Sic 0.7 Wt.% / Nano CNT 0.3 Wt.%. The 25.4 % increment in tensile strength (155.8 MPa to 195.4 MPa) was noticed compared to monolithic magnesium [58]. The 7% increment in tensile strength was reported for AZ91D/1.5wt.% CNTs/1.5 wt. % TiB_2 hybrid composite [59].

From the literature, it can be concluded that the increase in grain particle size causes porosity which reduces the load-bearing capacity. The chances of non-uniform dispersion of reinforcement particles are also there which causes high surface roughness, hence reducing the mechanical properties of the Mg-MMCs [56-60].

4. Effect of different reinforcements on tribological behavior of Mg-MMCs

Effect on corrosion characteristics. From a technical point of view, the proper selection of the process and material for the particular product cannot be decided without corrosion testing. The corrosion testing calculates the failure and life of the material. Thus, in order to find the corrosion rate of the Mg-MMCs, the corrosion current density (μA cm^{-2})/current potential (V) was noted, the greater the corrosion current potential/density greater the corrosion rate in the fabricated Mg-MMCs.

The immersion test was performed on the base and AZ91D-ZrO2 composite material samples ranging from 72 to 168 hours. Initially, at 72 hours, the increment in corrosion starts, and after immersion of 168 hours, it was found that the corrosion rate was reduced. The corrosion potential in the samples was decreased due to the fine dispersion of the reinforcement in the composite. The corrosion current density of MMC was increased to 1.05% (MMC corrosion current density 1.923 μA cm^{-2}) compared to the base metal. This enhancement of corrosion resistance makes the MMC biodegradable [46].

The investigation of Mg-Al_2O_3-SiC hybrid composite in which Al_2O_3 and SiC were used as reinforcement with magnesium matrix using powder metallurgy method. The effect on corrosion resistance was examined under the anodization and immersion process, and surface treatment was carried out using cerium oxide. The authors concluded that surface treatment enhances the corrosion resistance in both the MMCs, but Al_2O_3 particles help in achieving better corrosion resistance compared to SiC particles [61].

The liquid state processing (Stir casting) was used to fabricate Mg-MMCs of AZ41-samarium (sm) (x = 0%, 1%, 2%, and 3%) as alloy and reinforcement, respectively. The electrochemical impedance spectroscopy (EIS) and Tafel polarization (TP) methods were used to analyze corrosion behavior under NaCl solution in 3.5 wt. %. The research concluded that the corrosion resistance was increased due to an increment in the sm reinforcement compared to AZ41 Mg alloy. At 1wt.% of sm, the corrosion rate was 18.7 μA cm^{-2} which has been reported the best compared to AZ41, sm 2 wt.%-AZ41, and sm 3 wt.%-AZ41 (34.6,

25.7, and 23.2 μA cm^{-2} respectively). This enhancement was due to hydrogen evolution, which increases the soaking time and enhances the corrosion resistance of Mg-MMCs compared to Mg alloy [62].

The authors reported in their study that Mg Alloy/ 4wt.% of glass microsphere (GM), MMC was fabricated using stir casting to analyze the effect of corrosion behavior. EIS technique was utilized in the presence of 0.5m H_2SO_4 solution for corrosion characteristics of the developed Mg MMC's. The corrosion rate was enhanced by reinforcing the GM particle to the Mg alloy. The potential corrosion value (-1.16 V) and corrosion resistance (2.61 μA cm^{-2}) have been reported in the study. The deterioration and large crack formation decrease the corrosion resistance of the fabricated Mg MMC's [63]. The investigation was accomplished for the corrosion behavior of Mg/ zinc oxide (ZnO). ZnO powdered particles (5, 10, and 20 wt.%) were mixed with pure Mg metal matrix to form Mg-MMC's samples. The immersion test and electrochemical surface measurement were done to evaluate the corrosion behavior through Hank's solution. During the trial, reinforced particles were uniformly dispersed in the Mg matrix, which enhance corrosion resistance and mechanical properties in the developed Mg-MMC. The corrosion resistance of Mg-MMC was noticed as 95.02 μA $cm^{-2,}$ which was one-sixth of Mg alloy (549.2l μAcm^{-2}) [64].

Effects on wear and coefficient of friction. The interaction between two surfaces causes material loss. The loss and deformation are the results of mechanical action. It can be determined by the volume and mass loss of the material element.

Ting lei et al. investigated the COF and wear behavior of Mg/ zinc oxide (ZnO). The loss of material and COF in Mg-based MMC has been observed to be lower as compared to Mg alloy. The intense binding action of ZnO particles and low porosity is the reason for the enhancement of COF and wear resistance in Mg-MMCs. The analysis was done and found that Mg alloy had an average material loss of 0.85 mg and 0.18 mg was found in Mg-MMC sample. Figure 8 shows the wear loss comparison between the Mg alloy and Mg-MMC [64]. Khatkar et al. fabricated the AZ91D-xSiC-xGr hybrid composite, AZ91 alloy as matrix and reinforcements were SiC (3 and 5 wt. %) and Gr (0, 3, and 5 wt. %) with stir casting technique. The wear test had been performed on a pin on disc apparatus and concluded that the wear rate has been decreased as the percentage of Sic and Gr particles increased. The 0.0079 mm^3/m wear rate of Mg-MMC has been achieved at Sic-5 wt. % and Gr-5 wt. % as reinforcement in the Mg alloy. The delamination and oxidation of SiC particles increase the wear rate in Mg-MMC and decrease the coefficient of friction (COF) [65]. The effect of Sic and graphene oxide (Go) on Mg AZ91 alloy was studied. The wear damage was reduced due to fewer cracks and debris on the worn surfaces by adding Sic and GO particles in the Mg alloy. The graphene oxide gives the best result for wear loss; the volume loss of GO/Mg alloy has been reduced to 0.31 times compared to Mg alloy [66].

The powder metallurgy method was adopted to fabricate Mg-B_4C (0, 1.5, 3.5, and 10 wt. %) MMC's samples. The increment in wear resistance has been seen as the percentage of the B_4C reinforcement (0 to 10 wt. %) increases. The wear resistance was improved by 33 % with 10 wt.% of B_4C in the Mg-MMCs. This is due to the strong bonding of particles and the higher hardness of Mg-MMC's [67]. The wear resistance has increased 5.7 times in the Mg-SiC-Al_2O_3 composite. This increment in the wear resistance was due to the homogenous and uniform dispersion of SiC and Al_2O_3 particles in the fabricated composite. The Al_2O_3 particle gives better results compared to SiC particles in the composite [68].

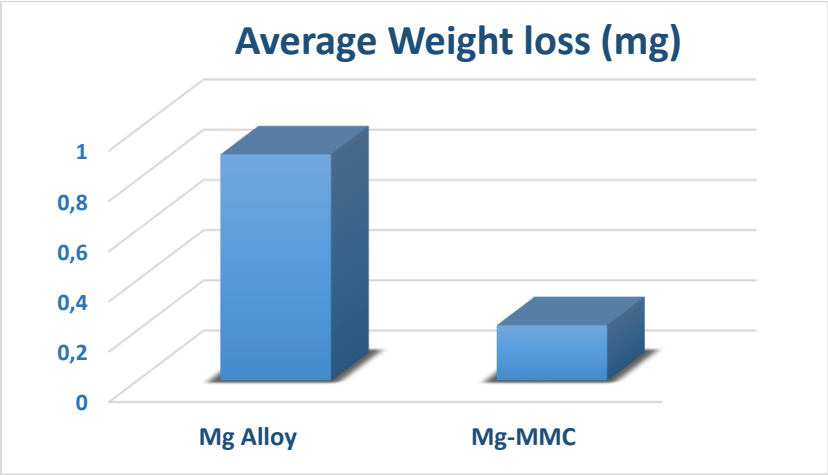

Fig. 8. Material loss determines the COF of Mg alloy and Mg-MMC [64]

The spark plasma sintering techniques were adopted to fabricate Mg-Ni composite. The wear resistance was low because of the softness present in the Mg-alloy. The enhancement in the wear resistance has been noticed just by adding 1.5 wt.% of Ni micro-sized particles in the Mg-alloy [69]. The study shows the improvement of wear resistance and COF at 3 wt. % of Sic particles present in Mg alloy-xSiC (x= 1, 3, and 5 wt. %) composite. The wear loss of 0.0174 g and 0.90 COF was noticed in Mg-MMCs and 0.0218 g (wear loss) and 0.24 (COF) in Mg alloy as shown in Fig. 9. The enhancement of particle distribution and breaking of the intermetallic phase was the reason for improved friction and wear properties in the Mg-MMC [70]. The research work shows the 150% and 350% increment to wear resistance in the fabricated Mg-SiC_p (Nano and Micro) MMC as compared to Mg alloy. The COF values are 0.0248, 0.0242, and 0.0234 for Mg alloy, Mg micro-composite, and Mg nano-composite, respectively. Due to nano SiC particles present in Mg nano-composite, strong bonding and uniform dispersion are the reason for the COF's decrement and increment in wear resistance [71]. The adhesive and abrasive wear was analyzed in AZ91-B_4C (15 Vol. %) Mg-MMCs. The friction stir processing was used in the fabrication of Mg-MMC. The outcome showed the enhancement of abrasive and adhesive wear in AZ91-B_4C composite due to delamination and oxidation of the reinforcement. In Mg-MMC, wear and friction resistance of 60% and 40% (respectively) were observed compared to Mg alloy [72].

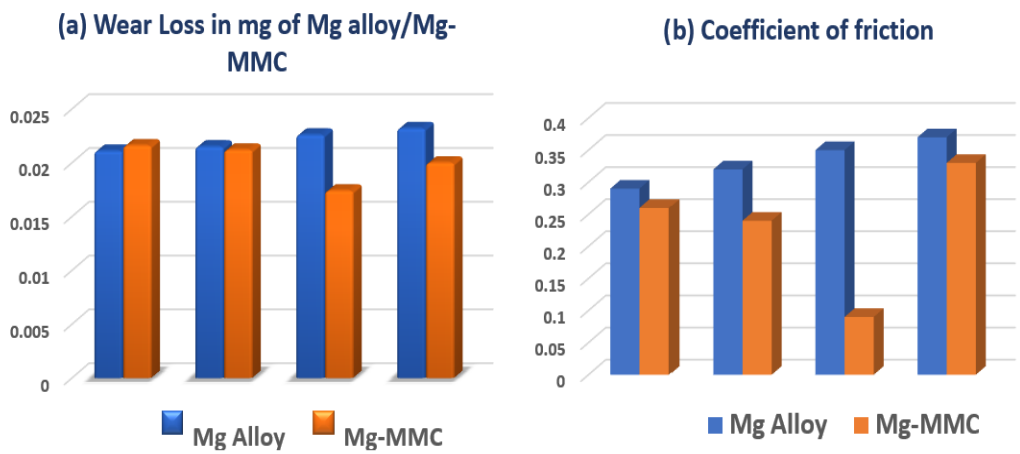

Fig. 9. Wear loss & COF of Mg alloy and Mg-MMCs [70]

The wear loss in RZ5-TiB_2 composite has gradually decreased due to the presence of TiB_2 reinforcement in Mg-MMCs. The strong bonding and wettability of TiB_2 particles

increased the wear resistance and decreased the friction coefficient in the fabricated composite. The wear loss and COF were noticed as 306.87 mg and 0.469 respectively for RZ5 alloy and 183.23 mg (wear loss) and 0.402 (COF) in the Mg-MMCs with 8 wt. % of TiB_2 reinforcement particles [73]. The Mg-xB_4C-xMoS_2 composite using the powder metallurgy method was fabricated. The reinforcements were taken as 0, 5, and 10 wt.% each. The best results for wear resistance have been achieved on B_4C-10 wt. % and MoS_2- 5 wt. %. The optimization of reinforcement stated that B_4C-10 wt. % contribute 78.06 % to the increment of wear resistance and decrement in COF in the Mg-MMC [74].

The common reasons for the reduction in surface characteristics are: oxidation, adhesion, abrasion, erosion, delamination, and ploughing formation on Mg-MMCs samples [72-75].

However, the effect of process parameters also affects the wear and friction of the fabricated MMC. The critical process parameters in measurements of friction and wear are; applied load, sliding velocity, sliding time, sliding distance, and reinforcement percentage. The effects of the parameters are discussed below:

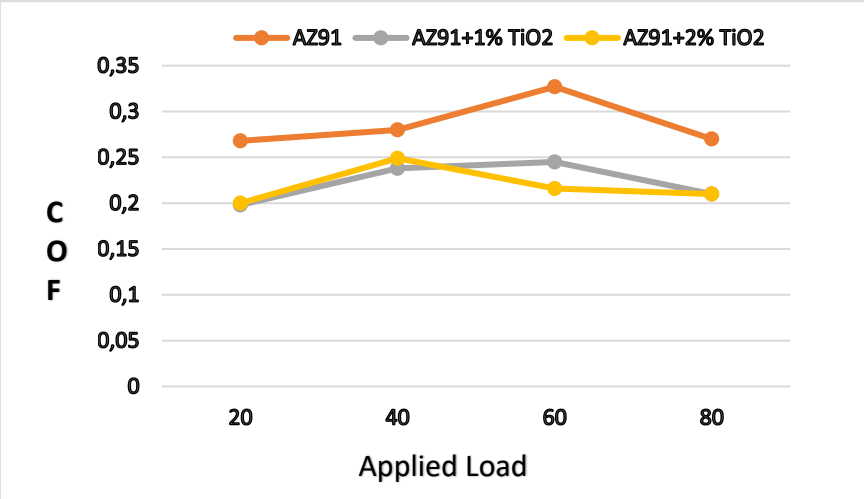

Fig. 10. COF with different applied loads [41]

Applied load effect on wear and friction. The friction and wear are predominantly dependent on the load applied during the testing of the composite. The outcomes indicate that the co-efficient of friction and wear resistance has increased as the average load was increased during analysis on the pin and disc wear test apparatus. The typical range for applied load is 10-80 N during COF and wear resistance measurement[51,76-80]. Figure 10 shows the COF of Mg-MMCs at different applied loads.

Sliding velocity effect on wear and friction. The friction and wear are also affected by sliding velocity during testing. The literature reported that sliding velocity could be in the range of 1-3 m/s and decrement in the wear rate happens by increments up to 3 m/s sliding velocities. On the other hand, the wear rate increases as we increase the sliding velocity beyond 3 m/s in the Mg-based composite [41,78,81-83].

Sliding time effect on wear and friction. The sliding time also affects the wear and friction in the composite material. As the sliding time increases, the material loss and higher friction also take place in the mg-based composite. The sliding time can be from 5 minutes to 30 minutes during the wear test of Mg-MMCs [39,65,84,85].

Sliding distance effect on wear and friction. The wear characteristic of the Mg-based composite had been analyzed. It was noticed that the increment in the sliding distance also increases the friction and wear in the composite as shown in Fig. 11. The sliding

distance was listed to be in the range of 100-2000 m and correspondingly increased the wear rate and COF [86-88].

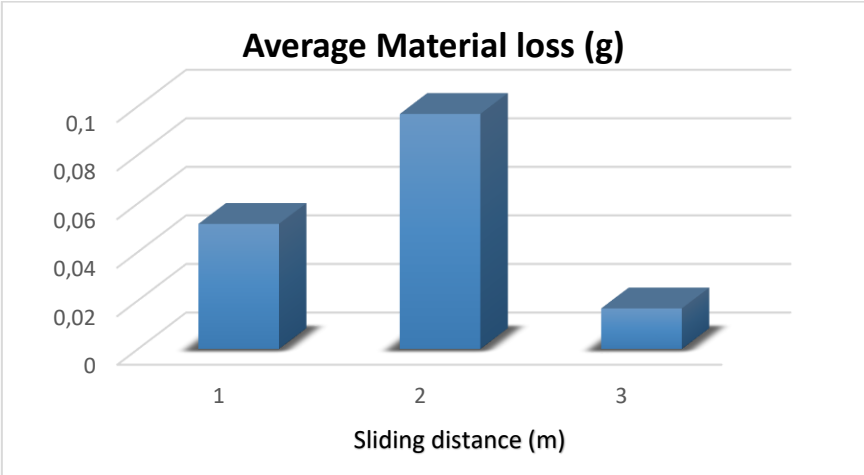

Fig. 11. Wear loss of Mg-MMC with sliding distance [89]

Reinforcement percentage effect on wear and friction. The weight percentage of the reinforcements affects the physical and mechanical properties of the composite. However, the reinforcement weight percentage also influences tribological properties like friction and wear. The decrement in the wear rate has been observed as the weight percentage of the reinforcement increases in the Mg-based composite. The excessive increment in the weight percentage of reinforcement leads to crack formation and deterioration, which causes wear and friction increment [89-91].

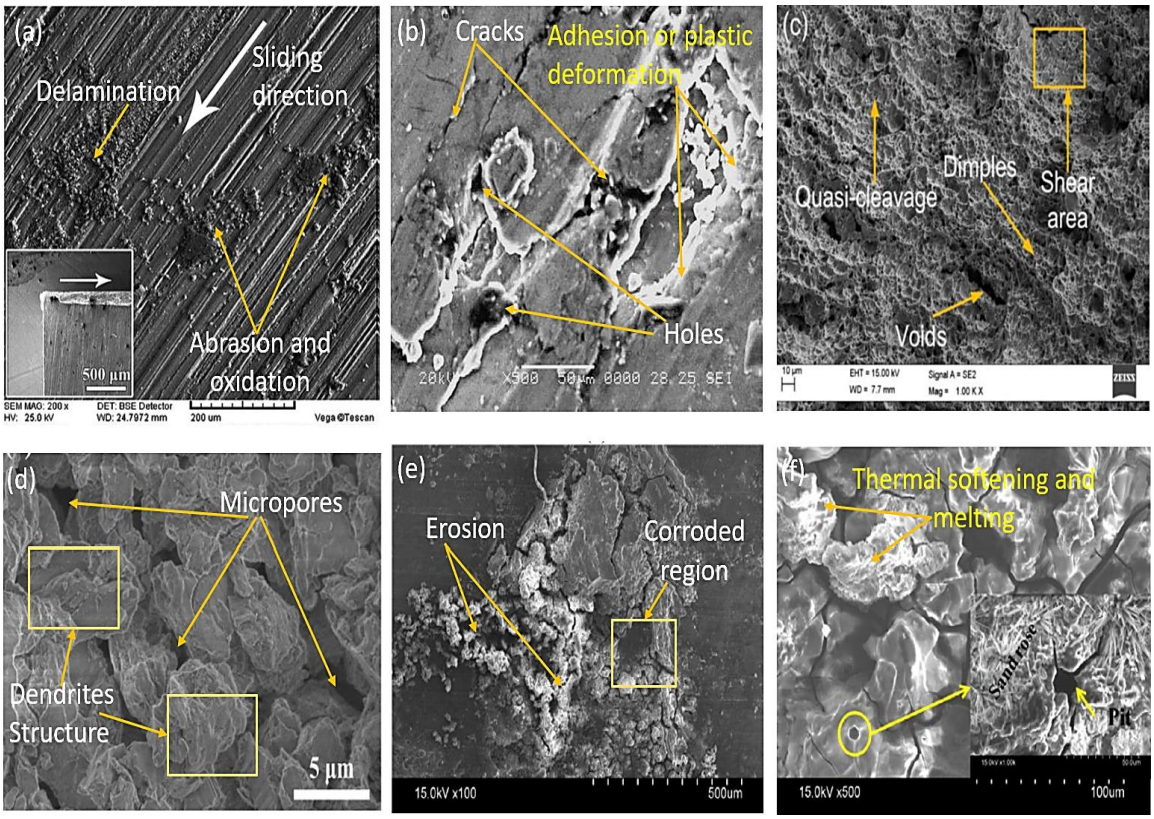

Fig. 12. SEM images represent the worn-out mechanisms for wear and corrosion

Mechanisms controlling the tribological behavior of Mg-MMCs. The current review article discusses the tribological behaviors of Mg-based composites. The degradation factors like delamination, oxidation, adhesion, abrasion, plastic deformation, erosion, cracks, and pit holes occurred during wear and corrosion examination. Figure 12 shows the graphical representation of degradation factors as reported in different research articles. Dey and Pandey observed the wear defects of AZ91 alloy reinforced with 2wt.% of Praseodymium as a rare earth element. The abrasion, oxidation and delamination were observed as primary wear mechanisms during the investigation as represented in Fig. 12 (a) [92].

Figure 12 (b) shows the plastic deformation, cracks, and holes during the dry sliding wear test of ZE41alloy as casted magnesium alloy [93]. The dimple, voids, and shear zone as major wear mechanisms were reported by Gupta and Wong in magnesium nano-reinforced composites as mentioned in Fig. 12 (c) [94]. Jiang et al. prepared a composite of AZ91D/ZnO to observe the corrosion behavior under NAOH solution. The microstructure behavior after the salt spray test was shown in Fig. 12 (d). The micropores and dendritic structure were the main corrosion mechanism observed during the investigation of Mg-MMCs surface [95]. The erosion, thermal softening, and melting of Mg-MMCs surface were shown as the mechanism in Fig. 12 (e) and 12 (f), respectively [96][97].

However, these degradation factors can be controlled by implementing the following suggestion in various studies. Moharana and Senapati suggested introducing a lubricant film and separating the mating surfaces in the study [98]. The wear defects can also be controlled with the help of heat treatment and making the wear surface hard. Various processes such as ion implantation, vapor deposition, hard chromium plating, and diffusion heat-treatment are developed for hard-facing surfaces [99-101].

The wear surface should be made fracture resistant because fracture resistance plays a significant role in the wear resistance of the material. In many cases, the fracture was the reason for wear progress. Also, the use of ceramic and carbide, etc. reinforcement addition led to fracture problems and causes higher material loss in the magnesium matrix composite surface [67,70,102]. Flores et al. concluded that surface erosion led to corrosion in the Mg-MMCs [103]. The liquid erosion, slurry erosion, and cavitation damage the surface and result in corrosion on the surface of the Mg-MMCs [104]. So, it is necessary to make the surface of Mg-MMCs erosion-resistant.

Abhijit and Krishna reported delamination wear caused due to metal-to-metal interfacing of two materials during sliding [92]. This type of wear can be avoided by providing some plating and diffusion hardening between the interfacing surfaces of Mg-MMCs [105]. The wear surfaces should also be fatigue resistant. The surface fatigue also led to wear in rolling elements and power transmission devices, where repeated line and point contact is made [106]. This causes stress between the interfacing surfaces and causes pits and cracks on the Mg-MMCs surface. The use of flame induction casing, electron beam casing, and laser hardening of the Mg-MMCs prevents stress formation and enhances the fatigue resistance, and correspondingly, improves the wear resistance of the Mg-MMCs [39].

5. Conclusion

In this research paper, the effect of different reinforcements on mechanical and tribological properties are discussed, and based on the discussion following conclusion are drawn:

- Magnesium has wide applications in the automotive and bio-medical industries due to its low density and high in strength to weight ratio. In general terms of manufacturing, the Mg-MMCs are more flexible, reliable, economical, eco-friendly, and biodegradable materials.
- Stir casting, friction stir processing, and powder metallurgy are the common processes to fabricate these composites.

- The hardness and tensile strength of Mg-MMCs largely depend upon uniform dispersion and grain refinement of the reinforcement particles. The hardness and tensile strength for commonly used Mg-MMC's range from 34-152.7 HV and 45-240 MPa respectively.
- The corrosion resistance of Mg-MMCs can be enhanced with the proper homogenous distribution of reinforcement particles. The corrosion current density is directly proportional to corrosion resistance and it reduces in the range of 549.21-1.923 $\mu A\ cm^{-2}$ for different Mg-MMCs.
- In Mg-MMCs the amount of wear and friction depends upon its process parameters like; applied load (10-80 N), sliding distance (100-2000 m), sliding velocity (1-3 m/s), sliding time (5-30 minutes) and various weight/volume percentage reinforcement (0-25%). The material loss during wear measurement and coefficient of friction (COF) of Mg-MMCs ranges from 0.0174-0.09 g and 0.90-0.0234, respectively.

References

1. Singh S, Angra S. Experimental evaluation of hygrothermal degradation of stainless steel fibre metal laminate. *Eng Sci Technol an Int J.* 2018;21(1): 170-179.
2. Kumar A, Vichare O, Debnath K, Paswan M. Fabrication methods of metal matrix composites (MMCs). *Mater Today Proc*. 2020;46: 6840-6846.
3. Sahu V, Gayathri V. Strength Studies of Dadri Fly Ash Modified with Lime Sludge – A Composite Material. *Int J Eng Technol Innov.* 2014;4(3): 161-169.
4. Charan NRKS. Experimental Analysis on Three Body Abrasive Wear Behaviour of Stir Cast Al LM 25 / TiC Metal Matrix Composite. *Trans Indian Inst Met.* 2017;70(9): 2233-2240.
5. Shoba C, Ramanaiah N, Nageswara Rao D. Effect of reinforcement on the cutting forces while machining metal matrix composites–An experimental approach. *Eng Sci Technol an Int J.* 2015;18(4): 658-663.
6. Fatile OB, AkinruliI J fedayo, Amori AA. Microstructure and Mechanical Behaviour of Stir-Cast Al-Mg-Sl Alloy Matrix Hybrid Composite Reinforced with Corn Cob Ash and Silicon Carbide. *Int J Eng Technol Innov.* 2014;4(4): 251-259.
7. Sahu V, Srivastava A, Gayathri V. Effect of lime and gypsum on engineering properties of badarpur fly ash. *Int J Eng Technol Innov*. 2016;6(4): 294–304.
8. Kumar D, Angra S, Singh S. Mechanical Properties and Wear Behaviour of Stir Cast Aluminum Metal Matrix Composite: A Review. *Int J Eng Trans A Basics*. 2022;35(4): 794–801.
9. Ramanathan A, Krishnan PK, Muraliraja R. A review on the production of metal matrix composites through stir casting – Furnace design, properties, challenges, and research opportunities. *J Manuf Process*. 2019;42(May): 213–245.
10. Anand N, Senthil Kumaran S. Development and influence of tribomechanical properties on magnesium based hybrid metal matrix composites-a review. *Mater Res Express*. 2020;7(3): 036520.
11. Gope PC. Maximum tangential stress coupled with probabilistic aspect of fracture toughness of hybrid bio-composite. *Eng Sci Technol an Int J.* 2018;21(2): 201–214.
12. Sinmazçelik T, Avcu E, Özgür M, Çoban O. A review : Fibre metal laminates, background, bonding types and applied test methods. *Materials & Design.* 2011;32(7): 3671–85.
13. Tan J, Ramakrishna S. Applications of magnesium and its alloys: A review. *Appl. Sci.* 2021;11(15): 6861.
14. Srivastava A, Bhatnagar N. Production and characterisation of new bioresorbable radiopaque Mg–Zn–Y alloy to improve X-ray visibility of polymeric scaffolds. *J. Magnes.*

Alloy. 2021;10(6): 1694-1703.
15. Yang Y, Lu C, Peng S, Shen L, Wang D, Qi F, et al. Laser additive manufacturing of Mg-based composite with improved degradation behaviour. *Virtual Phys. Prototyp.* 2020;15(3):278–93.
16. Marakini V, Pai S, Bhat A, Bangera S. Surface integrity optimization in high speed milling of AZ91 magnesium alloy using TOPSIS considering vibration signals. *Mater. Today Proc.* 2022;52: 802–809.
17. Joseph EJ, Panneerselvam K. Manufacturing and Characterization of Tungsten Particulate-Reinforced AW106 Epoxy Resin Composites. *Trans Indian Inst Met.* 2021;74(4): 817–825.
18. Surya MS, Prasanthi G. Manufacturing, microstructural and mechanical characterization of powder metallurgy processed Al7075/SiC metal matrix composite. *Mater Today Proc*. 2021; 39: 1175-1179.
19. Rotella G, Candamano S. Fabrication and characterization of zeolite coatings on aluminum and magnesium alloys. *Eng. Sci Technol. an Int. J*. 2020;23(5): 1273–1278.
20. Rohatgi P. Cast aluminum-matrix composites for automotive applications. *JOM*. 1991;43(4): 10–15.
21. Tun KS, Gupta M. Effect of extrusion ratio on microstructure and mechanical properties of microwave-sintered magnesium and Mg/Y2O3 nanocomposite. *Journal of Materials Science.* 2008;43: 4503–4511.
22. Prasad DS, Shoba C, Varma KR. Damping behavior of commonly used reinforcement powders – An experimental approach. *Eng. Sci. Technol. an Int. J.* 2015;18(4): 674–679.
23. Dash D, Samanta S, Rai RN. Study on Fabrication of Magnesium based Metal Matrix Composites and its improvement in Mechanical and Tribological Properties- A Review. *IOP Conf. Ser.: Mater. Sci. Eng*. 2018;377: 012133.
24. Hossain S, Rahman M, Chawla D, Kumar A, Prakash P, Gupta P, Kumar D, Agrawal R, Jamwal A. Materials Today : Proceedings Fabrication , microstructural and mechanical behavior of Al-Al2O3-SiC hybrid metal matrix composites. *Mater. Today Proc*. 2020;21: 3–6.
25. Alaneme KK, Bodunrin MO, Casting S. Mechanical behaviour of alumina reinforced AA 6063 metal matrix composites developed by two step-stir casting process. *Acta Technica Corviniensis – Bulletin of Engineering.* 2013;6: 105-110.
26. Meher A, Mahapatra MM, Samal P, Vundavilli PR. Study on effect of TiB2 reinforcement on the microstructural and mechanical properties of magnesium RZ5 alloy based metal matrix composites. *J. Magnes. Alloy.* 2020;8(3): 780–792.
27. Kumar NS, Sozhamannan GG. Investigating the effect of mechanical properties of magnesium alloy (AZ91D) reinforced with graphene metal matrix composite by stir casting method [preprint]. To be piblished in *Mater Today Proc*. 2022.
28. Arab MS, El Mahallawy N, Shehata F, Agwa MA. Refining SiCp in reinforced Al-SiC composites using equal-channel angular pressing. *Mater Des.* 2014;64: 280–286.
29. Singh GR, Singh SCE, Sivapragash M, Anselm L, Kumar RS, Lenin AH. Tensile and compression behaviour, microstructural characterization on Mg-3Zn-3Sn-0.7Mn alloy reinforced with SiCp prepared through powder metallurgy method. *Mater. Res. Express*. 2020;7(10): 106512.
30. Ghasali E, Alizadeh M, Niazmand M, Ebadzadeh T. Fabrication of magnesium-boron carbide metal matrix composite by powder metallurgy route: Comparison between microwave and spark plasma sintering. *J. Alloys Compd*. 2017;697: 200-207.
31. Prakash P, Om S, Devendra P. Studies on the Effect of Processing Parameters on Microstructure and Properties of Magnesium Compacts Prepared via Powder Metallurgy. *Trans Indian Inst Met.* 2020;73(11): 2715–2726.

32. Alem SAA, Latifi R, Angizi S, Hassanaghaei F, Aghaahmadi M, Ghasali E, Rajabi M. Microwave sintering of ceramic reinforced metal matrix composites and their properties: a review. *Mater Manuf Process.* 2020;35(3): 303–327.
33. Gibson BT, Lammlein DH, Prater TJ, Longhurst WR, Cox CD, Ballun MC, Dharmaraj KJ, Cook GE, Strauss AM. Friction stir welding: Process, automation, and control. *J. Manuf. Process.* 2014;16(1): 56-73.
34. Awasthi S, Gupta P, Pachuri P, Tyagi M, Aniruddha. Optimization of magnesium ZK60A/SiC/B4C hybrid composite fabricated by friction stir processing. *Mater. Today Proc*. 2022;62: 191-197.
35. Du Z, Tan MJ, Guo JF, Bi G, Wei J. Fabrication of a new Al-Al2O3-CNTs composite using friction stir processing (FSP). *Mater. Sci Eng. A*. 2016;667: 125–131.
36. Dinaharan I, Zhang S, Chen G, Shi Q. Assessment of Ti-6Al-4V particles as a reinforcement for AZ31 magnesium alloy-based composites to boost ductility incorporated through friction stir processing. *J. Magnes. Alloy*. 2022;10(4): 979-992.
37. Deepan M, Pandey C, Saini N, Mahapatra MM, Mulik RS. Estimation of strength and wear properties of Mg/SiC nanocomposite fabricated through FSP route. *J. Brazilian Soc. Mech. Sci Eng.* 2017;39(11): 4613–4622.
38. Sharma S, Handa A, Singh SS, Verma D. Influence of tool rotation speeds on mechanical and morphological properties of friction stir processed nano hybrid composite of MWCNT-Graphene-AZ31 magnesium. *J. Magnes. Alloy*. 2019;7(3): 487–500.
39. Mehra D, Mahapatra MM, Harsha SP. Processing of RZ5-10wt%TiC in-situ magnesium matrix composite. *J. Magnes. Alloy*. 2018;6(1): 100–105.
40. Sundaraselvan S, Senthilkumar N, Tamizharasan T, Sait AN. Materials Today : Proceedings Surface modification of AZ61 Magnesium Alloy with Nano TiO2/Al2O3 using Laser Cladding Technique. *Mater. Today Proc*. 2020; 21: 717-721.
41. Jayabharathy S, Mathiazhagan P. Investigation of mechanical and wear behaviour of AZ91 magnesium matrix hybrid composite with TiO2/graphene. *Materials Today: Proceedings.* 2019;27: 2394–2397.
42. Vasu C, Durga KJAN, Srinivas I, Dariyavali S. ScienceDirect Developing composite of ZE41 magnesium alloy- calcium by friction stir processing for biodegradable implant applications. *Mater. Today Proc*. 2019;18: 270–277.
43. Ram B, Deepak D, Bala N. Microstructural Refinement and Enhancement in Mechanical Properties of Magnesium/SiC as-Cast Composites via Friction Stir Processing Route. Trans Indian Inst Met. 2019;72: 1313–1321.
44. Karthick E, Mathai J, J MT, Marikkannan SK. Processing, Microstructure and Mechanical Properties of Al2O3 and SiC Reinforced Magnesium Metal Matrix Hybrid Composites. *Mater Today Proc.* 2017;4(6): 6750–6756.
45. Bala N. Evaluation Of Microstructural And Mechanical Behavior Of Some Magnesium Metal Matrix Composites. *Int. J. Adv. Mater. Manuf. Charact.* 2017;7(2): 38–43.
46. Seetharaman S, Subramanian J, Tun KS, Hamouda AS, Gupta M. Synthesis and Characterization of Nano Boron Nitride Reinforced Magnesium Composites Produced by the Microwave Sintering Method. *Materials.* 2013;6(5): 1940-1955.
47. Yang WZ, Huang WM, Wang ZF, Shang FJ, Huang W, Zhang BY. Thermal and mechanical properties of graphene-titanium composites synthesized by microwave sintering. *Acta Metall Sin English Lett*. 2016;29(8): 707–713.
48. Sundaraselvan S, Senthilkumar N, Tamizharasan T, Naveen Sait A. Surface modification of AZ61 Magnesium Alloy with Nano TiO2/Al2O3 using Laser Cladding Technique. *Mater Today Proc*. 2020;21: 717–721.
49. Gangil N, Nagar H, Kumar R, Singh D. Shape memory alloy reinforced magnesium matrix composite fabricated via friction stir processing. *Mater Today Proc*. 2020;33: 378–

381.
50. Satish J, Satish KG. Preparation of magnesium metal matrix composites by powder metallurgy process. *IOP Conf. Ser. Mater. Sci Eng*. 2018;310(1): 012130.
51. Vaira Vignesh R, Padmanaban R, Govindaraju M, Suganya Priyadharshini G. Investigations on the corrosion behaviour and biocompatibility of magnesium alloy surface composites AZ91D-ZrO2 fabricated by friction stir processing. *Trans Inst Met Finish.* 2019;97(5): 261–270.
52. Fatile BO, Adewuyi BO, Owoyemi HT. Synthesis and characterization of ZA-27 alloy matrix composites reinforced with zinc oxide nanoparticles. *Eng Sci Technol an Int J.* 2017;20(3): 1147–1154.
53. Wong WLE, Karthik S, Gupta M. Development of hybrid Mg/Al2O3 composites with improved properties using microwave assisted rapid sintering route. *Journal of Materials Science*. 2005;40: 3395–3402.
54. Wong WLE. Development of High Performance Mg/SiC Composites Containing Nano-Size SiC Using Microwave Assisted Rapid Sintering. In: *Proc. ASME 2005 International Mechanical Engineering Congress and Exposition*. ASME; 2016. pp.511-515.
55. Wong WLE, Gupta M. Development of high performance Mg/SiC composites containing nano-size SiC using microwave assisted rapid sintering. *Am. Soc. Mech. Eng. Aerosp. Div. AD*. 2005;70AD: 511–515.
56. Hassan SF, Nasirudeen OO, Al-Aqeeli N, Saheb N, Patel F, Baig MMA. Processing, microstructure and mechanical properties of a TiO2 nanoparticles reinforced magnesium for biocompatible application. Metall Res Technol. 2017;114(2): 1-8.
57. Hassan SF, Tun KS, Patel F, Gupta M. Effect of Copper Nano Particles on High Temperature Tensile Behavior. *Metals and Materials International.* 2015;21(3): 588–592.
58. Thakur SK, Kwee GT, Gupta M. Development and characterization of magnesium composites containing nano-sized silicon carbide and carbon nanotubes as hybrid reinforcements. *J. Mater. Sci*. 2007;42: 10040–10046.
60. Pradeep Raja C, Ramesh T. Influence of size effects and its key issues during microforming and its associated processes – A review. *Eng. Sci. Technol. an Int. J.* 2021;24(2): 556–570.
61. Nunes PCR, Ramanathan L V. Corrosion behavior of alumina-aluminum and silicon carbide-aluminum metal-matrix composites. *Corrosion*. 1995;51(8): 610–617.
62. Liu B, Wang H, Zhang Y, Yang Y, Ren X. Journal of Physics and Chemistry of Solids The influence of adding samarium on the microstructure , mechanical performance and corrosion behavior of as-extruded AZ41 alloys. *J. Phys. Chem. Solids.* 2021;150: 109851.
63. Liu L, Yu S, Zhu G, Li Q, Liu E, Xiong W, Wang B, Yang X. Corrosion and wear resistance of micro-arc oxidation coating on glass microsphere reinforced Mg alloy composite. *J. Mater Sci*. 2021;56(27): 15379–15396.
64. Lei T, Tang W, Cai SH, Feng FF, Li NF. On the corrosion behaviour of newly developed biodegradable Mg-based metal matrix composites produced by in situ reaction. *Corros Sci.* 2012;54(1): 270–277.
65. Khatkar SK, Verma R, Kharb SS, Thakur A, Sharma R. Optimization and Effect of Reinforcements on the Sliding Wear Behavior of Self-Lubricating AZ91D-SiC-Gr Hybrid Composites. *Silicon*. 2021;13: 1461-1473.
66. Liu T, Rui S, Li S. Layer-by-layer self-assembly composite coatings for improved corrosion and wear resistance of mg alloy for biomedical applications. *Coatings*. 2021;11(5): 515.
67. Rahmani K, Majzoobi GH, Ebrahim-Zadeh G, Kashfi M. Comprehensive study on quasi-static and dynamic mechanical properties and wear behavior of Mg—B4C composite compacted at several loading rates through powder metallurgy. 2021;31(2): 371-381.

68. Moustaf EB, Khalil AM, Ahmed HM, Hefni M, Mosleh AO. Microstructure, Hardness, and Wear Behavior Investigation of the Surface Nanocomposite Metal Matrix Reinforced by Silicon Carbide and Alumina Nanoparticles. *J. Miner. Met. Mater. Eng.* 2021;7: 57–62.
69. Olalekan ON, Abdul Samad M, Hassan SF, Elhady MMI. Tribological evaluations of spark plasma sintered Mg–Ni composite. *Tribol - Mater Surfaces Interfaces*. 2022;16(2): 110-118.
70. Ra'ayatpour M, Emamy M, Rassizadehghani J. Influence of Hot Extrusion on the Microstructure, Tensile and Wear Properties of Mg–5Sb–xSiC Hybrid Composites. *Metals and Materials International*. 2022;28: 679–694.
71. Sadooghi A, Rahmani K. Experimental study on mechanical and tribology behaviors of Mg-SiC nano / micro composite produced by friction stir process. *Journal of Mechanical Science and Technology*. 2021;35: 1121–1127.
72. Patle H, Ratna Sunil B, Anand Kumar S, Dumpala R. Effects of inert gas environment on the sliding wear behavior of AZ91/B4C surface composites. Proc Inst Mech Eng Part J J Eng Tribol. 2022;236(9): 1880-1888.
73. Meher A, Mahapatra MM, Samal P, Vundavilli PR. Abrasive Wear Behaviour of TiB2 Reinforced In-Situ Synthesized Magnesium RZ5 Alloy based Metal Matrix Composites. *Met Mater Int.* 2021;27(9): 3652–3665.
74. Kailasanathan C, Rajkumar PR, Rajini N, Sivakumar GD, Ramesh T, Ismail SO, et al. Characterization and optimization of influence of MoS2 hybridization on tribological behaviours of Mg–B4C composites. *Bull Mater Sci*. 2021;44: 192.
75. Jojith R, Sam M, Radhika N. Recent advances in tribological behavior of functionally graded composites: A review. *Eng Sci Technol an Int J.* 2022;25: 100999.
76. Sharma VK, Kumar V, Joshi RS. Experimental investigation on effect of RE oxides addition on tribological and mechanical properties of Al-6063 based hybrid composites. *Mater Res Express*. 2019;6(8): 0865d7.
77. Aktar Zahid Sohag M, Gupta P, Kondal N, Kumar D, Singh N, Jamwal A. Effect of ceramic reinforcement on the microstructural, mechanical and tribological behavior of Al-Cu alloy metal matrix composite. *Mater Today Proc.* 2020;21:1407–1411.
78. Nirala A, Soren S, Kumar N, Garg R, Kumar Sharma S, Shrivastava AK. Comprehensive study of magnesium based metal matrix composite. *Mater Today Proc*. 2020;46: 6587–6591.
79. Królczyk G, Feldshtein E, Dyachkova L, Michalski M, Baranowski T, Chudy R. On the microstructure, strength, fracture, and tribological properties of iron-based MMCs with addition of mixed carbide nanoparticulates. Materials. 2020;13(13): 2892.
80. Kumaar RK, Vinoth KS, Kavitha M. Dry sliding wear performance of AA7075/MoS2 composite materials. *J. Eng. Res*. 2021;9: 1–24.
81. Srinivas V, Jayaraj A, Venkataramana VSN, Avinash T, Dhanyakanth P. Effect of Ultrasonic Stir Casting Technique on Mechanical and Tribological Properties of Aluminium–Multi-walled Carbon Nanotube Nanocomposites. *J. Bio- Tribo-Corrosion*. 2020;6(2): 1–10.
82. Alaneme KK, Adewale TM, Olubambi PA. Corrosion and wear behaviour of Al-Mg-Si alloy matrix hybrid composites reinforced with rice husk ash and silicon carbide. *J. Mater. Res. Technol.* 2014;3(1): 9–16.
83. Danappa GT, Raghavendra CR, Swamy RP, Naik K. Dry sliding wear behaviour of Al7075/Gr/nano TiO2MMC using RSM. *Mater Today Proc.* 2020;38: 2797-2802.
84. Kumar P, Skotnicova K, Mallick A, Gupta M, Cegan T, Jurica J. Mechanical characterization of graphene nanoplateletsreinforced mg-3sn alloy synthesized by powder metallurgy. *Metals.* 2021;11(1): 1–14.
85. Natarajan N, Vijayarangan S, Rajendran I. Wear behaviour of A356/25SiCp

aluminium matrix composites sliding against automobile friction material. *Wear*. 2006;261(7–8): 812–822.
86. Kailasanathan C, Rajkumar PR, Rajini N, Sivakumar GD, Ramesh T. Characterization and optimization of influence of MoS 2 hybridization on tribological behaviours of Mg – B 4 C composites. *Bull Mater Sci.* 2021;44; 192.
87. Arunbharathi R, Rathish R, Vignesh RS, Seelan PS, Prasanth RV. Mechanical and Tribological Characteristics of Particulates Embedded Aluminium Based Composites - A Review. *PAIDEUMA JOURNAL.* 2021;XIV(3): 12–16.
88. Radhika N, Reghunath R, Sam M. Improvement of mechanical and tribological properties of centrifugally cast functionally graded copper for bearing applications. *Proceedings of the Institution of Mechanical Engineers, Part C: Journal of Mechanical Engineering Science*. 2019;233(9): 3208–3219.
89. Manu KMS, Sreeraj K, Rajan TPD, Shereema RM, Pai BC, Arun B. Structure and properties of modi fi ed compocast microsilica reinforced aluminum matrix composite. *JMADE.* 2015;88: 294–301.
90. Tang W, Kang S, Liu Z. Dynamic Compression Deformation and Constitutive Model of Extruded Mg–1Zn–2Y Bar. *Trans Indian Inst Met.* 2021;74(12): 2967–2975.
91. Mao G, Liu S, Gao W, Wang J, Liu D. Effect of Zn or Zn + Cu Addition on the Precipitation in Al–Mg–Si Alloys: A Review. *Trans Indian Inst Met.* 2021;74(12): 2925–2938.
92. Dey A, Pandey KM. Wear behaviour of Mg alloys and their composites-a review. *Int J Mater Res.* 2018;109(11): 1050–1070.
93. Anbu selvan S, Ramanathan S. Dry sliding wear behavior of as-cast ZE41A magnesium alloy. *Mater Des*. 2010;31(4): 1930–1936.
94. Gupta M, Wong WLE. Magnesium-based nanocomposites: Lightweight materials of the future. *Mater Charact.* 2015;105: 30–46.
95. Jiang S, Li W, Liu J, Jiang J, Zhang Z, Shang W, et al. ZnO@ZIF-8 core-shell structure nanorods superhydrophobic coating on magnesium alloy with corrosion resistance and self-cleaning [preprint]. To be published in: *J Magnes Alloy*. 2022.
96. Banerjee S, Poria S, Sutradhar G, Sahoo P. Corrosion behavior of AZ31-WC nano-composites. *J Magnes Alloy*. 2019;7(4): 681–695.
97. Johari NA, Alias J, Zanurin A, Mohamed NS, Alang NA, Zain MZM. Anti-corrosive coatings of magnesium: A review. *Mater Today Proc*. 2021;48: 1842–1848.
98. Moharana GB, Senapati AK. Tribological analysis of Al-Si alloy based MMCs at elevated temperature. *Mater Today Proc.* 2021;49: 1749–1755.
99. Ozerov MS, Klimova MV, Stepanov ND, Zherebtsov SV. Microstructure evolution of a Ti/TiB metal-matrix composite during high-temperature deformation. *Materials Physics and Mechanics.* 2018;38(1): 54–63.
100. Behnamian Y, Serate D, Aghaie E, Zahiri R, Tolentino Z, Niazi H. Tribology International Tribological behavior of ZK60 magnesium matrix composite reinforced by hybrid MWCNTs / B 4 C prepared by stir casting method. *Tribol Int.* 2022;165:107299.
101. Mansoor P, Dasharath SM. A review paper on magnesium alloy fabricated by severe plastic deformation technology and its effects over microstructural and mechanical properties. *Mater Today Proc.* 2021;45: 356–364.
102. Yousefpour F, Jamaati R, Aval HJ. Investigation of microstructure, crystallographic texture, and mechanical behavior of magnesium-based nanocomposite fabricated via multi-pass FSP for biomedical applications. *J Mech Behav Biomed Mater*. 2022;125: 104894.
103. Flores JF, Neville A, Kapur N, Gnanavelu A. Corrosion and erosion-corrosion processes of metal-matrix composites in slurry conditions. *J Mater Eng Perform*. 2012;21(3): 395–405.

104. Irfan OM, Alaboodİ AS. On the compression properties and erosion- corrosion behavior of Al 6061/15% Sic p composite On the Compression Properties and Erosion-Corrosion Behaviour of Al 6061 / 15 % Sic p Composite. *Journal of Polytechnic ,* 2020; 23 (2): 415-425
105. Althahban S, Jazaa Y, Bafakeeh O, Alomari AS, Sallam HEDM, Atta M. The Effect of Reinforcement Preheating Temperatures on Tribological Behavior of Advanced Quranic Metal-Matrix Composites (QMMC). *Materials.* 2022:15(2): 659.
106. Dobkowska A, Cie BA, Koralnik M, Chromi W. Corrosion behavior of fine-grained Mg-7.5Li-3Al-1Zn fabricated by extrusion with a forward-backward rotating die (KoBo). *Journal of Magnesium and Alloys.* 2022;10(3): 811–820.

THE AUTHORS

Kumar Dinesh
e-mail: dinesh_61900120@nitkkr.ac.in
ORCID: 0000-0003-1885-2431

Singh Satnam
e-mail: satnamsingh@nitkkr.ac.in

Angra Surjit
e-mail: surjit.angra@yahoo.com

Materials Physics and Mechanics. 2022;50(3): 459-474
Research article
http://dx.doi.org/10.18149/MPM.5032022_9

Submitted: October 15, 2021
Approved: August 17, 2022
Accepted: November 16, 2022

Corrosion cracking of low alloy steels. Testing methods

A.A. Alhimenko, A.D. Breki. N.O. Shaposhnikov, A.A. Kharkov, E.L. Alekseeva, A.A. Lapechenkov✉

Peter the Great St. Petersburg Polytechnic University, Polytechnicheskaya 29, St. Petersburg, 195251, Russia

✉ andreylapechenkov@gmail.com

Abstract. The paper presents a brief overview of modern literature describing the mechanisms behind stress corrosion cracking of low-alloy steels in aqueous environments saturated with aggressive gases, such as hydrogen sulfide, and carbon dioxide, where atomic hydrogen is produced due to electrochemical reactions, subsequently penetrating the metal in the locations where it is dissolved or other surface defects are present. We described the main testing methods for stress corrosion cracking, their differences, and the criteria for assessing the corrosion cracking tendency of steels. Examples were given for applying metallographic and electrochemical analysis to explore the mechanism of stress corrosion cracking in the given steels.
Keywords: low-alloy steels, stress corrosion cracking, testing methods, crack initiation, crack growth, anodic dissolution, hydrogen embrittlement

Acknowledgements. *The research is partially funded by the Ministry of Science and Higher Education of the Russian Federation as part of World-class Research Center program: Advanced Digital Technologies (contract No. 075-15-2020-934 dated 17.11.2020), the research was carried out at the expense of a grant from the Russian Science Foundation № 22-19-00178,* https://rscf.ru/en/project/22-19-00178/».

Citation: Alhimenko AA, Breki AD, Shaposhnikov NO, Kharkov AA, Alekseeva EL, Lapechenkov AA. Corrosion cracking of low alloy steels. Testing methods. *Materials Physics and Mechanics*. 2022;50(3): 459-474. DOI: 10.18149/MPM.5032022_9.

1. Introduction

Low-alloy steels are currently the most widespread engineering materials, commonly used in diverse industries in load-bearing structures, machinery, and different components. These materials are popular because they are weldable and allow fabricating workpieces with a efficient producibility. Also these steels with a wide range of strength and plastic properties can be obtained through thermal/thermomechanical treatment with a small concentration alloying elements used. Moreover, producing forgings, rolled and profiled sheets, or pipes from such steels costs substantially less than similar products made of high-alloy steels and alloys based on aluminum, nickel, or titanium.

However, aside from these benefits, low-alloy steels also have certain limitations due to their low corrosion resistance in a wide range of highly aggressive production environments. These include aqueous environments, such as seawater, humid environments, different salt solutions, acid solutions with low pH, and solutions saturated with corrosive gases, such as hydrogen sulfide, carbon dioxide, and sulfur dioxide, especially at high temperatures and pressures [1-25]. Protective paint or polymer coatings, corrosion inhibitors, and cathodic or

© A.A. Alhimenko, A.D. Breki. N.O. Shaposhnikov, A.A. Kharkov, E.L. Alekseeva, A.A. Lapechenkov, 2022.
Publisher: Peter the Great St. Petersburg Polytechnic University
This is an open access article under the CC BY-NC 4.0 license (https://creativecommons.org/li-censes/by-nc/4.0/)

sacrificial electrochemical protection are typically used to prevent corrosion in workpieces made of low-alloy steels or reduce it to acceptable levels [1,4,5,11,14,26-37].

Stress corrosion cracking (SCC) is one the most dangerous types of corrosive degradation, as it can lead not only to the failure of operating equipment but also to the collapse of structures or spills of transported products, polluting the surrounding areas with environmental consequences. SCC-induced damages account for 30% of all corrosion damage [39-47].

SCC is a type of local corrosive destruction of materials, evolving under simultaneous exposure to the corrosive environment and applied tensile stresses. The tendency towards SCC depends on the external conditions just as much as on both the chemical composition and the structural state of low-alloy steels.

The requirements imposed on chemical composition are primarily aimed at limiting harmful impurities as sulfur and phosphorus. Their content does not generally exceed 0.015% and 0.025%, respectively, in modern engineering low-alloy steels. Carbon concentration is limited to 0.3% to ensure weldability. Steels are alloyed with nickel, chromium, or sometimes copper to improve the technological properties; molybdenum, vanadium, niobium, and titanium are introduced in small quantities (no higher than 0.1%) to increase material strength. Depending on chemical composition and thermal or thermomechanical treatment, low-alloy steels can have structures ranging from ferrite-pearlite to martensite, providing different strengths in low-alloy steels (yield strength $\sigma_{0.2}$ can vary from 200 MPa to 1000 MPa and more).

Numerous studies have established that the strength of steel has the predominant effect on SCC sensitivity. Steels with higher strengths are more susceptible to SCC [34,41-44,48-52].

Depending on strength, low-alloy steels can be subjected to stress corrosion cracking in chloride solutions at room and elevated temperatures, including in seawater, in other salt and acid aqueous solutions with pH < 4, in hot alkalis, in solutions, saturated by hydrogen sulfide or carbon dioxide [43,46,53].

This paper briefly examines the key notions concerning the potential SCC mechanisms in low-alloy steels exposed to corrosive environments, primarily related to the production and transportation of oil and gas. We also described the most frequently used methods aimed at determining the SCC tendency in steel and understanding the processes behind this phenomenon.

2. Mechanism of stress corrosion cracking in low-alloy steels

Generally, SCC is a process of delayed fracture, that is, corrosion cracks originate and propagate in the metal volume until the acting stresses ahead of the crack front exceed the strength of the steel [39, 54]. Different theories have been proposed to explain the combined effect of stresses and the corrosive environment on the evolution of SCC in low-alloy steels.

One of the necessary conditions for SCC to occur is the main electrochemical reactions: anodic dissolution of the metal (AD) and cathodic reduction of the oxidant. The product extracted in oil and gas production contains, aside from hydrocarbons, a mineralized aqueous phase with dissolved carbon dioxide and, in many cases, hydrogen sulfide. Chlorides, sulfates of sodium, calcium, and other salts found in the aqueous phase make the solution highly electrically conductive, which contributes to the anodic dissolution of steel without any limitations [4]. It was established for the detected damaged sections of underground pipelines that corrosion cracks originate on the outer walls of pipes where protective coatings are destroyed when the metal comes into contact with groundwater containing carbonates and hydrocarbonates at pH 4-7. The rate of the anodic process depends on the degree of soil moisture [55-59].

The cathodic process associated with anodic dissolution is due to the reduction of oxidants on the metal surface in the external environment, for example, oxygen dissolved in groundwater, or hydrogen ions produced during the dissociation of carbon dioxide and hydrogen sulfide. CO_2 dissolved in water forms weak carbonic acid (H_2CO_3), which dissociates producing hydrogen, bicarbonate, and carbonate ions [3].

$$CO_2 + H_2O \leftrightarrow H_2CO_3, \quad (1)$$

$$H_2CO_3 \leftrightarrow H^+ + HCO_3^-, \quad (2)$$

$$HCO_3^- \leftrightarrow H^+ + CO_3^{2-}. \quad (3)$$

It follows from reactions (2) and (3) that hydrogen ions, directly participating in SCC of steels, act as the oxidant.

Molecular hydrogen sulfide in an aqueous solution also dissociates, producing H^+ and SH^- ions.

$$H_2S \rightarrow H^+ + SH^-. \quad (4)$$

The hydrogen ions formed through electrochemical reactions (2–4) on the metal surface are reduced to an atomic state by attaching electrons and partially combine into molecules. The rest of the hydrogen atoms are adsorbed on the surface, penetrating into the metal by means of diffusion. Sulfide ions SH^- in hydrogen sulfide solution prevent hydrogen atoms from combining into molecules; as a result, a significant part of atomic hydrogen penetrates into the volume of the metal. Cathodic polarization at potentials when reduction of hydrogen ions becomes possible can be a source of hydrogen [60-61].

The entire SCC process is generally divided into three stages: crack initiation, crack propagation under the influence of a corrosive environment, and mechanical failure as the acting stresses exceed the material strength [39,54].

The current consensus is that SCC in carbon and low-alloy steels begins with the anodic dissolution of the metal in the locations where various microinhomogeneities exist on the surface, with centers of non-uniform corrosion appearing, accompanied by simultaneous diffusion of hydrogen into the steel. Such corrosion centers serve as small stress raisers in loaded structures. Microcracks near the surface opened due to corrosion, can act as these raisers. If the level of local stresses at the tip of some defect exceeds the yield stress of steel, plastic flow initiates at a very slow rate, leading to further accumulation of atomic hydrogen. As a certain critical hydrogen concentration is reached due to hydrogen embrittlement (HE), crack jumping occurs by the distance of the embrittled zone. As a result, the metal surface at the top of the propagating crack and its opening edges at this moment is absolutely clean (fresh) from any corrosion products, rendering it highly corrosive [49].

It is assumed that the first stage of SCC ends at this point, and the cracking process moves into the second stage, when, after hydrogen is stored and supplied to the tip of the crack formed, local plastic deformation accumulates and brittle crack jumping occurs. Notably, both stages are always accompanied by electrochemical dissolution of the metal near the tip of the growing crack. An exception to this is SCC at high cathodic polarization when the process of metal dissolution becomes thermodynamically impossible. It is evident that the growth of a corrosion crack is a quasi-brittle process since the crack propagates abruptly.

The solution inside the growing crack is constantly acidified due to hydrolysis of corrosion products with hydrogen ions forming. In the case of intergranular corrosion cracking [62-64], the crack propagates deep into the metal at the stage of anodic dissolution, along the most active spots, which are typically grain boundaries. In the case of transgranular crack propagation in a neutral corrosive environment with a low concentration of hydrogen ions, the stage of surface dissolution at the crack tip may prevail over the stage of hydrogen embrittlement, which should lead to blunting of the crack tip. This weakens the effect of the crack as a stress raiser on the microplastic flow intensity and can completely stop the crack's further growth.

The third final stage of SCC begins when the size of the crack is large enough for the stresses to exceed the strength of the steel in the remaining section of the loaded structure, resulting in mechanical failure.

3. Methods for studying SCC in low-alloy steels

At least three factors are necessary for SCC to develop: a specific corrosive environment, the action of specific tensile stresses, and metallurgical factors (specific chemical composition and structure formed, ensuring the necessary mechanical properties). Consequently, corrosion cracking tests should involve stressed specimens contacting the corrosive environment. The main requirement is that the given testing method does not reject the materials that are resistant to corrosion in real operating conditions, and, conversely, the tests do not allow materials susceptible to SCC in practice. All methods applied can be divided into several groups depending on the approach to generating the stressed state: constant loading tests; constant strain tests; tests with step loading and constant strain rate [65].

Tests under constant tensile loading. Axial loading of specimens allows to accurately estimate tensile stresses if the specimen has a constant cross-section in the working area, that is, does not have a notch or other stress raiser. Tensile stress is then calculated by a simple formula:

$$=\sigma =\frac{R}{S}, \quad (5)$$

where R is the applied load, and S is the area of the cross-section tested in the specimen.

The general goal of SCC tests with a constant tensile load or constant strain rate is finding the threshold stresses for which the specimen is not destroyed during the given testing period. This period is typically chosen to be at least 720 (NACE TM0177 standard) [66] or 1000 (GOST 9.903) hours [67], but sometimes it is extended to several thousand hours. In the first case, it is exactly 30 days of tests or a calendar month, so counting time is convenient. Besides, a period of 720 hours or its multiple is recommended by standards for all types of corrosion tests. Choosing a 1000-hour period is more convenient for constructing a graphical dependence of time to failure on the applied stresses in logarithmic coordinates.

The threshold stresses are determined through a series of tests at different stresses, lowering the loading until the specimens remain intact and free of corrosion cracks at the last given load during the testing period of 720 hours. A curve representing the time to failure as a function of the applied stresses is plotted by the obtained data (see Fig. 1).

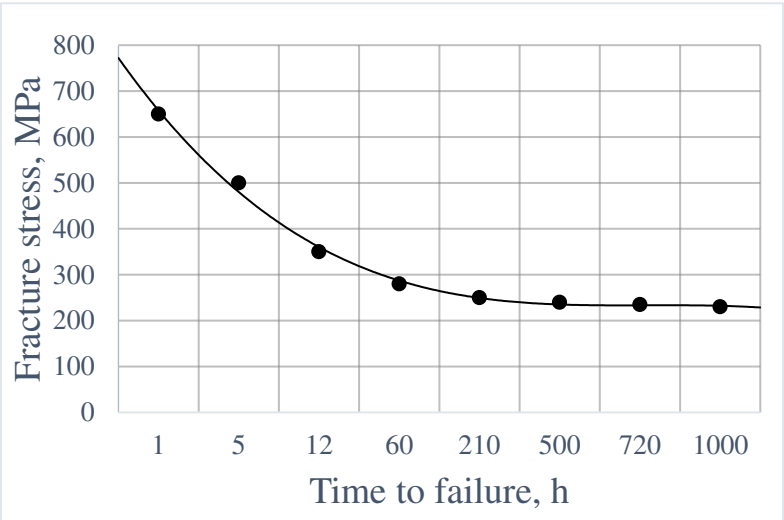

Fig. 1. Time to failure depending on applied tensile stress [66]

The dimensions of the section selected in the working area can also affect the specimen's time to failure. Tests with wire specimens or foils are not recommended, as general or pitting corrosion processes can cause such specimens to fracture before a stress corrosion crack can form.

Elastic devices shaped as rings or springs are the simplest for tests with constant loading. A loaded ring or spring generates tensile stresses in the specimens upon loading. To know the precise load applied, springs and rings are calibrated before the tests using a dynamometer, that is, the dependence of the load on the amount of their compression is plotted.

These devices are simple and convenient for use, but limited stresses can be set in the specimen because the relationship between the stress in the specimen and compressive strain in the ring or tensile strain in the spring is no longer linear at loads equal to or exceeding the yield stress. Therefore, it is impossible to use these devices to determine and maintain constant stress in the specimen if it exceeds the yield stress of the material. Since many metallic materials exhibit a tendency to SCC only at stresses above the yield, the loading machines required for the tests should be capable of setting and maintaining loads at any level, simultaneously recording the strain in the specimen with high accuracy.

The typical times to failure in SCC tests of smooth specimens in neutral aqueous environments, which are not usually highly corrosive, can amount to several thousand hours. Because the SCC mechanism in many steels and some alloys is associated with hydrogen transport to the maximum stress zone by mobile dislocation, SCC tests started to involve notched specimens. The maximum tensile stresses are always concentrated around the notch tip, i.e., the notch acts as a stress raiser. Notched specimens allowed shortening the test duration but it remained impossible to accurately determine the magnitude of the stress from the applied load. For this reason, several specimens are ruptured in air, and the fracture stress is measured in fractions of the fracture stress for air rather than in absolute units. The fracture stress is calculated as the ratio of the failure load to the cross-sectional area of the notched specimen. The stress calculated in this way is called *nominal* since this calculation is only valid for a smooth specimen.

In particular, notched specimens are convenient for finding the SCC resistance in different zones of a welded joint, when the notch is located either in the weld metal or in the heat-affected zone.

Constant strain rate tests. These tests are commonly performed for bending flat specimens since sheet metal products undergo bending deformation the most frequently. According to GOST 9.901.2-89, bending deformations are generated in flat beam specimens by two-, three- and four-point loading methods [68]. The specimens are tested at stresses below the elastic limit, arising under bending on their outer surface. Stresses are calculated by special formulas for each loading method, including the elastic modulus of the specimen material and the maximum deflection. C-shaped specimens are recommended by NACE TM0177 standard (Method C) for sulfide stress corrosion cracking tests in steels. It is especially convenient to use such specimens for tests at elevated temperatures and pressures, installing them into autoclaves in special vessels. The advantage of specimens stressed at a constant strain rate is that these specimens are loaded in the simplest fixtures and do not require machines for tensile strength testing. One of the most common drawbacks is significant to test length; furthermore, tests cannot be carried out at tensile stresses above the yield point.

Principles of fracture mechanics in SCC tests. These principles were first applied in the 1970s, as high-strength engineering materials gained wide popularity in metallurgy. The plastic properties are known to deteriorate with increasing strength. Such materials also have increased sensitivity to stress raisers, leading to brittle fracture. Finally, it was taken as an

axiom that metallurgical and technological defects always exist on the surface of products, especially in welded joints, acting as stress raisers sufficient for crack initiation and propagation even in the absence of a corrosive environment. Therefore, the durability of structures depends on the crack propagation rate.

The principles of linear fracture mechanics (LFM) were applied to determine the crack growth rate and the critical conditions under which the crack does not grow, i.e., the material becomes crack-resistant. Since the fastest crack propagation occurs under brittle fracture, it is the most dangerous, and therefore, the tests must be carried out under conditions when deformation under the action of tensile stresses can only occur in a plane perpendicular to the action of stresses. The initial specimen should be subjected to fatigue pre-cracking for this purpose. A small core of plastic deformation is formed at the tip of the fatigue crack under the action of the applied load in these conditions, generating a stress field. The measure of the stress field is the stress intensity factor K (SIF), related to the applied stress and the crack length by a certain dependence. Generally, $K = \sigma \cdot f(\sqrt{\ell})$, where l is the crack length, mm, σ is the tensile stress, MPa.

The LFM principles are implemented in practice by using specimens with sufficiently large cross-sections in order to satisfy the conditions for plane deformation. The obtained value of K in the air is called fracture toughness and is denoted by K_{1c}. The value of the intensity factor above which the crack begins to grow in tests in the corrosive environment is denoted as K_{Iscc}. Brown, Scully, Newman, Karpenko, Vasilenko, Marichev, and others made large contributions to developing the methods for testing the SCC resistance in steels and alloys using linear fracture mechanics [41, 43–45, 47, 68].

The main methods for SCC tests determining K_{1SCC} (K_{1KR}), outlined in GOST 9.903-81 [69], consist of the following steps.

According to the first method, tests are carried out with a constant K_{1SCC} (K_{1KR}), provided that $K_{1i} < K_{1C}$, in a corrosive environment for 1000 hours. If a specimen fails in a shorter time at a given value of K_{1i}, the test is carried out at lower K_{1i}, reducing the load to the value of K_{1i} at which the crack arrests and the specimen does not fail in 1000 hours. The obtained value of K_{1i} is taken as the threshold stress intensity factor K_{1SCC} (K_{1KR}).

According to method 2, the load on a fatigue-pre-cracked specimen placed in a corrosive environment is increased sequentially until the crack grows by more than 1 mm. The load is then gradually reduced until the crack arrests completely. $K_{1KR}$is calculated from the load at which the crack is arrested and its final length.

Cracked specimens are used in these methods for axial tensile tests, cantilever bending, and eccentric tension.

Method 3 consists in setting a fixed deformation and controlling the crack growth for a specimen exposed to a corrosive environment. As the crack propagates, the K_{1i} value decreases, and the crack growth rate slows down until the crack arrests completely. The resulting stress intensity factor is accepted as K_{1KR}.

Only eccentric tensile specimens are suitable for SCC tests by Method 3. A modified version of such specimens is shaped as a double cantilever beam, where the constant strain rate is generated with a wedge. Such specimens are recommended by the NACE TM0177 standard (Method D) for determining the resistance of steels to hydrogen sulfide cracking [66]. Figure 2 shows the threshold stress intensity factor depending on the yield stress for 1Cr-0.7Mo-type steel obtained from the results of sulfide stress corrosion cracking tests by Method D [70].

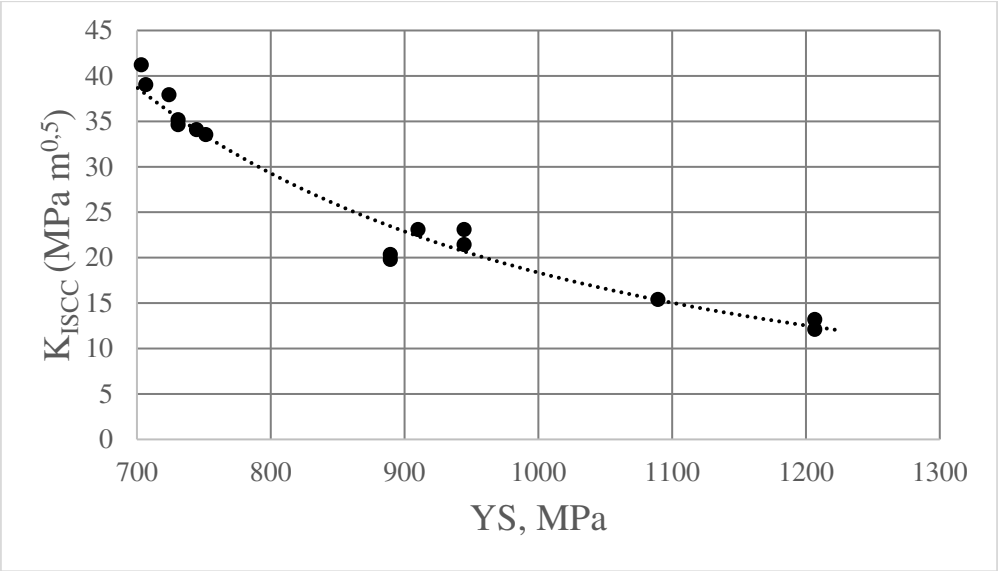

Fig. 2. Influence of yield stress in low-alloy steel on K_{ISCC} for tests of cracked specimens by Method D [70]

The conditions of LFM are virtually unattainable for assessing the fracture resistance in most modern low-alloy high-strength structural steels, as they are characterized by not only significant yield stresses but also increased ductility, which is the reason for a large plastic zone at the crack tip. Consequently, a model of quasi-viscous fracture underlying non-linear fracture mechanics (NLFM) is used. This model describes the values of the J-integral characterizing the work of plastic strain and fracture, as well as the stress and strain field under the elastoplastic deformation near the crack tip and the crack tip opening displacement ∂ (CTOD) [71-74]. The critical value of the J-integral is found by constructing the R-curve, which is the relationship between the value of the J-integral and the increment in depth (undergrowth) of the crack, Δa, characterizing the resistance of the material to slow stable crack growth under static loading. The critical value of ∂ (or *CTOD)* is found by constructing a ∂_R (the δ–Δa dependence). These are the so-called R-curves (*R* referring to rupture).

Force (SIF) and deformation (J-integral, CTOD) criteria are calculated by the formulas derived for each type of specimen and loading methods, described in GOST 25.506, GOST 9.903, ASTM E 1820, and other standards, as well as in specialized reference books [75-78].

The experience of SCC tests with cracked specimens has revealed the following key limitations of the method:

- it is difficult to manufacture specimens with a rather complex geometric shape, with exact dimensions of notches and side grooves, fatigue pre-cracking requires specialized equipment (resonant testing machines, vibrophores);
- LMR imposes stringent requirements on the dimensions of the specimens to produce plane deformation: consequently, the results obtained for metal products made of sufficiently ductile steels with low and medium strength may be inaccurate;
- it is necessary to determine the deformation criteria based on finding the undergrowth and CTOD; at the same time, it is difficult to visually measure the crack length in a corrosive environment, while CTOD sensors can be corroded and therefore malfunction quickly;
- complex testing machines have to operate for long periods (over a thousand hours) at high power during static loading tests;
- if the crack is branched or propagates along certain structural components of the metal (boundaries of sensitized grains, interphase boundaries, etc.), the methods of LMR may yield

incorrect results, because the clearly predominant SCC mechanism associated with anodic dissolution can weaken the effect of stress concentration.

Method for accelerated tests with step loading of cracked specimens by cantilever bending. This method was developed for SCC tests of small-sized specimens when it is impossible to satisfy the conditions for fracture mechanics [60,79,80]. Charpy-type specimens with a sharp notch and a failure crack were used for the tests. One end of the specimen subjected to cantilever bending was rigidly clamped, and a load was applied to the other end through an extension arm. Step loading is achieved by sequentially increasing the load, typically by a mass 1 of kg. A load is added in the elastic strain range every 2 hours, and, as short-term creep evolves, after it attenuates, which is recorded by a digital sensor capturing the specimen deflection (Fig. 3).

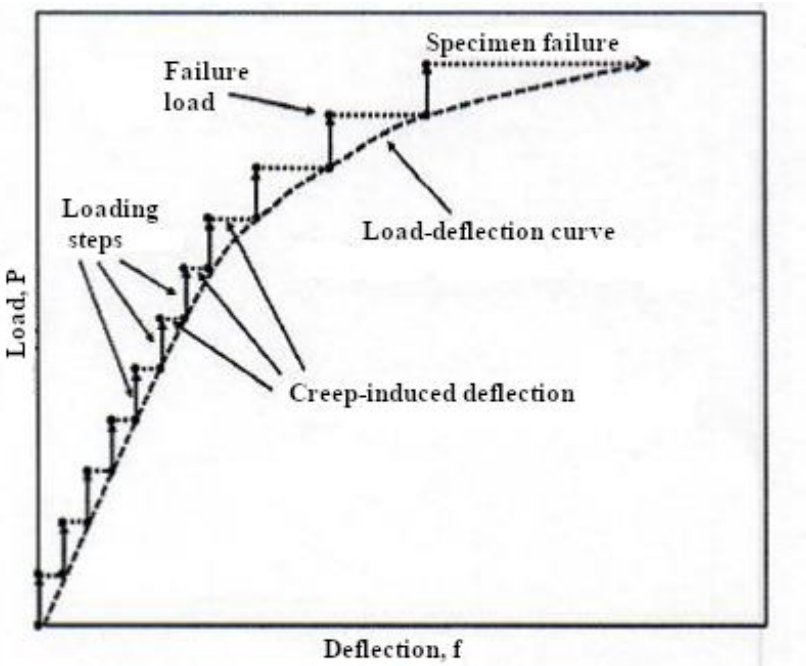

Fig. 3. Schematic step loading of a specimen during cantilever bending tests

The nominal tensile stresses leading to specimen fracture in a corrosive environment and in the air are calculated by the ISO 7539-6 standard.

Slow strain rate testing (SSRT) method. SSRT is widely used to assess the SCC tendency of steels and alloys. It is an accelerated test, where SCC completely follows the mechanisms including the stages of anodic dissolution and hydrogen embrittlement, accompanied by local plastic deformation in microvolumes of the metal.

SSRT was first used to study SCC in titanium alloys and steels, requiring very lengthy tests to obtain results under constant loading [81]. Agreement of the results of SCC tests obtained by the SSRT method with operational fractures and existing methods has long been a subject of much debate [82]. Essentially, cracking in tests with constant strain or constant loading tests also occurs under slow dynamic deformation but the conditions for constant rate tests are more stringent, and these tests cause the specimen to fracture rather quickly in any case.

The most important parameter in SSRT is the strain rate at which the SCC tendency of steel is the most pronounced [83]. Since ductile fracture develops at high strain rates before the corrosion reactions necessary for SCC can proceed, relatively low strain rates are required for the tests. The strain rates recommended by existing standards and procedures for testing steels and alloys are in the range (10^{-7} – 10^{-5}) s^{-1} [67,83-86]. Slow strain rate tests start at zero

loads, continuing until specimen fracture; a tensile stress-strain curve is constructed. To detect the effect of the corrosive environment, a similar curve of the tested material is constructed for comparison in an inert environment. As an example, Figure 4 shows the tensile stress-strain curves for 34CrMo steel with a strain rate of ~1×10^{-6} s^{-1}, obtained during tests in sodium chloride solution saturated with hydrogen sulfide or carbon dioxide, and, for comparison, in the air [86].

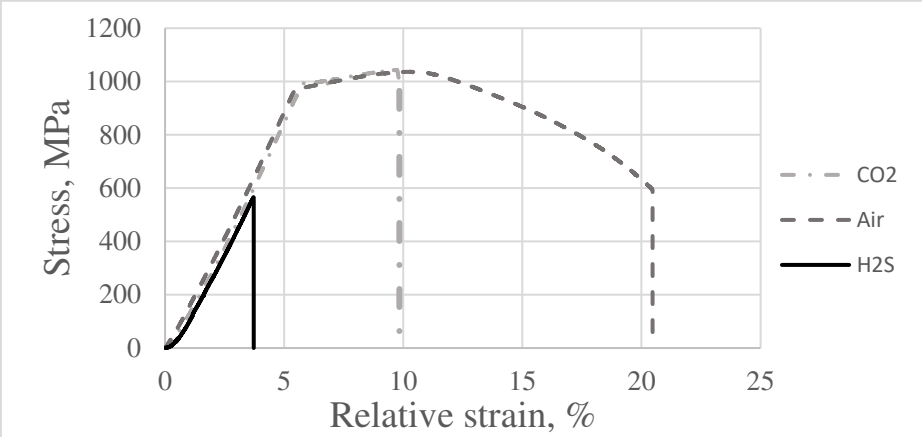

Fig. 4. Tensile stress-strain curves for 34CrMo steel in NaCl solution saturated with H_2S or CO_2 and in the air at room temperature [86]

One of the criteria characterizing the degree of corrosion susceptibility of material in SSRT is the relative strain at which specimen fracture starts in a corrosive environment (ε_{scc}). Another criterion is the stress at which crack propagation starts (σ_{scc}) [23,24]. The stress at which a crack initiates in a corrosive environment is determined from the point where the curves for the inert and the corrosive environment diverge. The ratios of ε_{scc} and σ_{scc} to the relative strain and the fracture stress, obtained during tests in the inert environment, can also be used. If the fracture occurs at stresses less than the yield stress of the material, it is convenient to determine the ratio of the fracture stress in the environment to the fracture stress in the air (or to the yield stress, which is customary for sulfide stress cracking tests under static loading with constant stress or strain applied).

According to [88], the strain criterion, which depends on the environment, temperature, and material properties, can characterize its state under static, quasi-static, and cyclic loading. Compared to the stress criterion, it more adequately reflects the physical nature of the fracture associated with stress corrosion cracking and how it is influenced by external and internal factors; the stress criterion is convenient as a direct characteristic in time-to-failure calculations of products and structures.

Initially, only smooth specimens, generally with circular cross-sections, were used in SSRT-SCC tests. Later tests were carried out with flat specimens, which are more convenient for determining the SCC sensitivity of thin-rolled steel sheets. Notched or fatigue pre-cracked specimens are convenient for testing welded joints with the fusion line metal and the heat-affected zone differing in structure and mechanical properties from the parent metal [90-92]. In such cases, the criterion for the steel's sensitivity to SCC can be the fracture stress in a corrosive environment or the corresponding threshold stress intensity factor. The latter criterion is used to determine the SCC resistance of high-strength low-alloy steels in hydrogen sulfide environments (K_{ISSC}) and is calculated by the formulas given in [92].

The methods aimed at finding the threshold value of K_{ISSC} have evolved over time: many present-day studies substantiate why nonlinear fracture mechanics methods should be applied for low-alloy steels with a yield stress of less than 1000 MPa [92]. Furthermore, the

SSRT method was proved to be effective in sulfide corrosion cracking tests with notched specimens (Fig. 5) [31], providing wider options for finding K_{ISSC} compared to static tests of specimens such as double cantilever beams (Method D NACE TM0177).

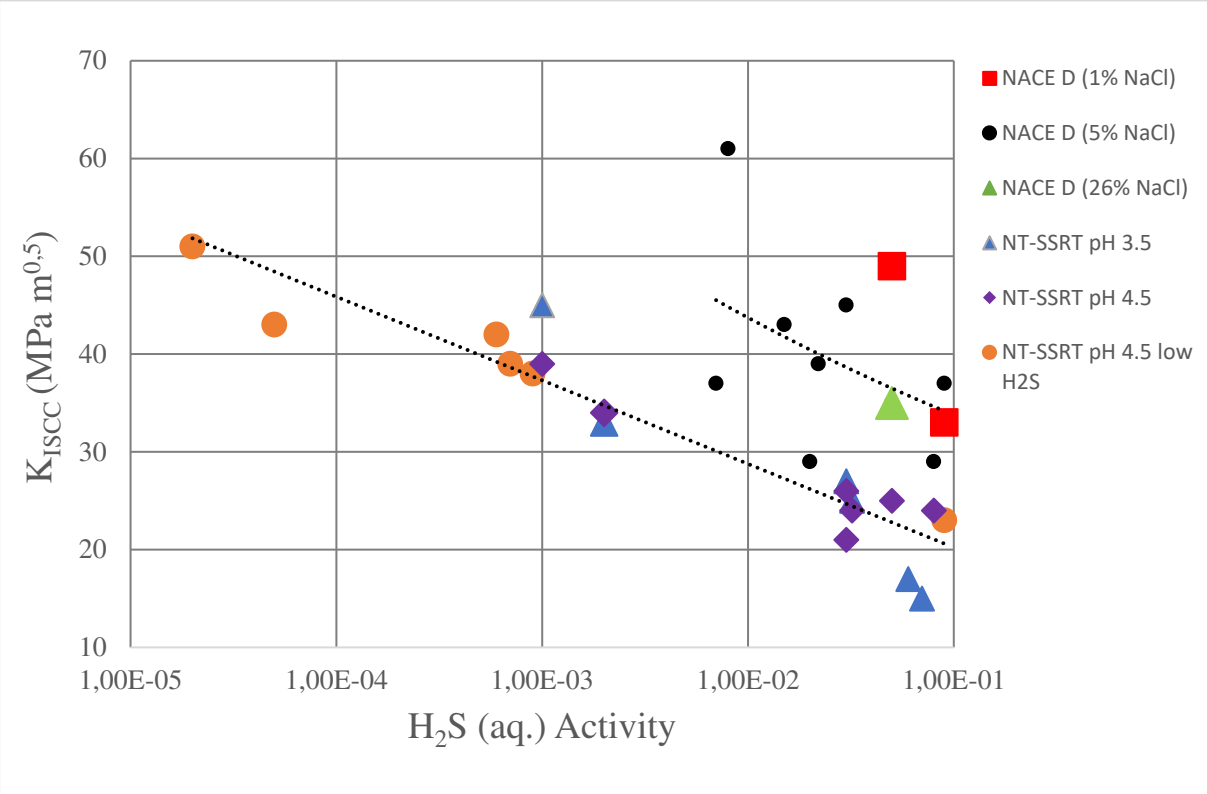

Fig. 5. Influence of hydrogen sulfide activity in sodium chloride solutions of different concentrations on K_{ISSC}, obtained by method D (NACE TM0177 standard) and SSRT for steel C-110 [31]

Apparently, the SSRT method is applicable for any concentration of hydrogen sulfide, yielding more rigorous results with a much smaller scatter.

SSRT allows obtaining results rather quickly, making the method the most convenient for studying the SCC mechanism, especially combined with analysis of fracture behavior in failed specimens and crack propagation trajectory, with simultaneous electrochemical studies. Analysis of the fracture surface of steel P110 after tests in solution A by the NACE TM0177 standard conducted in [93] established that the fracture structure bears a complex character resembling quasi-cleavage when ductile fracture regions alternate with brittle ones [93].

Ref. [62] studied the SCC mechanism in X52 steel by the SSRT method at various solution pH and applied potentials using polarization curves taken at different potential sweep rates. This allowed determining the electrochemical reactions leading to predominant HE or AD or their combined effect, ultimately governing the SCC mechanism [62].

Studies on SCC in low-alloy ferrite-pearlite steels by SSRT with cathodic polarization using metallographic analysis revealed that as the potential shifts to negative values, producing an increase in the hydrogen concentration in the solution, crack initiation and growth starts to be described by transgranular rather than intergranular mechanisms [93].

This paper does not consider the methods for SCC tests of low-alloy steels at high temperatures and pressures in the presence of corrosive gases (such as H_2S and CO_2), which requires separate consideration.

4. Conclusions

We have briefly reviewed the modern notions of the mechanism behind stress corrosion cracking in low-alloy steels, analyzing the methods for testing the tendency to SCC and drawing the following conclusions.

1. SCC in low-alloy steels is a complex multistage process combining electrochemical reactions of metal dissolution and oxidant reduction, diffusive penetration of atomic hydrogen into metal, and its accumulation in the zones with maximum stresses and local plastic strains, favoring the propagation of a corrosion crack.
2. The methods can be divided into several groups depending on the approach to generating the stressed state: constant loading tests; constant strain tests; tests with step loading and constant strain rate.
3. SCC tests with a constant tensile load or constant strain are generally aimed at finding the threshold stresses for which the specimen is not destroyed during the given testing period. While complex equipment is not necessary for such tests, a sufficiently large number of specimens is required.
4. SCC tests of high-strength steels involve fatigue-pre-cracked specimens, determining the threshold stress intensity factor or the J-integral. The main problem with the method is that producing specimens is very resource-consuming; furthermore, there are limitations to testing steels with a yield stress of less than 700 MPa. An accelerated method for SCC testing with a cantilever bend under step loading of cracked specimens is used to simplify the testing procedure and circumvent the limitations on steel strength.
5. The SSRT method is an accelerated type of SCC test, finding wide acceptance as it can greatly shorten the testing times, allowing to find the threshold stresses and strains with a small number of specimens. SSRT is most convenient for studying the SCC mechanism, particularly combined with the analysis of fracture behavior in failed specimens and crack propagation trajectories, with simultaneous electrochemical studies.

References

1. Gonik AA. *Korroziya neftepromyslovogo oborudovaniya i mery yeye preduprezhdeniya*. Moscow: Nedra; 1976. (In Russian)
2. Perez TI. Corrosion in the oil and gas industry: an increasing challenge for materials. *JOM*. 2013;65(8): 1033-1042.
3. Markin AN, Nizamov RE. *CO_2 – korroziya neftepromyslovogo oborudovaniya*. Moscow: OAO «VNIIOENG»; 2003. (In Russian)
4. Khaydersbakh R. *Zashchita ot korrozii i metallovedeniye oborudovaniya dlya dobychi nefti i gaza.* St. Petersburg: Professiya; 2013. (In Russian)
5. Mikhailov EY, Nigmatullin VI, Rybakina OG, Strogonova OA. The time effect on crack resistance of construction materials in presence of corrosion environment. In: *Proc. International Conference «Corrosion in the Oil & Gas Industry». CORROSION Oil&Gas 2019*. St. Petersburg: Peter the Great St. Petersburg Polytechnic University; 2019. p.47.
6. Darin A, Demidov A, Vashchenkov V, Farrakhov V, Krakhmal K, Kulev V. O korrozii magistralnykh truboprovodov. *Tekhnadzor.* 2016;3(112): 128-129. (In Russian)
7. Nesterova E, Borisenkova Ye, The investigation of oil microbocenosis influence on the corrosion process of pipe steel. *Samarskiy nauchnyy vestnik.* 2020;9(4): 125-131.
8. Liang P, Guo Y, Qin H, Shi Y, Li F, Jin L, Fang Z. Effects of pH on the electrochemical behavior and stress corrosion cracking of X80 pipeline steel in simulated alkaline soil solution. *International Journal of Electrochemical Science*. 2019;14: 6247-6256.
9. Quej-Aké L, Contreras A. Electrochemical study on the corrosion rate of X52 steel exposed to different soils. *Anti-Corrosion Methods and Materials.* 2018;65(1): 97-106.

10. Alkhimenko AA, Kolyushev IYe, Kharkov AA, Shaposhnikov NO, Tsvetkov AS. Corrosion resistance of steel piling supports in sea water. Korroziya. Materialy i zashchita. *Nauka i tekhnologii.* 2020: 16-20. (In Russian)
11. Contreras A, Quej LM, Liu HB, Alamilla JL, Sosa E. Role of Mexican Clay Soils on Corrosiveness and Stress Corrosion Cracking of Low-Carbon Pipeline Steels: A Case Study. *Corrosion.* 2020;76(10): 967-984.
12. Thodla R, Gui F, Holtam C. Environmentally Assisted Cracking of Subsea Pipelines in Oil & Gas Production Environments. Effect of Static Loading. *Corrosion*. 2020;76: 312-323.
13. Bogorad IYa, Iskra YeV, Klimova VA, Kuzmin YuL. Korroziya i zashchita morskikh sudov. *Sudostroyeniye.* 1973; 392. (In Russian)
14. Kobayashi K, Omura T, Amaya H. Effect of Buffer System on the Sulfide Stress Cracking Susceptibility of Low-Alloy Steel. *Corrosion.* 2018;74(7): 788-800.
15. Anderko A, Wang P, Smith S. Non-Ideal Gases and Solutions, Complexes and Ion Pairs in Corrosion. In: *CORROSION 2017*. New Orleans, Louisiana, USA; 2017. NACE-2017-8835
16. Markovich RA, Suprun LA. O korrozionnoy stoykosti i kinetike razrusheniya uglerodistoy stali v dvizhushcheysya morskoy vode. *Zashchita metallov.* 1970;6(5): 19-25. (In Russian)
17. Alkhimenko A. Corrosion testing of experimental steels for oilfield pipelines. *E3S Web of Conferences.* 2019;121: 01001.
18. Kostitsyna I, Shakhmatov A, Davydov A. Study of corrosion behavior of carbon and low-alloy steels in CO2-containing environments. *E3S Web Conferences.* 2019;121: 04006.
19. Sagara M. Study on Effect of Buffer Capacity on Corrosion Performance of CRAs in Simulated Well Condition. In: *CORROSION 2017. New Orleans, Louisiana, USA; 2017.* p. NACE-2017-9283.
20. Moiseeva LS. Carbon Dioxide Corrosion of Oil and gas Field Equipment. *Protection of metals.* 2005;41(1): 76-83.
21. Ravindranath K, Tanoli N, Al-Wakaa D. Effect of long-term service exposure on the localized corrosion and stress corrosion cracking susceptibility of type 347 stainless steel. *Corrosion.* 2018;74(3): 350-361.
22. Kharkov OA, Mushnikova SYU, Parmenova ON. On corrosion resistance of nitrogen-containing steel in abrasion conditions. *Voprosy materialovedeniya*. 2020;102(2): 156-163. (In Russian)
23. Kostitsyna IV, Parshukov VP, Biryukov AI, Tyurin AG. Apprasial of carbon and low-alloyed steels resistance to bacterial decomposition. *Vestnik YuUrGU*. 2011;12: 54-57. (In Russian)
24. Ivanovskiy VN. Teoreticheskiye osnovy protsessa korrozii neftepromyslovogo oborudovaniya. *Inzhenernaya praktika.* 2010;6: 4-14. (In Russian)
25. Kostitsyna IV. Issledovaniye korrozionnoy stoykosti materialov nasosno-kompressornykh i neftegazoprovodnykh trub na mestorozhdeniyakh OAO «Lukoyl». Podbor materialov dlya primeneniya v korrozionno-aktivnykh sredakh. *Inzhenernaya praktika.* 2011;11-12: 18-21. (In Russian)
26. Karpov VA, Kovalchuk YuL, Poltarukha OP, Ilin IN. *Kompleksnyy podkhod k zashchite ot morskogo obrastaniya i korrozii.* Moscow: Tovarishchestvo nauchnykh izdaniy KMK. 2007. 19.(In Russian)
27. Ermakov B, Alkhimenko A, Shaposhnikov N. The use of sprayed powders to create coatings in the welds of oilfield pipelines. *Materials Science and Engineering*. 2020;826: 012008.
28. Kuzmin YuL, Oryshchenko AS. *Korroziya i elektrokhimicheskaya zashchita morskikh sudov.* Saint-Petersburg. LA Professional. 2017; 288. (In Russian)

29. Kovalev M, Alekseeva E, Shaposhnikov N, Povyshev A. Predicting the durability of zinc coatings based on laboratory and field tests. *E3S Web of Conferences.* 2019;121: 301008.
30. Kamaletdinov RS. Obzor sushchestvuyushchikh metodov borby s korroziyey neftepromyslovogo oborudovaniya. *Inzhenernaya praktika*. 2010;6: 17-24. (In Russian)
31. Khusainov MF, Ryabkov AV. Sredstva dlya zashchity nefteprovodov ot korrozii. Konferentsiya *Problemy funktsionirovaniya sistem transporta. Tyumen. 2018*; 160-164. (In Russian)
32. Abdrakhmanova KN, Dyagilev IA, Abdrakhmanov NKh, Shaybakov RA. Problems of corrosion protection during safe operation on pipeline systems and equipment of oil and gas industry. *Bezopasnost tekhnogennykh i prirodnykh sistem*. 2020;3: 39-46. (In Russian)
33. Shafikov AS. Opyt primeneniya antikorrozionnoy zashchity i ekspluatatsii sistem korrozionnogo monitoringa promyslovykh truboprovodov ZAO «Vankorneft». *Inzhenernaya praktika.* 2011;8: 130-135. (In Russian)
34. Gutman EM, Getmanskiy MD, Klapchuk OV, Krigman LYe. *Zashchita gazoprovodov neftyanykh promyslov ot serovodorodnoy korrozii*. Moscow: Nedra; 1988. (In Russian)
35. Legezin NYe, Glazov NP, Kesselman GS, Kutovaya AA. *Zashchita ot korrozii neftepromyslovykh sooruzheniy v gazovoy i neftedobyvayushchey promyshlennosti.* Moscow: Nedra; 1973. (In Russian)
36. Golubev IA, Laptev AB, Alekseeva EL, Shaposhnikov NO, Povyshev AM, Kurakin MK. The effect of magnetic treatment on the effectiveness of inhibition in oilfields. *E3S Web of Conferences.* 2019;121: 02006.
37. Golubev IA, Golubev AV, LaptevAB. Practice of using the magnetic treatment devices to intensify the processes of primary oil treating. *Journal of Mining Institute*. 2020;245: 554-560.
38. Tomashov ND. *Teoriya korrozii i zashchity metallov.* AN SSSR; 1959. (In Russian)
39. Chuchkalov MV. *Teoriya i praktika borby s korrozionnym rastreskivaniyem pod napryazheniyem na magistralnykh gazoprovodakh.* MAKS Press; 2016. (In Russian)
40. Voronenko BI. Korrozionnoye rastreskivaniye pod napryazheniyem nizkolegirovannykh staley (obzor). 1. Kriterii i metody issledovaniya. *Zashchita metallov.* 1997;33(2): 132-143. (In Russian)
41. Karpenko GV, Vasilenko II. *Korrozionnoye rastreskivaniye staley.* Kiyev: Tekhnika; 1971. (In Russian)
42. Azhogin FF. *Korrozionnoye rastreskivaniye i zashchita vysokoprochnykh staley.* Moskva: Metallurgiya; 1974. (In Russian)
43. Vasilenko II, Melekhov RK. *Korrozionnoye rastreskivaniye staley*. Kiyev: Naukova dumka; 1977. (In Russian)
44. Brown BF. Stress-Corrosion Cracking. A Perspective Review of the problems. *Naval Research Laboratory.* 1970;7130: 27.
45. Scully JC. Stress corrosion crack propagation: A constant charge criterion. *Corrosion Science.* 1975;15: 207-224.
46. Logan KhL. *Korroziya metallov pod napryazheniyem.* Moscow: Metallurgiya; 1970. (In Russian)
47. Newman RC, Procter RPM. Stress Corrosion Cracking: 1965-1990. *British Corrosion Journal*. 1990;25(4): 259-269.
48. Voronenko BI. Korrozionnoye rastreskivaniye pod napryazheniyem nizkolegirovannykh staley. III. Vliyaniye struktury i termicheskoy obrabotki. *Zashchita metallov.* 1997;33(6): 573-589. (In Russian)
49. Konakova MA, Teplinskiy YuA. Korrozionnoye rastreskivaniye pod napryazheniyem trubnykh staley. *Nauchnoye izdaniye.* 2004; 358. (In Russian)

50. Omura T, Kobyashi K, Amaya N. Material design and application limits for low alloy steel sour resistant OCTG. Zairyo to Prosesu. *CAMP-ISIJ*. 2011;24(2): 663-666.
51. Matrosov YuI, Litvinenko DA, Golovanenko SA. *Stal dlya magistralnykh gazoprovodov.* Moscow: Metallurgiya; 1989. (In Russian)
52. Nasibov AG. *Povysheniye ekspluatatsionnykh kharakteristik nizkolegirovannykh staley massovogo naznacheniya.* Moscow: Chermetinformatsiya; 1991. (In Russian)
53. Jones RH, Ricker RE. Corrosion. Stress Corrosion Cracking. *ASM Handbook*. 1987;13: 311-360.
54. Gareyev AG, Ivanov IA, Abdullin IG. *Prognozirovaniye korrozionno-mekhanicheskikh razrusheniy magistralnykh truboprovodov.* IRTs Gazprom; 1997. (In Russian)
55. Gareyeva OA, Khudyakov MA, Klimov PV, Khazhiyev AD. Modelirovaniye korrozionnogo rastreskivaniya magistralnykh truboprovodov. *Zashchita metallov.* 2010;79(1): 87-92. (In Russian)
56. Gareyev AG. *Osobennosti razrusheniya materialov neftegazoprovodov.* Gilem; 2006. (In Russian)
57. Antonov VG, Baldin AV, Galiullin ZT, Grigoryev PA, Krivotsapova YeM, Matviyenko AF, Khatskevich MG. *Issledovaniye usloviy i prichin korrozionnogo rastreskivaniya trub magistralnykh gazoprovodov.* VNIIEgazprom. Korroziya i zashchita sooruzheniy v gazovoy promyshlennosti. 1991; 43. (In Russian)
58. Marshakov AI, Ignatenko VE, Bogdanov RI, Arabey AB. Effect of electrolyte composition on crack growth rate in pipeline steel. *Corrosion Science.* 2014;83: 209-216.
59. Arabey AV, Knoshinsky Z. *Stress corrosion cracking of gas transmission pipes.* Nauka. Moscow; 2006.
60. Malyshev VN, Stepanov IA, Troshchenko VN. *Vliyaniye katodnoy polyarizatsii na navodorozhivaniye i korrozionno-mekhanicheskuyu prochnost staley.* Varshava: nauchno-tekhnicheskaya konferenciya po probleme SEV; 1980;2(1): 140-144. (In Russian)
61. Ignatenko VE, Marshakov AI, Marichev VA, Mikhaylovskiy YuN, Petrov NA. Effect of cathodic polarization on the corrosion cracking rate in pipe steels. *Zashchita metallov*. 2000;36(2): 132-139. (In Russian)
62. Javidi M, Bahalaou Horeh S. Investigating the mechanism of stress corrosion cracking in near-neutral and high pH environments for API 5L X52 steel. *Corrosion science.* 2014;80: 213-220.
63. Wang S, Martin ML, Sofronis P, Ohnuki S, Hashimoto N, Robertson IM. Hydrogen-induced intergranular failure of iron. *Acta Materialia.* 2014;69: 275-282.
64. Novak P, Yuan R, Somerday BP, Sofronis P, Ritchie RO. A statistical, physicalbased, micro-mechanical model of hydrogen-induced intergranular fracture in steel. *Journal of the Mechanics and Physics of Solids*. 2010;58: 206-226.
65. GOST 9.901-89. *YeSZKS. Metally i splavy. Obshchiye trebovaniya k metodam ispytaniy na korrozionnoye rastreskivaniye.* (In Russian)
66. ANSI/NACE TM0177-2016. *Standard Test Method. Laboratory Testing of Metals for Resistance to Sulfide Stress Cracking and Stress Corrosion Cracking in H2S Environments.*
67. GOST 9.901.4-89. *YeSZKS. Metally i splavy. Ispytaniya na korrozionnoye rastreskivaniye obraztsov pri odnoosnom rastyazhenii.* (In Russian)
68. Marichev VA. Sovremennyye predstavleniya o vodorodnom okhrupchivanii pri zamedlennom razrushenii. *Zashchita metallov.* 1980;16(5): 531-543. (In Russian)
69. GOST 9.903. *YeSZKS. Stali i splavy vysokoprochnyye. Metody uskorennykh ispytaniy na korrozionnoye rastreskivaniye.* (In Russian)
70. Kobayashi K, Omura T, Souma A, Ohe T. Amaya H, Ueda M. Environmental Cracking Susceptibility of Low-Alloy Steels Under a High H2S Pressure and High-Temperature Sour Environment. *Corrosion*. 2018;74(5): 509-519.

71. Cherepanov GP. *Mekhanika khrupkogo razrusheniya.* Moscow: Nauka; 1974. (In Russian)
72. Rays D. *Razrusheniye. Matematicheskiye metody v mekhanike razrusheniya. (pod red. G. Libovitsa). T. 2. Matematicheskiye osnovy teorii razrusheniya.* Moscow: Mir, 1975: 204-335. (In Russian)
73. Terentyev VF. *Osnovy mekhaniki razrusheniya.* Moscow: Interkontakt Nauka; 2009. (In Russian)
74. Yan L, Gravel JP, Kang J, Xu L, Arafin M. Occurrence of Near-Neutral pH Stress Corrosion Cracking in X80 and X100 Pipe Steels Under Various Cathodic Protection Conditions. *Corrosion.* 2018;74(9): 1033-1043.
75. GOST 25.506-85. *Raschety i ispytaniya na prochnost. Metody mekhanicheskikh ispytaniy metallov. Opredeleniye kharakteristik treshchinostoykosti (vyazkosti razrusheniya) pri staticheskom nagruzhenii.* (In Russian)
76. ASTM Ye 1820. *Standard Test Method for Measurement of Fracture Toughness.*
77. *Spravochnik po koefficientam intensivnosti napryazhenij.* Moskva: Mir; 1990. (In Russian)
78. Kovchik SYe, Morozov YeM. *Spravochnoye posobiye. Mekhanika razrusheniya i prochnost materialov. T. 3. Kharakteristiki kratkovremennoy treshchinostoykosti materialov i metody ikh opredeleniya.* Kiyev: Naukova dumka; 1988. (In Russian)
79. Malyshev VN, Kharkov AA, Ivanov GN, Navyazhskaya IA. Issledovaniya korrozionnogo rastreskivaniya vysokoprochnyh stalej v nejtral'nyh rastvorah hloridov. *Sostoyanie i perspektivy sozdaniya i vnedreniya korrozionnostojkih materialov, sredstv i metodov protivokorrozionnoj zashchity sudov*, 1982; 2. (In Russian)
80. Mushnikova SYu, Kharkov AA, Popov VI, Kalinin GYu. Opredeleniye sklonnosti k korrozionnomu rastreskivaniyu sudostroitelnykh staley. *Fundamentalnyye aspekty korrozionnogo materialovedeniya i zashchity metallov ot korrozii*, Moscow, IFKhE RAN, FGUP VIAM, 2011; 38. (In Russian)
81. Parkins RN, Matstsa F, Royela ZhZh, Skalli ZhK. Metody ispytaniya na korroziyu pod napryazheniyem. *Zashchita metallov.* 1973;9(5): 515-540. (In Russian)
82. Nikitin VI. Korrozionnoye rastreskivaniye metallov pri postoyannom napryazhenii i postoyannoy skorosti deformirovaniya. *FKhMM.* 1987;25(1): 31-38. (In Russian)
83. Korb LJ, Olson DL. *Metals Handbook. Vol. 13. Corrosion*. ASM lntemational; 1994.
84. NACE Standard TM 0198-2016. Slow Strain Rate Test Method for Screening Corrosion-Resistant Alloys for Stress Corrosion Cracking in Sour Oilfield Service.
85. GB 15970.7-2017. National standard of China. Corrosion of metals and alloys. stress corrosion testing – slow strain rate testing.
86. Alkhimenko AA, Kharkov AA, Shemyakinskiy BA, Shaposhnikov NO. Razrabotka metodiki uskorennykh ispytaniy trubnykh staley neftyanogo sortamenta na korrozionnoye rastreskivaniye. *Zavodskaya laboratoriya. Diagnostika materialov.* 2020;86(9): 70-76. (In Russian)
87. Kharkov AA, Nemchikova LG, Mikhnevich AP, Bilina SYu. Otsenka sklonnosti staley k korrozionnomu rastreskivaniyu pri ispytanii s medlennoy skorostyu deformirovaniya. *Tekhnologiya sudostroyeniya.* 1990;3: 10-13. (In Russian)
88. Steklov OI, Polyarus AN. O deformacionnom kriterii nachala korrozionno-mekhanicheskogo razrusheniya. *Zashchita metallov*. 1980;16(5): 544-549. (In Russian)
89. Ma HC, Liu ZY, Du CW, Wang HR, Li XG, Zhang DW, Cui ZY. Stress corrosion cracking of E690 steel as a welded joint in a simulated marine atmosphere containing sulphur dioxide. *Corrosion Science.* 2015;100: 627-641.
90. Mustapha A, Charles EA, Hardie D. Evaluation of environment-assisted cracking susceptibility of a grade X100 pipeline steel. *Corrosion Science.*2012;54: 5-9.

91. Kim Y, Kim W, Kim J. Influence of Ultrasonic Nanocrystal Surface Modification on the Corrosion and Stress Corrosion Cracking Behavior of Low Carbon Steel (ASTM A139) Welded Joint in the Simulated District Heating Environment. *Corrosion.* 2018;74(1): 112-122.
92. Case RP, McIntyre DR, Rincon HE. Effect of Brine Ionic Strength on Sulfide Stress Cracking Resistance of High Strength Low Alloy Steel. *Corrosion.* Vancouver, British Columbia, Canada, 2016, NACE-2016-7685.
93. Boellinghaus T, Hoffmeiste N, Dietrich S. Slow Strain Rate Testing of Low Carbon Martensitic Stainless Steels. Advances in Corrosion Control and Materials in Oil and Gas Production. EFC 26. *European Federation of Corrosion.* 1999.
94. Husby H, Wagstaff P, Iannuzzi M, Johnsen R, Kappes M. Effect of nickel on the hydrogen stress cracking resistance of ferritic/pearlitic low alloy steels. *Corrosion.* 2018;74(7): 801-818.

THE AUTHORS

Alhimenko A.A.
e-mail: 9586435@mail.ru
ORCID: 0000-0001-6701-1765

Breki A.D.
e-mail: breki_ad@spbstu.ru
ORCID: 0000-0002-4452-3896

Shaposhnikov N.O.
e-mail: shaposhn_no@spbstu.ru

Kharkov A.A.
e-mail: a.a.harkov@mail.ru
ORCID: 0000-0002-8966-8802

Alekseeva E.L.
e-mail: alexeeva__ekaterina@mail.ru
ORCID: 0000-0002-8996-1507

Lapechenkov A.A.
e-mail: andreylapechenkov@gmail.com
ORCID: 0000-0002-7443-8852

Materials Physics and Mechanics. 2022;50(2): 475-484
Research article
http://dx.doi.org/10.18149/MPM.5032022_10

Submitted: June 29, 2022
Approved: September 9, 2022
Accepted: October 28, 2022

Strength analysis of thin-wall structures operating in aggressive environments for prolonged periods

I.G. Emelyanov[1]✉, A.N. Kislov[2]

[1]Institute of Engineering Science, Ural Branch, Russian Academy of Sciences, 34 Komsomol'skaya st., Ekaterinburg, 620049, Russia

[2]Ural Federal University, 19 Mira st., Ekaterinburg, 620002, Russia

✉ emelyanov.ig.2016@mail.ru

Abstract. A method is proposed for determining the strength of a metal shell structure under mechanical loading and prolonged contact with an aggressive hydrogen-containing medium. The mechanical properties of the structural material change under the influence of such media. Steels exhibit a decrease in ductility, which is called hydrogen embrittlement. This effect must be taken into account when assessing the strength of steel structures operating in contact with hydrogen-containing media. The method is illustrated with an example of a steel cylindrical pipe in contact with a hydrogen sulfide-containing medium. Data obtained in the course of an earlier experiment are used to determine the mechanical parameters of the pipe material. The possibility of determining the mechanical parameters beyond the saturation time of the samples in the experiment is shown.

Keywords: shell, hydrogen sulfide environment, tension diagram, brittleness, neural networks, long-term strength

Acknowledgements. *No external funding was received for this study.*

Citation: Emelyanov IG, Kislov AN. Determination of the strength of thin-wall structures working for a long time in aggressive environments. *Materials Physics and Mechanics*. 2022;50(3): 475-484. DOI: 10.18149/MPM.5032022_10.

1. Introduction

Metal shells are widely used as structural elements in different branches of technology. Sometimes such structural elements are exposed not only to external thermomechanical loads during operation, but also come into contact with aggressive environments. Strength calculations should take into account all scenarios of operation up to failure. Strength calculations are generally carried out in a limited range of steady processes of metal deformation. The last stage of operation, i.e., failure, is a new phenomenon in the behavior of structures that has been insufficiently studied so far. The purpose of deterministic strength calculations consists in prohibiting operational modes close to the limit state for the structure. However, even such simplified calculations appear to be nontrivial, if the structure contacts a penetrating aggressive environment, for example, that containing hydrogen. In this case, extensive fracture processes occur in the structure metal under the action of external loads and an aggressive environment, potentially leading to failure in the structure's elements [1,2]. The strength may change, depending on the concentration of the aggressive environment and the

© I.G. Emelyanov, A.N. Kislov, 2022.
Publisher: Peter the Great St. Petersburg Polytechnic University
This is an open access article under the CC BY-NC 4.0 license (https://creativecommons.org/li-censes/by-nc/4.0/)

stressed state at a given time [2-5]. Some studies have observed a decrease in the yield strength with an increase in the degree of hydrogen charging [6,7]. Furthermore, one theory of hydrogen embrittlement, known as hydrogen-enhanced localized plasticity (HELP), claims that reduction in the overall ductility under the action of hydrogen occurs due to facilitated plastic deformation at the crack tip [8,9].

These facts must be taken into account in strength analysis during the long-term operation of steel structural elements in aggressive hydrogen-containing environments. The hydrogen-induced change in the properties of some steels is manifested as hydrogen embrittlement, i.e., a decrease in the ductility of the material as it is saturated with hydrogen. No universal model has been constructed so far to produce reliable forecasts for the lifetimes of structures taking into account the embrittlement of the material. This is also a crucial issue for strength analysis of steel pipes transporting the so-called sour gas, i.e., natural gas with increased content of hydrogen sulfide. Since strong hydrogen charging of metal occurs in environments containing hydrogen sulfide, pores filled with hydrogen are produced in the steels, leading to delamination. Predicting the behavior of such metal structures is a major problem that is yet to be addressed definitively.

This paper proposes a method for determining the strength of a metal shell structure under mechanical loading taking into account prolonged contact with an aggressive environment containing hydrogen sulfide. Since it is difficult to conduct long-term experimental studies of the material for the whole variety of possible load combinations that can affect the structure during operation, the model representation was based on the extrapolation of mechanical parameters. The method is illustrated in the case of a cylindrical steel pipe used for wells and gas collection systems of pipelines.

The problem of determining the long-term strength in thin-walled metal structures consists of several independent problems of applied mechanics, mathematical physics, and materials science. The general problem can be represented as:

– determining the stressed state in the given structural element;

– determining the mechanical parameters, depending on the saturation time of the material specimens with hydrogen sulfide;

– extrapolating the mechanical properties of the material to the potential lifetime of the structure;

– selecting the strength criterion and determining the instant in the lifecycle of the structure when the limit state occurs.

2. Materials and methods

Determination of the stressed state. We assume that the thin-walled structure considered is a shell of revolution with a thickness of h and a length of L, with variable geometric and mechanical parameters along the generatrix. Let us relate the shell to a middle surface determined by curvilinear orthogonal coordinates s, θ, γ, where s is the meridional coordinate, θ is the circumferential coordinate, and the coordinate γ is measured in the direction of the outer normal to the shell surface.

There are diverse computational programs for determining the stress state in thin-walled structures based on various numerical methods. Mathematical formalization of the problems is typically based on a specific shell theory. In this paper, we rely on the classical shell theory based on the Kirchhoff–Love hypotheses to determine the stress-strain state of a thin-walled structure [10]. The stress-strain state of an arbitrarily loaded shell of revolution is described by a system of eight partial differential equations [10-12]

$$\partial\bar{Y}/\partial s = \sum_m A_m(s,\theta)\partial^m\bar{Y}/\partial\theta^m + \bar{f}(s,\theta),\ (s_0 \le s \le s_L) \quad (1)$$

with the boundary conditions

$$B_1\bar{Y}(s_0) = \overline{b_1},\ B_2\bar{Y}(s_L) = \overline{b_2}. \quad (2)$$

Here $\bar{Y}$ is the vector of the required solution; $\bar{f}$ is the vector whose components depend on the loads applied to the shell; B_1 and B_2 are the given matrices; $\overline{b_1}$ and $\overline{b_2}$ are the given vectors; the elements of the matrix A_m depend on the geometric and mechanical characteristics of the shell.

The internal surface of the shell comes into contact with the aggressive hydrogen-containing environment with the excess pressure p. Considering that the shell considered is loaded only with a pressure p during operation, its stress-strain state is axially symmetrical. The stressed state under axisymmetric deformation of the shell can be determined by integrating a system of six ordinary differential equations [13-16]

$$d\bar{Y}/ds = P_{ij}\bar{Y} + \bar{f} \tag{3}$$

with the vector of the solution

$$\bar{Y} = \{N_r, N_z, M_s, u_r, u_z, \vartheta_s\}, \tag{4}$$

where N_r, N_z are the radial and axial forces; u_r, u_z are the displacements; M_s is the meridional bending moment; ϑ_s is the normal rotation angle.

Discrete orthogonalization developed by S. Godunov [10,17,18] is applied to solve the linear boundary-value problem (3): this method 'normalizes' the solution and is used to solve various problems for shell structures [10-16]. The boundary-value problem solved by accounting for plastic deformation becomes nonlinear. The nonlinear problem is solved by the method of elastic solutions proposed by Ilyushin [19]. The method for linearization of the problem is considered in detail in [13,15]. The volumetric stress state of the shell is compared with the uniaxial state under simple stretching of the specimen.

$$S = \sigma/\sqrt{3}, H = \varepsilon(1+\mu^*)/\sqrt{3}, \tag{5}$$

where σ and ε are the stresses and strains under simple stretching of the specimen, μ^* is the coefficient of transverse deformation, defined as in [13,14]

$$\mu^* = 0.5 - \sigma(1-2\mu)/2E\varepsilon, \tag{6}$$

where E is the elastic modulus; μ is Poisson's ratio. The intensities of shear stresses S and shear strains H for the shell are given as

$$S = \sqrt{(\sigma_s^2 + \sigma_s\sigma_\theta + \sigma_\theta^2)/3}, \tag{7}$$

$$H = \sqrt{\left[\left(\varepsilon_s - \varepsilon_\gamma\right)^2 + \left(\varepsilon_\gamma - \varepsilon_\theta\right)^2 + (\varepsilon_\theta - \varepsilon_s)^2\right]/6}, \tag{8}$$

where σ_s and σ_θ are the meridional and circumferential stresses, respectively; ε_s, ε_θ and ε_γ are the strain components along the meridian, circumference, and normal to the surface of the shell.

The meridional and circumferential stresses $\sigma_s(\gamma)$, $\sigma_\theta(\gamma)$ and the corresponding strains $\varepsilon_s(\gamma)$, $\varepsilon_\theta(\gamma)$, as well as the intensities of shear stresses $S(\gamma)$ and shear strains $H(\gamma)$ are determined at each point of the shell after integration of system (3).

Mechanical parameters of the material. The stress state of the given structure is established by finding the mechanical parameters of the material depending on the time of saturation with hydrogen sulfide. The problem of hydrogen diffusion into the metal wall of the shell was solved in [16], determining the distribution of hydrogen concentration as a function of time for bodies of revolution [16]. Considering shells with a small wall thickness, we assume that hydrogen concentration along the thickness is the same. This hypothesis is confirmed by computational experiments for thin-walled structures, with a long period of hydrogen charging [16]. Therefore, the change in the mechanical parameters of the shell material depends only on the time t of saturation with hydrogen sulfide.

To illustrate the method for determining the strength of thin-walled structures, we examine shells of 12GB pipe steel, whose mechanical characteristics change under contact with an aggressive hydrogen sulfide medium. Measurements of the mechanical characteristics

in 12GB pipe steel specimens exposed to hydrogen sulfide for 96–384 hours are given in [20], along with measurements for specimens in the initial state, directly under uniaxial tensile stresses up to failure. Potential plastic deformations of the structure can be taken into account by obtaining stress-strain curves for this material $\sigma = f(\varepsilon, t)$ with the specimens stretched in the initial state and after hydrogen charging. These curves can be fitted fairly accurately by bilinear lines with points of yield strength $(\sigma_Y, \varepsilon_Y)$ and ultimate tensile strength $(\sigma_{ult}, \varepsilon_{ult})$ for different times t of contact with an aggressive environment, where σ_{ult} and ε_{ult} are the maximum stresses and strains under fracture. Table 1 shows the coordinates of the points for constructing such diagrams.

Table 1. Coordinates of points for approximating the diagrams $\sigma = f(\varepsilon, t)$

Time, h	Point 1		Point 2		Point 3	
	ε_0	σ_0, MPa	ε_Y	σ_Y, MPa	ε_{ult}	σ_{ult}, MPa
0	0	0	0.00187	374	0.23	474
96	0	0	0.00181	361	0.22	458
192	0	0	0.00213	426	0.14	498
384	0	0	0.00218	437	0.12	500

Figure 1 shows one of the diagrams corresponding to the initial state of the specimen material. Squares correspond to experimental data from [20].

Extrapolation of mechanical properties of the material. Stresses and strains during the time range for which the specimen is saturated with hydrogen sulfide can be determined by interpolation. The change in the mechanical parameters of material under saturation with hydrogen sulfide can be extrapolated beyond the experimental time range t_{exp} to the structure's period of safe operation t_w.

We accept the hypothesis that the physico-chemical processes in the metal exposed to hydrogen sulfide are monotonic. Therefore, the change in the mechanical parameters of the material during contact with hydrogen sulfide can be extrapolated beyond the experimental time range. Apparently, extrapolation is correct up to a time comparable to the time in which the experiment was conducted with the same conditions for temperature and loading and within the limits of the same type of failure. However, it is suggested in [21] that extrapolation can be also applied for a time exceeding the maximum durability (for which the rupture strength curves were experimentally obtained) by an order of magnitude.

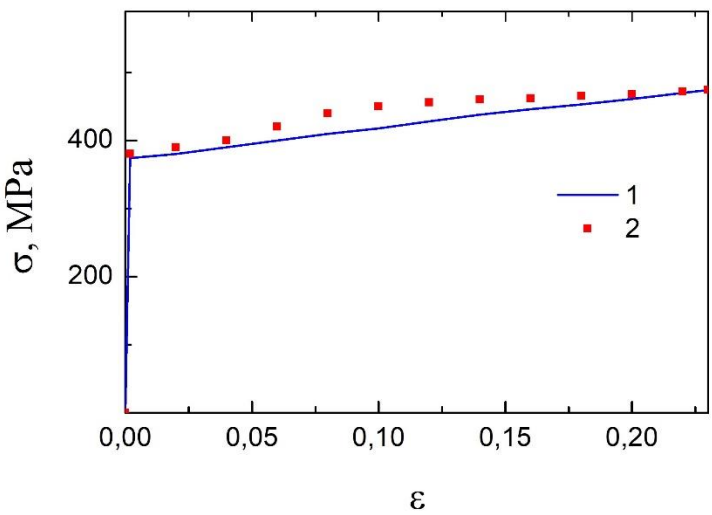

Fig. 1. Approximated diagram $\sigma = f(\varepsilon, 0)$

Different variants of neural networks can be used to calculate the required values outside the experimental time range. Neural networks can be used in various fields of science and technology due to their approximating capabilities and the options for calculating different nonlinearities [22,23]. After training, the network can predict the future value for some sequences based on several previous values of existing factors. At the training stage, the neural network reconstructs the target function from a set of training samples, that is, solves the problem of interpolation. The trained neural network can use the reconstructed dependence to obtain the predicted value and solve the extrapolation problem. This method of neural networks is integrated into the later versions of the Wolfram Mathematica 11.3 package for symbolic calculations.

Determination of the structure's operating time. We assume that the limit state of the structure occurs during long-term operation when the strength criterion of the material is violated at the most loaded point of the shell. This instant determines the structure's time of safe operation t_w. The condition commonly taken as the strength criterion of the structural material in the volumetric stress state is that the intensity of shear stresses (7) at the most loaded point of the shell reaches the uniaxial stresses for the specimen $\sigma_{ult}/\sqrt{3}$ during fracture.

In accordance with the well-known scheme constructed by Ioffe, a decrease in temperature is accompanied by a decrease in the ductility of the metal up to embrittlement [24]. A similar phenomenological effect is observed with an increase in hydrogen concentration during electrochemical hydrogen charging in steels. The yield strength σ_Y and the ultimate tensile strength σ_{ult} depend on the concentration of hydrogen sulfide, and, therefore, on the operating time t of the shell structure. The constructed kinetic curves $\sigma_Y(t)$ and $\sigma_{ult}(t)$ approach each other for many materials, converging at a time $t = t_{BR}$ in the point $\sigma_Y(t_{BR}) = \sigma_{ult}(t_{BR})$ [25]. This time point in the operating cycle separates the ductile fracture range in the material from the brittle fracture range. However, this condition only holds true for a local zone with plastic deformation and maximum intensity of shear stresses.

Thus, the following condition can be used as the criterion for the rupture strength of structures under constant loading:

$$S(t) = \sigma_{ult}(t)(\sqrt{3})^{-1}. \tag{9}$$

Violation of condition (9) determines the permissible operating time of the shell and its lifetime.

3. Results and discussion

Let us determine the stress state and the strength of the cylindrical shell (pipe), operating in a hydrogen-containing medium for a long time. The outer diameter of the pipe is D = 0.114 m, the thickness is h = 0.013 m, the length is L = 1 m, and the material is 12GB steel (equivalent to X42SS steel according to the classification of the American Petroleum Institute). The pipe experiences a plane stress state from the alternating internal pressure p during operation. If we assume that the pipe is sufficiently long, boundary conditions (2) do not considerably affect the stress state in the section that interests us, $s = 0.5\,L$.

As noted above, by integrating a system of equations (3) at each point of the shell, we can determine the meridional and circumferential stresses and strains, as well as the intensities of shear stresses and shear strains at any internal pressure. At an overpressure of p = 80 MPa, the entire material of the shell is still in the elastic strain range, and the maximum intensity of shear strain H reaches $0.00111 < \varepsilon_Y$. Meridional and circumferential stresses σ_s = –7.04 MPa and σ_θ = 307.38 MPa act on the outer surface of the shell, σ_s = 0 and σ_θ = 309.5 MPa on the centerline, and σ_s = 7.04 MPa and σ_θ = 311.61 MPa on the inner surface. As a test, the obtained stresses were compared with the stress calculated for a shell loaded with internal

pressure using the momentless theory [26] $\sigma_\theta = pR_{cp}h^{-1} = 310.76$ MPa, where R_{cp} is the mid-radius of the shell. The results are in good agreement.

Table 2 gives the intensities of shear stresses $S = f(p)$ and shear strains $H = f(p)$ for the shell at different internal pressures p for $t = 0$ hours.

Table 2. Intensities of shear stresses and shear strains for t = 0 h

p, MPa	S, MPa	H
80	177.9	0.00111
90	200.0	0.00125
100	224.1	0.01962
110	248.8	0.09412
120	273.2	0.16724

When the overpressure p = 90 MPa is reached, plastic deformations occur at the most loaded point on the inner surface of the shell. The problem becomes physically nonlinear, and an iterative process is applied to obtain the given relative accuracy of 0.01 for the solution of the nonlinear problem [15].

Because the influence of hydrogen sulfide on the mechanical parameters of the material starts to manifest beyond the yield point σ_Y in the specimen's plastic strain range, we consider the kinetics of the stress state in the shell with p = 100 MPa, when plastic deformation zones appear near the most loaded point. Table 3 gives the intensities of shear stresses $S = f(t)$ and shear strains $H = f(t)$ for the shell with different operating times t of the structure in contact with hydrogen sulfide.

The given relative accuracy of the nonlinear problem for the operating time t = 0 h can be achieved in 86 approximations, 70 approximations are required for the time of 96 h, 3 approximations for 192 h, and only one approximation is sufficient for 384 h (the entire material of the shell is in the elastic range). Consequently, embrittlement of the shell material occurs at t = 384 h.

Table 3. Values S and H for p = 100 MPa

t, h	S, MPa	H
0	224.1	0.01962
96	224.9	0.04435
192	222.4	0.00142
384	222.4	0.00146
800	222.4	0.00142

It follows from Table 3 that the intensities of shear stresses S and shear strains H practically do not change during the operating time limited by the experiment.

A particular configuration of neural network was used to calculate the required values outside the experimental time range. A three-layer neural network from the Wolfram Mathematica 11.3 package with a hyperbolic tangent as an activation function was used in this study to interpolate and extrapolate the curves $\sigma_Y = f(t)$ and $\sigma_{ult} = f(t)$. Figures 2(a) and 2(b) show the yield strength σ_Y and ultimate tensile strength σ_{ult}, respectively, depending on the time limited by the experiment considering the influence of hydrogen sulfide on the metal. The experimental data from [20] are marked by points, the solid lines correspond to the interpolation values.

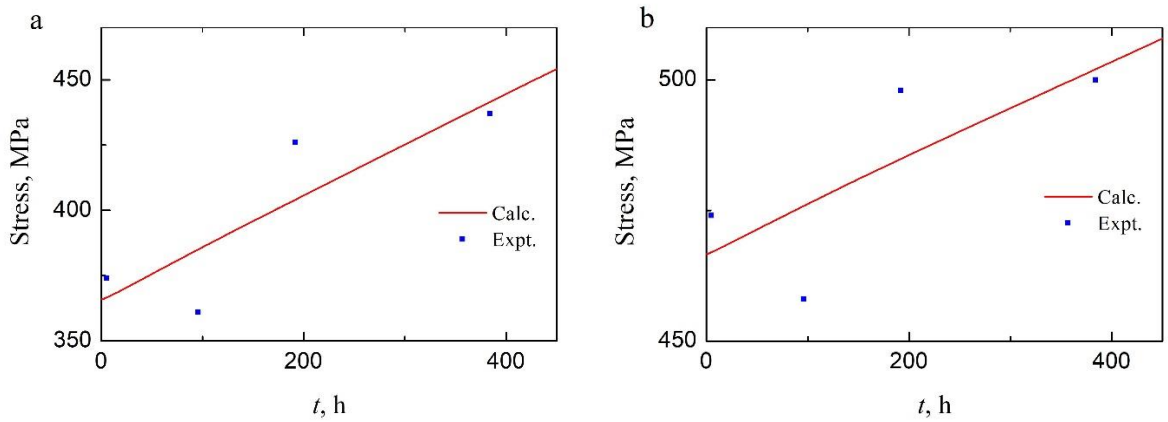

Fig. 2. Yield strength (a) and ultimate tensile strength (b) depending on the saturation time of the specimen with hydrogen sulfide

Figure 3 shows the variation in the yield strength (curve 1) and ultimate tensile strength (curve 3) during the time of contact between specimens and hydrogen sulfide up to 1000 hours. Evidently, the constructed kinetic curves $\sigma_Y(t)$ and $\sigma_{ult}(t)$ converge with a time close to t_{BR} =1000 h, $\sigma_Y(t_{BR}) = \sigma_{ult}(t_{BR})$.

If inequality $t > t_{BR}$ is satisfied, the steel considered becomes brittle and, therefore, the stress state and the strength condition can be determined within the framework of linear elasticity theory. If $t < t_{BR}$, then the physical equations describing the properties of steel should follow plasticity theory.

Thus, the stress-strain state of the shell for the particular operating time of the structure t^* = 800 hours can be determined using the kinetic curves $\sigma_Y(t)$ and $\sigma_{ult}(t)$, shown in Fig. 3. In this case, we obtain σ_Y^* = 510 MPa and σ_{ult}^* = 530 MPa.

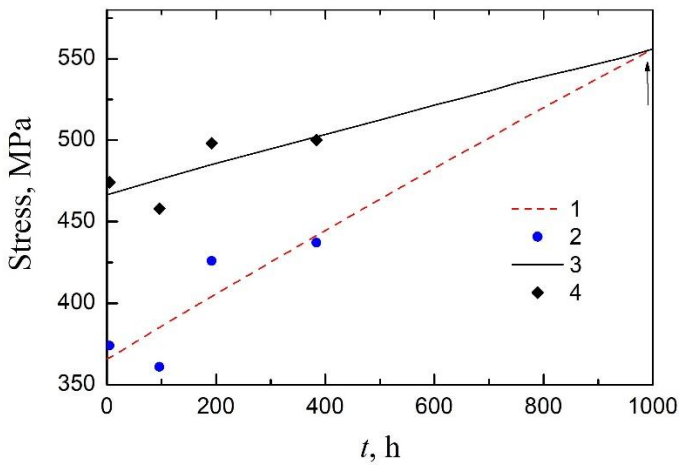

Fig. 3. Computational dependences of yield strength (curve 1) and ultimate stress (curve 3) on the contact time of the specimen with hydrogen sulfide. Dots and squares correspond to experimental values [20]

The approximated diagram $\sigma = f(\varepsilon, t^*)$ for t^* = 800 h can be constructed by finding ε_Y^* and ε_{ult}^*. Given that Young's modulus E practically does not change when the specimens are saturated with hydrogen sulfide, the yield-point strain is $\varepsilon_Y^* = \sigma_Y^* E^{-1} = 0.00255$. The fracture strain beyond the elastic limit consists of two components: elastic and residual δ. Therefore, when the specimen is fractured, the relative ultimate strain is defined as $\varepsilon_{ult}^* = \sigma_{ult}^* E^{-1} + \delta^*$.

Figure 4 shows the variation of residual strain $\delta(t)$ over the contact time of the specimens with hydrogen sulfide up to t = 900 h. The points denote the experimental values $\delta(t)$given in [20]. Therefore, we have δ^* = 0.04 for time t = 800 h.

Thus, to determine the stress state for the operating time t^* = 800 h, the tensile curve should be approximated by a bilinear function with the points of yield strength σ_Y^* = 510 MPa, $\varepsilon_Y^* = 0.00255$ and ultimate tensile strength σ_{ult}^* = 530 MPa, ε_{ult}^* = 0.04265. After integrating the system of equations (3) at each point of the shell, we can easily find the necessary components of stress and strain at any value of internal pressure. Table 3 shows the intensities of shear stresses S and shear strains H for the shell during the operating time of 800 hours.

Considering the point found for the operating time of t_{BR} =1000 h, which separates the ductile fracture range of the material from the brittle fracture range for the shell considered, two conditions should be imposed for strength. We assume that fracture of the shell for the operating time $t < t_{BR}$ (plastic strain range) occurs when the integral intensity of shear stresses $S_h(\gamma)$ at the most loaded point reaches the ultimate tensile stress σ_{ult} upon fracture of the specimen material.

$S_h = \sigma_{ult}\left(\sqrt{3}\right)^{-1}$,

where $S_h = [\int_{-h/2}^{h/2} S(\gamma)d\gamma]/h$ is the integral intensity of shear stresses in the shell.

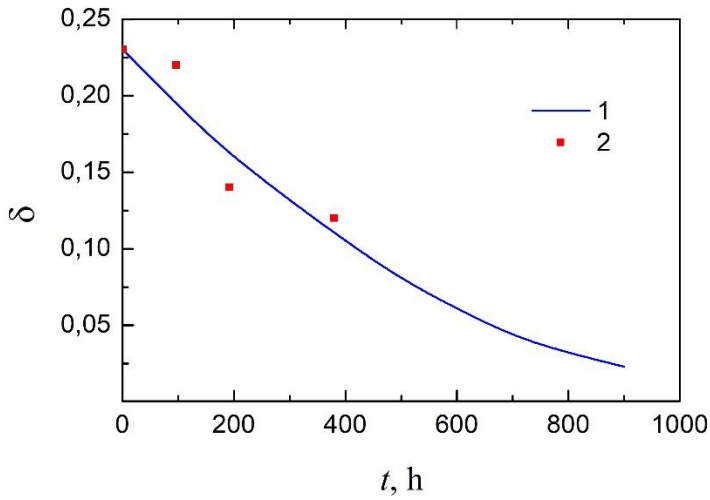

Fig. 4. Variation of residual strain

Fracture of the shell for the operating time $t > t_{BR}$ (brittle deformation range) occurs when the intensity of shear stresses S at the most loaded point reaches the ultimate tensile stress σ_{ult} upon fracture of the specimen material. The continuity of the material at the most loaded point of the structure is violated provided that (9).

4. Conclusion

The paper proposes a method for determining the stress state, strength, and lifetime of thin-walled structures exposed to aggressive environments containing hydrogen sulfide for prolonged periods, with estimates produced for the safe operation of the shell structure. The method is illustrated by an example of a cylindrical steel pipe used to transport hydrogen-containing gas mixtures.

The method is based on the hypothesis that the yield and ultimate tensile strengths of the specimen material depend on the time of contact with the hydrogen-containing environment. The mechanical parameters of the pipe material were determined using the data obtained during an earlier experiment in a limited time range. An increase in yield strength

and ultimate tensile strength was observed with an increase in the degree of hydrogen charging. We used extrapolation methods to obtain results suggesting that the yield and ultimate tensile strengths converge to a single point at longer operating times. This point of convergence allows us to establish which criterion should be used in strength analysis for the safe operation of shell structures. The brittle fracture criterion is applied for a time exceeding the value of the convergence point; otherwise, the criterion for shell strength under elastoplastic deformation should be used. Furthermore, no point of convergence may be observed for other materials, since the yield strength can decrease. Other representations will have to be adopted for the model in the calculations for these cases.

Thus, we established that the change in mechanical parameters can be described depending on the time of material exposure to hydrogen sulfide. The proposed criterion for the strength of the shell structure and the model for extrapolation of mechanical parameters beyond the experimental time range make it possible to determine the time in the life cycle of the structure, at which the limit state occurs.

References

[1] Olden V, Thurlow C, Johnsen R. Modelling of hydrogen diffusion and hydrogen induced cracking in supermartensitic and duplex stainless steels. *Materials and Design*. 2008;29(10): 1934-1948.

[2] Rebyakov YN, Chernyavskij AO, Chernyavskij OF. Deformation and fracture of materials and structures under diffusion conditions. *Vestnik SUSU*. 2010;10: 4-16. (In Russian)

[3] Jemblie L, Olden V, Akselsen O. A coupled diffusion and cohesive zone modelling approach for numerically assessing hydrogen embrittlement of steel structures. *International Journal of Hydrogen Energy*. 2017;42(16): 11980-11995.

[4] Fassina P, Bolzoni F, Fumagalli G, Lazzari L, Vergani L, Sciuccati A. Influence of hydrogen and low temperature on mechanical behaviour of two pipeline steels. *Engineering Fracture Mechanics*. 2012;81(2): 43-55.

[5] Pluvinagea G, Capelleb J, Meliani M. Pipe networks transporting hydrogen pure or blended with natural gas, design and maintenance. *Engineering Failure Analysis*. 2019;106: 104164.

[6] Chu WY, Li SQ, Hsiao CM, Ju SY. Effect of hydrogen on the apparent yield stress – research on the cause of hydrogen induced delayed plasticity. *Corrosion -Houston*. 1981;37(9): 514-521.

[7] Merson ED, Myagkikh PN, Klevtsov GV, Merson DL, Vinogradov A. Effect of hydrogen concentration and strain rate on hydrogen embrittlement of ultra-fine-grained low-carbon steel. *Advanced Structured Materials*. 2021;143: 159-170.

[8] Birnbaum HK, Sofronis P. Hydrogen-enhanced localized plasticity – a mechanism for hydrogen-related fracture. *Mater. Sci. Eng*. A. 1994;176(1-2): 191-202.

[9] Robertson IM. The effect of hydrogen on dislocation dynamics. *Eng. Fract. Mech*. 2001;68(6): 671–692.

[10] Grigorenko YM, Vasilenko AT. *Theory of Shells of Varying Stiffness. Vol. 4. Methods of Shell Design.* Kiev: Naukova Dumka; 1981. (In Russian)

[11] Vasilenko AT, Emelyanov IG. Determination of the Stressed State of Three-Layer Cylindrical Shells with Allowance for Layer Separation. *International Applied Mechanics*. 1999;35(5): 501-507.

[12] Vasilenko AT, Emelyanov IG, Kuznetsov VY. Stress Analysis of Laminated Shells of Revolution with an Imperfect Interlayer Contact. *International Applied Mechanics*. 2001;37(5): 662-669.

[13] Shevchenko YN, Babeshko ME, Piskun VV. *Solution of the axisymmetric thermoplastic problem for thin-walled and thick-walled bodies of revolution on a Unified Electronic Computer System*. Kiev: Naukova Dumka; 1980. (In Russian)
[14] Shevchenko YN, Prokhorenko IV. *Computational Methods for Shells. Vol. 3. Theory of Elastoplastic Shells with Noisothermal Loading Processes*. Kiev: Naukova Dumka; 1981. (In Russian)
[15] Emel'yanov IG. *Contact problems of the theory of shells.* Yekaterinburg: Ural Branch of the Russian Academy of Sciences; 2009. (In Russian)
[16] Emel'yanov IG, Mironov VI. Strength of Shell Structure Operating in Hydrogenous Media under Pressure. *Transportation Research Procedia*. 2021;54: 484-494.
[17] Godunov SK. Numerical solution of boundary-value problems for systems of linear ordinary differential equations. *Uspexi Matematicheskix Nauk*, 1961;16(3): 171-174. (In Russian)
[18] Grigorenko YM. Using Discrete Fourier Series to Solve Boundary-Value Stress Problems for Elastic Bodies with Complex Geometry and Structure. *International Applied Mechanics*. 2009;45(5): 469-513.
[19] Ilyushin AA. Plasticity. Fundamentals of general mathematical theory. Moscow: Publishing House of the Academy of Sciences of the USSR; 1963. (In Russian)
[20] Gorkunov ES, Zadvorkin SM, Veselov IN, Mitropol'skaya SY, Vichuzhanin DI. Influence of Uniaxial Tension on Magnetic Characteristics of the 12ÉÅ Pipe Steel Exposed to Hydrogen Sulfide. *Russian Journal of Nondestructive Testing*. 2008;44(8): 566-573.
[21] Troshchenko VT, Krasovsky AY, Pokrovsky VV, Sosnovsky LA, Strizhalo VA. *Strength of materials to deformation and destruction. Reference manual. Part 2*. Kiev: Naukova Dumka; 1994. (In Russian)
[22] Golubev YF. *Neural network methods in mechatronics*. Moscow: Mosk. Univ.; 2007 (In Russian).
[23] Aladjev VZ, Shishakov ML, Vaganov VA. *Mathematica: Functional and procedural programming*. 2rd ed. USA: KDP press; 2020.
[24] Ioffe AF. *Selected works. Vol. 1, Mechanical and electrical properties of crystals.* Leningrad: Nauka; 1974. (In Russian)
[25] Emel'yanov IG, Mironov VI, Lukashuk OA. Procedure for solving a physical-mechanical problem of determining stress fields, temperatures and hydrogen concentration. *AIP Conference Proceedings*. 2022; 2456(1): 020026.
[26] Pisarenko GS, Yakovlev AP, Matveev VV. *Handbook. Strength of materials.* Kiev: Naukova Dumka; 1988. (In Russian)

THE AUTHORS

Emelyanov I.G.
e-mail: emelyanov.ig.2016@mail.ru
ORCID: 0000-0002-9733-5485

Kislov A.N.
e-mail: a.n.kislov@urfu.ru
ORCID: 0000-0002-6600-7913

Materials Physics and Mechanics. 2022;50(2): 485-494
Research article
http://dx.doi.org/10.18149/MPM.5032022_11

Submitted: July 17, 2022
Approved: October 7, 2022
Accepted: October 20, 2022

Applications of waste egg shell and egg shell membrane: a review

Naveen Kumar[1]✉, Ajaya Bharti[2], Pradeep Kumar[3]

[1]Mechatronics Engineering Department, Sanjivani College of Engineering, Kopargaon, India-423601

[2]Applied Mechanics Department, Motilal Nehru National Institute of Technology Allahabad, Prayagraj, India-211004

[3]Mechanical Engineering Department, Kashi Institute of Technology, Varanasi, India-221307

✉ kumarnaveenmkcoe@sanjivani.org.in

Abstract. As poultry egg is a rich source of protein, World Health Organisation and all other health experts recommend human beings eat an egg daily. Therefore, there is a very high consumption of eggs throughout the world. The edible part of the egg is covered by a protective hard covering egg shell. With increasing egg consumption, egg shell waste is generated in huge amounts around the globe. Therefore, egg shell waste management became necessary to protect the environment as this can be hazardous. To overcome this problem, researchers and waste management experts are working on the development of techniques by which the egg shell waste can be used efficiently. As egg shell comprises mainly calcium carbonate and phosphate, it can be used for various industrial applications as a rich source of calcium, carbonates, CaO, etc. Because of the advantages of egg shell waste, it can be used for various industrial and household applications such as adsorbent, matrix, or reinforcement materials for making biocomposites, biotemplate, biocoating, glass foams, catalysts, etc. The present work discusses the egg shell and egg shell membrane applications in detail.
Keywords: applications of egg shell waste, egg, egg shell, egg shell membrane, waste management

Acknowledgements. *No external funding was received for this study.*

Citation: Naveen Kumar, Ajaya Bharti, Pradeep Kumar. Applications of waste egg shell and egg shell membrane: a review *Materials Physics and Mechanics*. 2022;50(3): 485-494. DOI: 10.18149/MPM.5032022_11.

1. Introduction

Poultry eggs are a very good source of protein and have been eaten by humans for thousands of years [1]. Egg white (albumen), vitellus (egg yolk), and egg shell are significant components of a poultry egg [2]. The egg shell is the protective covering that prevents the egg white and yolk from the external environment. The structure of the egg is shown in Fig. 1.

The egg shell is made up primarily (94%) of the ceramic material calcium carbonate ($CaCO_3$); its other constituents are organic matter, calcium phosphate, and magnesium carbonate [3,4]. At the same time, the major constituents of the egg shell membrane are protein (60%), glucosamine (10%), chondroitin (9%), and hyaluronic acid (5%). The physical properties of egg shell are significantly dependent on the housing system of laying hens. Lewko et al. studied the effect of the housing system of laying hens on the physical properties of egg contents [5].

© Naveen Kumar, Ajaya Bharti, Pradeep Kumar, 2022.
Publisher: Peter the Great St. Petersburg Polytechnic University
This is an open access article under the CC BY-NC 4.0 license (https://creativecommons.org/li-censes/by-nc/4.0/)

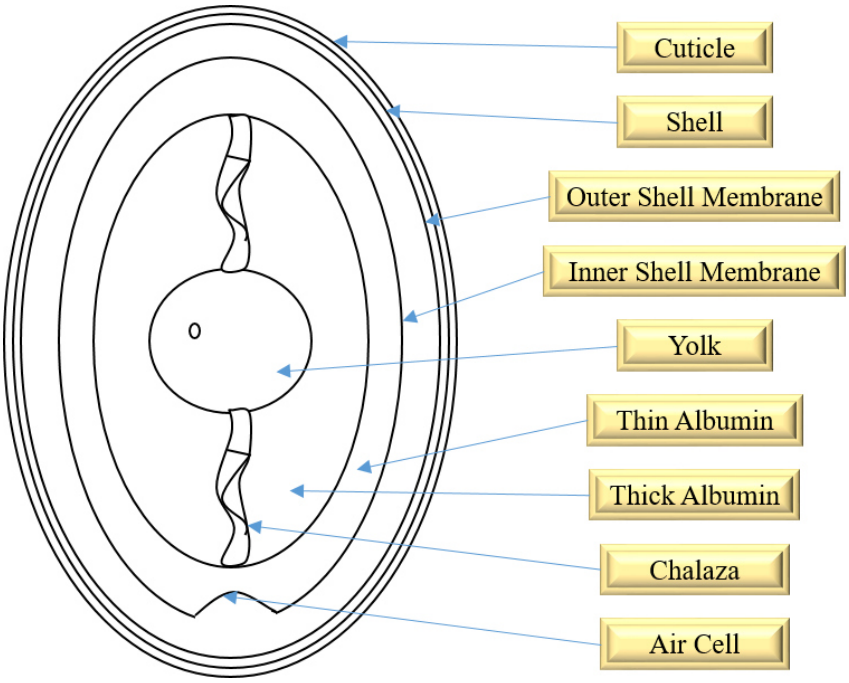

Fig. 1. Egg structure

The physical properties of egg shell are given in

Table *1*. It can be observed that the shell thickness, percentage shell content, and shell weight were highest for free-range laying hens. On the other hand, the cage has an adverse effect on the shell thickness and strength.

Table 1. Physical properties of egg shell [5]

Characteristic	Housing System		
	Cage	Litter	Free Range
Shell content (%)	8.77	9.03	9.93
Shell weight (g)	4.93	5.50	5.76
Shell Thickness (μm)	317.7	333.7	360.1
Density (mg/cm^2)	70.77	74.88	81.01

Due to the very large consumption of eggs, a high volume of waste materials egg shell and the egg shell membrane is generated [6]. It has become a challenge for food industries to dispose of these waste materials. To overcome this problem, researchers around the globe are working to find the application of these waste materials to generate valuable materials. Quina et al. suggested various possible applications of egg shell to reduce the environmental impact [7]. Fig. ***2*** shows the year-wise increasing applications of egg shell and egg shell membrane (captured on 5 October 2022 from sciencedirect.com). Date represents the number of publications year-wise on the use of egg shell and egg shell membrane [2,7]. It can be seen that the number of research on the use of egg shell and egg shell membranes during the year 1999-2002 was relatively very less (1294). From 1999 to 2022, research on egg shell and egg shell membranes have been increased by more than 477%. Still, there is a need for further research to enhance the utilization of waste egg shell and egg shell membranes.

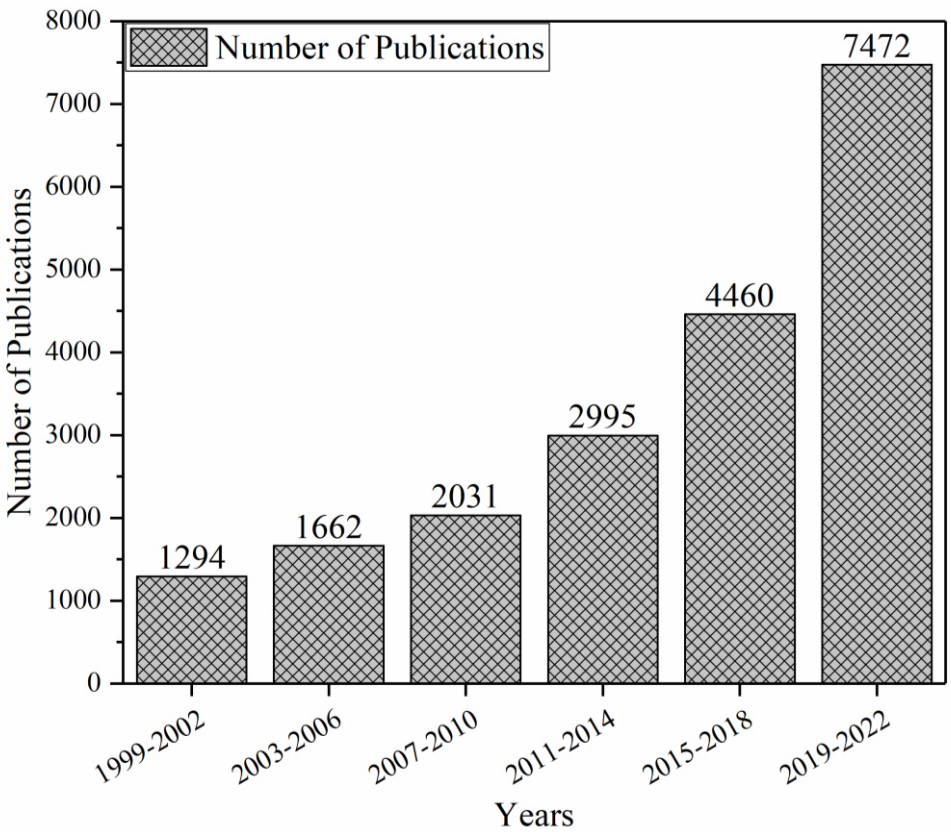

Fig. 2. Increasing applications of egg shell and egg shell membrane

Today egg shell and egg shell membranes are used for various industrial applications [8]. Industrial applications of egg shell and egg shell membranes can be divided into two categories i.e., as raw material and for operating supply. Applications of egg shell such as matrix or reinforcement materials for biocomposites, biotemplate, biocoating, glass foams, etc. belong to the raw material category [9,10]. On the other hand, applications of egg shell such as adsorbent or catalyst belong to the operating supply category.

One of the important industrial applications of waste egg shell is as a purifier. Egg shell is a very good adsorbent. Egg shell is used for the purification of water and other solvents [2]. Because of the high absorbance of egg shells, Xavier et al. used waste egg shells to remove arsenic from liquid industrial waste [11]. The use of waste egg shells as an adsorbent is discussed in detail in the next section.

Another important industrial application of waste egg shell is in the synthesis of carbon dots. Carbon dots are prepared using either a bottom-up approach or a top-down approach. In the bottom-up approach, pyrolysis of waste egg shells is done using microwave heating to produce carbon [12]. Waste egg shells are also used for the fabrication of various metal oxides. Ramya et al. effectively fabricated TiO_2 using waste egg shells [13].

Apart from industrial applications, egg shells can be used for household purposes. As egg shells are rich in calcium and mineral, these can be used to feed wild birds and chickens. The bitterness of coffee can also be reduced by adding crushed egg shells to ground coffee. Crushed egg shells can also be used as a rich source of minerals for houseplants. Also, egg shells to soil increase porosity and make soil aerated. Crushed egg shells can also be used as a natural abrasive for cleaning cooking utensils and other pots because these are hard and brittle. Heat-treated egg shells (at around 350°C for 8-10 minutes) after grinding to fine powder can be added to juice as a calcium supplement. Egg shells, after fine crushing, can be

added to paint for decorative wall texture. Therefore, there is no need to through used egg shells. Egg shells and egg shell membranes can be reused.

Considering various advantages of egg shells and egg shell membranes, the present work mentioned industrial applications of egg shell and egg shell membranes such as adsorbent, matrix or reinforcement materials for making biocomposites, biotemplate, biocoating, glass foams, and catalyst, are discussed in detail.

2. Applications of egg shell and egg shell membrane

Various industrial applications of egg shell and egg shell membranes are shown in Fig. 3. These applications are discussed in detail in the following sub-sections.

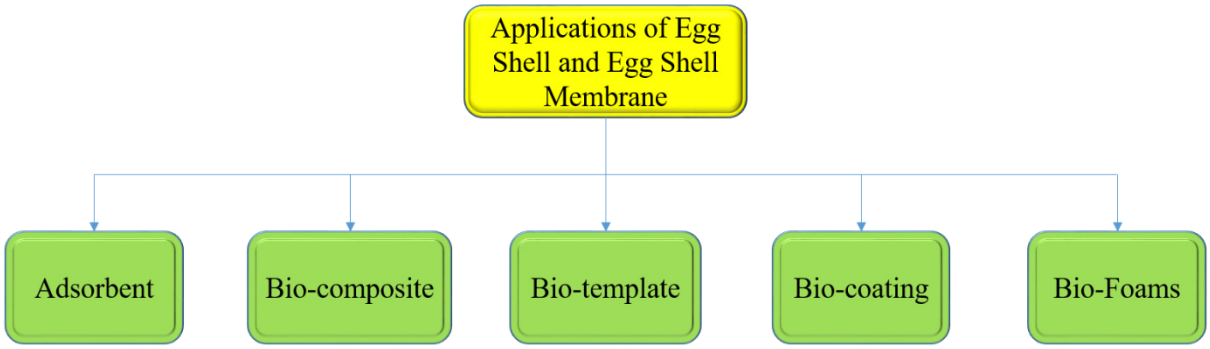

Fig. 3. Applications of egg shell and egg shell membrane

As an adsorbent. Egg shell and egg shell membranes have been purifying wastewater for ten years [2,14]. Hazardous chemicals (organic or inorganic) from water can be removed by adsorbing them on egg shell and egg shell membranes because of the inherent properties of an adsorbent [15,16]. Egg shell membrane is a better adsorbent than the egg shell due to the presence of various basic functional groups on its surface such as (-OH), (-COOH), (-SH), (-NH_2), (-$CONH_2$), etc. [17]. Egg shell membrane can be crushed and milled to nanoparticle size and can be used for removing very harmful lead and cadmium ions from water.

Abdi et al. used egg shells to bleach soybean oil [18]. It was observed that the 2wt.% egg shell powder decreased carotenoids amount by nearly 83%, and at the same time, chlorophyll content decreased by nearly 47%. Therefore, egg shells can be recommended as a very good adsorbent and bleaching agent for edible oils as it efficiently removes unwanted contents from oils.

As a matrix or reinforcement for fabricating bio-composites. As egg shell is composed mainly of ceramic material calcium carbonate, it found applications |as a reinforcement material for making low-cost biocomposites [19]. Egg shell is also being utilised as a matrix material to fabricate novel bio-composites. Agarwal et al. fabricated coconut jute fibre reinforced egg shell ceramic biocomposites by powder processing technology [1]. Gelatin gel was used as a binder. It was observed that the coconut jute fibre formed interfacial bonds with egg shell particulate in the gelatin gel matrix. The highest hardness was obtained for egg shell biocomposites reinforced with one wt.% coconut jute fibre.

Lertcumfu et al. also fabricated ceramic biocomposites [3]. Hydroxyapatite/beta-tricalcium phosphate composites with different compositions were fabricated by solid-state technique. Calcium carbonate used for making composites was obtained from cockle and egg shell. Calcium carbonate was then reacted with diammonium phosphate to produce hydroxyapatite and beta-tricalcium phosphate. Obtained hydroxyapatite and beta-tricalcium phosphate were then mixed in ethanol by mechanical mixing. After mixing, powders were compacted and heat-treated to form the bio-composites.

Okoye et al. fabricated egg shell reinforced aluminium matrix composites [6]. Composites with 15 wt.% carbonised egg shells were fabricated by stir casting technique. Bose et al. also fabricated aluminium matrix composites by reinforcing carbonised egg shell and snail shells and SiC by stir casting [20]. It was observed that the addition of egg shells in the aluminium matrix enhanced the mechanical strength and corrosion resistance. At the same time, the cost of the composite decreased.

Reddy et al. used egg shells as a cement replacement in concrete structures as the cost of cement increases due to its high demand and consumption. It was observed that the compressive strength increased with the addition of 10wt.% of concrete in cement [21].

Viswanath et al. studied the effect of egg shells on the mechanical properties of polyester composites [22]. It was observed the mechanical properties improved significantly with the addition of 12wt.% egg shell. Channabasavanna et al. also observed a similar effect of egg shell on the mechanical properties of polymer composites [23].

Asha et al. fabricated polymer matrix composites by reinforcing egg shell powder [24]. Composites were fabricated by an injection molding technique. It was observed that the mechanical properties enhanced significantly with the addition of egg shell powder.

As a bio-template. Egg shell and egg shell membranes are also used as a bio-template to produce bio-morphic materials. The natural structure of egg shell and egg shell membranes is replicated by various techniques to produce functional materials. Sabu et al. fabricated bio-morphic alumina using an egg shell membrane as a template [9]. Fibrous alumina was prepared by replicating the fibrous structure of the egg shell membrane. Egg shell membrane was shocked in a hydrated aluminium nitrate solution and calcinated over a temperature range (400°C-1200°C).

As a bio-coating material. Bio-coating is done on the implants to increase their life. Currently, hydroxyapatite is used for coating implant material, but its cost is very high [25,26,27,28]. So, researchers are working on developing low-cost bio-coating material for bio-implants [29,30,31]. Venkatesh et al. used egg shell, alumina, and seashell powders to form bio-coating on polyvinyl chloride, Teflon, and polyurethane [10]. Venkatesh et al. also alumina, egg shell, and sea shell bio-coated stainless steel 316L and Ti-6Al-4V bio-implant materials [32]. It was observed that the coating of egg shell on the implant materials was more uniform and free from defects than the coating of alumina and sea shell due to its high cohesiveness.

Kathiravan et al. produced activated charcoal from egg shell to coat paper for humidity sensing [33]. It was observed that the sensor was fast responding with very less recovery time. Therefore, egg shells can be used to produce activated charcoal-based eco-friendly humidity sensors.

Fine egg shell powder can also be used to coat ferrous materials to prevent rusting. Also, cooking utensils holders can be coated with egg shell to reduce the heat transfer rate as egg shell is ceramic in nature and hence have poor thermal conductivity and high thermal stability. Egg shell powder is also used for texturing of house walls by mixing fine grinded egg shell powder with paint. The addition of egg shell in paint also enhances the anti-bacterial properties of walls. Therefore, coating of egg shell is very useful.

As a foaming agent. The egg shell is composed mainly of calcium carbonate (95%); it is also used as a foaming agent to fabricate glass foams. On heating to a temperature of around 600°C -800°C, oxidation of egg shells takes place, and CO_2 gas is released, which expands and foaming in the material takes place. Fernandes et al. used egg shell waste as a foaming agent to produce glass foams from cathode ray tube glass waste [34,35].

Egg shell waste after crushing can also be used as a space holder material to produce copper, iron, and steel foams by powder metallurgy technique [36,37,38,39,40,41]. During sintering of the green compacts of the above-mentioned materials above 800°C, carbonate

will oxidise to release CO_2. Produced CO_2 will try to escape through the pores present in the materials and as a result foaming in the material will take place.

As a raw material for bio-foams. Egg shell ceramic and other materials such as silica are also for fabricating glass-ceramic foams. Ayawanna et al. fabricated porous glass-ceramic material for orbital implant using egg shell waste, SiO_2, and $NaCO_3$ by foam replication method [42]. Glass-ceramic implants fabricated from egg shells had an open-macropore structure and more stability than the glass-ceramic implants produced from commercial $CaCO_3$.

Leszczynska et al. fabricated polyurethane foams with egg shells as a filler material [43]. It was observed that the addition of egg shells reduced the bacterial infection on the foam surface.

As a catalyst. Egg shell and egg shell-derived materials such as CaO are also used to catalyse various chemical reactions [44,45]. Zhang et al. derived CaO from egg shell and used it to catalyse the bio-diesel formation from chicken feather meal oil [46]. It was observed that the 95% conversion of chicken feather meal oil into bio-diesel just took place in 5 minutes. Therefore, egg shell-derived CaO proved to be an efficient and low-cost catalyst. Rahman et al. also used egg shells to produce Zn/CaO catalyst to produce biodiesel [47]. The Zn/CaO catalyst proved to be an efficient catalyst for the trans-esterification of waste-frying oil to biodiesel.

Le et al. studied the catalytic effect of egg shell on hydrocarbon processing [48]. It was observed that the use of egg shells significantly improved the catalysis of hydrocarbon processing.

Proenca et al. also used egg shells as a catalyst to convert macauba oil into methyl esters [49]. It was observed that the use of egg shells as a catalyst resulted in a 91% conversion of macauba oil into methyl esters.

3. Conclusions

The following conclusions are drawn after the detailed literature survey on the reuse of egg shell and egg shell membrane waste:

- Egg shell waste is mounting because of the very high consumption of eggs.
- Researchers and waste management officials are looking for the applications of egg shell waste so that it can be used efficiently without affecting the environment.
- Egg shell and egg shell membranes are very useful for industrial applications and household purposes.
- The egg shell powder can be used efficiently as an adsorbent and bleaching agent.
- Egg shell can be used to produce other necessary chemicals such as activated charcoal and CaO.
- Egg shell powder is also very useful for fabricating bio-composites and bio-foams.
- Egg shell and egg shell derived chemicals are very effective in catalysing oil conversion into biodiesel.
- Therefore, the reuse of egg shell waste is very beneficial in cost-saving and environmental protection.

4. Future scope

As discussed above, egg shell and egg shell membranes can be used for various industrial applications such as catalyst, reinforcement, raw material, adsorbent, etc. Still, there is a need for further research to enhance the percentage utilization of egg shell and egg shell membranes. As egg shell an excellent adsorbent, the use of egg shell as an environment purifier should be deeply investigated so that air pollution in cities can be controlled.

References

1. Agarwal M, Shukla KN. Processing and interfacial effect of gelatin gel on coconut jute reinforced egg shell bio-composite. *Materials Today: Proceedings.* 2020;26(2): 520-524.
2. Mittal A, Teotia M, Soni RK, Mittal J. Applications of egg shell and egg shell membrane as adsorbents: A review. *Journal of Molecular Liquids*. 2016;223: 376-387.
3. Lertcumfu N, Jaita P, Manotham S, JarupoomP, Eitssayeam S, Pengpat K, Rujijanagul G. Properties of calcium phosphates ceramic composites derived from natural materials. *Ceramics International*. 2016;42: 10638-10644.
4. Tsai WT, Yang JM, Lai CW, Cheng YH, Lin CC, Yeh CW. Characterization and adsorption properties of eggshells and eggshell membrane. *Bioresource Technology*. 2006;97(3): 488-493.
5. Lewko L, Gornowicz E. Effect of Housing System on Egg Quality in Laying Hens. *Annals of Animal Science*. 2011;11(4): 607-616.
6. Okoye CCN, Uzochukwu CU. RSM and ANN modeling for production of Al 6351/ egg shell reinforced composite: Multi objective optimization using genetic algorithm. *Materials Today Communications*. 2020;22: 100674.
7. Quina MJ, Soares MAR, Ferreira RQ. Applications of industrial eggshell as a valuable anthropogenic resource. *Resources, Conservation and Recycling*. 2017;123: 176-186.
8. Park S, Choi KS, Lee D, Kim D, Lim KT, Lee KH, Seonwoo H, Kim J. Eggshell membrane: Review and impact on engineering. *Biosystems Engineering*. 2016;151: 446-463.
9. Sabu U, Rashad M, Logesh G, Kumar K, Lodhe M, Balasubramanian M. Development of biomorphic alumina using egg shell membrane as bio-template. *Ceramics International*. 2018;44(5): 4615-4621.
10. Venkatesh N, Hanumantharaju HG, Aravind, Harish. A Study of Bio-Active Coating of Al2O3, Egg and Sea Shell Powder On Pvc, Teflon, And Polyurethane. *Materials Today: Proceedings*. 2018;5: 13392-13399.
11. Xavier LF, Mohan MK, Thomas S, Josen V. Removal of arsenic using ecofriendly egg shell and black toner powder. *Materials Today: Proceedings*. 2022;65(9): 3946-3950.
12. Ramalechume C, Krishnaveni R, Sivaramakrishnan T, Vijayarohini P, Mercy C, Swamidoss A. Synthesis of carbon dots from waste materials: analytical applications. In *Carbon Dots in Analytical Chemistry*. Elsevier;2022. p.225-239.
13. Ramya S, Vijayakumar S, Vidhya E, Bukhari NA, Hatamleh AA, Nilavukkarasi M, Vijayakumar S, Pham TH. TiO2 nanoparticles derived from egg shell waste: Eco synthesis, characterization, biological and photocatalytic applications. *Environmental Research*. 2022;2014: 113829.
14. Sun Y, Yang G, Zhang L. Hybrid adsorbent prepared from renewable lignin and waste egg shell for SO2 removal: Characterization and process optimization. *Ecological Engineering*. 2018;115: 139-148.
15. Ruhaimi AH, Aziz MA. Spherical CeO2 nanoparticles prepared using an egg-shell membrane as a bio-template for high CO2 adsorption. *Chemical Physics Letters*. 221;779: 138842.
16. Park B, Kim J, Ghoreishian SM, Rethinasabapathy M, Huh YS, Kang SM. Generation of multi-functional core-shell adsorbents: simultaneous adsorption of cesium, strontium and rhodamine B in aqueous solution. *Journal of Industrial and Engineering Chemistry*. 2022;112: 201-209.
17. Shi Y, Liu G, Li M, Wang L. Egg shell waste as an activation agent for the manufacture of porous carbon. *Chinese Journal of Chemical Engineering*. 2022;28(3): 896-900.
18. Abdi E, Gharachorloo M, Ghavami M. Investigation of using egg shell powder for bleaching of soybean oil. *LWT*. 2021;140: 110859.

19. Manikandan R, Abbas SM, Sathish S, Ahamed JI, Ahamed AT, Miandad MKJ, Thovheed SJ. Experimental analysis of basalt fiber reinforced egg shell/water hyacinth loaded epoxy composites. *Materials Today: Proceedings*. 2021;45(2): 1660-1663.
20. Bose S, Pandey A, Mondal A. Comparative analysis on aluminum-silicon carbide hybrid green metal matrix composite materials using waste egg shells and snail shell ash as reinforcements. *Materials Today: Proceedings*. 2018;5: 27757-27766.
21. Reddy YM, Prasad JSR, Balguri PK. Durability and strength properties of concrete by using egg shell powder and copper slag. *Materials Today: Proceedings*. 2022;62: 2996-3000.
22. Viswanath SB, Kumar SS, Sudarsan D, Muthalagu R. Mechanical attributes of coir fibre, rice husk and egg shell reinforced hybrid polyester composites. *Materials Today: Proceedings*. 2021;46(1): 874-877.
23. Channabasavanna SG, Gowda TV, Manjunatha LH, Shekar PRS, Kumar SMC. Development and testing of glass/kenaf inter-ply hybrid polymer composites with egg shell powder as filler. *Materials Today: Proceedings*. 2021;45(1): 270-276.
24. Asha A, Sekhar VC. Investigation on the Mechanical Properties of Egg Shell Powder Reinforced Polymeric Composites. *International Journal of Engineering Research & Technology*. 2014;3(12): 288-291.
25. Dong-Ping L, Yan-Hong L, Bao-Xiang C. Surface properties of diamond-like carbon films prepared by CVD and PVD methods. *Chinese Physics*. 2006;15(3): 575.
26. Hsiung JC, Tzeng J, Kung K, Chen H. A Study of Thermal Spray Coating on Artificial Knee Joints. *Life Science Journal*. 2013;10(2): 236-241.
27. León B, Jansen J. *Thin Calcium Phosphate Coatings for Medical Implants*. Springer; 2009.
28. Pesode PA, Barve SB. Recent advances on the antibacterial coating on titanium implant by micro-Arc oxidation process. *Materials Today: Proceedings*. 2021;47: 5652-5662.
29. Qiao Y, Liu X. Biocompatible Coating. In: *Comprehensive Materials Processing*. China; 2014. p.425-447.
30. Radin SR, Ducheyne P. Plasma spraying induced changes of calcium phosphate ceramic characteristics and the effect onin vitro stability. *Journal of Materials Science: Materials in Medicine*. 1992;3: 33-42.
31. Ritwik A, Saju KK, Binsi PK, Reghuraj AR. Development of biocompatible coating on Ti6Al4V implant materials using chitosan extracted from shellfish waste. *Materials Today: Proceedings*. 2021;47: 5209-5216.
32. Venkatesh N, Hanumantharaju HG, Aravind, Jacob. A Study of Bio-Active Coating of Al2O3, Egg and Sea Shell Powder on Ss316l and Ti-6al-4v. *Materials Today: Proceedings*. 2018;5: 22687-22693.
33. Kathiravan D, Huang BR, Saravanan A. Surface modified highly porous egg-shell membrane derived granular activated carbon coated on paper substrate and its humidity sensing properties. *Materials Chemistry and Physics*. 2022;277: 125486.
34. Fernandes HR, Andreol F, Barbieri L, Lancellotti I, Pascual MJ, Ferreira JMF. The use of egg shells to produce Cathode Ray Tube (CRT) glass foams. *Ceramics International*. 2013;39(8): 9071-9078.
35. Fernandes HR, Ferreira DD, Andreola F, Lancellotti I, Barbieri L, Ferreira JMF. Environmental friendly management of CRT glass by foaming with waste egg shells, calcite or dolomite. *Ceramics International*. 2014;40: 13371-13379.
36. Kumar N, Bharti A. Review on Powder Metallurgy: A Novel Technique for Recycling and Foaming of Almunium-based Materials. *Powder Metallurgy and Metal Ceramics*. 2021;60(1-2): 52-59.

37. Kumar D, Bharti A, Azam SM, Kumar N, Tripathi H. Investigations of Mechanical Properties of Copper Matrix Hybrid Composite. In: *Advances in Mechanical Engineering*. Singapore. Springer; 2020. p.671-676.
38. Kumar N, Bharti A, Saxena KK. A re-analysis of effect of various process parameters on the mechanical properties of Mg based MMCs fabricated by powder metallurgy technique. *Materials Today: Proceedings*. 2020;26: 1953-1959.
39. Kumar N, Bharti A, Saxena KK. A re-investigation: Effect of powder metallurgy parameters on the physical and mechanical properties of aluminium matrix composites. *Materials Today: Proceedings*. 2021;44: 2188-2193.
40. Kumar N, Bharti A, Tripathi H. Investigation of Microstructural and Mechanical Properties of Magnesium Matrix Hybrid Composite. In: *Advances in Mechanical Engineering*. 2020. p.661-669.
41. Kumar N, Bharti A, Dixit M, Nigam A. Effect of Powder Metallurgy Process and its Parameters on the Mechanical and Electrical Properties of Copper-Based Materials: Literature Review. *Powder Metallurgy and Metal Ceramics*. 2020;59: 401-410.
42. Ayawanna J, Kingnoi N, Laorodphan N. A feasibility study of egg shell-derived porous glass–ceramic orbital implants. *Materials Letters*. 2019;241: 39-42.
43. Leszczynska M, Ryszkowska J, Szczepkowski L, Kuranska M, Prociak A, Leszczynski MK, Gloc M, Antos-Bielska M, Mizera K. Cooperative effect of rapeseed oil-based polyol and egg shells on the structure and properties of rigid polyurethane foams. *Polymer Testing*. 2020;90: 106696.
44. Thakur S, Singh S, Pal B. Time-dependent growth of CaO nano flowers from egg shells exhibit improved adsorption and catalytic activity. *Advanced Powder Technology*. 2021;32(9): 3288-3296.
45. Ge S, Brindhadevi K, Xia C, Elesawy BH, Elfasakhany A, Unpaprom Y, Doan HV. Egg shell catalyst and chicken waste biodiesel blends for improved performance, combustion and emission characteristics. *Fuel*. 2021;306: 121633.
46. Zhang M, Ramya G, Brindhadevi K, Alsehli M, Elfasakhany A, Xia C, Chi NTL, Pugazhendhi A. Microwave assisted biodiesel production from chicken feather meal oil using Bio-Nano Calcium oxide derived from chicken egg shell. *Environmental Research*. 2022;205: 112509.
47. Rahman WU, Yahya SM, Khan ZA, Khan NA, Halder G, Dhawane SH. Valorization of waste chicken egg shells towards synthesis of heterogeneous catalyst for biodiesel production: Optimization and statistical analysis. *Environmental Technology & Innovation*. 2021;22: 101460.
48. Le TT, Shilpa K, Choongsze, Lee, Han S, Weiland C, Bare SR, Dauenhauer PJ, Rimer JD. Core-shell and egg-shell zeolite catalysts for enhanced hydrocarbon processing. *Journal of Catalysis*. 2022;405: 664-675.
49. Proenca BDSG, Fioroto PO, Heck SC, Duarte VA, Filho LC, Feihrmann AC, Beneti SC. Obtention of methyl esters from macauba oil using egg shell catalyst. *Chemical Engineering Research and Design*. 2021;169: 288-296.

THE AUTHORS

Naveen Kumar
e-mail: kumarnaveenmkcoe@sanjivani.org.in
ORCID: 0000-0002-6918-4384

Ajaya Bharti
e-mail: abharti@mnnit.ac.in
ORCID: 0000-0003-2809-9674

Pradeep Kumar
e-mail: pradeepsachan@kashiit.ac.in
ORCID: 0000-0002-3554-234X

Materials Physics and Mechanics. 2022;50(3): 495-508
Research article
http://dx.doi.org/10.18149/MPM.5032022_12

Submitted: July 29, 2022
Approved: October 11, 2022
Accepted: November 10, 2022

Anisotropic mechanical properties of elastomeric nanocomposites filled by carbon black, few-layer graphene, and carbon nanotubes

O.K. Garishin[1]✉, A.L. Svistkov[1], A.P. Voznyakovskii[2], I.M. Tchypkina[2], A.Yu. Neverovskaya[2], V.V. Shadrin[1]

[1]Institute of Continuous Media Mechanics of the Ural Branch of Russian Academy of Science, 1, Academician Korolev Street, Perm, Russia, 613013

[2]Federal unitary state enterprise "Lebedev Research Institute for Synthetic Rubber", 1, Gapsal'skaya St., St. Petersburg, Russia, 198035

✉ gar@icmm.ru

Abstract. The mechanical properties of nanocomposites based on styrene-butadiene rubber with fillers of carbon black, few-layer graphene and single-walled and multi-walled carbon nanotubes have been studied. Carbon nanotubes were subjected to preliminary purification according to a special technology developed by the authors using self-propagating high-temperature synthesis. It has been established that in elastomers filled with single-walled carbon nanotubes, the anisotropy of mechanical properties may appear, which is expressed in a significant increase of material rigidity and growth of dissipative tensile losses in the direction corresponding to the movement of vulcanized rubber compound during rolling. This effect was absent in composites filled with carbon black and few-layer graphene.
Keywords: styrene-butadiene rubber, few-layer graphene, single-walled and multi-walled carbon nanotubes, SHS purification of carbon nanotubes, cyclic loading, viscoelasticity, anisotropy of mechanical properties

Acknowledgements. *Regional Grant of RFBR and Perm Territory, project number 20-48-596013.*

Citation: Garishin OK, Svistkov AL, Voznyakovskii AP, Tchypkina IM, Neverovskaya AYu, Shadrin VV. Anisotropic mechanical properties of elastomeric nanocomposites filled by carbon black, few-layer graphene, and carbon nanotubes. *Materials Physics and Mechanics*. 2022;50(3):495-508. DOI: 10.18149/MPM.5032022_12.

1. Introduction

In recent decades, the use of nanosized fillers in elastomeric composites has become increasingly widespread in various industries, successfully competing with traditionally used materials [1,2].

Historically, one of the first, and still the most common nanofillers is carbon black (CB). The addition of CB into an elastomer significantly improves its mechanical characteristics (especially strength and deformability) [3-6]. Its particles are globules (3D filler) consisting of degraded graphite structures. These globules can form strong associations of several dozen particles ranging in size from 13 to 350 nm, and these, in turn, stick together into even larger, but much less durable agglomerates with sizes up to a micron. That is, these

© O.K. Garishin, A.L. Svistkov, A.P. Voznyakovskii, I.M. Tchypkina, A.Yu. Neverovskaya, V.V. Shadrin, 2022.
Publisher: Peter the Great St. Petersburg Polytechnic University
This is an open access article under the CC BY-NC 4.0 license (https://creativecommons.org/li-censes/by-nc/4.0/)

are structures that are very complex in their morphology. Today, CB is more often used not in pure form but in conjunction with other fillers [7-12].

The effects of carbon black used in elastomeric composites are well studied, and further progress requires the search for new non-traditional types of fillers. One of the promising directions is the use of carbon in other allotropic states. These are mainly detonation nanodiamonds, graphene, and its oxides, as well as carbon nanotubes.

Detonation nanodiamonds (3D filler) are synthesized by the explosive decomposition of powerful mixed explosives with a negative oxygen balance in a non-oxidizing environment. Such explosive compositions are both a source of energy and carbon. Detonation nanodiamonds combine nanosize (4-6 nm), chemical resistance of the core, and chemical activity of the peripheral shell. These fillers are currently widely used in the production of filled elastomers [13-16].

Graphene particles are 2D plates made of one or more layers of this material. According to its structure, graphene is a two-dimensional crystal consisting of a single layer of carbon atoms assembled into a hexagonal lattice. Graphene filler, as well as its oxides [11,17], are widely used in the production of elastomeric composites, both in pure form and together with other fillers [13,16,18-20].

Carbon nanotubes (it would be more correct to call them graphene nanotubes) are 1D filler in the form of randomly oriented flexible fibers from 2D single-crystal graphene plates "rolled into a tube" [21,22]. Depending on the synthesis technology, both single-walled (SWCNT) [23-25] and multi-walled carbon nanotubes (MWCNT) can be obtained – several SWCNTs (usually 15-20) inserted one into the other) [26-31]. It is still impossible to justify which type of nanotubes will be preferable for use as fillers in elastomers. Until recently, the advantage of MWNTs was a good development of the technology of their synthesis and, accordingly, unlike SWNTs, an acceptable price for real application. However, the development in 2013 by the firm "OCSiAl" (Novosibirsk, Russia) of a high-performance technology for the synthesis of single-walled carbon nanotubes largely leveled this shortcoming.

Quite often, nanotubes are used as a second filler [11,12,32-35]. Also, [36] described the combined use of a mixture of SWCNTs and MWCNTs in silicone elastomers.

Elastomeric nanocomposites are the subject of intensive fundamental and applied research both at the structural and macro levels today. In experimental studies of the internal structure of polymer nanocomposites, both electronic (scanning – SEM, transmission – TEM) [37-39] and atomic force microscopes (AFM) [37,41] are widely used, and quite often they are used together. The inner structure geometry is studied with the help of electron microscopy, and atomic force microscopes make it possible to obtain additional information about the "local" physical and mechanical properties of the material at the microlevel (which can differ very significantly from the macroscopic ones [42]).

At the macro level, elastomeric nanocomposites exhibit complex mechanical behavior. They are able to withstand significant deformations (up to hundreds of percent) without loss of performance, and can demonstrate elastic, viscous, and plastic properties. Therefore, in experimental studies of these materials, in addition to standard monotonic tension-compression tests, special methods with complex loading trajectories are often used. As usual, they are based on the cyclic deformation of samples with a variable amplitude over deformations and periodic stops to reveal relaxation processes and creep [10,13,43-51]. Such an approach, which makes it possible to obtain complex data on the viscoelastic and elastoplastic properties of a material in one test, was used in the experiments presented in this study.

The article describes the technology for producing elastomeric composites with carbon black fillers, as well as single-walled and multi-walled carbon nanotubes. Its novelty lies in

the method proposed by the authors for the purification of nanotubes from harmful impurities by the method of self-propagating high-temperature synthesis (SHS). Chemical reactions under the conditions of the SHS process proceed according to a specific mechanism of non-isothermal branched-chain processes, which are characterized by the combined action of two fundamentally different factors accelerating the process - avalanche multiplication of active intermediate particles and self-heating. Branched-chain ignition, in contrast to thermal one, is caused by an avalanche multiplication of active intermediate products – free atoms, radicals, and sometimes also excited particles – in their rapid reactions with the initial reagents and among themselves. Physically, SHS is a process of moving a wave of a strongly exothermic reaction through a mixture of reactants (oxidizing agent and reducing agent), in which heat release is localized in a layer and is transferred from layer to layer by heat transfer. The SHS version we use refers to the "solid-gas" systems, that is, the active component of the process is not the oxidizer itself, but the gaseous products of its thermal decomposition. This dramatically reduces the requirements for reactors, both in terms of design and thermal stability. To date, the most common method of such purification is oxidation with strong acids [52-55]. In this case, the impact of aggressive oxidizing media on SWCNTs and MWCNTs often leads to both an increase in the number of structural defects and the disintegration of the tubes themselves. It is also impossible not to take into account the inconsistency of such a technique with modern stringent environmental requirements – the formation of a significant amount of acid effluents, the disposal of which is a separate task.

The approach proposed, based on the use of self-propagating high-temperature synthesis (SHS) in the production of elastomeric nanocomposites with fillers from single-walled and multi-walled carbon nanotubes in combination with carbon black (or few-layer graphene), is largely free from these disadvantages, which makes it rather promising.

It is established that the resulting composite samples are significantly anisotropic in terms of viscoelastic properties. This effect was studied in detail in this article using specially developed by us techniques of mechanical testing.

2. Materials, equipment, and experimental technique

Materials. The main object of research was elastomeric nanocomposites containing carbon black or few-layer graphene and combinations of these fillers with single-walled and multi-walled carbon nanotubes.

A styrene-butadiene rubber SBR-1500 (Russian analog is SKMS-30ARKM-15) was chosen as a binder (matrix). It is a well-known elastomer that is commercially produced. For example, it is, widely used in car tires and various rubber shock absorbers (i.e., in rather complex and difficult operating conditions).

Industrial carbon black of the N-330 grade with a particle size of 28-36 nm and a specific surface area of 82 m^2/g was taken as 3D filler.

A few-layer graphene (FLG) was applied as the 2D filler. It was manufactured according to the original method developed by the authors from NIISK [56]. The method is based on the SHS synthesis of graphene nanostructures from hydrolytic lignin, a natural biopolymer that is a waste product of the woodworking industry. The characteristic particle size of few-layer graphene was about 100-300 nm, and the specific surface area was 499 m^2/g.

Two types of carbon nanotubes were used as a 1D filler: single-walled TUBALL (manufactured by OCSiAl) and multi-walled (manufactured at the Institute of Catalysis, Siberian Branch, Russian Academy of Sciences). Both manufacturers are from Novosibirsk, that is, these are domestic developments. The characteristic dimensions of SWCNT and MWCNT (according to the manufacturer data) are presented in Table 1 (d is the nanotube diameter, L – its length, S – its specific surface area).

Table 1. Characteristic dimensions of single-walled and multi-walled carbon nanotubes

Filler	*d*, nm	*L*, μm	*S*, m^2/g	Nested layers (walls) number
SWCNT	1.6±0.4	> 5	500–1000	1
MWCNT	10–12	30–40	260±15	5–15

Purification of carbon nanotubes. It should be noted that carbon nanotubes contain rather significant amounts of amorphous carbon and undesirable inorganic impurities (mainly metallic) formed during the technological process. For example, according to the information provided by OCSiAl, the mass fraction of SWCNTs in dry powder was only 75%-wt. The rest accounted for inorganic impurities (9%-wt.) and carbon of unknown structure (16%-wt.). For MWCNTs, the situation with impurities was approximately similar. Therefore, it is necessary to somehow remove these impurities for further practical application of carbon nanotubes as composite fillers.

The method developed by the authors from NIISK for the purification of carbon nanotubes using self-propagating high-temperature synthesis (SHS) is largely devoid of the disadvantages inherent in more conventional methods based on the use of strong acids. This approach involves simultaneous exposure of nanotubes to extremely high temperatures generated by the SHS process in an aggressive oxidizing environment [24]. With this treatment, amorphous carbon passes into the gas phase and is removed from the reaction zone, while metal impurities are converted into nitrate salts (water-soluble form) and washed with water.

The purification process began with the addition of crushed ammonium nitrate in a ratio of 1/1 to a sample of the initial nanotubes. NH_4NO_3 plays the role of a precursor that generates powerful oxidizing agents upon thermal degradation. Thus, under conditions of rapid heating to a temperature of (220±10)°C, ammonium nitrate decomposes into highly active atomic nitrogen, oxygen, and water. The reaction products may also contain a trace amount of NO_2 and NO.

The mixture obtained after stirring was transferred into a heat-resistant vessel and placed in a bath preheated to 220°C. The passage of the SHS process reaction was judged by the power of gas evolution. After the onset of intense gas formation, the heating was turned off, and the reaction continued in an autonomous mode. The SHS process was considered completed when the evolution of gases from the heated mixture completely stopped. Next, the resulting powder was washed with distilled water and dried in a thermostat to constant weight.

Figures 1(a) (scale size 5 μm) and 1(b) (scale size 1 μm) show images of dry SWCNT powder taken by scanning and transmission electron microscopy before (SEM) and after (TEM) SHS purification, respectively.

A visual analysis of these pictures showed that the SHS method, although it does not allow the complete destruction of SWCNT aggregates to the level of individual nanotubes, still significantly increases the dispersity of SWCNTs compared to that obtained using the "OCSiAl" technology.

Figure 2 shows micrographs of dry MWCNT powder after cleaning by the SHS method, taken using a transmission electron microscope with different resolutions. The frame size in Fig. 2(a) is 500 nm, in Fig. 2(b) – 100 nm, and in Fig. 2(c) – 10 nm. It can be seen from them that the multi-walled carbon nanotubes after cleaning are quite well dispersed over the volume of the powder.

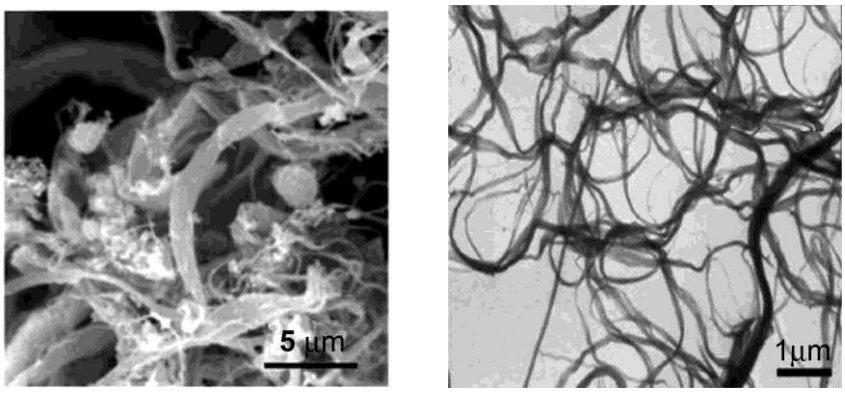

a *b*

Fig. 1. Electron micrographs of the initial dry SWCNT powder (SEM) (*a*) and purified by the SHS method (TEM) (*b*)

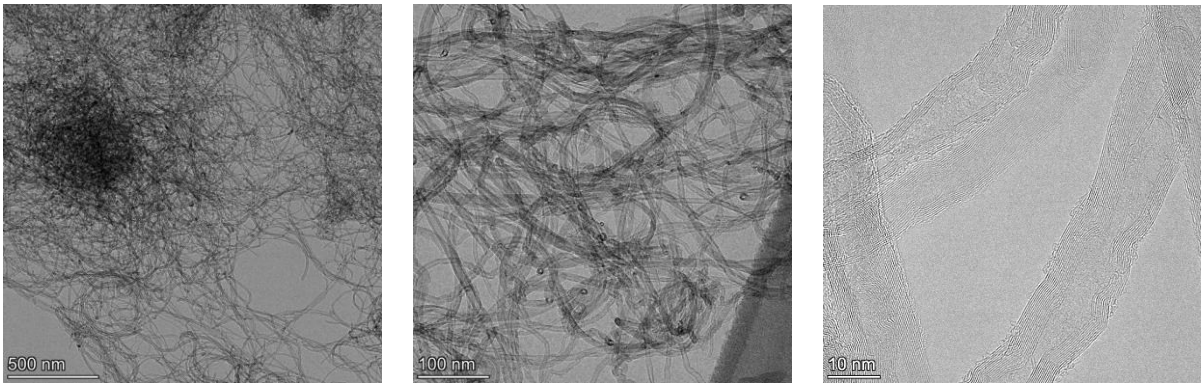

a *b* *c*

Fig. 2. Micrographs of purified MWCNT powder taken with a transmission electron microscope. Frame size: *a* – 500 nm, *b* – 100 nm, *c* – 10 nm

These microphotographs were taken on a Supra55VP scanning microscope (Carl Zeiss Group, Germany) and a Tesla BS-500 transmission electron microscope (Tesla, Czech Republic).

Composites manufacturing. A standard rubber formulation based on styrene-butadiene rubber was used to obtain composite materials. The composition of the standard rubber compound included (phr – parts per hundred of rubber): rubber (100 phr), zinc oxide (3 phr), N-tert-butyl-2-benzothiazolylsulfenamide (1 phr), sulfur (1.75 phr), stearic acid (1 phr) and carbon black grade N-330 (50 phr). Rubber compounds containing nanocarbons were produced on rubber processing rollers. The mass fraction of CB decreased by the corresponding value with the addition of MWCNTs or SWCNTs. The addition of nanotubes was carried out first of all before all technological additives for the purpose of more efficient interaction of nanocarbon with the polymer matrix. The vulcanization process was carried out at 145°C for 35 minutes in a vulcanizing press.

The production of rubber mixtures was carried out on laboratory rollers LB 320160/160; Mooney viscosity was determined on the MV-2000 viscometer manufactured by Alfa Technology.

Equipment and technique of mechanical experiments. A Zwick/Roell (Germany) four-vector biaxial test bench was used for mechanical testing. It also includes a video extensometer that can non-contactly measure displacements between any selected points on the sample surface. The experimental samples had a blade shape, corresponding to the international standard ISO 527-2 5A. The dimensions of the working part were 20×4×2 mm.

The same program of cyclic tests with increasing amplitude over deformations was used for all samples. It consisted of five cycles, on each of which the following actions were carried out:

1) stretching at a constant rate of 25%/min. up to the value of deformation ε_n (n=1÷5) specified for the given n-th cycle;
2) stop for 10 minutes (to relieve stress);
3) unloading at a constant rate of 25%/min. until the applied load is completely removed;
4) again stop for 10 minutes (check for residual deformations).

The deformation amplitude increased by 10% at each subsequent cycle, respectively, and the cycle maximum extension ratio of sample λ_n (λ_n=1+ε_n) was 1.10, 1.20, 1.30, 1.40, and 1.50.

3. Experiment and results discussion

Before carrying out mechanical tests of rubbers based on composite samples, the rheometric parameters of their unvulcanized mixtures were studied. SWCNTs (only purified), MWNTs (purified and unpurified), and carbon black were used for filling. The choice of only purified SWCNTs for experiments is associated with a large number of variable valence metals in their composition, which negatively affects the thermomechanical stability of rubbers. The analysis of publications available to date has shown that such studies of the rheological properties of unvulcanized composite mixtures containing purified or unpurified carbon nanotubes have not yet been carried out by anyone.

Figure 3 shows the dependences of the torque moment [57] on the vulcanization time, obtained on a non-rotor rheometer.

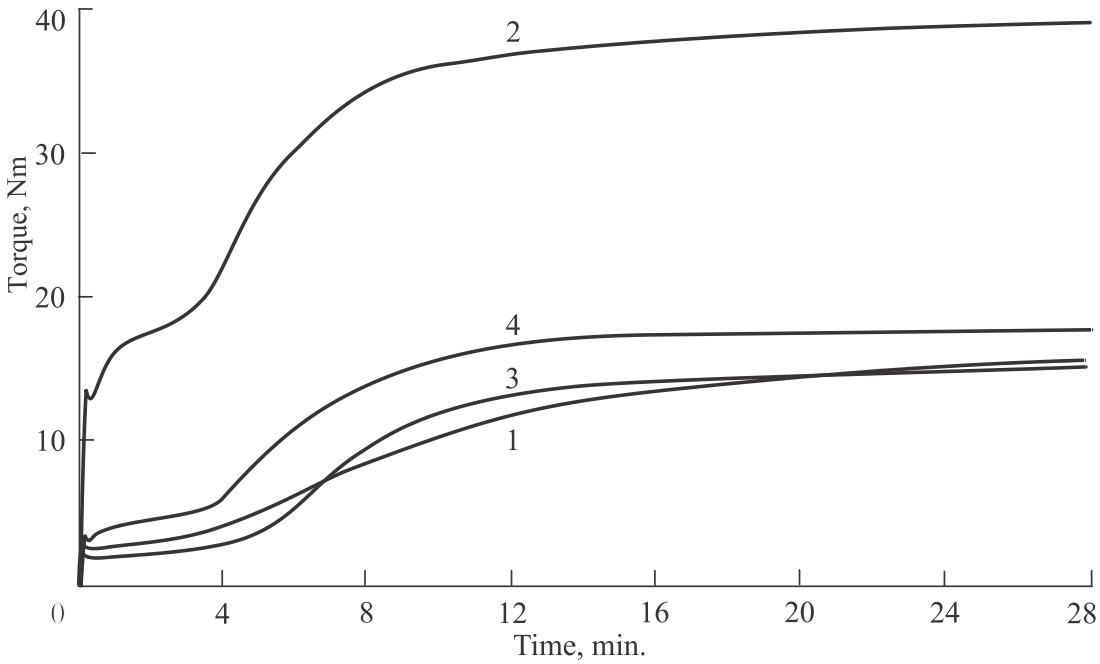

Fig. 3. Kinetics of isothermal vulcanization of rubber mixtures filled with SWCNT, MWCNT, and CB: 1 – 50 phr CB; 2 – 43 phr CB + 7 phr purified SWNTs; 3 – 43 phr CB + 7 phr original MWCNTs; 4 – 43 phr CB + 7 phr purified MWCNTs

It has been found that purification of all types of nanotubes shortens the induction period of vulcanization. It can be assumed that the process of purification and activation of nanotubes affects the efficiency of interaction between the nanotube surface and the binder. So, if the input of unpurified MWCNTs (curve 3 in Fig. 3) has practically no effect on the

vulcanization process in comparison with SBR-1500 filled with only CB (curve 1), then the use of purified MWCNTs gives a fairly noticeable increase in torque, i.e., the mixture viscosity growth. A particularly strong effect of increasing the viscosity of the rubber mixture was observed for purified SWNTs (curve 2). In this case, the torque increased by more than 2.5 times. It can be assumed that such a strong effect is associated with the activation of SWCNTs, namely, with the removal of decorating unstructured impurities from their surface.

A significant increase in the viscosity of the rubber mixture containing purified SWCNTs (curve 2 in Fig. 3) indicates a significant rearrangement of its internal structure under the action of a shear flow initiated in a non-rotor rheometer. As a result, long and flexible SWNTs are reoriented in the corresponding direction, which is confirmed by the viscosity indices of these composites (Table 2).

Table 2. Viscosity values (Mooney viscosity) of composite mixtures

	50 phr CB	43 phr CB + 7 phr purified SWNT	43 phr CB + 7 phr original MWCNT	43 phr CB + 7 phr purified MWCNT
Mooney viscosity	61.4	219.0	78.1	87.2

However, such processes should be accompanied by the appearance of anisotropy of mechanical properties (along and across the shear). Similar phenomena can also occur in the manufacture of elastomeric composites after processing on a roller. That is, there is a technological possibility of creating composite materials with a given anisotropy of mechanical properties. To test this hypothesis, the following experimental studies were carried out.

In accordance with the technology described in the previous section, composite materials for mechanical testing were obtained in the form of rectangular plates with a thickness of about 2 mm. The sides of the plates were oriented along and across the direction of their rolling during manufacture. Accordingly, the blade samples for each of the studied materials were cut in two mutually perpendicular directions parallel to the sides of the original plate, that is, so that the expected anisotropy of mechanical properties would manifest itself to the maximum.

Since the main goal of the work was to study precisely the anisotropic properties of elastomeric nanocomposites depending on the type of filler, and not its limiting characteristics, the maximum stretching deformation of samples was limited to 50%. That is, the loading range most typical for the operation of these materials was considered.

The test results are depicted in Figs. 4-7. The ordinate shows the nominal stress σ (the force related to the initial cross-sectional area of the sample working part), and the abscissa shows the extension ratio λ (the ratio of the length of the deformed sample to the original length). The dashed lines correspond to samples cut along the rolling direction (further, for convenience, we will call them "longitudinal"), and the solid lines correspond to samples cut across the rolling ("transverse").

Figure 4 shows the results of cyclic tests for SBR-1500 filled only with carbon black (50 phr). The deformation curves under loading along and across the rolling direction practically coincided, that is, this material can be considered isotropic.

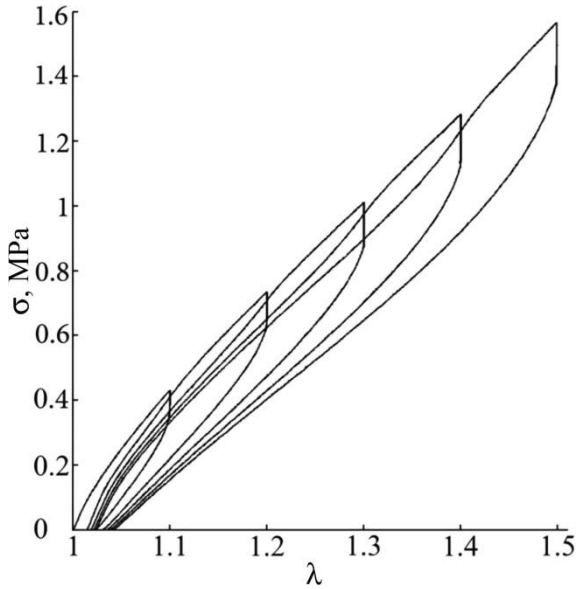

Fig. 4. Cyclic tests of SBR-1500 (100 phr), filled with 50 phr CB

Figure 5 depicts similar dependencies for SBR-1500, filled with 43 phr CB and 7 phr purified MWCNT.

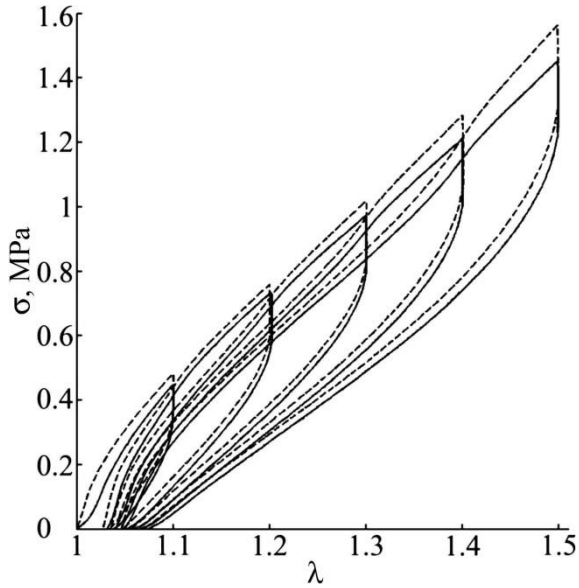

Fig. 5. Cyclic tests of SBR-1500 (100 phr), filled with 43 phr CB + 7 phr purified MWCNT

The graphs show that this material has a slight anisotropy of mechanical properties. The hysteresis areas (that is, dissipative losses) are about the same, but the sample cut along the rolling direction turned out to be slightly stiffer.

We also tested samples of a composite based on SBR-1500, in which not carbon black, but nanoparticles of few-layer graphene were used as the first filler. The second filler was purified multilayer carbon nanotubes. The obtained deformation dependencies are shown in Fig. 6. As a result of this replacement, the mechanical rigidity of the material has almost halved, and the residual deformations have approximately doubled. Dissipative losses (viscous properties) remained virtually unchanged. Thus, the introduction of graphene nanoparticles into the elastomer instead of CB and MWCNTs leads to a significant softening of the material, but the anisotropy of mechanical properties remains at the same level (i.e., insignificant).

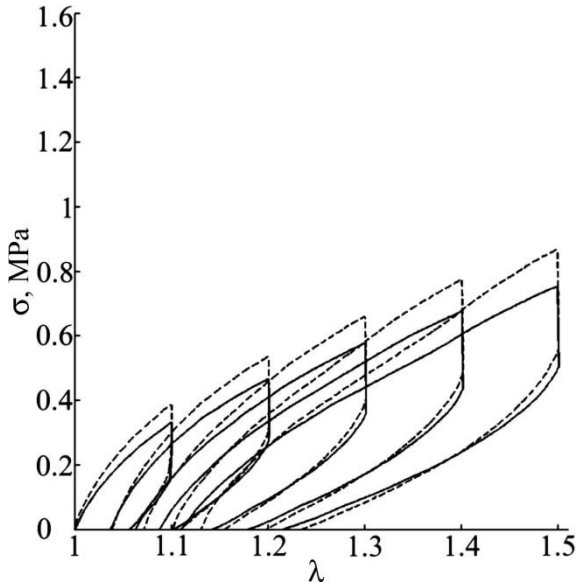

Fig. 6. Cyclic tests of SBR-1500 (100 phr), filled with 43 phr FLG + 7 phr purified MWCNTs

In our opinion, of greatest interest are the results obtained on samples filled with carbon black and purified single-walled carbon nanotubes (Fig. 7).

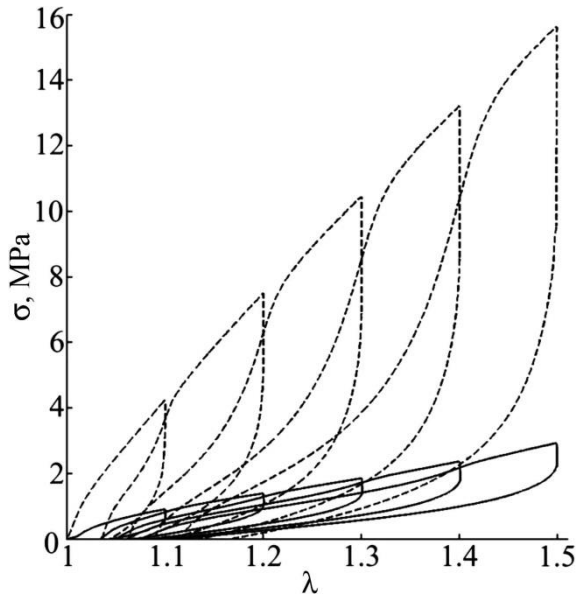

Fig. 7. Cyclic tests of SBR-1500 (100 phr), filled with 43 phr CB + 7 phr purified SWCNT

The graphs show that the maximum cycle stress amplitudes for the "longitudinal" samples are about 5 or more times higher than for the "transverse" ones, while the differences in the unloading curves for both turned out to be much smaller. Thus, in the first case, there was simply a huge increase in dissipative losses (4-5 times) and, accordingly, an improvement in damping properties. The areas of cyclic hysteresis loops for transverse samples were approximate of the same order as for other composites studied in this work (see Figs. 4-6). As regards residual deformations, for “longitudinal” samples filled with CB+SWCNT, they turned out to be 1.5-2 times greater than for composites filled with CB or CB+MWCNT. For "transverse" samples with CB+SWCNTs, these values turned out to be approximate of the same order as for elastomers containing CB and CB+MWCNTs.

The master Table 3 presents the values of the initial modules E_x and E_y, as well as the maximum values of conditional stresses σ_x and σ_y (at λ=1.5). Index "x" corresponds to specimens cut along the rolling direction, and index "y" – to the transverse direction.

Table 3. Mechanical characteristics of composite samples (test results)

Filler	E_x, MPa	E_y, MPa	σ_x, MPa	σ_y, MPa
50 phr CB (fig. 4)	7.14	7.13	1.56	1.56
43 phr CB + 7 phr purified MWCNT (fig. 5)	9.70	7.01	1.57	1.46
43 phr FLG + 7 phr purified MWCNT (fig. 6)	5.42	4.34	0.85	0.75
43 phr CB + 7 phr purified SWCNT (fig. 7)	74.67	16.17	15.65	2.94

According to the authors, such a difference in the mechanical properties of composites is due to the length of single-walled nanotubes, which is much longer than that of multi-walled ones. In the case of SWCNTs, a spatial framework can be formed in the composite from interconnected (both physically and chemically) very long fibers even at low filler concentrations. In the process of mechanical processing of a vulcanizing rubber compound (rolling), this carcass is reoriented in a certain direction and, accordingly, the material eventually becomes anisotropic. The same phenomena can also be observed when filling an elastomer with multilayer nanotubes, but due to the fact that they are much shorter, the effect should be much less pronounced.

4. Conclusion

As a result of the studies, it was found that in elastomers filled and purified with single-walled carbon nanotubes, the appearance of a significant anisotropy of mechanical properties associated with the peculiarities of sample preparation is possible. It is expressed in multiple increases in the rigidity of the material and an increase in dissipative losses during its deformation in the direction corresponding to the movement of the vulcanized mixture during rolling (whereas this effect is much less pronounced in the perpendicular direction). The initial modulus for composites filled with CB+SWCNT was about 7.7 times greater than for composites containing CB+MWCNT, and the maximum stresses (at λ=1.5) were 10 times greater. For composites with CB+SWCNT, the anisotropy in modulus (E_x/E_y) was 4.6, and in maximum stresses (σ_x/σ_y) it reached 5.3.

According to the authors, this is due to the fact that the length of SWCNTs is much larger compared to MWCNTs, and even more so with the characteristic sizes of soot and graphene particles.

This effect can be very important and useful in terms of various applications. For example, with the help of several fairly easy-to-implement technological operations, it is possible to significantly improve the damping properties of a rubber shock absorber made of rubber filled with SWCNTs.

References

1. Caldona EB, De Leon ACC, Pajarito BB, Advincula RC. A review on rubber-enhanced polymeric materials. *Polymer Reviews.* 2016;57(2): 311-338.

2. Roy K, Debnath SC, Potiyaraj P. A critical review on the utilization of various reinforcement modifiers in filled rubber composites. *Journal of Elastomers & Plastics*. 2019;52(2): 167-193.

3. Kraus G. Reinforcement of elastomers by carbon black. *Rubber Chemistry and Technology.* 1978;51(1): 297-321.
4. Kim J-H, Jeong H-Y. A study on the material properties and fatigue life of natural rubber with different carbon blacks. *International Journal of Fatigue.* 2005;27: 263-272.
5. Koga T, Takenaka M, Aizawa K, Nakamura M, Hashimoto T. Structure factors of dispersible units of carbon black filler in rubbers. *Langmuir.* 2005;21: 11409-11413.
6. Jovanovich V, Smarzija-Jovanovich S, Budinski-Simendich J, Markovich G, Marinović-Cincovich M. Composites based on carbon black reinforced NBR/EPDM rubber blends. *Composites Part B: Engineering.* 2013;45(1): 333-340.
7. Ulfah IM, Fidyaningsih M, Rahayu S, Fitriani DA, Saputra DA, Winarto DA, Wisojodharmo LA. Influence of carbon black and silica filler on the rheological and mechanical properties of natural rubber compound. Procedia Chemistry. 2015;16: 258-264.
8. Bokobza L, Rahmani M, Belin C, Brunell J-L, El Bouni N-E. Blends of carbon blacks and multiwall carbon nanotubes as reinforcing fillers for hydrocarbon rubbers. *Journal of Polymer Science: Part B: Polymer Physics.* 2008;46: 1939-1951.
9. Gao J, He Y, Gong X, Xu J. The role of carbon nanotubes in promoting the properties of carbon black-filled natural rubber/butadiene rubber composites. *Results in Physics.* 2017;7: 4352-4358.
10. Garishin OK, Shadrin VV, Svistkov AL, Sokolov AK, Stockelhuber WK. Visco-elastic-plastic properties of natural rubber filled with carbon black and layered clay nanoparticles Experiment and simulation. *Polymer Testing.* 2017;63: 133-140.
11. Zhang H, Wei YT, Kang ZR, Zhao GZ, Liu YQ. Influence of graphene oxide and multiwalled carbon nanotubes on the dynamic mechanical properties and heat buildup of natural rubber/carbon black composites. *Journal of Elastomers and Plastics.* 2017;50(5): 403-418.
12. Negri RBP, da Silva AHMFT, de Sousa AMF, da Silva ALN, da Rocha EBD. Improved mechanical and rheological behavior of nitrile rubber reinforced with multi-walled carbon nanotubes and carbon black dual-filler system. *Materials Today Communications*. 2021;26: 101884(1-10).
13. Mokhireva KA, Svistkov AL, Solod'ko VN, Komar LA, Stöckelhuber KW. Experimental analysis of the effect of carbon nanoparticles with different geometry on the appearance of anisotropy of mechanical properties in elastomeric composites. *Polymer Testing.* 2017;59: 46-54.
14. Karami P, Khasraghi S, Hashemi M, Rabiei S, Shojaei A. Polymer/nanodiamond composites – a comprehensive review from synthesis and fabrication to properties and applications. *Advances in Colloid and Interface Science.* 2019;269: 122-151.
15. Liu C, Zang J, Yan S, Yuan Y, Xu H, Yang G, Wang Y. Synthesis of novel nanocomposites reinforced with 3D graphene/highly-dispersible nanodiamonds nano-hybrids. *Ceramics International.* 2019;45(10): 13158-13163.
16. Bisht A, Samant SS, Jaiswal S, Dasgupta K, Lahiri D. Quantifying nanodiamonds assisted exfoliation of graphene and its effect on toughening behavior of composite structure. *Composites Part A: Applied Science and Manufacturing.* 2020;132: 105840-105853.
17. Maya MG, Abraham J, Arif PM, Moni G, Jacob George JJ, George SC, Thomas S. A comprehensive study on the impact of RGO/MWCNT hybrid filler reinforced polychloroprene rubber multifunctional nanocomposites. *Polymer Testing*. 2020;87: 106525(1-13).
18. Mittal G, Dhand V, Rhee KY, Park S-J, Lee WR. A review on carbon nanotubes and graphene as fillers in reinforced polymer nanocomposites. *Journal of Industrial and Engineering Chemistry.* 2015;21: 11-25.

19. Li Y, Wang S, Wang Q, Xing M. A comparison study on mechanical properties of polymer composites reinforced by carbon nanotubes and graphene sheet. *Composites: Part B.* 2018;133: 35-41.
20. Mensah B, Gupta KC, Kim H, Wang W, Jeong K-U, Nah C. Graphene-reinforced elastomeric nanocomposites: A review. *Polymer Testing.* 2018;68: 160-184.
21. Lu Y, Liu J, Hou G, Ma J, Wang W, Wei F, Zhang L. From nano to giant? Designing carbon nanotubes for rubber reinforcement and their applications for high performance tires. *Composites Science and Technology.* 2016;137: 94-101.
22. Mitrofanov VV, Slepchenkov MM, Zhang G, Glukhova OE. Hybrid carbon nanotube-graphene monolayer films: Regularities of structure, electronic and optical properties. *Carbon.* 2017;115: 803-810.
23. Krestinin AV, Dremov NN, Knerel'man EI, Blinova LN, Zhigalina VG, Kiselev NA. Characterization of SWCNT products manufactured in Russia and the prospects for their industrial application. *Nanotechnologies in Russia.* 2015;10(7-8): 537-548.
24. Voznyakovskii AP, Neverovskaya AY, Melenevskaya EY, Chubarova EV, Kutin AA, Sukhanova TE. Peculiarities of single-walled carbon nanotubes distribution in polystyrene matrix. *Nanotechnologies: Science and Production.* 2018; N4: 64-72. (In Russian)
25. Gumede JI, Carson J, Hlangothi SP, Bolo LL. Effect of single-walled carbon nanotubes on the cure and mechanical properties of reclaimed rubber/natural rubber blends. *Materials Today Communications.* 2020;23: 100852.
26. Jia Z, Wang Z, Liang J, Wei B, Wu D. Production of short multi-walled carbon nanotubes. *Carbon.* 1999;37: 903-906.
27. Fakhru'l-Razi A, Atieh MA, Girun N, Chuah TG, El-Sadig M, Biak DRA. Effect of multi-wall carbon nanotubes on the mechanical properties of natural rubber. *Composite Structures.* 2006;75: 496-500.
28. Elango N, Srinivasa Gupta NS, Jiun YL, Golshahr A. The effect of high loaded multiwall carbon nanotubes in natural rubber and their nonlinear material constants. *Journal of Nanomaterials.* 2017;2017: 6193961.
29. Kong L, Li F, Wang F, Miao Y, Huang X, Zhu H, Lu Y. High-performing multi-walled carbon nanotubes/silica nanocomposites for elastomer application. *Composites Science and Technology.* 2018;162(7): 23-32.
30. Zhan Y, Yan N, Fei G, Xia H, Meng Y. Crack growth resistance of natural rubber reinforced with carbon nanotubes. *J. Appl. Polym. Sci.* 2020;137: 48447(1-9).
31. Sementsov Yu, Yang W, Ivanenko K, Makhno S, Kartel M. Modification of rubber compositions by carbon nanotubes. *Applied Nanoscience.* 2022;12: 621–628.
32. Li P, Duan HY, Liu YF, Chi WD, Huang QG. Multi-walled carbon nanotubes as secondary fibre fillers for property improvement of short carbon fibre-reinforced silicone rubber. *Bull. Mater. Sci.* 2019;42: 177(1-8).
33. Krainoi A, Kummerlöwe C, Nakaramontri Y, Wisunthorn S, Vennemann N, Pichaiyut S, Kiatkamjornwong S, Nakason C. Novel natural rubber composites based on silver nanoparticles and carbon nanotubes hybrid filler. *Polymer Composites.* 2020;41: 443-458.
34. Xu Z, Jerrams S, Guo H, Zhou Y, Jiang L, Gao Y, Zhang L, Li LL, Wen S. Influence of graphene oxide and carbon nanotubes on the fatigue properties of silica/styrene-butadiene rubber composites under uniaxial and multiaxial cyclic loading. *International Journal of Fatigue.* 2020;131: 105388.
35. Kitisavetjit W, Nakaramontri Y, Pichaiyut S, Wisunthorn S, Nakason C, Kiatkamjornwong S. Influences of carbon nanotubes and graphite hybrid filler on properties of natural rubber nanocomposites. *Polymer Testing.* 2021;93: 106981.

36. Kumar V, Lee DJ. Rubber nanocomposites reinforced with single-wall and multiwall carbon nanotubes for industrial applications. *Rubber Chemistry and Technology.* 2020;93(1): 157-171.
37. Shadrinov NV, Nartakhova SI. Structure and properties of nitrile-butadiene rubber filled with carbon and basalt fibers. *Inorganic Materials: Applied Research.* 2017;8(1): 140-144.
38. Qian M, Sui J, Wang X, Zhu Y. Mechanical properties of silicon carbon black filled natural rubber elastomer. *Chemical Research in Chinese Universities.* 2019;35: 139-145.
39. Li X, Yang Q, Ye Y, Zhang L, Hong S, Ning N, Tian M. Quantifying 3D-nanosized dispersion of SiO2 in elastomer nanocomposites by 3D-scanning transmission electron microscope (STEM). *Composites Part A.* 2020;131: 105778.
40. Gabriel D, Karbach A, Drechsler D, Gutmann J, Graf K, Kheirandish S. Bound rubber morphology and loss tangent properties of carbon-black-filled rubber compounds. *Colloid and Polymer Sci.* 2016;294: 501-511.
41. Cole DP, Henry TC, Gardea F, Haynes RA. Interphase mechanical behavior of carbon fiber reinforced polymer exposed to cyclic loading. *Composites Science and Technology*. 2017;151: 202-210.
42. Butt H, Capella B, Kappl M. Force measurements with the atomic force microscope: Technique, interpretation and applications. *Surface Science Reports*. 2005;59: 1-152.
43. Ayoub G, Zairi F, Nait-Abdelaziz M, Gloaguen JM. Modelling large deformation behavior under loading–unloading of semicrystalline polymers: application to a high density polyethylene. *Int. J. Plasticity.* 2010;6: 329-347.
44. Drozdov AD, Klitkou R, Christiansen JC. Cyclic viscoplasticity of semicrystalline polymers with finite deformations. *Mechanics of Materials.* 2013;56: 53-64.
45. Svistkov AL, Shadrin VV. *Method for uniaxial cyclic testing of the material*. RU 2549841 (Patent), 2015.
46. Marckmann G, Chagnon G, Le Saux M, Charrier P. Experimental investigation and theoretical modelling of induced anisotropy during stress-softening of rubber. *Int. J. Solids Struct*. 2016;97-98: 1-43.
47. Plagge J, Klüppel M. A physically based model of stress softening and hysteresis of filled rubber including rate- and temperature dependency. *International Journal of Plasticity*. 2017;89: 173-196.
48. Ragni L, Tubaldi E, Dall'Asta A, Ahmadi H, Muhr A. Biaxial shear behaviour of HDNR with Mullins effect and deformation-induced anisotropy. *Eng. Struct.* 2018;154: 78-92.
49. Garishin OK, Shadrin VV, Kornev YuV Mechanical studies of rubber micro- and nanocomposites promising for the tire industry. Uniaxial and biaxial tests. *Materials Physics and Mechanics.* 2019;42(4): 445-454.
50. Plagge J, Ricker A, Kröger NH, Wriggers P, Klüppel M. Efficient modeling of filled rubber assuming stress-induced microscopic restructurization. *International Journal of Engineering Science.* 2020;151: 103291.
51. Garishin OK, Shadrin VV. Study of mechanical behavior of elastomeric nanocomposites under large cyclic shear deformations. *Bulletin of Perm University. Physics*. 2021;(3): 63-72. (In Russian)
52. Rinzler AG, Liu J, Dai H, Nilolaev P, Huffman CB, Rodriguez-Macias FJ, Boul PJ, Lu AH, Heymann D, Colbert DT, Lee RS, Fischer JE, Rao AM, Eklund PC, Smalley RE. Large scale purification of single-wall carbon nanotubes: process, product, and characterization. *Appl. Phys. A.* 1998; 67: 29-37.
53. Dillon AC, Gennet T, Jones KM, Alleman JL, Parilla PA, Heben MJ. A simple and complete purification of single-walled carbon nanotube materials. *J. Adv. Mater*. 1999;11: 1354-1358.

54. Holzinger M, Hirsch A, Bernier P, Duesberg GS, Burghard M. A new purification method for single-wall carbon nanotubes (SWNTs). *Appl. Phys. A.* 2000;70: 599-602.
55. Zhao B, Hu H, Niyogi S, Itkis ME, Hamon MA, Bhowmik P, Meier MS, Haddon RC. Chromatographic purification and properties of soluble single-walled carbon nanotubes. *J. Am. Chem. Soc.* 2001;123: 11673-11677.
56. Voznyakovskii AP, Neverovskaya AY, Otvalko JA, Gorelova EV, Zabelina AN, Lebedev SV. Facile synthesis of 2D carbon structures as a filler for polymer composites. *Nanosystems: Physics, Chemistry, Mathematics.* 2018;9(1): 125-128.
57. GR 54552-2011. *Rubbers and rubber compounds. Determination of viscosity, stress relaxation, and scorch characteristics using a Mooney viscometer*. Moscow: Standartinform; 2018.

THE AUTHORS

Garishin O.K.
e-mail: gar@icmm.ru
ORCID: 0000-0001-7384-7366

Svistkov A.L.
e-mail: svistkov@icmm.ru
ORCID: 0000-0002-4754-5214

Voznyakovskii A.P.
e-mail: voznap@mail.ru
ORCID: 0000-0002-5979-3661

Tchypkina I.M.
e-mail: vniisk@bk.ru

Neverovskaya A.Yu.
e-mail: anna-neverovskaya@yandex.ru
ORCID: 0000-0001-7813-666X

Shadrin V.V.
e-mail: shadrin@icmm.ru

Materials Physics and Mechanics. 2022;50(3): 509-517
Research article
http://dx.doi.org/10.18149/MPM.5032022_13

Submitted: July 8, 2022
Approved: September 13, 2022
Accepted: October 7, 2022

Impact of forced cooling of the joint zone and thermal effect on the distribution values of residual stress generated by arc welding

A.V. Tkacheva✉, E.E. Abashkin

Institute of Machinery and Metallurgy of the Far Eastern Branch of the Russian Academy of Sciences, 1, Metallurgov st., Komsomolsk-na-Amure, 681005, Russia

✉ 4nansi4@mail.ru

Abstract. The search for technological options to obtain strong units with small deformation values determines the study of the local thermal effect on the distribution of residual stresses in permanent joints of metal structures made by arc welding with forced cooling. The mathematical model is based on the Prandtl-Reiss model in which the Hooke law is replaced by the Duhamel-Neumann law and the Mises criterion is supplemented by the Johnson-Cook strain hardening function. The elastic moduli, as well as the yield strength, are assumed to be temperature-dependent. The calculated values of residual stresses show the positive effect of forced cooling of the welded zone.
Keywords: welding, mathematical model, Johnson-Cook strain hardening function, residual stresses, deformation, heat affected zone

Acknowledgements. *The work was carried out within the state assignment of Khabarovsk Federal Research Center of the Far Eastern Branch of the Russian Academy of Sciences.*

Citation: Tkacheva AV, Abashkin EE. Impact of forced cooling of the joint zone and thermal effect on the distribution values of residual stress generated by arc welding. *Materials Physics and Mechanics*. 2022;50(3): 509-517. DOI: 10.18149/MPM.5032022_13.

1. Introduction.

Welding technology is used extensively in modern industry to produce metal structures. A large part of welded constructions is not only in one-piece and small batch production but also in mass production. This makes it necessary to increase productivity and reduce the cost of all operational cycles. At the same time, products must have improved material performance and physical and mechanical properties.

There are different welding techniques, such as electric arc, plasma, electro slag, electro-beam, induction, laser, and friction welding. Each method has its own advantages and disadvantages. Of the above-mentioned technologies, electrode wire arc welding is the most common and in demand due to its ease of use, mobility of use, and inexpensive consumables [1-4]. Increasing the productivity of arc welding requires an increase in speed, which in turn increases the thermal capacity of the arc flow. This negatively affects the strength properties of permanent joints. One of the ways to solve this problem is seen in the additional removal of heat from the zone of local thermal impact. The need for forced cooling of the weld metal and the heat-affected zone of the welded joint occurs when welding materials are with high sensitivity to high-temperature heating. Such as high-chromium ferritic steels and single-phase iron-chromium-aluminium alloys, as well as materials whose properties are determined

© A.V. Tkacheva, E.E. Abashkin, 2022.
Publisher: Peter the Great St. Petersburg Polytechnic University
This is an open access article under the CC BY-NC 4.0 license (https://creativecommons.org/li-censes/by-nc/4.0/)

by the degree of dispersion of the precipitated phases, which, in turn, depends on the cooling rate of the crystallizing metal [5-14].

However, due to a significant number of factors affecting the formation of the weld metal and the heat-affected zone (HAZ), predicting the result of heat-affected zone cooling on the strength and deformation characteristics of the welded joint becomes very difficult.

It has been established that the material of the part should be considered elastoplastic, as only in this case there is a possibility of quantitative and qualitative estimation of processes of formation of residual stress fields in the near-weld zone, which influence the quality of joint is mainly negative. [15].

Elastic and plastic properties are temperature dependent, so the main difficulty is in iterative tracking the nucleation and disappearance of plastic flow zones. Plastic flow generates irreversible deformations which then form residual stresses during unloading and cooling. Since all coefficients depend on temperature, it is not possible to find a solution analytically. Despite a considerable number of theoretical and experimental studies on the prediction of the final properties of the resulting permanent joint, the processes of forced cooling of the welding zone, which determine the behaviour of the material under these conditions, are poorly studied at present.

Welding technology is being modernised both experimentally [16-19] and theoretically using a mathematical apparatus [20-23].

Mathematical modeling of the process of electric arc welding with forced cooling, taking into account the geometric parameters and thermophysical properties of the heat removal, makes it possible to optimise this technology without resorting to long and expensive experiments. It is enough to build a correct mathematical model once based on the mechanical behavior of the object under study in order to further analyze the influence of various thermophysical factors.

This work is aimed at obtaining a mathematical model of the evolution of thermal stresses in the near-weld zone and calculating the thermomechanical parameters of the process, taking into account the dependences of the yield strength, elastic models, and the hardening coefficient of resistance to plastic flow on temperature, including the calculation of their final values and the distribution of residual stresses. The aim of the work is to determine the effect of forced cooling on the level and distribution of residual stresses in the area of the weld.

2. Materials and Methods

Temperature studies of the welding area. Process modeling is shown in Fig. 1. The plates 3 mm thick, made from mild steel, are joined using an electric arc welding at a speed V. Behind there is a curvilinear horseshoe-shaped heat removal, which reduces the temperature in the HAZ. After cooling, the connection of the plates becomes inseparable. Now it is necessary to calculate the residual stresses in the connection zone and the HAZ. We divide the problem into two: temperature and mechanical and solve them in this sequence.

In arc welding, the process of heat distribution in a solid body is described by a nonlinear differential thermal conductivity equation, taking into account the active heat source:

$$c(T)\rho(T)\frac{\partial T}{\partial t} = div(\lambda(T)gradT) + q, \quad (1)$$

where $\lambda(T)$ – thermal conductivity $Wt/(m°\mathrm{C})$, $c(T)$ – thermal capacity $J/(kg°\mathrm{C})$, $\rho(T)$ – density kg/m^3, q – volumetric power density of the heat source Wt/m^3.

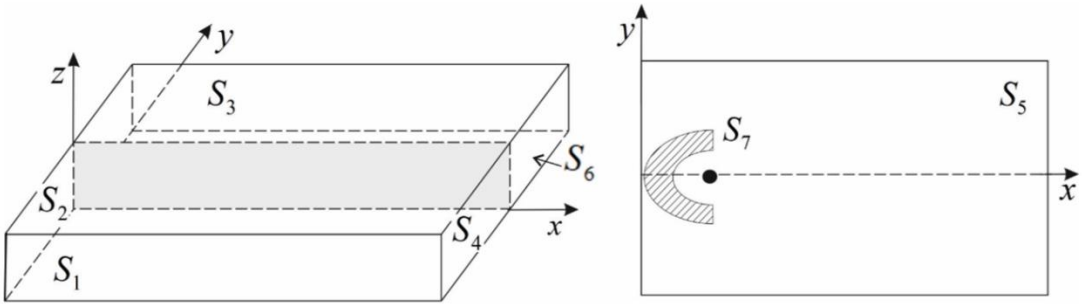

Fig. 1. Problem diagram

The heat source is modelled by the well-known ellipsoid proposed by John A. Goldak [24]. Figure 2 shows the shape of the heat flux in platinum during welding.

$$q_s = f_s \frac{6\sqrt{3Q}}{a_s bc\pi^{1.5}} e^{-3\left(\left(\frac{x+v(\tau-t)}{a_s}\right)^2+\left(\frac{y}{b}\right)^2+\left(\frac{z}{c}\right)^2\right)};\ q_l = f_l \frac{6\sqrt{3Q}}{a_l bc\pi^{1.5}} e^{-3\left(\left(\frac{x+v(\tau-t)}{a_l}\right)^2+\left(\frac{y}{b}\right)^2+\left(\frac{z}{c}\right)^2\right)}, \quad (2)$$

where Q – effective thermal capacity of the heating source (for arc welding Q = η·I·U, Wt), τ – time elapsed since the start of the source, sec; t – current time, sec; v – travel rate of the heating source (welding rate), m/sec; x, y, z – ellipsoid semi-axes in the coordinate directions OX, OY, OZ, m; f_s and f_l – coefficients defining the ratios for the heat input to the front and back of the ellipsoid; a_s, a_l, b, c – the corresponding radii of the normal distribution, m.

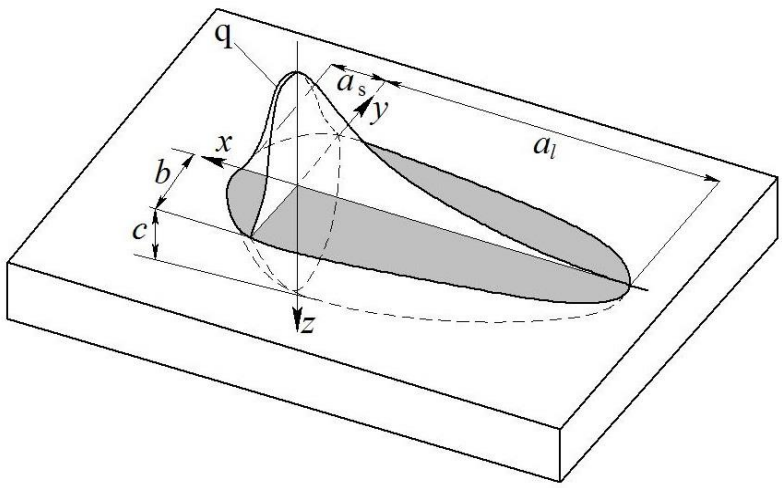

Fig. 2. Heating source diagram

Based on the above, there is the following relationship between the coefficients f_s and f_l: $f_s = \frac{2a_s}{a_s + a_l}$; $f_l = \frac{2a_s}{a_s + a_l}$; $f_s + f_l = 2$.

On the surface free from heat removal and the heat source, the boundary conditions are given by

$$S_1\ -\lambda\frac{\partial T}{\partial y} = \kappa(T - T_0)\ \ S_2\ -\lambda\frac{\partial T}{\partial x} = \kappa(T - T_0);\ S_3\ \lambda\frac{\partial T}{\partial y} = \kappa(T - T_0)\ \ S_4\ -\lambda\frac{\partial T}{\partial x} = \kappa(T - T_0)$$

$$S_5\ -\lambda\frac{\partial T}{\partial z} = \kappa(T - T_0)\ \ S_6\ \lambda\frac{\partial T}{\partial z} = \kappa(T - T_0),\ T_0 = 20\ ^\circ\mathrm{C}.$$

In the cooling area depicted as a horseshoe S_7 (Fig. 1) the boundary conditions are the following: $\lambda \frac{\partial T}{\partial z} = -q$.

Mechanical study. It is assumed that at first there are no irreversible deformations in the plate. The deformations are assumed to be small d_{ij} and combined reversible e_{ij} and irreversible p_{ij}.

$$d_{ij} = 0.5(u_{i,j} + u_{j,i}) = e_{ij} + p_{ij} \tag{3}$$

Stresses, elastic deformation, and temperature are connected by the Duhamel-Neumann relation

$$\sigma_{ij} = (\lambda e_{kk} - 3\alpha K(T - T_0))\delta_{ij} + 2\mu e_{ij}, \tag{4}$$

where λ, μ, $K = \frac{2}{3}\mu + \lambda$ elastic moduli, α – linear expansion coefficient.

At high temperatures, the elastic moduli depend on temperature, which is confirmed experimentally [25-32]. For our case, we use their linear dependence.

$$E(x,y,z,t) = E_p - (E_p - E_0)\theta(x,y,z,t),$$
$$v(x,y,z,t) = 0.5 - (0.5 - v_0)\theta(x,y,z,t), \tag{5}$$
$$\mu = \frac{E}{2(1+v)},\ \lambda = \frac{vE}{(1+v)(1-2v)},$$
$$\theta = (T_p - T)(T_p - T_0)^{-1}.$$

In (5) E_0 – Young's Modulus at room temperature T_0, E_p – at melting temperature T_p, v_0 – Poisson's ratio at room temperature. After the beginning of the cooling process due to phase solid-state transformations, the elastic moduli v_0 fix their values $E_0'(x)$ and $v_0'(x)$, by this we simulate phase transitions.

Irreversible deformations begin to increase when the stress state reaches the loading surface $f(\sigma_{ij}, \sigma)$ in the stress space, where σ – strain hardening function. Write down the associated plastic flow rule

$$\varepsilon_{ij}^p = dp_{ij} = d\varphi \frac{\partial f(\sigma_{ij}, \eta)}{\partial \sigma_{ij}};\ d\varphi > 0. \tag{6}$$

As the loading surface, we take the Mises plastic flow condition, in the left part of which we write the Johnson-Cook strain hardening function [34]

$$\sqrt{\frac{3}{8}\tau_{ij}\tau_{ij}} = \left(A + B(\varepsilon^p)^n\right) \cdot \left(1 + C\, ln \frac{\dot{\varepsilon}^p}{\dot{\varepsilon}_0^p}\right)\theta, \tag{7}$$

where A, B, C, n – material parameters which are found by selection from experimental curves, ε^p – intensity of plastic deformation, $\dot{\varepsilon}^p$ – rate intensity of plastic deformation, $\dot{\varepsilon}_0^p$ – initial rate intensity of deformation, $\dot{\varepsilon}_0^p = 0.0006$ 1/sec.

The equilibrium equation supplements the system of equations (3,4,6,7)

$$\sigma_{ij,j} = 0. \tag{8}$$

The boundary conditions simulate the free surface; as the initial conditions of the mechanical problem, we take the temperature of the plate in a free state equal to room temperature $T_0 = 20$ °C. Young's Modulus at room temperature is $E_0 = 210$ hPa, $E_p = 0.3E_0$

at melting temperature $T_p = 1400\,°\mathrm{C}$, Poisson's ratio is 0.27, linear expansion coefficient is 11.1×10^{-6}, and yield strength at room temperature is $k_0 = 260$ MPa.

3. Results and discussion

Consider solving the above-described temperature problem for a steel plate. Dependencies $\lambda(T)$, $c(T)$, $\rho(T)$ are taken from source [33]. Plate thickness is 0.003 m, dimensions are 0.2 m×0.2 m, and thermal spot rate is 45 m/h. The heat source characteristics are $Q = 2.5\times10^7$ W, and the source of cooling is 5% of the electric arc power Q.

Figure 3 shows two cases of temperature propagation in platinum material. In the first case, welding took place without forced heat removal; in the second case, forced heat removal was taken into account.

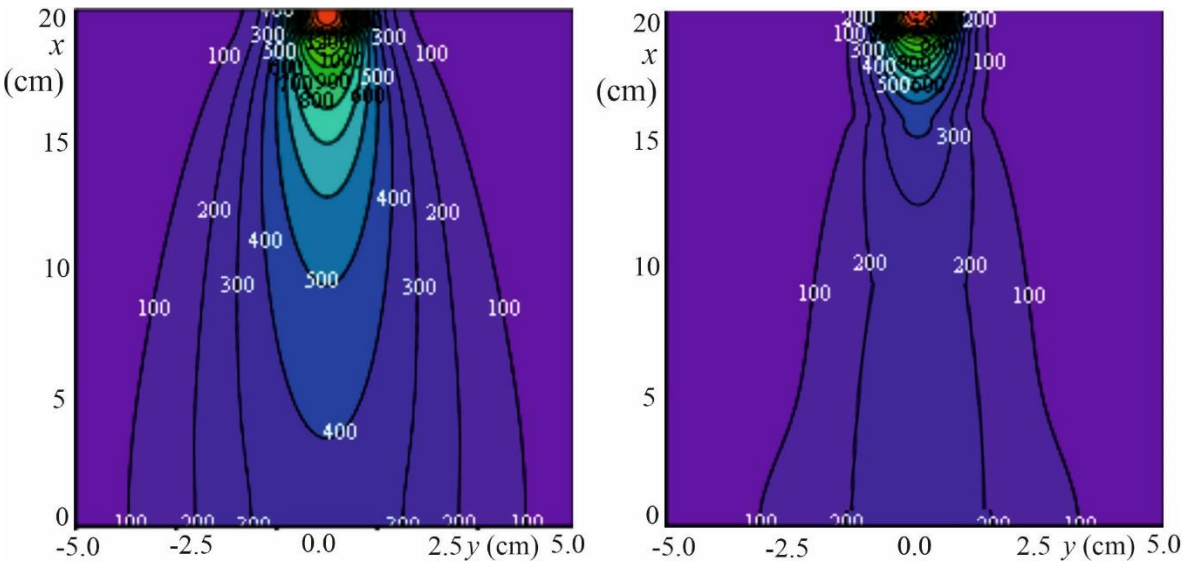

Fig. 3. Temperature distribution within the plate at a distance of 5 cm from the weld at the moment of stopping the welding: a) without cooling; b) with cooling

The data show that the proposed method allows, due to more intensive cooling, to ensure the formation of a narrower weld with a smaller HAZ.

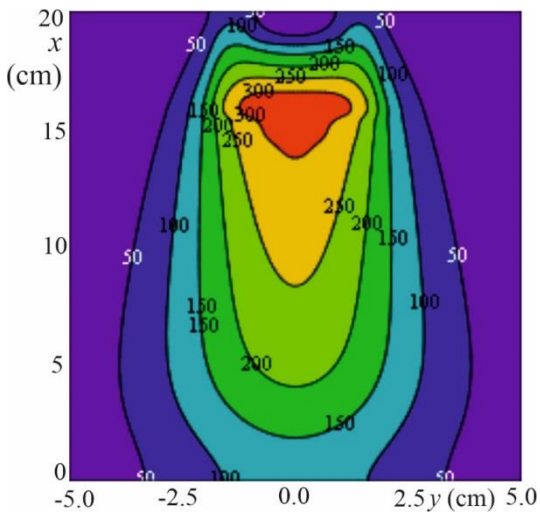

Fig. 4. Temperature difference

The curvilinear shape of the horseshoe-shaped heat removal affects the geometry of the temperature field distribution during welding (Fig. 4), the temperature difference in the weld zone was 300°C.

We solve the problem numerically using the difference method and Newton's iterative method. We use free surface conditions as boundary conditions. For clarity, the distribution of stresses is given on the diagram.

Figure 5 shows the residual stresses generated after the local thermal effect in the plate volume from the center of the weld to the edge of the heat-affected zone. According to the data, during electric arc welding of a thin plate in a butt, residual stresses are formed in the surface layer on the side of the heat source. The tensile stresses are highest in the weld zone and decrease with distance from the weld. Forced cooling reduces the level of residual stresses in comparison with the traditional welding method and reduces the zone of their distribution due to the reduced HAZ.

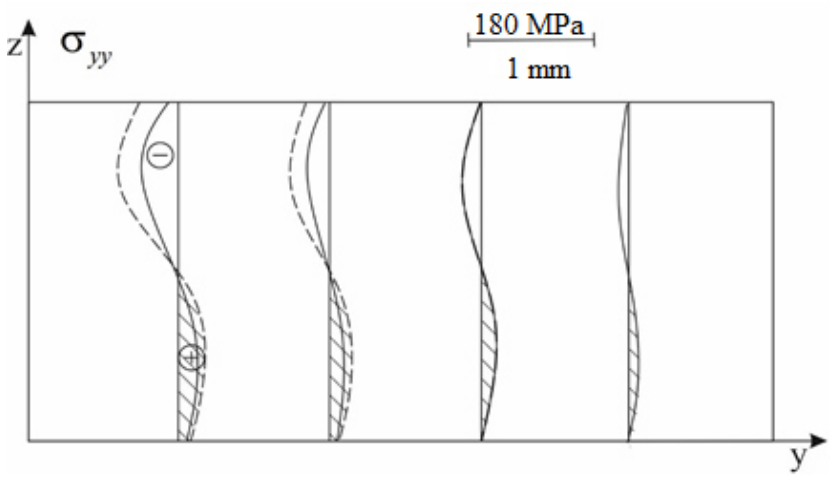

Fig. 5. Stress diagram. The solid line indicates the stress formed in the platinum material with active heat removal, and the dotted line – without it

4. Conclusions

Using small elastoplastic deformations and the Johnson-Cook strain hardening model, the problem of the local thermal effect of movable heat source on a steel plate with active heat removal in the impact area has been solved. The heat removal was 5% of the electric arc power. During its action, residual stresses and the area of their distribution are significantly reduced. This occurs due to a reduction in the time over which irreversible deformations would have grown.

As a result of solving the problem, it has been found that when joining low-carbon steel plates, optimal results are achieved when the welding zone is cooled by a curvilinear heat removal of a horseshoe-shaped configuration with the area of 1336 mm^2 and the speed of electrode movement V = 45 m/h. Forced cooling reduces the level of residual stresses by 28-30% in comparison with the traditional method of welding and reduces the zone of their distribution due to a reduced HAZ by 14%.

Thus, it has been established that the use of electric arc welding with forced cooling will increase the productivity of the process, improving the operational and physical, and mechanical properties of the material.

References

[1] Zhang J, Huang Z, Fang Y, Gu Z, Xie J, Lei J. Experiments and numerical simulations for the mechanical properties of Ni-based superalloys fabricated by laser melting deposition. *Optics & Laser Technology.* 2021;140: 107058.

[2]. Nekrasov R, Galinskii A, Tempel O. Surfacing Technology Materials. *Today Proceedings*. 2019;11: 101-106.

[3]. Wang G, Suder W, Ding J, Williams S. The effect of wire size on high deposition rate wire and plasma arc additive manufacture of Ti-6Al-4V. *Journal of Materials Processing Tech*. 2020. Available from: https://doi.org/10.1016/j.jmatprotec.2020.116842.

[4]. Sokolov NG, Zorin IV, Artemyev AA, Elsukov SC, Fastov SA, Fedosyuk EI, Polunin IA, Mokovozov ND. Surfacing of composite thermo- and wear-resistant alloys using materials containing nanoparticles of refractory chemical compounds. *Proceedings of the Volgograd State Technical University.* 2019;4(227): 61-67.

[5] Vlasov SN, Lapin IE, Savinov AV, Lysak VI, Potapov AN, Atamanyuk VI. *Method of welding in shielding gases with forced cooling of the seam and the heat-affected zone*. RU2232668 (Patent) 2004.

[6] Sołtysiak S. Analysis of structure and material properties in individual zones ofwelded joint. *Journal of Constructional Steel Research.* 2021;187(106978): 290-297.

[7] Zhanga Y, Dinga K, Huob X, Zhaoa B, Fanb B, Zhangb Y, Wanga Y, Weia T, Wua G, Gao Y. Effect of the additional heat input on the microstructure and property in NiCrMoV welded joint simulated by multiple thermal cycles. *Journal of Materials Processing Tech*. 2020;284: 116740.

[8] Yang Y, Pan X. Effect of Mn/N ratio on microstructure and mechanical behavior of simulated welding heat affected zone in 22% Cr lean duplex stainless steel Effect of Mn/N ratio on microstructure and mechanical behavior of simulated welding heat affected zone in 22% Cr lean duplex stainless steel. *Materials Science & Engineering: A*. 2022;835: 142676.

[9] Tao Y, Zhang Z, Xue Z, Ni D, Xiao BL, Ma ZY. Effect of post weld artificial aging and water cooling on microstructure and mechanical properties of friction stir welded 2198-T8 Al-Li joints. *Journal of Materials Science & Technology*. 2022;123: 92-112.

[10] Ebrahimnia M, Malek Ghaini F, Gholizade Sh, Salari M. Effect of cooling rate and powder characteristics on the soundness of heat affected zone in powder welding of ductile cast iron. *Materials and Design*. 2012;33: 551-556.

[11] Echols J, Garrison L, Silva Ch, Lindquist E. Temperature and time effects of post-weld heat treatments on tensile properties and microstructure of Zircaloy-4. *Journal of Nuclear Materials*. 2021;551: 152952.

[12] Lia J, Lia H, Liangc Y, Liuc P, Yanga L, Wanga Y. Effects of heat input and cooling rate during welding on intergranular corrosion behavior of high nitrogen austenitic stainless steel welded joints. *Corrosion Science*. 2020;166: 108445.

[13] Moon J, Lee J, Lee Ch. Reheating cracking susceptibility in the weld heat-affected zone of re duce d activation ferritic-martensitic steels and the effect of Cr content. *Journal of Nuclear Materials.* 2020; 542: 152499.

[14] Kumar S, Natha SK, Kumar V. Continuous cooling transformation behavior in the weld coarse grained heat affected zone and mechanical properties of Nb-microalloyed and HY85 steels. *Materials and Design*. 2016;90: 177-184.

[15] Abashkin EE, Burenin AA, Zhilin SG, Komarov ON, Tkacheva AV. Modeling the distribution of residual stresses in a welded joint. *Physics and mechanics of materials*. 2019;42(5): 671-689.

[16] Becker A, Schroepfer D, Kromm A, Kannengiesser Th. Determination of residual stress evolution during repair welding ofhigh-strength steel components. *Forces in Mechanics.* 2022;6: 100073.

[17] Huaqiang L, Yulong W, Shengdan L, Xiaorong Zh. Effect of cooling conditions on microstructure and mechanical properties of friction stir welded 7055 aluminium alloy joints. *Materials Characterization*. 2018;141: 74-85.
[18] Shojaati M, Bozorg SF, Vatanara M, Yazdizadeh M, Abbasi M. The heat affected zone of X20Cr13 martensitic stainless steel after multiplerepair welding: Microstructure and mechanical properties assessment. *International Journal of Pressure Vessels and Piping*. 2020;188: 104205.
[19] Dak G, Pandey Ch. Experimental investigation on microstructure, mechanical properties, andresidual stresses of dissimilar welded joint of martensitic P92 and AISI 304L austenitic stainless steel. *International Journal of Pressure Vessels and Piping*. 2021;194: 104536.
[20] Farias FWC, Passos AV, Moraes e Oliveira VHP. Microstructural characterization of the physical simulated and welded heat-affected zone of 9% Ni steel pipe. *Journal of materials research and technology*. 2022;17: 3033-3046.
[21] Farias RM, Teixeira PRF, Vilarinho LO. Variable profile heat source models for numerical simulations of arc welding processes. *International Journal of Thermal Sciences*. 2022;179: 107593.
[22] Sun Z, Yu X. Prediction of welding residual stress and distortion in multi-layer butt-welded 22SiMn2TiB steel with LTT filling metal. *Journal of materials research and technology*. 2022;18: 3564-3580.
[23] Afkhami S, Javaheri V, Amraei M, Skriko T, Piili H , Zhao X, Björk T. Thermomechanical simulation of the heat-affected zones in weldedultra-high strength steels: Microstructure and mechanical properties. *Materials & Design.* 2022;213: 110336.
[24] Goldak JA, Akhlagi M. *Computational Welding Mechanics.* U.S.: Springer; 2005.
[25] Cunha Lima RO, Alves Jr C, Alves de Melo AC, Alves SM, Filho L. New technique for deposition and thermochemical treatment of small parts with complex geometry applied to machining inserts. *Journal of materials research and technology*. 2020;9(6): 15811-15823.
[26] Azhar D, Israr E, Kumar A. An investigation on the feasibility of fused deposition modelling process in EDM electrode manufacturing. *CIRP Journal of Manufacturing Science and Technology.* 2019;26: 10-25.
[27] Wang X, Wana J, Wang J, Zhu L, Ruan H. Anomalous sudden drop of temperature-dependent Young's modulus of a plastically deformed duplex stainless steel. *Materials and Design*. 2019;181: 108071.
[28] Xue H, Liu D, Ge R, Pan L, Peng W. The delay loop phenomenon in high temperature elasticity modulus testby in-situ ultrasonic measurements. *Measurement*. 2020;160: 107833.
[29] Latella BA, Humphries SR. Young's modulus of a 2.25 Cr–1Mo steel at elevated temperature. *Scripta Materialia*.2004;51: 635-639.
[30] Lindgren L, Back JG. Elastic properties of ferrite and austenite in low alloy steels versus temperature and alloying. *Material*. 2019;5: 100193.
[31] Rokilan M, Mahendran M. Elevated temperature mechanical properties of cold-rolled steelsheets and cold-formed steel sections. *Journal of Constructional Steel Research*. 2020;167: 105851.
[32] Sung JH, Kim JH, Wagoner RH. A plastic constitutive equation incorporating strain, strain-rate, and temperature. *Int. J. Plast*. 2010;26: 1746-1771.
[33] Kazantsev EI. *Industrial ovens. Reference guide for calculations and design*. Moscow: Metallurgy; 1975.

THE AUTHORS

Tkacheva A.V.
e-mail: 4nansi4@mail.ru
ORCID: 0000-0003-1795-0021

Abashkin E.E.
e-mail: abashkine@mail.ru
ORCID: 0000-0002-9308-1326

Materials Physics and Mechanics. 2022;50(3): 518-535
Research article
http://dx.doi.org/10.18149/MPM.5032022_14

Submitted: August 10, 2020
Approved: July 6, 2021
Accepted: November 19, 2022

Role of in-situ developed intermetallic phases on the mechanical properties and corrosion behaviour of Mg-Sb-Sn and Mg-Sb-Ca ternary alloys

Vignesh S.[1,2], Rajesh Kumar[1], Srinivasan A.[1], Pillai U.T.S.[1]✉

[1]CSIR- National Institute for Interdisciplinary Science and Technology,Thiruvananthapuram, India

[2]Kalasalingam Academy of Research and Education, Krishnankoil, India

✉e-mail:utspillai@rediff.com

Abstract. The development of new Mg-based alloys is one of the prime objectives for the researcher to make use of high specific properties of this material in more applications in transport industries. In the present study, few Mg-Sb-Sn and Mg-Sb-Ca alloys were prepared, and their microstructure, mechanical, and corrosion properties were studied systematically, compared with base Mg-4wt % Sb alloy. The results revealed that microstructure of the Mg-4wt % Sb alloy composed of α-Mg, Mg_3Sb_2 phases, Mg-4Sb-(2,4wt%)Sn alloys consisted of α-Mg, Mg_2Sn, Mg_3Sb_2, SbSn phases, and Mg-4Sb-(2,4wt %) Ca alloys composed of α-Mg, MgSbCa phases. The ternary alloys exhibited greater tensile strength and creep resistance in comparison with Mg-4Sb alloy. Corrosion studies suggested that Mg-4Sb-(2,4wt %) Sn alloys exhibited higher corrosion resistance than the base alloy whereas Mg-4Sb-(2,4wt %) Ca alloys have lower corrosion resistance than the base alloy. The increase of tensile strength with increasing ternary element content was mainly attributed to microstructural refinement and an increased fraction of secondary phases in both types of alloys. Regarding creep and corrosion behavior, 2 wt% ternary elements added alloys were shown superior resistance than the 4 wt% ternary elements added alloys. Due to the suppression of thermally stable Mg_3Sb_2 phases in Mg-4wt % Sb-4wt % Sn alloy, it showed lower creep resistance compared to Mg-4wt % Sb-2wt % Sn alloy. The lower creep resistance of Mg-4wt % Sb-4wt % Ca alloy in comparison with Mg-4wt % Sb-2wt % Ca alloy was ascribed because of the morphological change of the MgSbCa phase from a shorter network to a lengthy skeleton structure. The Mg_2Sn phases could be acted as pitting initiation sites, hence due to the existence of an enlarged quantity of Mg_2Sn phases, Mg-4wt % Sb-4wt % Sn alloy exhibited lower corrosion resistance among Sn contained ternary alloys. The addition of a higher % of Ca (4 wt %) led to an increase in the cathode (MgSbCa) to anode (α-Mg) surface area; Consequently, galvanic corrosion promoted more in Mg-4wt % Sb-4wt % Ca alloy related to Mg-4wt % Sb-2wt % Ca alloy.

Keywords: α-Mg, microstructure, hardness, tensile, creep, corrosion

Acknowledgments. *The authors would like to thank the department of Science and Technology (DST) SERB/F/5487/2012-13 Government of India for providing financial support of this work. The authors wish to acknowledge the Director, CSIR-National Institute for Interdisciplinary Science and Technology, Thiruvananthapuram for allowing us to carry out and publish this work.*

© S. Vignesh, Rajesh Kumar, A. Srinivasan, U.T.S. Pillai, 2022.
Publisher: Peter the Great St. Petersburg Polytechnic University
This is an open access article under the CC BY-NC 4.0 license (https://creativecommons.org/li-censes/by-nc/4.0/)

Citation: Vignesh S, Kumar R, Srinivasan A, Pillai UTS. Microstructural modeling of a TiNi beam bending. Materials Physics and Mechanics. 2023;50(3): 518-535. DOI: 10.18149/MPM.1512022_14.

Introduction

As light-weight materials, magnesium alloys are more desirable candidates for structural applications in the automotive and aerospace industries [1]. Nevertheless, to date, the usage of magnesium alloy parts in cars is approximately 5-6 kg, which is very much lower compared to the overall weight of the vehicle (around 1500 kg) [2]. To extend the application of magnesium alloys in automotive parts, currently many R&D activities are underway worldwide. The power train components such as engine blocks, engine pistons, and transmission cases hold a significant weight percentage of the overall weight of the vehicle. Replacement of Fe and Al based alloys by magnesium alloys in power train components have greater potential for significant weight reduction in automotive applications. Thus, the current R&D efforts mainly focus on the use of magnesium in power train components. The service temperature of the aforementioned power train components is in the range of 150-200°C [3]. Mg-Al based alloys are the most widely used commercial alloys due to their attractive properties; greater castability, decent corrosion resistance, and satisfactory mechanical properties at room temperature [4]. However, it is worth mentioning that, when a service temperature exceeds greater than 125°C Mg-Al based alloys exhibit poor creep resistance. Microstructure of Mg-Al alloys mainly composed of second phase $Mg_{17}Al_{12}$ phase which coarsens and dissolves into Mg matrix at elevated temperature due to its poor thermal stability [5]. Hence, these alloys are not suitable for high-temperature applications particularly for power train applications [3]. Numerous attempts have been made to improve the creep resistance of die-cast Mg-Al alloys through alloying include rare-earth, Ca, Sr [6]. Unfortunately, the additions of Ca, Sr lead to casting problems such as die sticking and hot cracking [3]. Mg-Al based alloy systems namely Mg-Al-Si, Mg-Al-Ca-Sr, Mg-Al-Si-Sb, Mg-Al-Zn-Ca-RE, Mg-Al-Zn-Sn also have been developed for creep resistance applications. Unfortunately, most of the developed alloys are not commercialized owing to their inferior die castability [7]. On the other hand, alloys that are completely free from aluminum content, such as Mg-RE-Zn-Mn, Mg-Y-Nd-Zr, Mg-RE-Zn-Zr developed through gravity casting exhibit significant creep resistance [8]. Mg-Gd based alloys are of major interest because of their good tensile and creep properties at service temperatures greater than 200°C [9]. However, due to the high cost and lack of availability of rare earth elements make these alloys unsuitable for industrial applications [10]. On the other hand, low-cost zinc-containing Mg-Zn-Al alloys have been developed for creep applications. The proper Zn/Al ratio in ZA alloys or (Mg-Zn-Al) alloys suppresses the formation of $Mg_{17}Al_{12}$ phase and introduces Mg-Zn-Al ternary phase [11]. However, ZA alloys exhibit limited creep resistance compared to Mg-RE alloys. Further, ZA alloys are more susceptible to the hot tearing problem. Hence, the development of low-cost high creep resistance magnesium-based alloys for high-temperature applications is of major interest among researchers. Recently few new Mg-Sb alloys were designed and their microstructure and mechanical properties were evaluated [12]. Though it was found that Mg-4Sb alloy exhibits good mechanical properties, further improvement in properties is necessary for its practical applications. The addition of ternary elements is an effective way to improve the mechanical properties of the Mg-4Sb alloy. Si was added to Mg-4Sb alloy and found that creep resistance of the alloy improved significantly. Identifying similar low-cost and still effective alloying elements for Mg-Sb alloys is an important task. Sn is a cost-effective alloying element that can be used to improve the creep and corrosion resistance of magnesium alloys [13-14]. Nayyeri et al. [15] have demonstrated that the higher solid solubility of Sn in magnesium and distribution of thermally

stable Mg_2Sn phases along grain boundaries are the possible reasons for the improvement in both ambient and high-temperature mechanical properties of Mg-5Sn alloy. Similarly Ca is another important alloying element for Mg alloys [16-17]. In the present study, Mg-4Sb-(2,4wt % Sn) and Mg-4Sb-(2,4wt % Ca) alloys are developed and microstructure, mechanical and corrosion properties of the developed alloys have been investigated in detail.

Experimental details

Alloy preparation. Alloys with a composition of Mg-4Sb-(2,4wt % Sn) and Mg-4Sb-(2,4wt % Ca) were prepared in a mild steel crucible under, Ar and SF6 gas mixture. The preheated alloying elements Ca, Sb or Sn covered with an aluminum foil were added into the molten magnesium at a temperature of 740°C. After being hold for 10 min. the melt was mechanically stirred for 2 min for attaining homogeneous composition. The melt was poured into a permanent mold preheated at 250°C after removing the oxides and other contaminants. The composition and alloy codes of base and experimental alloys were listed in Table 1.

Table 1. Alloy code and alloy composition

Alloy code	Alloy composition
M1	Mg- 4wt % Sb
M2	Mg- 4wt % Sb-2wt % Sn
M3	Mg- 4wt % Sb-4wt % Sn
M4	Mg- 4wt % Sb-2wt % Ca
M5	Mg- 4wt % Sb-4wt % Ca

Microstructure characterization. For the microstructural analysis, samples with 15 mm×15 mm dimensions were machined from the investigated alloys. The machined samples were initially ground with SiC emery papers up to 1000 grit and subsequent polishing was done by using 6μm, 3μm, and 0.25 μm diamond pastes. Prior to the microstructural examination, the polished samples were etched with a picric-acetic acid solution (5ml acetic acid, 10ml H_2O, 6g picric acid, and 100ml ethanol). The microstructure of the two alloys was investigated through optical microscopy (OM: LEICA DM2500-M) and scanning electron microscope (SEM) equipped with an energy-dispersive X-ray spectroscopy analysis system (SEM-EDS: ZEISS-EV018).

Tensile test. The tensile specimens were machined from the castings as per ASTM standard E-8 [18]. The gauge length of the samples was 50 mm. The tensile tests were conducted at a crosshead speed of 2 mm/min using 5 ton universal testing machine (STS make India) at room temperature.

Creep test. As per the ASTM test standard of E-139 [18], the creep test was carried out on the fabricated alloys under constant load at 150°C for 100h on a 5 ton servo-electric creep testing machine (STS make India). The creep strain was measured using a high-temperature extensometer. The sample was heated in a three-zone temperature-controlled furnace and the temperature was maintained within ± 1° throughout the testing.

Electrochemical measurements. The electrochemical tests were carried out in 3.5 wt% NaCl solution at room temperature using electrochemical equipment (CH Instruments Inc., Model 680A). Three electrodes were used to conduct the experiment. The working electrode, reference electrode, and counter electrode were the alloy sample, saturated calomel electrode (SCE), and platinum electrode respectively. The samples were polished with SiC emery papers up to 1000 grit before the experiment. The exposed area of the sample was $1cm^2$. Prior to electrochemical tests, initially, the open circuit potential (OCP) of the

samples was measured through the immersion of samples in an electrolyte around 30 min. The polarization test was conducted at a scan rate of 0.2 mV/s from cathodic to the anodic region between -250 mV to +250 mV with respect to OCP value. EIS tests were performed at the OCP with the frequency range from 10^5 to 10^{-1} Hz using the amplitude of 5mV. The Z view software with an equivalent circuit was used to analyze the EIS spectrum obtained from the samples.

Immersion test. Preparation of samples for immersion test followed the same procedure as electrochemical tests. The prepared samples were immersed in 250 ml of 3.5 wt% NaCl solution at room temperature for 100 hr. After the completion of the test, the samples were cleaned with distilled water and ethanol and dried. In order to remove the corrosion products, the dried samples were immersed in a 200 g/L CrO_3 solution for 20 min. The weight loss of the samples was measured.

Results and discussion

XRD, microstructure, and EDS analysis. The XRD patterns were obtained from the as cast alloys depicted in Fig.1. The base M1 alloy is composed of α-Mg, Mg_3Sb_2 phases where as M3 alloy consisted of α-Mg, Mg_2Sn, Mg_3Sb_2, and SbSn phases. The absence of Mg_2Sn and SbSn phases diffraction peaks in M2 alloy could be possibly due to its lesser amount.

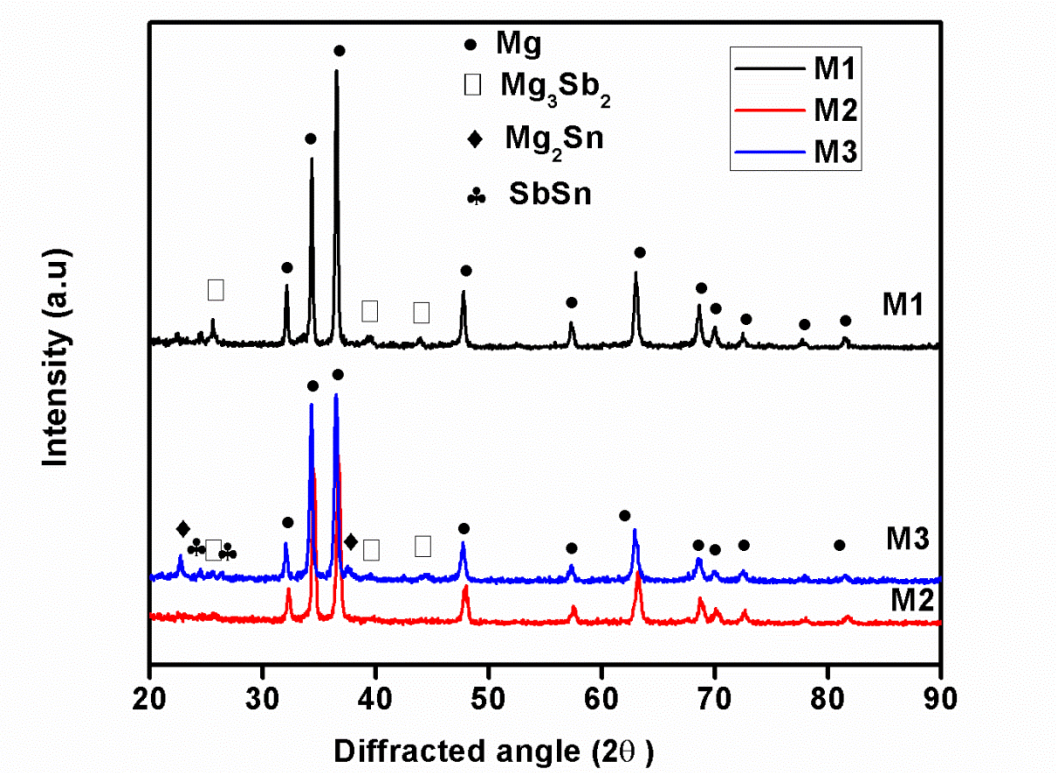

Fig. 1. X-ray diffraction patterns of base Mg-4wt % Sb and Mg-4Sb- X Sn (X =2 and 4 wt%) alloys

The optical microstructure of M1 alloy showed in Fig. 2(a). The microstructure consisted of magnesium matrix as well as secondary Mg_3Sb_2phases. It was noticed that the secondary phases were distributed at the dendrite boundaries. The higher magnification SEM image of M1 alloy (Fig. 2(b)) clearly displayed the needle-shaped morphology of secondary Mg_3Sb_2 phases.

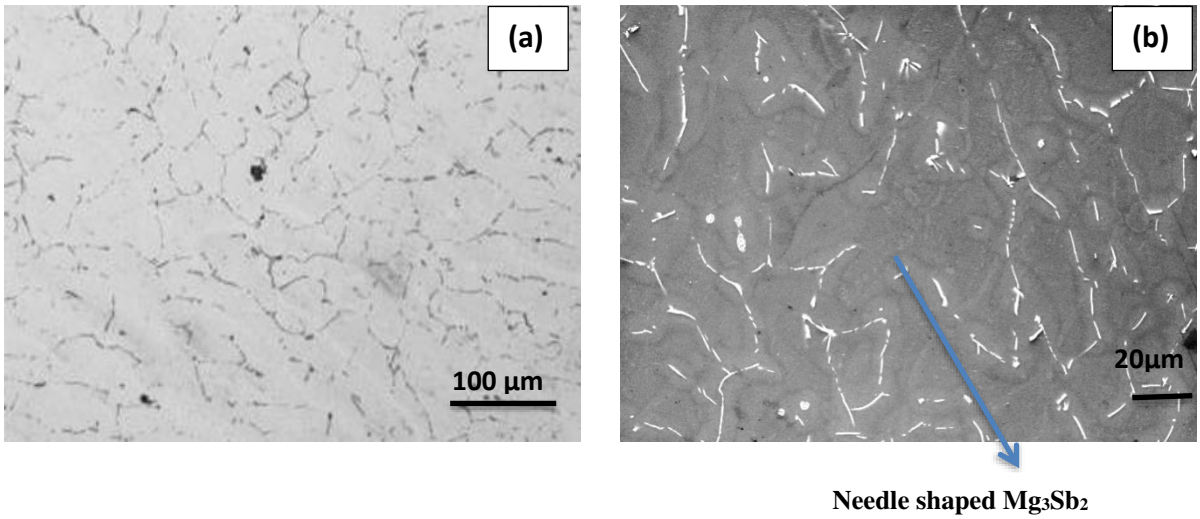

Fig. 2. Microstructure of M1 alloy: (a) optical (b) SEM micrograph

Figures 3 and 4 display the microstructure of M2, M3, and M4, M5 alloys respectively. The microstructure of both ternary alloys displayed a similar feature of fine dendrites arm spacing of α-Mg with an increase in the amount of ternary element from 2 to 4 wt%.

The microstructure of M2 and M3 alloys was composed of primary α-Mg and secondary Mg_2Sn, Mg_3Sb_2, and SbSn phases. The primary α-Mg (white region) was a solid solution of Sn. Normally, Mg-Sn alloy exhibits divorced eutectic: Mg_2Sn phase solidifies separately and eutectic α-Mg solidifies around the Mg_2Sn phase [19]. Compared to primary α-Mg, eutectic α-Mg consisted of a higher amount of Sn. Due to the above fact, the eutectic α-Mg reacted more with the etchant and became dark [20]. The higher magnification optical micrographs that are exemplified in Fig. 3 (c, d), clearly show the dark eutectic α-Mg in both the alloys. As can be seen in Fig. 3 (c, d), as Sn content increased the spherical shaped Mg_2Sn phases correspondingly increased. Also, the needle-shaped Mg_3Sb_2 and plate-shaped Mg_2Sn phases were seemed to be finer when the Sn content increased from 2 to 4wt %. The morphology of secondary phases in as cast experimental alloys depicted in Fig. 3 (e, f). The Mg_2Sn phase is exhibited in spherical and plate-shaped morphologies. On the other hand, Mg_3Sb_2 phase and SbSn phases had needle shape and irregular shape respectively.

The microstructure of M4 and M5alloys consisted of primary α-Mg and secondary MgSbCa phases. The addition of Ca to Mg-4Sb alloy led to form ternary MgSbCa secondary phases instead of binary Mg_3Sb_2 and Mg_2Ca phases. Hence, the formation of Mg_3Sb_2phase in M1 alloy was suppressed by the addition of Ca resulted in the formation of MgSbCa ternary phase. Fig.4 (c, d) displayed SEM images of as cast experimental alloys. The black regions in the microstructure were primary α-Mg and the white regions were secondary MgSbCa ternary phases. As seen from Fig. 4 (c, d), it was clear that as the Ca addition increased the volume fraction of MgSbCa ternary phase increased correspondingly. The morphology of the secondary phases was clearly seen in Fig. 4 (e and f). It was impressive to notice that, microstructure morphologies of secondary phases are varied with different alloying additions of Ca. The morphologies of M4 and M5 alloys were shorter network and lengthy skeleton-like structures respectively.

It was reported that the eutectic temperature of Mg-Sb, Mg-Sn, and Mg-Ca systems were 629°C, 561°C, and 517°C respectively [21]. Due to the higher eutectic temperature, while solidification, the nucleation of Mg_3Sb_2 occurs prior to the nucleation of other phases in both the ternary alloys. Thus, Mg_3Sb_2 might act as nucleation sites for α-Mg solidification in M2, M3, and M4, M5 alloys. However, owing to the fixed amount of Sb (4wt %) in both

studied alloys, the number of nucleation sites could not be varied much. This implied that α-Mg refinement was not determined by the Sb element in the alloys. Therefore variation in the amount of ternary Sn and Ca played a vital role for α-Mg dendrite refinement in the respective alloys. During non-equilibrium solidification, the ternary alloying element can be enriched in the solid/liquid interface because of a faster cooling rate. This enrichment led to restricting the growth of dendrites. Hence, when the ternary element content increased from 2 to 4wt % the growth restriction effect provided by the ternary elements could be more, thus the pronounced dendritic refinement was achieved. Similar dendrite refinement with the solute segregation during cooling has been reported earlier in Mg alloys [22-23].

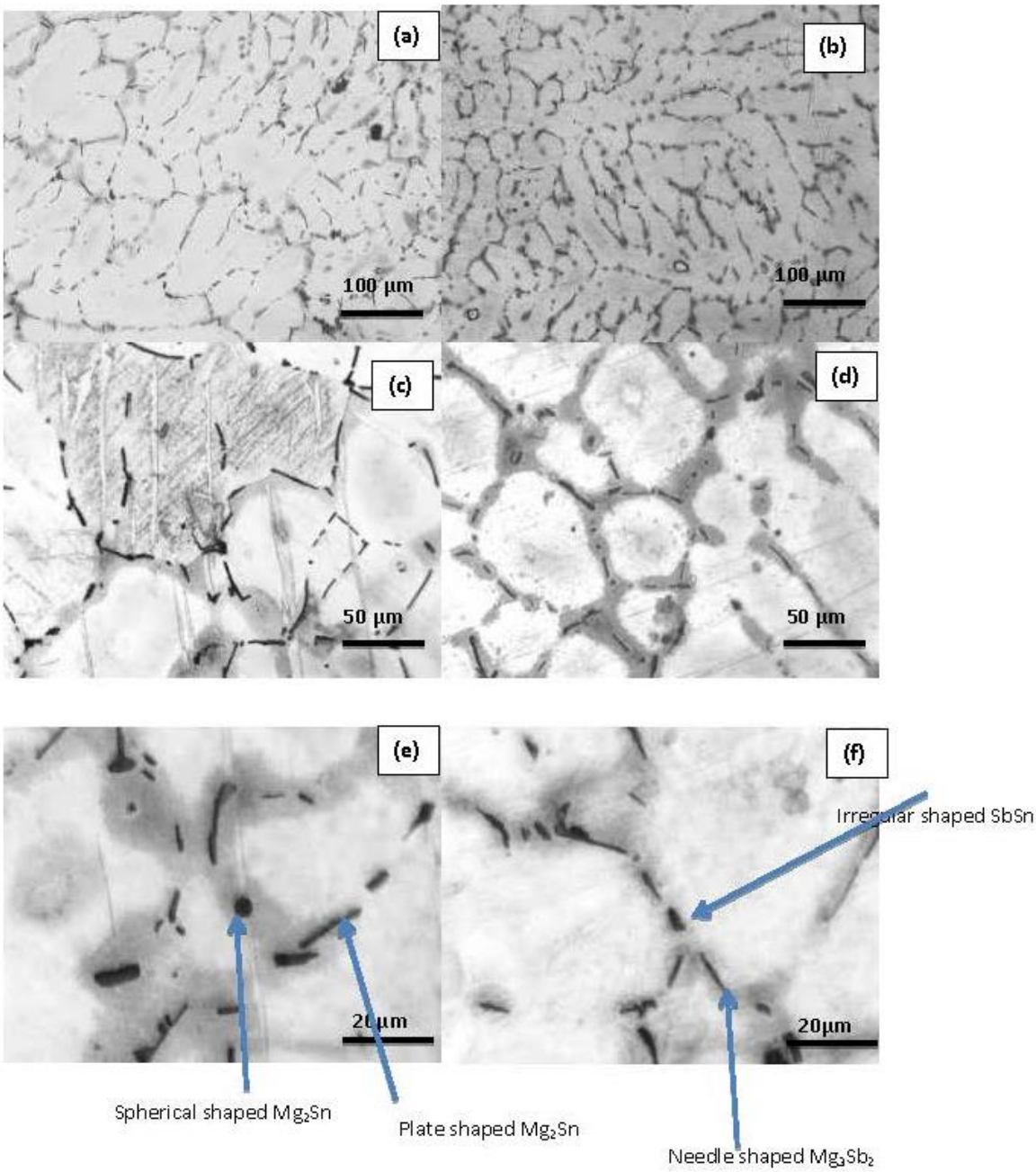

Fig. 3 Optical microstructures of: (a) & (c) M2 alloy (b-f) M3 alloy

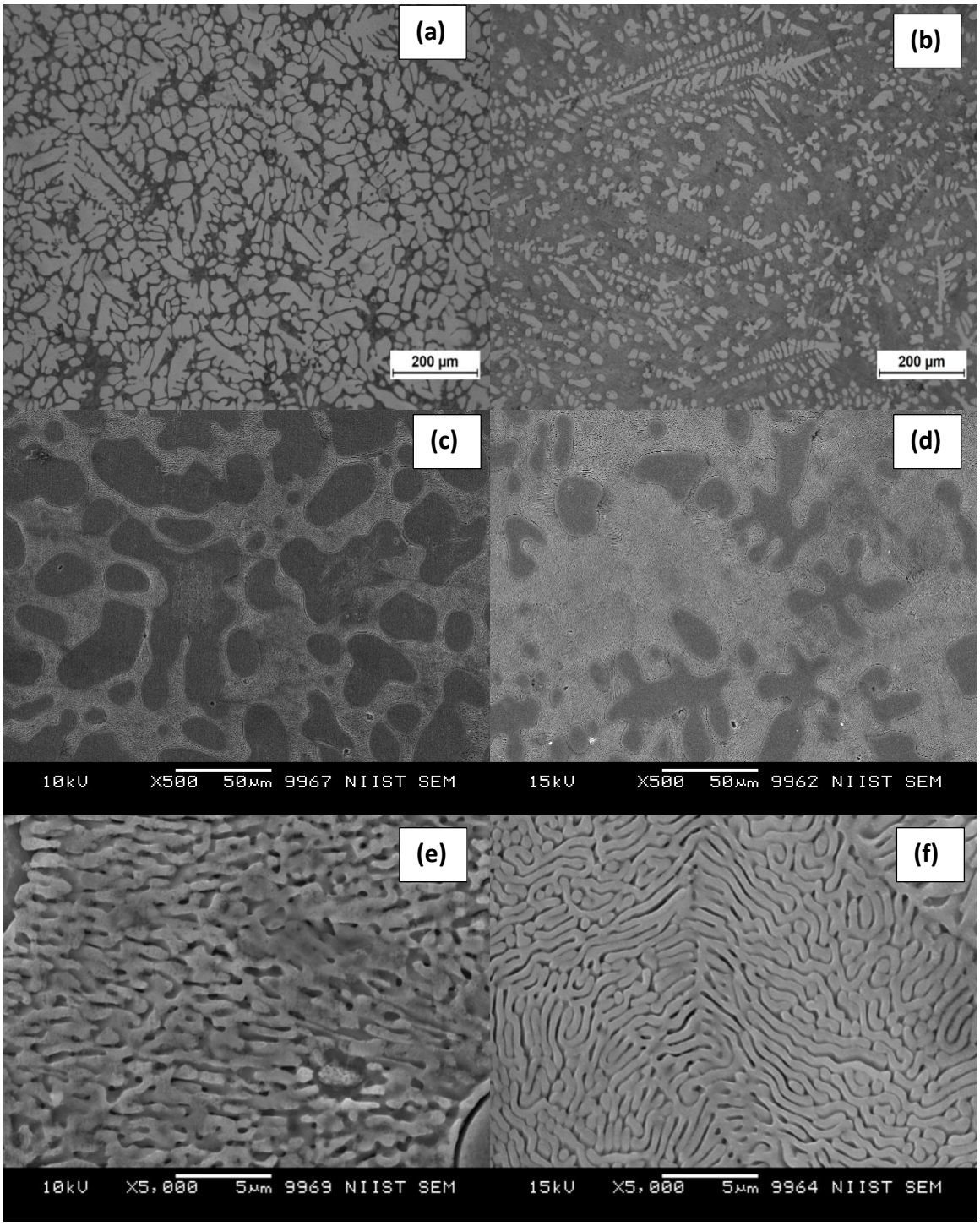

Fig. 4. Optical images of (a) M4 and (b) M5 alloys; SEM images of as cast: (c) M4 and (d) M5 alloys at lower magnification; higher magnification SEM images shown morphologies of secondary phases in (e) M4 and (f) M5 alloys

Fig. 5(a) demonstrates EDS analysis at position A (matrix) indicated the presence of calcium suggesting that little amount of Ca presence in the α-Mg solid solution. However, the amount of Ca in α-Mg solid solution was minimum (0.1 at%). The EDS spectrum on secondary network phases at position B (Fig. 5(b)) composed of Mg, Sb, and Ca elements, and it must be a ternary MgSbCa phase. However, no ternary MgSbCa phase existing in the XRD database.

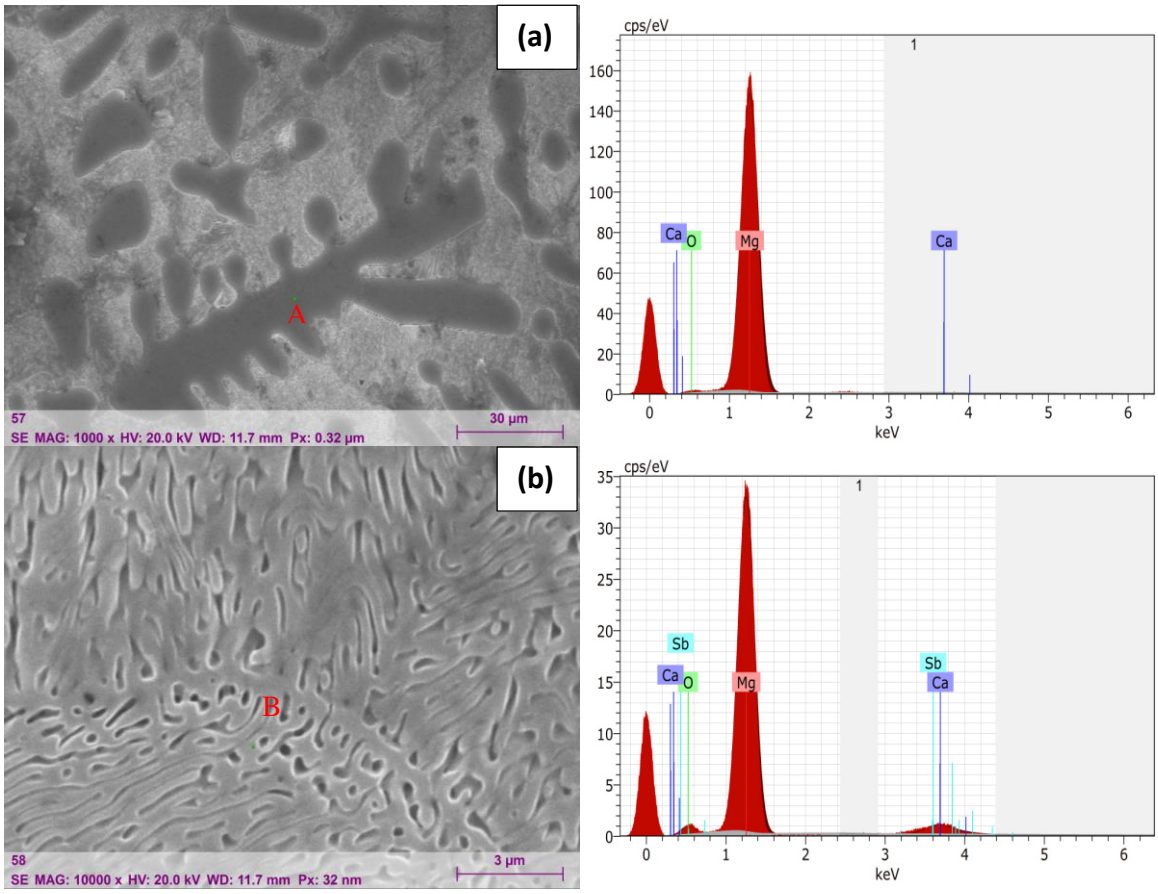

Fig. 5. EDS analysis of Mg-4Sb-(2,4)Ca alloys at (a) matrix (b) secondary phases

Room temperature tensile properties of the alloys. Figure 6 displayed the room tensile properties of experimental alloys. The M1 alloy showed UTS of 95MPa and an elongation to failure of 7.2%. Compared toM1alloy, the ternary alloys showed a higher value of UTS. However, elongation to failure of the alloys was lower in all the ternary alloys in comparison with M1 alloy. The M2 alloy exhibited UTS of 110 MPa and an elongation to failure of 6.2%. The addition of Sn from 2 to 4 wt.% increased the UTS to 118 MPa whereas elongation to failure reduced to 6.1%. The UTS and elongation to failure of M4 and M5 alloys were 93MPa, 1.3%, and 135MPa, 1.7% respectively.

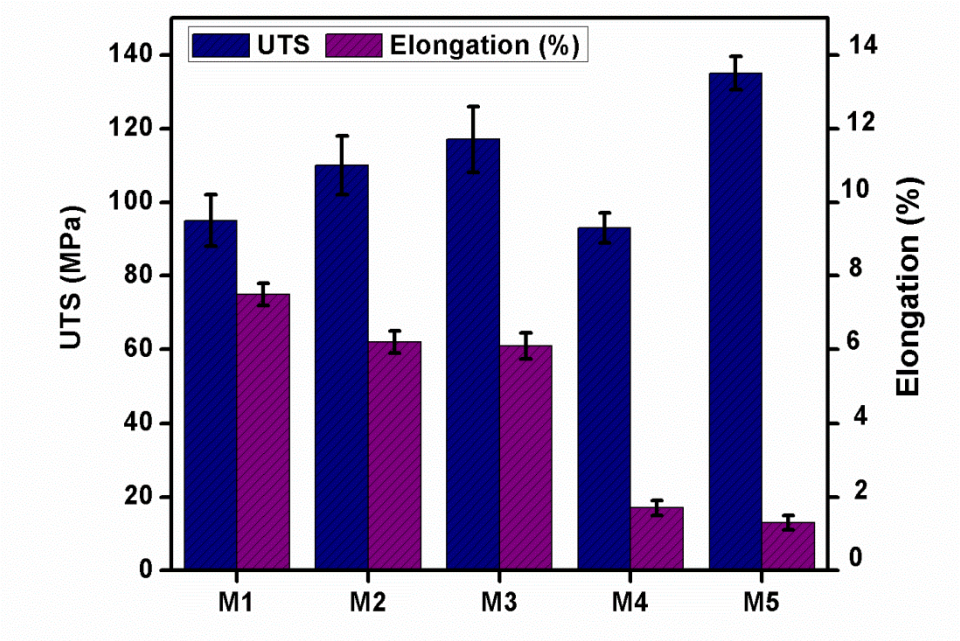

Fig. 6. Tensile properties of experimental alloys

The strengthening mechanism in the casted alloys was mainly attributed to the following aspects: (1) solid solution strengthening (2) secondary phase strengthening. According to the phase diagram of Mg-Sb [21], the solubility of Sb in magnesium is nil. Therefore, Sb addition did not provide a solid solution strengthening effect in the casted alloys. On the other hand, binary phase diagrams of Mg-Sn, as well as Mg-Ca, reveals that Sn and Ca can form a solid solution with magnesium [21]. The EDS spectrum on the magnesium matrix of M5 ternary alloy (as seen from Fig. 5) consisted of Mg and Ca elements which confirmed that Ca formed a solid solution with magnesium. Hence, in both the casted alloys the solid solution strengthening effect can be attributed due to the presence of Sn and Ca atoms and not by Sb atoms. The results indicate that in both Sn contained and Ca contained ternary alloys the tensile properties of 4wt % Sn or Ca alloys were comparatively superior to that of corresponding 2wt % alloys. In the case of 4wt % ternary alloys, dendrite arm spacing and boundaries were finer than the 2wt % ternary alloys which were one of the reasons for the improvement in tensile strength of 4wt % ternary alloys. The enhancement in the amount of Mg_2Sn phases in M3 alloy increased the resistance against dislocation motion, thereby increasing the strength of the M3alloy compared to M2. The strength of an alloy also strongly depends on the distribution, size, and shape of the secondary intermetallic phases [20]. The exhibited secondary phases in M3 alloy seemed to be finer compared to M2 alloy. The above observation could be another possible reason for the improvement in the strength of the M3 alloy. Interestingly, not much variation was obtained in the elongation of the experimental M2 and M3alloys. When the Ca concentration increased from 2 to 4 wt% the volume fraction of MgSbCa phases correspondingly increased. Due to this, the dispersion strengthening effect was more pronounced in the case of M5 compared to M4 alloy. The differences in % elongation of the M4 and M5 alloys were possibly related to the size of the secondary MgSbCa phases. The initiation and propagation of cracks in the interface between coarse MgSbCa and α-Mg matrix became easier; hence the existence of coarse MgSbCa phases in M5 alloy provided an adverse effect on % elongation.

Creep performance of the alloys. Figure 7 depicted the tensile creep curves of experimental alloys under testing conditions of 150°C and 50MPa for 100 h. Strain (%) Vs Time (h) curves of experimental alloys were shown in Fig. 7 (a). The creep strain of the M1 alloy for the given conditions was 1.78%. The M1 alloy experienced more strain compared to

all ternary alloys. Under a given set of conditions, the creep strain of M2 and M3 alloys for 100 h were 0.54% and 0.81% respectively. On the other hand, the M4 and M5 alloys exhibited lower creep strain i.e.0.036% and 0.198% respectively. Hence, when the amount of ternary element increased from 2 to 4 wt%, alloys experienced more strain under the same experimental conditions. In order to further understand the creep performance of the alloys, their respective strain rate vs. time plots was also analyzed (Fig. 7 (b)). At the beginning of the curves, the creep rate diminished quickly, and then it was continued with a constant creep rate. All the ternary alloys showed higher creep resistance than the M1 alloy. In the case of ternary alloys, the creep rate increased with the increment in the amount of ternary element addition.

The creep resistance of M2 and M3 alloys could be mainly attributed to the thermal stabilities of the intermetallic phases. In general, dispersion strengthening (through thermally stable phases) is an effective approach to achieve a higher creep resistance in alloys. The thermal stability of the intermetallic phases is based on their respective melting points. Generally, the higher the melting point of intermetallic phases greater the thermal stability and vice-versa [24]. The melting points of Mg_3Sb_2, Mg_2Sn, and SbSn phases are 1228°C [25], 770°C [26], and 350°C [15] respectively. Hence, because of their higher thermal stabilities, intermetallic phases such as Mg_3Sb_2 and Mg_2Sn are more effective to increase the elevated temperature performance of the alloys. Since, Mg_3Sb_2 and Mg_2Sn phases were distributed at dendrite boundaries, sliding of boundaries were decelerated at the higher temperature. In addition, dispersion of these intermetallic phases inside the dendrites led to hinder the dislocation annihilation and therefore restrict the plastic deformation in the interior of dendrites at elevated temperature. The relatively higher creep resistance of M2 compared to M3 alloys could be possibly related to the following aspect: As the Sn content increased from 2 to 4wt.% the amount of SbSn intermetallic phases were increased which in turn reduced the amount of Mg_3Sb_2 phase formation. However, in the case of M2 alloy, the amount of SbSn phases was low i.e the Mg-4Sb-2Sn consisted of more Mg_3Sb_2. Thus the presence of more quantity of thermally stable Mg_3Sb_2 in M2 alloy can give a beneficial effect on the creep resistance.

The differences in creep resistance among M4 and M5 alloys were possibly correlated to the microstructures of the respective alloys. The distributed MgSbCa secondary phases at dendrite boundaries and interior regions acted as obstacles to boundary sliding and movement of dislocations thereby improving creep resistance of the investigated alloys. The M5 alloy exhibited lower creep resistance than the M4 alloy. It was reported that grain size, microstructure homogeneity, and the morphology and thermal stability of secondary phases have a pronounced effect on creep resistance of magnesium alloys [27]. It was believed that the morphological changes from short network to the lengthy skeleton in 4 wt % concentrated alloy, predominantly affected the creep resistance.

Table 2. Creep properties of alloys at 150^0C and 50 MPa for 100 h

Alloy	**Creep strain (%)**	**Creep rate (s^{-1})**
M1	1.78	1.61×10^{-7}
M2	0.54	1.51×10^{-8}
M3	0.81	2.28×10^{-8}
M4	0.036	1×10^{-9}
M5	0.198	5.5×10^{-9}

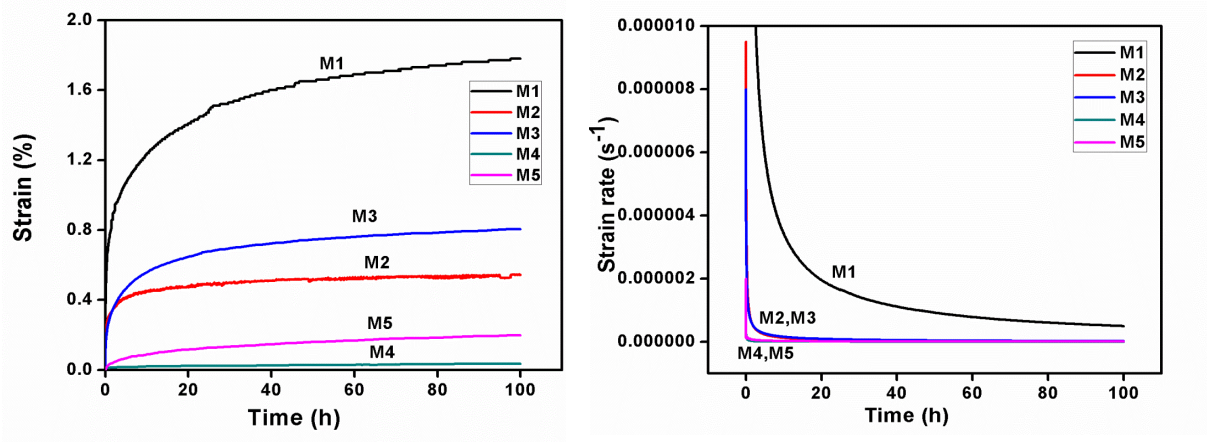

(a) **(b)**

Fig. 7. Creep curves of experimental alloys (a)Strain (%) Vs Time (h) and(b) Strain rate (s^{-1}) Vs Time (h)

Corrosion behavior of the alloys. The polarization behavior of the investigated alloys is depicted in Fig. 8 (a). Previous reports suggest that magnesium alloys exhibited a negative differential effect (NDE) during anodic polarization that leads to deviation in Tafel behavior [28-29]. Therefore in the present experiment, only cathodic polarization was considered for estimating corrosion current density (I_{corr}) value. The method used for determining I_{corr} value is illustrated in Fig. 8 (b). In this method, initially, a horizontal line was sketched at the corrosion potential (E_{corr}) and then a slope drawn in the cathodic curve at 100mV from the $E_{corr.}$ The current density at the intersection point of the slope line and the horizontal line drawn from the $E_{corr}$was taken as $I_{corr.}$

The corrosion potential (E_{corr}) and corrosion current density (I_{corr}) derived from the polarization curves of the alloys were listed in Table 3. The M2 and M3 alloys showed higher corrosion resistance than M1 alloy. However, the corrosion resistance of M4 and M5 alloys was lower than M1 alloy. It was observed that, as the ternary element content increased the corrosion current densities (I_{corr}) were correspondingly increased. The addition of Sn from 2 to 4 wt. % led to an increase in the I_{corr} value from 31.6 μA/cm^2 to 100 μA/cm^2. The E_{corr} of the M2 and M3 alloys were -1.61 (±0.04) Vvs.SCE and -1.59 (±0.02) Vvs.SCE respectively. Based on the above E_{corr} values, it was identified that 4Sn added alloy was nobler than the 2Sn added alloy. This implied M3 alloy was thermodynamically stable than M2 alloy. However, due to the obtained higher I_{corr} value in M3 alloy, it was confirmed that, kinetically this alloy corroded faster than the M2 alloy. The E_{corr}, I_{corr} values of M4 and M5 alloys were -1.64(±0.03), 630(±7.8) and -1.68(±0.02), 5000(±6.3). These results suggest that M4 was thermodynamically as well as kinetically stable than M5 alloy.

Table 3. The E_{corr} and I_{corr} values extracted from the polarization curve

Alloy	E_{corr} (V vs. SCE)	I_{corr}(μA/cm^2)
M1	-1.64(±0.01)	125(±4.8)
M2	-1.61(±0.02)	31.6(±6.1)
M3	-1.59(±0.04)	100(±5.4)
M4	-1.64(±0.03)	630(±7.8)
M5	-1.68(±0.02)	5000(±6.3)

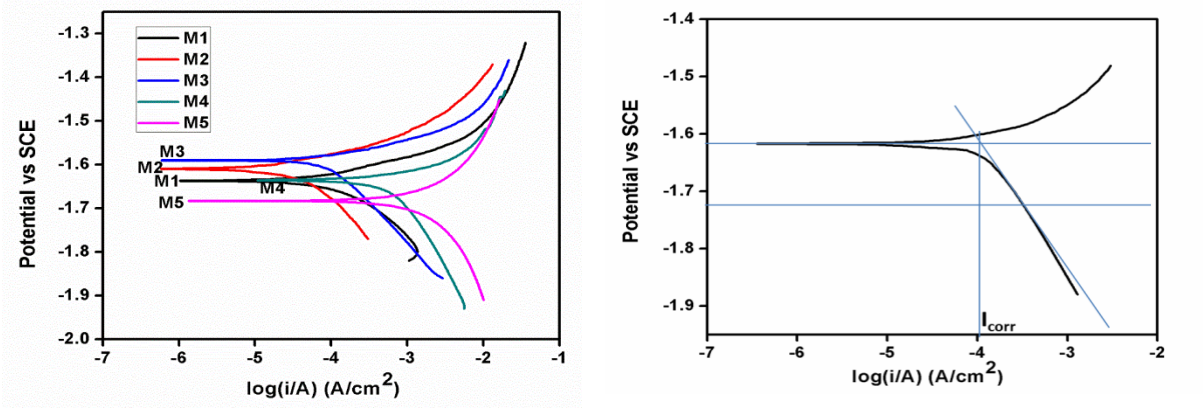

(a) (b)

Fig. 8. (a)Polarization curves of experimental alloys (b) Method used for determining I_{corr}value from polarization curve

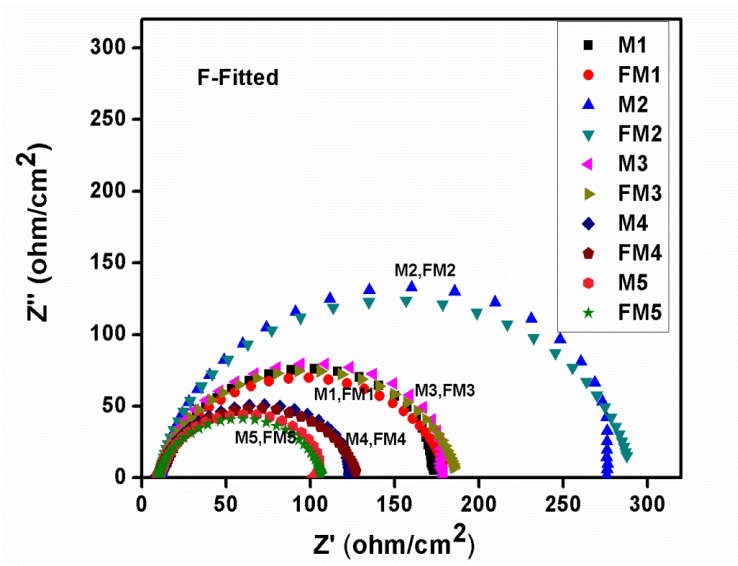

Fig. 9. Nyquist plots of experimental alloys

Figure 9 displayed the Nyquist plots of experimental alloys. It was observed that all the alloy consisted of a single capacitance loop. Compared to M1 alloy, M2 and M3 alloys exhibited higher corrosion resistance whereas the corrosion resistance of M4 and M5 alloys was lower than the base alloy. It could be noticed that the diameter of the loop decreasing when the ternary addition increased from 2 to 4 wt%. This inferred 2 wt% ternary element addition has higher corrosion resistance than the 4 wt % ternary element added alloys.

Fig. 10. The equivalent circuit used to fit EIS data

Table 4. The fitted results of the electrochemical impedance data

Alloy	Rs (Ω-cm^2)	CPE$_o$-T	CPE$_o$-P	R (Ω-cm^2)	χ^2
M1	10.57	7.79×10^{-5}	0.87	171.2	9×10^{-3}
M2	10.07	3.68×10^{-5}	0.92	279.8	1×10^{-2}
M3	9.558	4.54×10^{-5}	0.89	177.3	1×10^{-2}
M4	9.74	6.53×10^{-5}	0.87	124	6×10^{-3}
M5	10.03	4.32×10^{-5}	0.89	103	9×10^{-3}

The equivalent circuit as shown in Fig. 10 was applied to fit the Nyquist plots represented in Fig. 9. This circuit is composed of three elements as follows; solution resistance (R_s), charge transfer resistance (R), and constant phase element (CPE1). The constant phase element (CPE1) was parallel with the charge transfer resistance. It was reported that the usage constant phase element (CPE) delivered good fitting between experimental and theoretical data compared to pure capacitor [30]. Due to this, rather than a pure capacitor, a constant phase element (CPE) was chosen in the equivalent circuit. The Solution resistance (R_s) has no effect on the electrode process and this value was mainly influenced by the geometry of the cell as well as the conductivity of the electrolyte [31]. The fitted results of the EIS data were listed in Table 3. It was noticed that fitted data results have the same trend as the displayed Nyquist plots. Both Nyquist plots and fitted data were shown higher resistance with 2 wt% ternary elements added alloys.

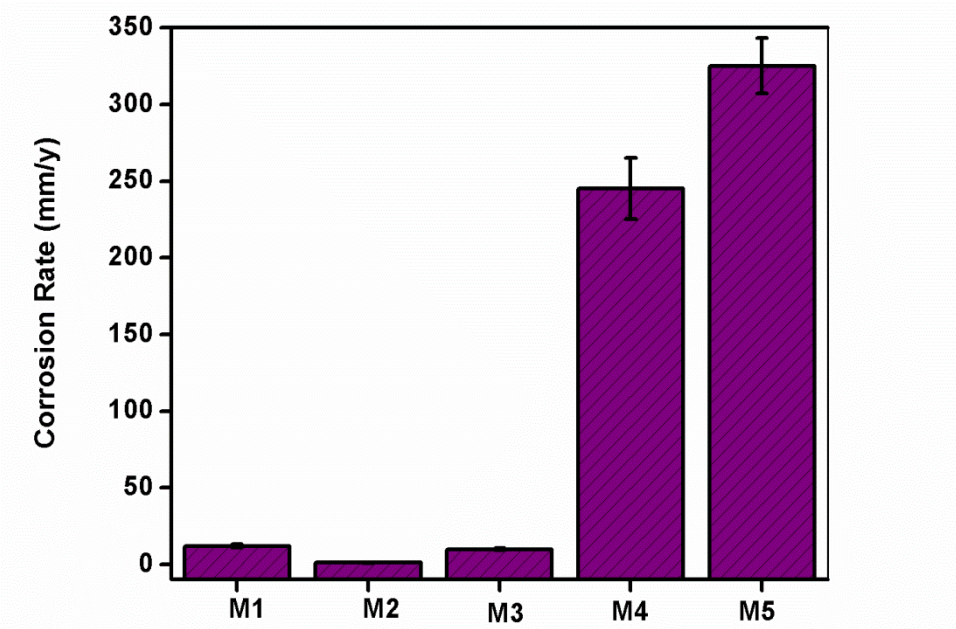

Fig. 11. Immersion test results show corrosion rate of experimental alloys

Figure 11 showed the immersion test results of the investigated alloys. The trends observed from the immersion tests were in good agreement with polarization as well as EIS results. It could be noticed that 4 wt% ternary element added alloys exhibited an enlarged value of corrosion rate compared to 2 wt% ternary element added alloys. The corrosion rate values of M1, M2, M3, M4, M5 alloys were 12 mm/yr, 1 mm/yr,10 mm/yr, 245 mm/yr, and 325 mm/yr respectively.

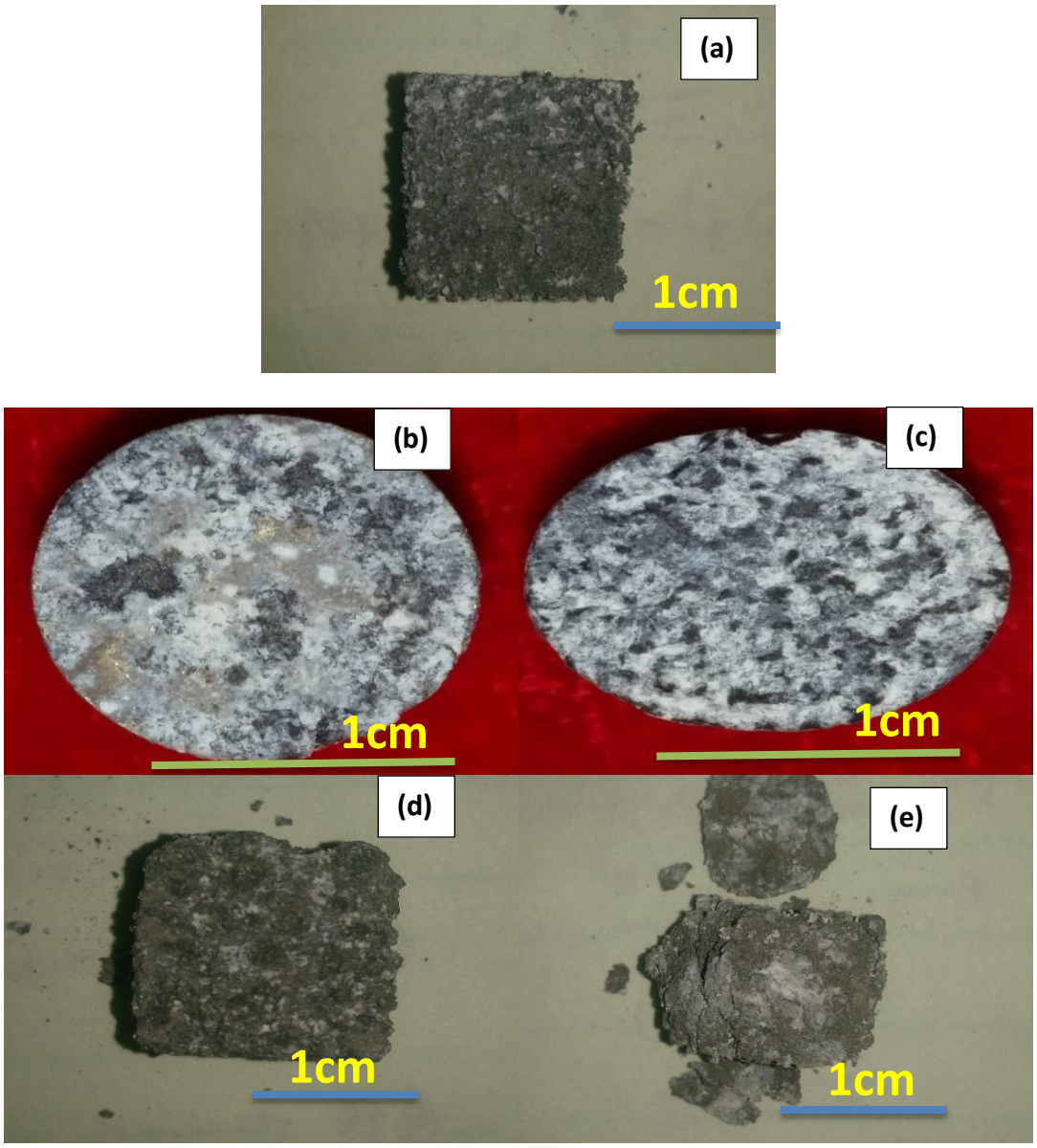

Fig. 12. Photographs of corroded samples after immersion test (a) M1 (b) M2 (c) M3 (d) M4 and (e) M5

The corroded surface of the experimental alloys after the immersion test was presented in Fig. 12. In the case of M2 and M3 alloys, pitting corrosion was dominated as both the alloy samples consisted of multiple pits on their surface. The number of corrosion pits was seemed to be more in M3 alloy. Moreover, in M4 and M5 alloys, it could be identified that among the two alloys, M5corroded severely.

C.D Yim et al. [32] reported the following points related to surface films in magnesium alloys: (1). Stability of the passive film on magnesium alloys is poor; (2). Re-passivity behavior after the breakdown of passive film is not effective. Due to the above-mentioned reasons, it is understandable that the passivity of the surface film could not play a vital role in the experimental alloys. Once the passive film is a breakdown, the surface of the alloys is directly exposed to the solution. In this case, the metal dissolution rate should be equal to the hydrogen evaluation rate [32-33]. Thus, hydrogen evaluation rate was considered to be an important factor for evaluating the overall corrosion rate than the passive film [32,34]. The hydrogen evaluation rate of the alloys could be estimated from the cathodic current densities values of the investigated alloys. In the present study, cathodic current density values of the

alloys were considered as I_{corr} values. As seen from table 2, 4 wt% ternary element added alloys exhibited higher cathodic current density which means that the hydrogen evaluation rate in these alloys was higher. Furthermore, it was reported that hydrogen evaluation rate was directly correlated to the degree of weight loss [33-34]. Therefore, due to the higher degree of weight loss through immersion tests, 4 wt% ternary element added alloys showed a higher hydrogen evaluation rate or overall corrosion rate. Earlier experimental evidence suggest that Mg_2Sn intermetallic phases could be acted as pitting initiation sites [35-36]. Hence, the corrosion of the Sn contained ternary alloys accelerated when the quantity of Mg_2Sn phases increased. The higher I_{corr} in M3 alloy primarily resulted from the enhanced quantity of Mg_2Sn phases in its microstructure.

The formation of micro galvanic coupling between magnesium matrix and secondary phases increases the corrosion rate [37]. Previous experimental evidence suggest that the Ca addition in magnesium alloys usually forms a Ca based intermetallic phase which formed a galvanic couple with magnesium that deteriorates the corrosion resistance of the alloys [38-40]. Thus, the galvanic coupling phenomenon between Mg and MgSbCa phases influences the corrosion rate in M4 and M5alloys. In general, when the cathode to anode surface area was lower the rate of galvanic corrosion diminished [41]. Thus, the higher corrosion resistance of M4 alloy was mainly attributed to the lower surface ratio of the cathode (MgSbCa phase) to the anode (Mg-matrix) compared to M5 alloy.

Conclusions

The findings of the present research work could be summarized in the following points.

1. The microstructure of base Mg-4wt % Sb alloy is composed of α-Mg andMg_3Sb_2phase. The microstructure of ternary Mg-4wt % Sb-(2,4wt %)Sn alloys consisted of α-Mg, Mg_2Sn, Mg_3Sb_2, and SbSn phases whereas Mg-4wt % Sb-(2,4wt %)Ca alloys composed of α-Mg and MgSbCa phases.
2. In ternary alloys, when the ternary element content increased from 2 to 4 wt% the dendrite arm spacing of α-Mg was refined remarkably. Enrichment in ternary element atoms ahead of solid/liquid interface during solidification offered constitutional undercooling that led to a decrease in the size of α-Mg dendrites.
3. The ternary alloys exhibited higher tensile strength than the Mg-4wt % Sb alloy. Superior tensile strength was achieved in 4 wt% ternary elements added alloys. Enhanced quantity of Mg_2Sn and SbSn phases and the α-Mg refinement resulted in an increment in strength and hardness of Mg-4wt % Sb-4wt % Sn alloy compared to Mg-4wt % Sb-2wt % Sn alloy. The refinement α-Mg dendrites and a higher volume fraction of MgSbCa phases offered a more pronounced dispersion strengthening effect in Mg-4wt % Sb-4wt % Ca alloy compared to Mg-4wt % Sb-2wt % Ca alloy.
4. Compared to the base Mg-4wt % Sb alloy, the ternary alloys showed higher creep resistance. Increasing ternary element content from 2 to 4 wt% decreased the creep performance of the investigated alloys. Increased addition of Sn from 2 to 4 wt% not only increased Mg_2Sn phases but also promoted the amount of SbSn phases. This implied Mg_3Sb_2 phases could be suppressed in Mg-4wt % Sb-4wt % Sn alloy related to Mg-4wt % Sb-2wt % Sn alloy. Due to its higher melting point, Mg_3Sb_2 phases have higher thermal stability. Hence, it was reasonable to conclude that, the suppression of Mg_3Sb_2 in Mg-4wt % Sb-4wt % Sn alloy could be the possible reason for the deterioration of creep properties. The morphological change from shorter network to lengthy skeleton-type played a key role in the reduction in creep resistance of the Mg-4wt % Sb-4wt % Ca alloy compared to Mg-4wt % Sb-2wt % Ca alloy.
5. Corrosion studies confirmed that Mg-4wt % Sb-(2,4wt %) Sn alloys exhibited higher corrosion resistance than the base alloy whereas Mg-4wt % Sb-(2,4wt %) Ca alloys have

lower corrosion resistance than the base alloy. Th 4wt% ternary element added alloys exhibited poor corrosion resistance than the 2 wt% ternary elements added alloys. As the Sn content increased, the amount of Mg_2Sn phases also was correspondingly increased. These intermetallic phases acted as pitting initiation sites thereby increased the overall corrosion rate in Mg-4wt % Sb-4wt % Sn alloy compared to Mg-4wt % Sb-2wt % Sn alloy. The micro-galvanic circuit between magnesium matrix (anode) and MgSbCa phases (cathode) induced corrosion in Mg-4wt % Sb-(2,4wt %)Ca alloys. Due to the cathode/anode surface area in 2wt % Ca added alloy, it showed higher corrosion resistance.

References

1. Mo W, Zhang L, Wu G, Zhang, Y, Liu W, Wang C. Effects of processing parameters on microstructure and mechanical properties of squeeze-cast Mg–12Zn–4Al–0.5Ca alloy. *Materials & Design.* 2014;63: 729-737.
2. Cole G. Magnesium Vision 2020: A North American Automotive Strategic Vision for Magnesium. In: Quinn J, Hetrick E, Bairley S. (Eds.) *Automotive Materials Partnership Committee.* 2006.
3. Luo A. Recent magnesium alloy development for elevated temperature applications. *International Materials Reviews*. 2004;49(1): 13-30.
4. Nayyeri G, Mahmudi R. The microstructure and impression creep behavior of cast, Mg–5Sn–xCa alloys. *Materials Science and Engineering: A*. 2010;527(7-8): 2087-2098.
5. Khalilpour H, Mahdi Miresmaeili S, Baghani A. The microstructure and impression creep behavior of cast Mg–4Sn–4Ca alloy. *Materials Science and Engineering: A*. 2016;652: 365-369.
6. K. Pekguleryuz AA, Mihriban O. Magnes. Alloy. Their Appl. *Proc. 6th Int. Conf. Magnes*. 2004. p.74–93.
7. Polmear I. Magnesium alloys and applications. *Materials Science and Technology*. 1994;10(1): 1-16.
8. Yang Z, Li J, Zhang J, Lorimer G, Robson J. Review on Research and Development of Magnesium Alloys. *Acta MetallurgicaSinica (English Letters).* 2008;21(5): 313-328.
9. Xu W, Zhang Y, Peng L, Ding W, Nie J. Formation of denuded zones in crept Mg–2.5Gd–0.1Zr alloy. *Acta Materialia*. 2015;84: 317-329.
10. Pan H, Ren Y, Fu H, Zhao H, Wang L, Meng X, Qin G. Recent developments in rare-earth free wrought magnesium alloys having high strength: A review. *Journal of Alloys and Compounds.* 2016;663: 321-331.
11. Zhang Z, Tremblay R, Dube D. Microstructure and mechanical properties of ZA104 (0.3–0.6Ca) die-casting magnesium alloys. *Materials Science and Engineering A*. 2004;385(1-2): 286-291.
12. Rajeshkumar R, Jayaraj J, Srinivasan A, Pillai U. Investigation on the microstructure, mechanical properties and corrosion behavior of Mg-Sb and Mg-Sb-Si alloys. *Journal of Alloys and Compounds*. 2017;691: 81-88.
13. Yang M, Pan F. Effects of Y addition on as-cast microstructure and mechanical properties of Mg–3Sn–2Ca (wt.%) magnesium alloy. *Materials Science and Engineering: A*. 2009;525(1-2): 112-120.
14. Kim B, Park K, Park Y, Park I. Effect of Ca and Sr additions on high temperature and corrosion properties of Mg–4Al–2Sn based alloys. *Materials Science and Engineering: A*. 2011;528(3): 808-814.
15. Nayyeri G, Mahmudi, R. Effects of Sb additions on the microstructure and impression creep behavior of a cast Mg–5Sn alloy. *Materials Science and Engineering: A*. 2010;527(3): 669-678.

16. Lee Y, Dahle A, StJohn D. The role of solute in grain refinement of magnesium. *Metallurgical and Materials Transactions A*. 2000;31(11): 2895-2906.
17. Vogel M, Kraft O, Arzt E. Effect of calcium additions on the creep behavior of magnesium die-cast alloy ZA85. *Metall. Mater. Trans. A.* 2005;36: 1713–1719.
18. *ASTM Specifications E8, E21 and E-139*. West Conshohocken, USA: ASTM International; 1994,
19. Liu H, Chen Y, Tang Y, Wei S, Niu G. The microstructure, tensile properties, and creep behavior of as-cast Mg–(1–10)%Sn alloys. *Journal of Alloys and Compounds.* 2007;440(1-2): 122-126.
20. Poddar P, Bagui S, Ashok K, Murugesan A. Experimental investigation on microstructure and mechanical properties of gravity-die-cast magnesium alloys. *Journal of Alloys and Compounds.* 2017;695: 895-908.
21. Okamoto H, Schlesinger ME, Mueller EM. *ASM Handbook Volume 3: Alloy Phase Diagrams.* ASM International; 1992.
22. Yang Y, Wang Y, Liang H, Deng S, Zhang X. Clinical effects of dezocine plus propofol vs fentanyl plus propofol in painless colonoscopy. *World Chinese Journal of Digestology*. 2014;22(22): 3340.
23. Tahreen N, Chen D, Nouri M, Li D. Influence of aluminum content on twinning and texture development of cast Mg–Al–Zn alloy during compression. *Journal of Alloys and Compounds*. 2015;623: 15-23.
24. Hort N, Huang Y, Kainer K. Intermetallics in Magnesium Alloys. *Advanced Engineering Materials*. 2006;8(4): 235-240.
25. Guangyin Y, Yangshan S, Wenjiang D. Effects of Sb addition on the microstructure and mechanical properties of az91 magnesium alloy. *Scripta Materialia.* 2000;43(11): 1009-1013.
26. Liu H, Chen Y, Tang Y, Wei S, Niu G. The microstructure, tensile properties, and creep behavior of as-cast Mg–(1–10)%Sn alloys. *Journal of Alloys and Compounds.* **2007;**440(1-2): 122-126.
27. Liu J, Wang W, Zhang S, Zhang D, Zhang H. Effect of Gd–Ca combined additions on the microstructure and creep properties of Mg–7Al–1Si alloys. *Journal of Alloys and Compounds*. 2015;620: 74-79.
28. Song G, Atrens A, Dargusch M. Influence of microstructure on the corrosion of diecast AZ91D. *Corrosion Science*. 1998;41(2): 249-273.
29. Chu YR, Lin CS. Citrate gel conversion coating on AZ31 magnesium alloys. *Corrosion Science*. 2014;87: 288-296.
30. Duan H, Yan C, Wang, F. Effect of electrolyte additives on performance of plasma electrolytic oxidation films formed on magnesium alloy AZ91D. *Electrochimica Acta*. 2007;52(11): 3785-3793.
31. Hussein R, Northwood D, Nie X. The effect of processing parameters and substrate composition on the corrosion resistance of plasma electrolytic oxidation (PEO) coated magnesium alloys. *Surface and Coatings Technology*. 2013;237: 357-368.
32. Yim C, Yang J, Woo S, Ha H, You B. The effects of microstructural factors on the corrosion behaviour of Mg–5Sn–xZn (x= 1, 3 wt%) extrusions. *Corrosion Science.* 2015;90: 597-605.
33. Birbilis N, Williams G, Gusieva K, Samaniego A, Gibson M, McMurray H. Poisoning the corrosion of magnesium. *Electrochemistry Communications*. 2013;34: 295-298.
34. Ha H, Kang J, Yang J, Yim C, You B. Limitations in the use of the potentiodynamicpolarisation curves to investigate the effect of Zn on the corrosion behaviour of as-extruded Mg–Zn binary alloy. *Corrosion Science*. 2013;75: 426-433.

35. Liu X, Shan D, Song Y, Chen R, Han E. Influences of the quantity of Mg_2Sn phase on the corrosion behavior of Mg–7Sn magnesium alloy. *Electrochimica Acta*. 2011;56(5): 2582-2590.
36. Ha H, Kang J, Kim S, Kim B, Park S, Yim C, You B. Influences of metallurgical factors on the corrosion behaviour of extruded binary Mg–Sn alloys. *Corrosion Science*. 2014;82: 369-379.
37. Cao F, Song G, Atrens A. Corrosion and passivation of magnesium alloys. *Corrosion Science*. 2016;111: 835-845.
38. Jeong Y, Kim W. Enhancement of mechanical properties and corrosion resistance of Mg–Ca alloys through microstructural refinement by indirect extrusion. *Corrosion Science*. 2014;82: 392-403.
39. Zeng R, Qi W, Cui H, Zhang F, Li S, Han E. In vitro corrosion of as-extruded Mg–Ca alloys—The influence of Ca concentration. *Corrosion Science*. 2015;96: 23-31.
40. Zeng R, Sun L, Zheng Y, Cui H, Han E. Corrosion and characterisation of dual phase Mg–Li–Ca alloy in Hank's solution: The influence of microstructural features. *Corrosion Science*. 2014;79: 69-82.
41. Song G, Johannesson B, Hapugoda S, StJohn D. Galvanic corrosion of magnesium alloy AZ91D in contact with an aluminium alloy, steel and zinc. *Corrosion Science*. 2004;46(4): 955-977.

Submission of papers:
Manuscript should be submitted (**both MS Word and PDF**) by e-mail to: **mpmjournal@spbstu.ru**
After a confirmation of the paper acceptation, the authors should send the signed hard copy of the "Transfer of Copyright Agreement" form (available at http://www.mpm.spbstu.ru section "Authors") by regular post to "Materials Physics and Mechanics" editorial office:
Periodicals Editorial Office, Institute of Advanced Manufacturing Technologies, Peter the Great St.Petersburg Polytechnic University, Polytechnicheskaya, 29, St.Petersburg 195251, Russia.
The scanned copy of the signed "Transfer of Copyright Agreement" should be send by e-mail to: mpmjournal@spbstu.ru.

Filetype:
Authors are invited to send their manuscripts **as MS Word file with PDF format copy.**
MS Word file should be prepared according to the general instructions bellow; we are kindly asking the authors to look through the detail instruction at: http://www.mpm.spbstu.ru.

Length:
Papers should be limited to 30 typewritten pages (including Tables and Figures placed in the proper positions in the text).

Structure of the manuscript:

PAPER TITLE: CENTERED,

TIMES NEW ROMAN 14 BOLD, CAPITAL LETTERS

A.B. Firstauthor[1], C.D. Secondauthor[2*] –Times New Roman 12, bold, centered

[1]Affiliation, address, country - Times New Roman 10, centered

*e-mail: e-mail of the corresponding author - Times New Roman 10, centered

Abstract. Times New Roman 12 font, single line spacing. Abstract should not exceed 12 lines.
Keywords: please, specify paper keywords right after the abstract.

Paper organization. Use Times New Roman 12 font with single line spacing. Use *Italic* font in order to stress something; if possible, please, use **bold** for headlines only.

Page numbering. Please, do not use page numbering.

Tables, Figures, Equations. Please, see the sample file at http://www.mpm.spbstu.ru for more details.

References
References should be subsequently numbered by Arabic numerals in square brackets, e.g. [1,3,5-9], following the sample style below:
[1] Koch CC, Ovid'ko IA, Seal S, Veprek S. *Structural Nanocrystalline Materials: Fundamentals and Applications*. Cambridge: Cambridge University Press; 2007.
[2] Hull D, Bacon DJ. *Introduction to Dislocations*. 5nd ed. Amsterdam: Butterworth-Heinemann; 2011 Available from: https://www.sciencedirect.com/science/book// 9780080966724?via%3Dihub [Accessed 19th June 2018].
[3] Romanov AE, Vladimirov VI. Disclinations in crystalline solids. In: Nabarro FRN (ed.) *Dislocations in Solids*. Amsterdam: North Holland; 1992;9. p.191-402.
[4] Mukherjee AK. An examination of the constitutive equation for elevated temperature plasticity. *Materials Science and Engineering: A*. 2002;322(1-2): 1-22.

[5] Soer WA, De Hosson JTM, Minor AM, Morris JW, Stach EA. Effects of solute Mg on grain boundary and dislocation dynamics during nanoindentation of Al–Mg thin films. *Acta Materialia*. 2004;52(20): 5783-5790.
[6] Matzen ME, Bischoff M. A weighted point-based formulation for isogeometric contact. *Computer Methods in Applied Mechanics and Engineering*. 2016;308: 73-95. Available from: doi.org/10.1016/j.cma.2016.04.010.
[7] Joseph S, Lindley TC, Dye D. Dislocation interactions and crack nucleation in a fatigued near-alpha titanium alloy. To be published in *International Journal of Plasticity. Arxiv.* [Preprint] 2018. Available from: https://arxiv.org/abs/1806.06367 [Accessed 19th June 2018].
[8] Pollak W, Blecha M, Specht G. *Process for the production of molded bodies from silicon-infiltrated, reaction-bonded silicon carbide*. US4572848A (Patent) 1983.
[9] Brogan C. *Experts build pulsed air rig to test 3D printed parts for low carbon engines*. Available from: http://www.imperial.ac.uk/news/186572/experts-build-pulsed-test-3d-printed/ [Accessed 19th June 2018].

Правила подготовки статей:
Рукопись (**английский язык, MS Word и копия PDF**) должна быть направлена в редакцию журнала по электронной почте: **mpmjournal@spbstu.ru**.
После подтверждения принятия статьи в печать, авторы должны отправить подписанные:
1. Соглашение о передаче авторских прав (http://www.mpm.spbstu.ru, раздел «Авторам»);
2. Экспертные заключения о том, что материалы статьи не содержат сведений, составляющих государственную тайну, и информацию, подлежащую экспортному контролю; по адресу:
Россия, 195251, Санкт-Петербург, Политехническая, д. 29, Санкт-Петербургский политехнический университет Петра Великого, Институт передовых производственных технологий, Редакция периодических изданий.
Скан-копии подписанных документов просим направить по электронной почте: mpmjournal@spbstu.ru
Тип файла:
Редакция принимает **файлы MS Word с копией в формате PDF**. Статья должна быть подготовлена в соответствии с настоящей инструкцией, мы просим авторов также следовать более подробным инструкциям на сайте журнала http://www.mpm.spbstu.ru в разделе «Авторам».
Длина статьи:
Статья не должна превышать 30 страниц формата А4, включая Таблицы и Рисунки, размещенные непосредственно в соответствующих местах.
Общие правила оформления статьи:

НАЗВАНИЕ СТАТЬИ: ВЫРОВНЯТЬ ПО ЦЕНТРУ, ШРИФТ, TIMES NEW ROMAN 14 BOLD, ЗАГЛАВНЫЕ БУКВЫ

Автор(ы): **А.Б. Первыйавтор[1], В.Г. Автор[2*]** - шрифт Times New Roman 12, bold, по центру

[1]Наименование организации, адрес, страна - шрифт Times New Roman 10, по центру

* e-mail автора, представившего статью - шрифт Times New Roman 10, по центру

Аннотация. Аннотация статьи составляет не более 12 строк. Используйте шрифт Times New Roman 12, одинарный межстрочный интервал.
Ключевые слова: укажите ключевые слова после аннотации.

Как организовать текст статьи. Используйте шрифт Times New Roman 12, одинарный межстрочный интервал. При необходимости выделить какую-либо информацию используйте *курсив*. Используйте **полужирный** шрифт только для заголовков и подзаголовков.

Номера страниц. Пожалуйста, не используйте нумерацию страниц

Таблицы, Рисунки, Уравнения. Подробные правила оформления данных элементов статьи приведены в инструкции на сайте журнала http://www.mpm.spbstu.ru

Литература
Ссылки приводятся в тексте в квадратных скобках [1,3,5-9]. Стиль оформления ссылок:
[1] Koch CC, Ovid'ko IA, Seal S, Veprek S. *Structural Nanocrystalline Materials: Fundamentals and Applications*. Cambridge: Cambridge University Press; 2007.
[2] Hull D, Bacon DJ. *Introduction to Dislocations*. 5nd ed. Amsterdam: Butterworth-Heinemann; 2011 Available from: https://www.sciencedirect.com/science/book// 9780080966724?via%3Dihub [Accessed 19th June 2018].
[3] Romanov AE, Vladimirov VI. Disclinations in crystalline solids. In: Nabarro FRN (ed.) *Dislocations in Solids*. Amsterdam: North Holland; 1992;9. p.191-402.
[4] Mukherjee AK. An examination of the constitutive equation for elevated temperature plasticity. *Materials Science and Engineering: A*. 2002;322(1-2): 1-22.

[5] Soer WA, De Hosson JTM, Minor AM, Morris JW, Stach EA. Effects of solute Mg on grain boundary and dislocation dynamics during nanoindentation of Al–Mg thin films. *Acta Materialia*. 2004;52(20): 5783-5790.
[6] Matzen ME, Bischoff M. A weighted point-based formulation for isogeometric contact. *Computer Methods in Applied Mechanics and Engineering*. 2016;308: 73-95. Available from: doi.org/10.1016/j.cma.2016.04.010.
[7] Joseph S, Lindley TC, Dye D. Dislocation interactions and crack nucleation in a fatigued near-alpha titanium alloy. To be published in *International Journal of Plasticity. Arxiv.* [Preprint] 2018. Available from: https://arxiv.org/abs/1806.06367 [Accessed 19th June 2018].
[8] Pollak W, Blecha M, Specht G. *Process for the production of molded bodies from silicon-infiltrated, reaction-bonded silicon carbide*. US4572848A (Patent) 1983.
[9] Brogan C. *Experts build pulsed air rig to test 3D printed parts for low carbon engines*. Available from: http://www.imperial.ac.uk/news/186572/experts-build-pulsed-test-3d-printed/ [Accessed 19th June 2018].

МЕХАНИКА И ФИЗИКА МАТЕРИАЛОВ

50 (3) 2022

Учредители: Санкт-Петербургский политехнический университет Петра Великого,

Институт проблем Машиноведения Российской академии наук

Издание зарегистрировано федеральной службой по надзору в сфере связи,

информационных технологий и массовых коммуникаций (РОСКОМНАДЗОР),

свидетельство ПИ №ФС77-69287 от 06.04.2017 г.

Редакция журнала

Профессор, д.т.н., академик РАН, А.И. Рудской – главный редактор

Профессор, д.ф.-м.н., член-корр. РАН, Д.А. Индейцев – главный редактор

Профессор, д.ф.-м.н. И.А. Овидько (1961 - 2017) – основатель и почетный редактор

Профессор, д.ф.-м.н. А.Л. Колесникова – ответственный редактор

А.Ю. Ромашкина, к.т.н. – ответственный редактор

Л.И. Гузилова – выпускающий редактор, корректор

Телефон редакции

+7(812)552 77 78, доб. 224

E-mail: mpmjournal@spbstu.ru

Компьютерная верстка Л.И. Гузилова

Подписано в печать xx.xx.2022 г. Формат 60x84/8. Печать цифровая
Усл. печ. л. 10,0. Тираж 100. Заказ____.

Отпечатано с готового оригинал-макета, предоставленного автором
в Издательско-полиграфическом центре Политехнического университета Петра
Великого. 195251, Санкт-Петербург, Политехническая ул., 29.
Тел.: +7(812)552 77 78, доб. 224.

Heat transfer in infinite one-dimensional crystal considering the third coordination sphere 365-372
R.V. Rubinova, O.S. Loboda, A.M. Krivtsov

Synthesis and wear behavior of varying particle sized B4C reinforced Al2618 alloy composites 373-387
G. Veeresha, B. Manjunatha, M. Nagaral, V. Auradi, V. Bharath

Mathematical model of extrusion in FDM 3D printing technology 388-400
O.B. Kudryashova, N.E. Toropkov, M.I. Lerner, A.B. Vorozhtsov

The void evolution kinetics driven by residual stress in icosahedral particles 401-409
A.S. Khramov, S.A. Krasnitckii, A.M. Smirnov, M. Yu. Gutkin

Bearing capacity of spherical thick-walled shell taking into account compressibility and nonlinear plasticity 410-419
I.K. Andrianov, S.I. Feoktistov

Flexible microwave absorbers based on powdered activated coconut charcoal and moisture-containing ceramsite 420-430
O.V. Boiprav, S.E. Savanovich, E.S. Belousova

Grain-boundary nanoprecipitates-mediated mechanism of strengthening in Al-Cu-Zr alloy structured by high-pressure torsion 431-438
M.Yu. Gutkin, N.V. Skiba, T.S. Orlova

Effect of reinforcements on mechanical and tribological behavior of magnesium-based composites: a review 439-458
Dinesh Kumar, Satnam Singh, Surjit Angra

Corrosion cracking of low alloy steels. Testing methods 459-474
A.A. Alhimenko, A.D. Breki. N.O. Shaposhnikov, A.A. Kharkov, E.L. Alekseeva, A.A. Lapechenkov

Strength analysis of thin-wall structures operating in aggressive environments for prolonged periods 475-484
I.G. Emelyanov, A.N. Kislov

Applications of waste egg shell and egg shell membrane: a review 485-494
Naveen Kumar, Ajaya Bharti, Pradeep Kumar

Anisotropic mechanical properties of elastomeric nanocomposites filled by carbon black, few-layer graphene, and carbon nanotubes 495-508
O.K. Garishin, A.L. Svistkov, A.P. Voznyakovskii, I.M. Tchypkina, A.Yu. Neverovskaya, V.V. Shadrin

Impact of forced cooling of the joint zone and thermal effect on the distribution values of residual stress generated by arc welding 509-517
A.V. Tkacheva, E.E. Abashkin

Role of in-situ developed intermetallic phases on the mechanical properties and corrosion behaviour of Mg-Sb- Sn and Mg-Sb-Ca ternary alloys 518-535
S. Vignesh, Rajesh Kumar, A. Srinivasan, U.T.S. Pillai

MPM SCIENTIFIC JOURNAL

MPM, Vol. 50, No. 3, 2022